



The  
University  
Of  
Sheffield.

**The design and performance of a civil marine reactor with regard  
to the thermal performance of the fuel**

**Kris Geraint James**

**A thesis submitted in partial fulfilment of the requirements for  
the degree of Doctor of Philosophy**

**The University of Sheffield**

**Faculty of Engineering**

**Department of Material Science and Engineering**

**July 2017**

## **Dedication**

This PhD is dedicated to Marta, my one and only who has forever been there for me through this process, a massive thank you also goes out to my family for the support and for everything throughout.

## **Abstract**

There is a concerted world wide effort to limit greenhouse gases into the atmosphere [1], [2]. Civil shipping accounts for a 3 % proportion of greenhouse gas emissions [3], [4], and to combat this problem, nuclear power is proposed as an alternative energy source.

This thesis set out to evaluate the use of a civil marine nuclear reactor for commercial shipping purposes. A review was carried out to determine past uses of civil marine nuclear reactors to assist specification of the criteria for a civil ship reactor e.g. reactor type, operating conditions. The refuelling period of such ships was understood as an issue for commercial success and so having fuel in the reactor for periods of 15 years was determined to be a key goal, as well as keeping the fissile enrichment of the fuel low.

Computational simulation of the thermo-mechanical performance on fuel rods under expected operating conditions for a civil marine reactor were conducted. Higher thermal efficiency in the fuel rods was determined to be key in achieving long refuelling periods.

Fabrication of simulant fuel cermets was undertaken with spark plasma sintering to produce simulant cermet fuel pellets with improved thermal conductivity and was evaluated to be an efficient cermet production route. This was achieved with YSZ as a simulant for  $\text{UO}_2$  fuel, with metallic Mo and W to produce stable cermets at varying metallic loading. The thermal conductivity values were found to increase by a factor of 2-3 with up to 30 % metallic loading.

The final aspect of this thesis focused on finite element simulation, studying the shape of metallic loading inside a cermet to determine a suitable layout to provide the greatest thermal transfer with several candidate geometries determined to be appropriately suitable.

## **Acknowledgements**

I have enjoyed the highs and the lows of doing a PhD. Through this process I have had support from colleagues, friends and family. In particular, my wife Marta, has been there from the very start supporting me.

From Sheffield, firstly my supervisor Prof. Neil Hyatt who has put up with me and helped me along this process, my sincere thanks to him. A thank you to other members of academic and technical staff that have assisted me with understanding and staying safe in the lab. In particular Karl, Martin, Claire and Mouldy.

The guys at Manchester, again firstly my supervisor Prof. Tim Abram who has provided a countless amount of tea during our meetings and biscuits, how can I every repay you! Also Joel Turner for his help and support and lunches, as well as Marc Schmidt for his technical knowledge and for trusting me with his equipment!

There are also a countless amount of other postgraduate students and staff between Sheffield and Manchester that have my thanks for their help, as well as providing a great office atmosphere to be in.

## **Nomenclature and Abbreviations**

Symbols and notations are presented below that are commonly used. Others are defined as they appear in the text.

IPCC – Intergovernmental Panel on Climate Change

IMO – International Maritime Organization

GHG – Greenhouse gas

NS – Nuclear ship

PWR – Pressurised water reactor

PCI – Pellet clad interaction

SPS – Spark plasma sintering

FEA – Finite element analysis

FGR – Fission gas release

SEM – Scanning electron microscopy

XAS – X-ray absorption spectroscopy

XRD – X-ray diffraction

$\lambda$  – Thermal conductivity

$\alpha$  – Thermal diffusivity

$\rho$  – Density

$C_p$  – Heat capacity

# Table of Contents

Dedication .....	ii
Abstract .....	iii
Acknowledgements .....	iv
Nomenclature and Abbreviations .....	v
Table of Contents .....	vi
List of Figures .....	xi
List of Tables .....	xvii
Chapter 1 Introduction .....	1
1.1 Background .....	2
1.2 Justification for work .....	3
1.2.1 Shipping emissions .....	3
1.2.2 Price of oil .....	6
1.2.3 Fuel security .....	6
1.3 Other alternatives to nuclear .....	7
1.3.1 Liquid natural gas .....	7
1.3.2 Different fuel oil blends.....	8
1.3.3 Photovoltaics .....	8
1.3.4 Kites.....	9
1.3.5 Ship design .....	10
1.4 Other issues around a marine reactor .....	11
1.4.1 Political .....	11
1.4.2 Crew training .....	11
1.4.3 Security issues .....	12
1.4.4 Owner considerations .....	12
1.4.5 Insurance.....	12
1.5 Other potential uses of a ship's reactor .....	13
1.6 Sponsoring organisation.....	14
1.7 Scope of the project.....	14
1.8 Aims and objectives .....	15
1.9 Thesis structure .....	15
1.10 References .....	16
Chapter 2 Previous marine reactors and potential fuel types.....	20
2.1 Introduction .....	21
2.2 Past civil marine reactors .....	21
2.2.1 NS Savannah .....	21
2.2.2 NS Otto Hahn .....	24

2.2.3 NS Mutsu.....	26
2.2.4 NS Sevmorput .....	28
2.2.4 Russian ice breakers .....	31
2.2.5 Naval marine reactors.....	31
2.2.6 Civil marine reactors summary and discussion .....	31
2.3 Reactor placement and type .....	32
2.3.1 Reactor in the ship .....	34
2.3.2 Mothership.....	35
2.3.3 Reactor placement and type summary and discussion .....	36
2.4 Different nuclear fuel types.....	36
2.4.1 Uranium dioxide.....	37
2.4.2 Uranium nitride .....	38
2.4.3 Uranium silicide .....	39
2.4.4 Uranium carbide .....	40
2.4.5 Uranium molybdenum alloy.....	41
2.4.6 Uranium metal .....	42
2.4.7 Uranium Zirconium Hydride.....	43
2.4.8 Mixed oxide fuel.....	44
2.4.9 Rod/plate design .....	44
2.4.10 Cermet fuels.....	46
2.4.11 Other fuels types not being considered.....	47
2.4.12 Summary and discussion of fuel investigation .....	47
2.5 Conclusions .....	50
2.6 References .....	50
Chapter 3 Civil marine reactor design and thermo-mechanical fuel rod simulation .....	55
3.1 Introduction .....	56
3.2 ENIGMA.....	56
3.3 Fuel failure mechanisms.....	58
3.3.1 Cladding corrosion failure .....	58
3.3.2 Fuel rod swelling, ballooning .....	59
3.3.3 Pellet clad interaction .....	60
3.3.4 Fuel/clad melting .....	61
3.4 Marine reactor design criteria .....	61
3.4.1 Marine reactor type and fuel.....	61
3.4.2 Operating behaviour of proposed reactor .....	62
3.4.3 Fuel rod and reactor design .....	63
3.5 Results and discussions .....	64
3.5.1 UO <sub>2</sub> simulation .....	64

3.5.2 Annular UO <sub>2</sub> fuel pellets .....	68
3.5.3 Plenum increase of fuel rod .....	70
3.5.4 Plenum and annulus hybrid .....	72
3.5.5 Increase grain size of pellets.....	73
3.5.6 Improved UO <sub>2</sub> thermal conductivity pellets.....	75
3.5.7 Improved UO <sub>2</sub> thermal conductivity pellets and annulus.....	77
3.5.8 Improved UO <sub>2</sub> thermal conductivity pellets and increased plenum .....	79
3.5.9 Other literature studies.....	80
3.6 Conclusions .....	81
References .....	84
Chapter 4 Fabrication of simulant cermet nuclear fuels .....	86
4.1 Introduction .....	87
4.2 Experimental techniques .....	88
4.2.1 Powder preparation.....	88
4.2.2 Spark Plasma Sintering (SPS) .....	89
4.2.4 Sample preparation .....	92
4.2.5 Laser flash .....	92
4.2.6 Vickers hardness.....	93
4.2.7 XAS spectroscopy .....	93
4.3 Yttrium stabilised zirconia as a UO <sub>2</sub> fuel simulant.....	93
4.4 Cermets choice and SPS past work .....	94
4.5 Furnace work.....	96
4.6 Materials used .....	98
4.6.1 Powder characterisation.....	98
4.7 Matrix of pellets .....	101
4.8 Yttria stabilised zirconia molybdenum cermets .....	102
4.8.1 Density.....	103
4.8.2 XRD.....	105
4.8.3 SEM analysis .....	108
4.8.4 SEM EDX.....	113
4.8.5 XAS spectroscopy .....	118
4.8.6 Laser flash thermal conductivity .....	120
4.8.7 Hardness testing.....	124
4.9 YSZ W pellets .....	126
4.9.1 Density.....	126
4.9.2 XRD.....	128
4.9.3 SEM analysis .....	131
4.9.4 SEM EDX.....	134

4.9.5 Laser flash thermal conductivity .....	139
4.9.6 Hardness testing.....	142
4.10 Conclusion.....	144
5.10 References .....	147
Chapter 5 Fuel pellet simulation .....	151
5.1 Introduction .....	152
5.1.2 ANSYS software .....	152
5.1.3 Shape of pellet materials .....	155
5.1.4 Material information for simulations.....	156
5.2 Reference simulation and setup .....	157
5.3 Fuel pellet with Mo spherical particles .....	159
5.3.1 Spherical 10 % Mo .....	160
5.3.2 Spherical 20 % Mo .....	162
5.3.3 Spherical 30 % Mo .....	163
5.3.4 Summary.....	164
5.4 Fuel pellet with W spherical particles .....	165
5.4.1 Spherical 10 % W .....	165
5.4.2 Spherical 20 % W .....	166
5.4.3 Spherical 30 % W .....	167
5.4.4 Summary.....	168
5.5 Fuel pellet with 20 % Mo metallic in different designs .....	169
5.5.1 Horizontal strips .....	169
5.5.2 Vertical strips.....	171
5.5.3 Disk spacers.....	173
5.5.4 Grid layout.....	176
5.6 Comparison of simulations .....	178
5.7 Conclusions .....	180
5.8 References .....	182
Chapter 6 Conclusions and recommendations .....	184
6.1 Conclusions .....	185
6.1.1 Design of civil marine reactor .....	185
6.1.2 Fuel design for civil marine reactor.....	187
6.2 Recommendations for further work .....	188
6.2.1 Fabrication of zirconium pellets with metallic material in different forms.....	188
6.2.2 Fabrication of uranium cermets by SPS .....	189
6.2.3 Grain size investigation .....	189
6.2.4 Ansys fuel pellet simulations.....	189
6.2.5 Reactor design .....	190
6.2.7 Other research areas.....	191

6.3 References .....	191
Appendix 1 Experimental Techniques .....	192
A1.1 Density measurements.....	192
A1.1.1 Gas Pycnometer .....	192
A1.1.2 Archimedes principle.....	193
A1.1.3 Geometric .....	193
A1.2 Particle size analysis.....	194
A1.3 Laser flash .....	194
A1.4 X-ray Diffraction.....	197
A1.5 Scanning Electron Microscopy (SEM).....	198
A1.7 XAS spectroscopy .....	202
A1.8 References .....	203

## List of Figures

Figure 1.1 – The distribution of all shipping GHG emissions from a merged data set.	4
Figure 1.2 – Yearly average contribution from all ships and ports of A NO <sub>2</sub> and B SO <sub>2</sub> .	5
Figure 1.3 – Historical price of oil.	6
Figure 1.4 – A SkySails kite attached to a cargo ship.	9
Figure 2.1 – NS Savannah.	22
Figure 2.2 A – Top view of the reactor core for the NS Savannah showing fuel bundles in a circular lattice, B – Side schematic of the NS Savannah showing the reactor compartment in the middle of the ship.	22
Figure 2.3 – NS Otto Hahn.	24
Figure 2.4 – NS Mutsu.	27
Figure 2.5 – NS Mutsu PWR reactor two loop configuration.	28
Figure 2.6 – The Russian nuclear merchant ship Sevmorput.	29
Figure 2.7 – Typical PWR design layout.	33
Figure 2.8 – Mothership configuration showing the rear section of the ship would split from the cargo section.	35
Figure 2.9 – Design of a fuel rod and fuel plate	46
Figure 3.1 – Representation of fuel pellets and cladding to demonstrate pellet clad interaction.	60
Figure 3.2 – Final rod internal pressure or varying power ratings of initial UO <sub>2</sub> fuel rod conditions. The red line indicates the maximum safe limit. Error bars that can be represented are shown.	65
Figure 3.3 – Total FGR from the pellet at varying power ratings of initial UO <sub>2</sub> fuel rod conditions. Error bars that can be represented are shown.	65
Figure 3.4 – The oxidation accumulation for each power rating at the end of each 15 year simulation. Error bars that can be represented are shown.	66
Figure 3.5 – Cladding wall cross section to demonstrate the loss of 10 % wall material to oxidation.	67
Figure 3.6– Final rod temperature from the hottest section of the fuel rod, A Clad surface temperature, B fuel surface temperature, C fuel centreline temperature.	67
Figure 3.7 – Computer aided design drawing using Solidworks of the geometry of an annular pellet.	68
Figure 3.8– Final rod internal pressure for varying annulus diameters at power ratings A 7 kW/m, B 8 kW/m, C 9 kW/m. The red line indicates the maximum safe limit.	69
Figure 3.9 – Total FGR from varying annulus diameters and at power ratings A 7 kW/m, B 8 kW/m, C 9 kW/m.	70

Figure 3.10 – Final rod internal pressure for varying plenum length at power ratings A 7 kW/m, B 8 kW/m, C 9 kW/m. The red line indicates the maximum safe limit.	71
Figure 3.11 – Total FGR from varying plenum length and at power ratings A 7 kW/m, B 8 kW/m, C 9 kW/m.	71
Figure 3.12 – Final rod internal pressure for varying plenum length at power ratings A 7 kW/m, B 8 kW/m, C 9 kW/m. The red line indicates the maximum safe limit.	72
Figure 3.13 – Total FGR from varying plenum length and at power ratings A 7 kW/m, B 8 kW/m, C 9 kW/m.	73
Figure 3.14– Final rod internal pressure for varying grain size at power ratings A 7 kW/m, B 8 kW/m, C 9 kW/m.	74
Figure 3.15 – Total FGR from varying grain size at power ratings A 7 kW/m, B 8 kW/m, C 9 kW/m.	74
Figure 3.16 – Final rod internal pressure for increasing thermal conductivity of UO <sub>2</sub> at power ratings A 7 kW/m, B 8 kW/m, C 9 kW/m.	76
Figure 3.17– Total FGR for increasing thermal conductivity of UO <sub>2</sub> at power ratings A 7 kW/m, B 8kW/m, C 9 kW/m.	76
Figure 3.18 – Centreline end of life temperature with increasing thermal conductivity values at power ratings A 7 kW/m, B 8kW/m, C 9 kW/m.	77
Figure 3.19 – Final rod internal pressure for increasing thermal conductivity of uranium oxide at power ratings A 7 kW/m, B 8 kW/m, C 9 kW/m all with an annulus diameter of 0.004 m and D 7 kW/m, E 8 kW/m, F 9 kW/m with an annulus diameter of 0.002 m.	78
Figure 3.20 – Total FGR for increasing thermal conductivity of UO <sub>2</sub> at power ratings A 7 kW/m, B 8 kW/m, C 9 kW/m all with an annulus diameter of 0.004 m and D 7 kW/m, E 8 kW/m, F 9 kW/m with an annulus diameter of 0.002 m.	78
Figure 3.21 – Final rod internal pressure for increasing thermal conductivity of UO <sub>2</sub> at power ratings A 7 kW/m, B 8 kW/m, C 9 kW/m all at a plenum height of 0.25 m.	79
Figure 3.22 – Total FGR for increasing thermal conductivity of UO <sub>2</sub> at power ratings A 7 kW/m, B 8 kW/m, C 9 kW/m all at a plenum height of 0.25 m.	80
Figure 4.1 – Dried milled powder before being removed for sieving.	88
Figure 4.2 – Sieve apparatus for uniform powder size.	88
Figure 4.3 – A – Graphite die with graphite paper lining inside, graphite plungers and graphite disks. B – Graphite die assembled with plungers and green powder inside.	89
Figure 4.4 – Schematic of an SPS main equipment.	90
Figure 4.5 – SPS equipment during a run, with the main chamber right, control panel left.	91
Figure 4.6 – Two pellets sintered by SPS after graphite paper removed.	91
Figure 4.7 – YSZ 10 % Mo fabricated pellet sintered in an open air muffle furnace.	96
Figure 4.8 – YSZ with 10% Mo pellets sintered in a tube furnace with argon atmosphere held at 1300°C for 4 hours.	97

Figure 4.9 –XRD pattern of green yttria-stabilised zirconium powder used for pellet fabrication.	99
Figure 4.10 –XRD pattern of green metallic molybdenum powder used for pellet fabrication.	100
Figure 4.11–XRD pattern of green metallic tungsten powder used for pellet fabrication.	100
Figure 4.12 – YSZ 10 % Mo sample after grinding wheel has removed graphite paper and interaction layer. A – Whole SPS pellet, B – Top part after core drilling, C – Bottom part after core drilling with chips on the side.	103
Figure 4.13 – Density of fabricated YSZ Mo cermets at each temperature by Archimedes method, geometrically, and theoretical density error bars with standard deviation of greater than 0.01 shown.	104
Figure 4.14 – Density of fabricated Mo pellets at each temperature by water immersion method, error bars with standard deviation of greater than 0.01 shown.	105
Figure 4.15 – Normalised XRD patterns of molybdenum samples heated at 1300°C.	106
Figure 4.16 – Normalised XRD patterns of molybdenum samples heated at 1400°C.	107
Figure 4.17 – Normalised XRD patterns of molybdenum samples heated at 1500°C.	107
Figure 4.18 – Normalised XRD patterns of molybdenum samples heated at 1600°C.	108
Figure 4.19 – SEM backscattered micrographs are control samples of YSZ at magnifications 100x, 1000x, and 2000x; A, B, C heated at 1300°C; D, E, F heated at 1400°C; G, H, I heated at 1500°C; J, K, L heated at 1600°C.	109
Figure 4.20 – SEM backscattered micrographs of 10 % Mo sample at magnifications 100x, 1000x, and 2000x; A, B, C heated at 1300°C; D, E, F heated at 1400°C; G, H, I heated at 1500°C; J, K, L heated at 1600°C.	110
Figure 4.21 – SEM backscattered micrographs of 20 % Mo sample at magnifications 100x, 1000x, and 2000x; A, B, C heated at 1300°C; D, E, F heated at 1400°C; G, H, I heated at 1500°C; J, K, L heated at 1600°C.	111
Figure 4.22 – SEM backscattered micrographs of 30 % Mo sample at magnifications 100x, 1000x, and 2000x; A, B, C heated at 1300°C; D, E, F heated at 1400°C; G, H, I heated at 1500°C; J, K, L heated at 1600°C.	112
Figure 4.23 –SEM micrograph of EDX scanned area and EDX scans of each element composition present. Samples are control samples of YSZ; A, B heated at 1300°C; C, D heated at 1400°C; E, F heated at 1600°C.	114
Figure 4.24 –SEM micrograph of EDX scanned area and EDX scans of each element composition present. Samples are 10 % Mo; A, B heated at 1300°C; C, D heated at 1400°C; E, F heated at 1500°C; G, H heated at 1600°C.	115
Figure 4.25 –SEM micrograph of EDX scanned area and EDX scans of each element composition present. Samples are 20 % Mo; A, B heated at 1300°C; C, D heated at 1400°C; E, F heated at 1500°C; G, H heated at 1600°C.	116
Figure 4.26 –SEM micrograph of EDX scanned area and EDX scans of each element composition present. Samples are 30 % Mo; A, B heated at 1300°C; C, D heated at 1400°C; E, F heated at 1500°C; G, H heated at 1600°C.	117

Figure 4.27 – XAS patterns of the 10 %, 20 %, and 30 % Mo pellet compositions, Mo foil, MoO <sub>2</sub> , and MoO <sub>3</sub> .	119
Figure 4.28 – XAS patterns from the literature of other studies done using Mo metal, MoO <sub>2</sub> , and MoO <sub>3</sub> samples.	119
Figure 4.29 – Thermal conductivity of Mo samples fabricated at 1300°C of composition; A 100 % YSZ, B 10 % Mo, C 20 % Mo, D 30 % Mo. Error bars on data with a standard deviation of greater than 0.1.	121
Figure 4.30 – Thermal conductivity of Mo samples fabricated at 1400°C of composition; A 100 % YSZ, B 10 % Mo, C 20 % Mo, D 30 % Mo. Error bars on data with a standard deviation of greater than 0.1.	122
Figure 4.31 – Thermal conductivity of Mo samples fabricated at 1500°C of composition; A 100 % YSZ, B 10 % Mo, C 20 % Mo, D 30 % Mo. Error bars on data with a standard deviation of greater than 0.1.	122
Figure 4.32 – Thermal conductivity of Mo samples fabricated at 1600°C of composition; A 100 % YSZ, B 10 % Mo, C 20 % Mo, D 30 % Mo. Error bars on data with a standard deviation of greater than 0.1.	123
Figure 4.33 – Vickers hardness of YSZ Mo samples for each sintering temperature.	125
Figure 4.34 – Vickers hardness of YSZ Mo samples for each sample comparatively shown for each Mo loading. Error bars have been removed for clarity.	125
Figure 4.35 – Density of fabricated YSZ W cermets at each temperature by Archimedes method and geometrically, error bars with standard deviation of greater than 0.01 shown.	127
Figure 4.36 – Density of fabricated W pellets at each temperature by water immersion method, error bars with standard deviation of greater than 0.01 shown.	127
Figure 4.37 – Normalised XRD patterns of W samples heated at 1300°C.	129
Figure 4.38 – Normalised XRD patterns of W samples heated at 1400°C.	129
Figure 4.39 – Normalised XRD patterns of W samples heated at 1500°C.	130
Figure 4.40 – Normalised XRD patterns of W samples heated at 1600°C.	130
Figure 4.41 – SEM backscattered micrographs of 10 % W sample at magnifications 100x, 1000x, and 2000x; A, B, C heated at 1300°C; D, E, F heated at 1400°C; G, H, I heated at 1500°C; J, K, L heated at 1600°C.	132
Figure 4.42 – SEM backscattered micrographs of 20 % W sample at magnifications 100x, 1000x, and 2000x; A, B, C heated at 1300°C; D, E, F heated at 1400°C; G, H, I heated at 1500°C; J, K, L heated at 1600°C.	133
Figure 4.43 – SEM backscattered micrographs of 30 % W sample at magnifications 100x, 1000x, and 2000x; A, B, C heated at 1300°C; D, E, F heated at 1400°C; G, H, I heated at 1500°C; J, K, L heated at 1600°C.	134
Figure 4.44 – SEM micrograph of EDX scanned area and EDX scans of each element composition present. Samples are 10 % W; A, B heated at 1300°C; C, D heated at 1400°C; E, F heated at 1500°C; G, H heated at 1600°C.	136

Figure 4.45 –SEM micrograph of EDX scanned area and EDX scans of each element composition present. Samples are 20 % W; A, B heated at 1300°C; C, D heated at 1400°C; E, F heated at 1500°C; G, H heated at 1600°C.	137
Figure 4.46 –SEM micrograph of EDX scanned area and EDX scans of each element composition present. Samples are 30 % W; A, B heated at 1300°C; C, D heated at 1400°C; E, F heated at 1500°C; G, H heated at 1600°C.	138
Figure 4.47 – Thermal conductivity of W samples fabricated at 1300°C of composition A 100 % YSZ, B 10 % W, C 20 % W, D 30 % W. Error bars on data with a standard deviation of greater than 0.1.	140
Figure 4.48 – Thermal conductivity of W samples fabricated at 1400°C of composition A 100 % YSZ, B 10 % W, C 20 % W, D 30 % W. Error bars on data with a standard deviation of greater than 0.1.	140
Figure 4.49 – Thermal conductivity of W samples fabricated at 1500°C of composition A 100 % YSZ, B 10 % W, C 20 % W, D 30 % W. Error bars on data with a standard deviation of greater than 0.1.	141
Figure 4.50– Thermal conductivity of W samples fabricated at 1300°C of composition A 100 % YSZ, B 10 % W, C 20 % W, D 30 % W. Error bars on data with a standard deviation of greater than 0.1.	141
Figure 4.51 – Vickers hardness of YSZ W samples for each sintering temperature.	143
Figure 4.52 – Vickers hardness of YSZ W samples for each sample comparatively shown for each Mo loading. Error bars have been removed for clarity.	144
Figure 5.1 – Example of meshing used in Ansys; A – Pellet of one material, B – Mesh applied to pellet in A, C – Pellet with two different materials, D – Mesh applied to pellet shown in C.	153
Figure 5.2 – Representation of a 2D half axis of symmetry YSZ pellet in ANSYS for thermal simulation.	158
Figure 5.3 – 2D simulation of YSZ pellet at steady state conditions with contour plot and plot of the temperature gradient across the pellet.	159
Figure 5.4 – Representation of a 2D half axis of symmetry spherical 10 % Mo evenly distributed in ANSYS for thermal simulation.	160
Figure 5.5 – 2D simulation of spherical 10 % Mo at steady state conditions and temperature gradient plot of A – pure YSZ pellet, B – spherical 10 % Mo pellet.	161
Figure 5.6 – Representation of a 2D half axis of symmetry spherical 20 % Mo evenly distributed in ANSYS for thermal simulation.	162
Figure 5.7 – 2D simulation of spherical 20 % Mo at steady state conditions and temperature gradient plot of A – pure YSZ pellet, B – spherical 20 % Mo pellet.	163
Figure 5.8 – Representation of a 2D half axis of symmetry YSZ pellet with 30% Mo as spherical particles evenly distributed in Ansys for thermal simulation.	164
Figure 5.9 – 2D simulation of YSZ pellet with 30% Mo as spherical particles at steady state conditions with uniform contour plot.	165
Figure 5.10 – 2D simulation of YSZ pellet with 10% W as spherical particles at steady state conditions with uniform contour plot.	167

Figure 5.11 – 2D simulation of YSZ pellet with 20% W as spherical particles at steady state conditions with uniform contour plot.	168
Figure 5.12 – 2D simulation of YSZ pellet with 30% W as spherical particles at steady state conditions with uniform contour plot.	169
Figure 5.13 – Representation of a 2D half axis of symmetry YSZ pellet with 20% Mo as metal filing particles evenly distributed horizontally in Ansys for thermal simulation.	171
Figure 5.14 – 2D simulation of YSZ pellet with 20% Mo as metal filing particles evenly distributed horizontally at steady state conditions with uniform contour plot.	172
Figure 5.15 – Representation of a 2D half axis of symmetry YSZ pellet with 20% Mo as metal filing particles evenly distributed vertically in Ansys for thermal simulation.	173
Figure 5.16 – 2D simulation of YSZ pellet with 20% Mo as metal filing particles evenly distributed vertically at steady state conditions with uniform contour plot.	174
Figure 5.17 – Representation of a 2D half axis of symmetry YSZ pellet with Mo disks top and bottom in Ansys for thermal simulation.	176
Figure 5.18 – 2D simulation of YSZ pellet with Mo disks top and bottom at steady state conditions with uniform contour plot.	177
Figure 5.19 – Representation of a 2D half axis of symmetry YSZ pellet with 20% Mo in the form of a connect grid in Ansys for thermal simulation.	178
Figure 5.20 – 2D simulation of YSZ pellet with Mo in the form of a connect grid at steady state conditions with uniform contour plot.	179
Figure 5.21 – All simulations undertaken with a non-uniform contour plot for comparison.	180

## List of Tables

Table 2.1 – NS Savannah ship and reactor specifications.	23
Table 2.2 – NS Otto Hahn ship and reactor specifications.	25
Table 2.3 – NS Mutsu ship and reactor specifications.	27
Table 2.4 – Sevморput ship and reactor specifications.	30
Table 2.5 – UO <sub>2</sub> material properties at standard conditions.	38
Table 2.6 – Uranium nitride material properties at standard conditions.	39
Table 2.7 – Uranium silicide material properties at standard conditions.	40
Table 2.8 – Uranium carbide material properties at standard conditions.	41
Table 2.9 – Uranium molybdenum material properties at standard conditions.	42
Table 2.10 – Uranium metal material properties at standard conditions.	43
Table 2.11 – Uranium zirconium hydride material properties at standard conditions.	44
Table 2.12 – Mixed oxide material properties at standard conditions.	44
Table 2.13 – Summary of advantages and disadvantages to taking forward the discussed fuel types for a civil marine reactor.	49
Table 3.1 – Design criteria used for ENIGMA simulations.	63
Table 3.2 – Fuel rod key criteria design safety limits.	64
Table 3.3 – Calculation for the oxidation limit of the clad wall.	66
Table 3.4 – 10 year and 15 year burn-up for each linear power rating of simulated.	81
Table 4.1 – Summary table of different methods tried to sinter CeO <sub>2</sub> 10 % Mo and YSZ 10 % Mo.	97
Table 4.2 – Summary of YSZ and YSZ 10 % Mo testing conditions via SPS that did not form a stable solid pellet.	98
Table 4.3 – Powder density of material measured by a gas pycnometer.	98
Table 4.4 – Particle size analysis of green powders.	99
Table 4.5 – List of pellets fabricated with their volume percentage content of each material and heating conditions.	102
Table 4.6 – Tabulated values from laser flash testing of all Mo fabricated samples.	123
Table 4.7 – Tabulated values from laser flash testing of all W fabricated samples	142
Table 4.8 – Comparison of the averaged Vickers hardness measurements of the fabrication temperatures 1300°C, 1400°C, 1500°C, and 1600°C for each loading content of Mo and W.	144
Table 5.1 – Material properties used for FEA simulation.	156
Table 6.1 – Proposed design criteria for civil marine reactor, developed by the research conducted in this thesis.	190

## **Chapter 1 Introduction**

## 1.1 Background

Anthropological climate change has now been accepted as a worldwide problem. There is a wide consensus that great efforts are required if catastrophic climate change is to be avoided. Greenhouse gas emissions, currently, and in the future, will have serious consequences from environmental to economic issues. Among climate change scientists, it is widely believed a 2°C world rise in average temperature will be the tipping point for irreversible climate change. However, we do not know with any confidence what will happen past this 2°C rise [1], [2].

Efforts are being made by governments to tackle climate change to reduce CO<sub>2</sub> emissions to 1992 levels [2]. Contributing areas are being identified and combated individually, such as electricity generation, transportation, and improved efficiency of households and industries. One approach is legislation that is designed to either moderate, or encourage by incentive, use of cleaner fuels and practices. For example, the European large combustion plant directive, which limits the amount of emissions that large scale (50 MW and above) power plants can produce [5]. In some circumstances, conventional fuel use is not able to be adapted economically and so other environmentally cleaner fuels sources are used. Other approaches are applied such as higher taxes on transport fuel or the use of carbon credits on an international level.

One focus for reduced CO<sub>2</sub> emissions which has not attracted considerable attention is global shipping. A reason for this is the shipping industry is very complex and is an international business, rather than a single state which would be easier to regulate. Currently, ship owners will register their ships in a different country to where they are operationally based in order to avoid regulation [6]. In a recent maritime report, Panama and Liberia had the most ships registered with 7068 and 3126 respectively, as they offer low regulation to ship owners, as well as low taxation [7].

However, there is momentum to tackle the issue of reducing CO<sub>2</sub> emissions from maritime transits, which forms the basis for this project to evaluate an alternative power source for shipping. Potentially this might be achieved in different ways, as elaborated below, but this project seeks to understand how the experience and knowledge available from on shore civil and current naval reactor technology could be used to develop a design for a marine reactor to be used for civil ships.

The project's main focus of research is to develop a nuclear fuel concept to be utilised in the reactor. To be viable, a commercial marine reactor will need to operate for long periods of time without having to be refuelled, unlike every one to two years for conventional land electrical generation reactors, such as PWRs [8]. At the same time, such a reactor would need to utilise low enriched fuel material to be acceptable with non-proliferation treaty norms.

## **1.2 Justification for work**

### **1.2.1 Shipping emissions**

One of the drivers behind this thesis is to use alternative methods to power the world's ships in order to reduce the amount of GHG emissions currently produced. The IMO has commissioned several reports that found that global shipping contributed 3.3 % in 2009 [3] and 3.1 % in 2014 [4] to world GHG emissions. To note, CO<sub>2</sub> is by far the most significant GHG emitted with respect to methane, nitrous oxide, and other fluorinated oxides and has remained that way for previous decades according to an EPA report [9] based on WRI (World Resource Institute) climate data. As such, the biggest driver of reducing GHG emissions is targeted at CO<sub>2</sub> emissions, with the intended consequence of also reducing other GHG's.

Aviation GHG emissions, for comparison, are reported to contribute 2 % to world total GHG emissions by the International Civil Aviation Organization (ICAO) [10]. A 2010 IMO report drew a comparison of the size of world shipping GHG emissions to be equivalent to the

emissions produced by countries such as Brazil and Japan estimated at 2 % and 3 % respectively of GHG emissions.[11].

A global map of calculated yearly GHG emissions (Figure 1.1) from shipping, shows the areas that are most impacted [12]. The map has been compiled from different mathematical predictive calculations by Dalsøren [12] and, in essence, shows the main concentration areas of GHG emissions.

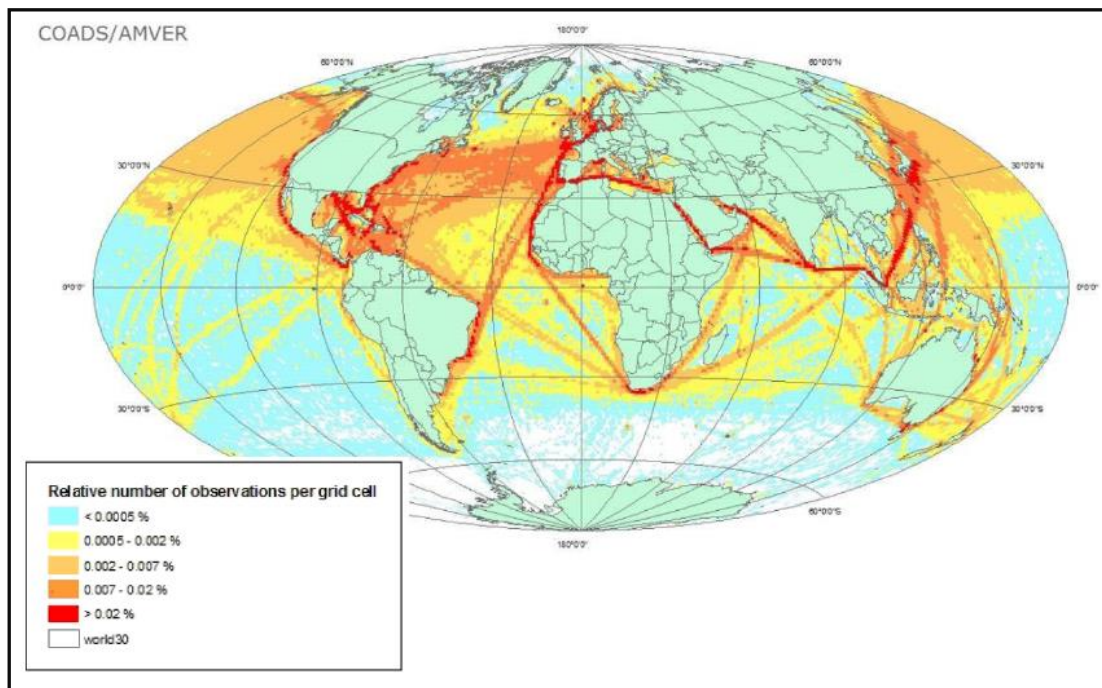


**Figure 1.1 – The distribution of all shipping GHG emissions from a merged data set [12].**

Dalsøren also found, using a chemical transport model, that the dominant contributor to NO<sub>2</sub> and SO<sub>2</sub> levels in the world’s oceans was from shipping. These emissions have been visually modelled (Figure 1.2) and show the world’s most effected regions [12], such as transit routes from east Asia to Europe through the Suez canal, as well as routes that follow the coast line of Africa, North, and South America, which are indicated by the regions in red. Thus coastal populations have been adversely impacted with regard to GHG emissions of carbon particulates, NO<sub>2</sub>, and SO<sub>2</sub>.

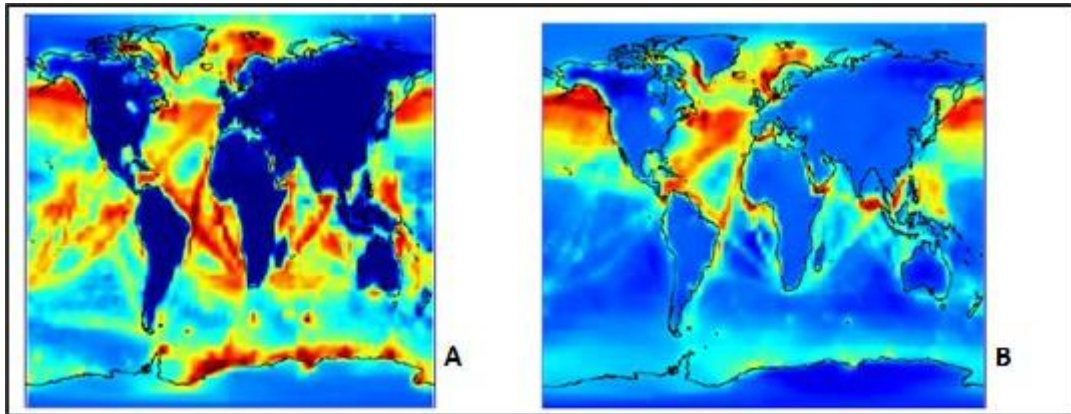


**Figure 1.2 – Yearly average contribution from all ships and ports of A NO<sub>2</sub> and B SO<sub>2</sub> [12].**

NO<sub>2</sub> and SO<sub>2</sub> are GHGs that have some of the biggest effect on atmosphere components aside from CO<sub>2</sub>. This has been recognised by world bodies who call for the IMO to take action on the contribution of maritime transport, due to the fact that international shipping is not linked to one country and is therefore a separate entity. One approach to combat this issue is the further implementations of ECA (Emission Control Areas) in zones that have higher GHG emissions and target certain specific gases such as NO<sub>2</sub> and SO<sub>2</sub>. These zones exist in places such as the North Sea and Baltic Sea[13] which limit sulphur content of fuel to <1 % and limits to come into force in 2020 will be <0.1 % [14], and could be implemented in the affected areas in Figure 1.1-1.2. A quick solution for ship owners would be to use low sulphur fuels as one option. Ultimately, this links to higher costs to owners for either paying fines for noncompliance or having to pay higher costs due to purchasing low sulphur fuel.

The argument given to move towards a non GHG power source, such as nuclear, has two aspects. The first is a moral objective as the world tries to reduce its reliance on GHG forms of energy, and as the international shipping industry is a large contributor, it should look at ways in which it can do this. Secondly, costs for fines or possibly permits required in the future to

restrict the use of GHG fuels in ships could be avoided and ship owners could help their financial situations if they were to use a non GHG fuel source.

### 1.2.2 Price of oil

The price of oil has been shown over the past decade to fluctuate significantly from high to low prices, as shown in Figure 1.3. This causes unpredictability for ship owners over the operating costs. In contrast, the fuel for a nuclear reactor would be paid for ahead of time, reducing uncertainty. The capital cost of a nuclear reactor, as well as security for the ship when sailing have to be considered, but the benefit to a ship owner having fixed costs for a 15 year period is a huge advantage.

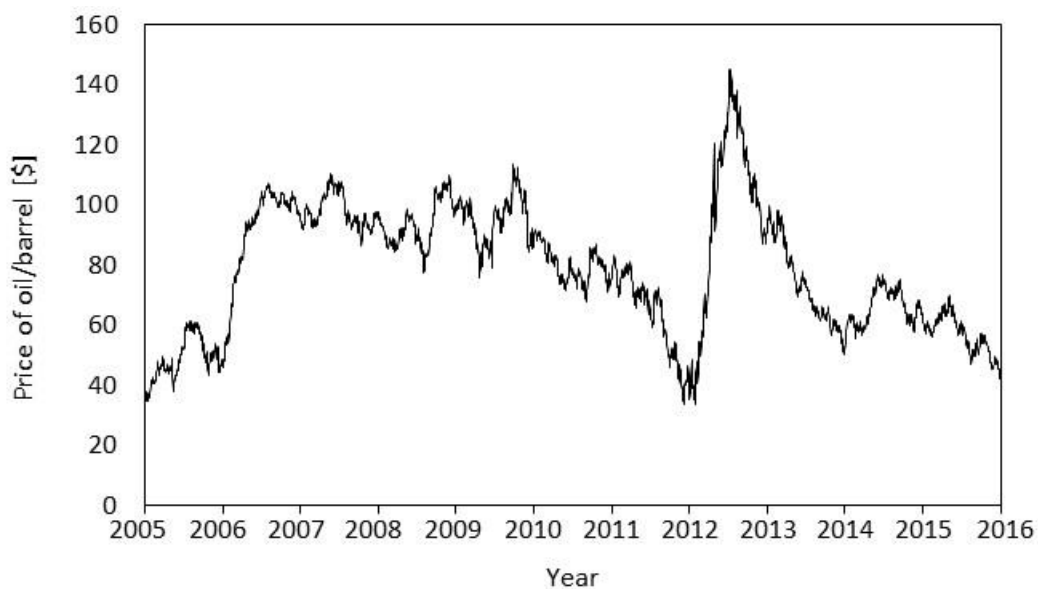


**Figure 1.3 – Historical price of oil [15].**

### 1.2.3 Fuel security

A nuclear powered ship would operate with well-known and essentially stable fixed costs, so a ship operator would have the advantage that all the fuel is paid for, and that capital and disposal costs are known. Therefore, a ship can sail at a designed speed rather than at low speed

or slow steaming in order to save fuel, since speed has an exponential relationship with the power required to sail at that speed [16], [17].

Further benefits here would be that the ship would not have to load fuel each time in port, although there would be no time gain as the ship will be docked for at least half a day for cargo unloading [18]. There is also the reduction of labour activity for this function, as well as reducing the chance of fuel spills or accidents during this process.

### **1.3 Other alternatives to nuclear**

Discussed in brief here are other options that potentially could be used to solve the same problems that the design of a civil marine nuclear reactor is setting out to address.

#### **1.3.1 Liquid natural gas**

Liquid natural gas (LNG) is a fuel source that could be used to provide a cleaner fuel than conventional marine fuel [19]. The concept is for smaller ships and vessels rather than the larger container ships that this project is considering. This approach might be more suitable for vessels constrained to national waters such as tugs, pilot boats and fishing vessels [20] that operate in a local vicinity so that the infrastructure could be installed for refuelling at one central point. Initially, there would be a requirement for central refuelling, as the cost of implementing a new fuel system would be high, as LNG is more volatile than conventional fuel, and thus the delivery mechanisms for distribution have to be more robust [21].

A key disadvantage in using LNG is that it is still a CO<sub>2</sub> emitting fuel source. The use of LNG would ultimately lead to an increase in global demand due to the volume required to power large ships. A further growth in world refining capacity would be envisaged in order to accommodate the extra demand, with current demand for natural gas expected to increase by 2

trillion m<sup>3</sup> by the year 2040 [21] for current usage needs. Similar to oil prices, LNG fuel also follows trends in price fluctuation [22], which gives an uncertain cost to owners.

### **1.3.2 Different fuel oil blends**

A considerable amount of marine fuel used in conventional engines is heavy fuel oil, which contains sulphur contents of 3.5 % or less and produces high emissions and particulates. One way to tackle this issue, currently used in emission controlled zones, is the use of marine distillate fuels, or low sulphur residual fuel, which have lower sulphur content of 1 % or less [23]. These are more expensive due to the refining process required and, if carried out on a larger scale, would need investment in refining facilities to increase production. This would then have the knock on effect of crashing the price of heavy oil fuel as there would be lower demand. If the heavy fuel oil would not be used then other solutions on how to use or dispose of it would need to be considered.

### **1.3.3 Photovoltaics**

An area that is currently being investigated is the use of photovoltaics to generate electrical power for a ship. Large container and oil tanker ship types have a large surface area on the top of the ship, as well as on the sides, which could be suitable for mounting photovoltaics. Especially with oil tankers, there are surface areas that are not needed for access or loading and unloading of cargo. Studies have been undertaken to evaluate hybrid photovoltaic/diesel ships and show a good reduction in GHG emissions, if high photovoltaics penetration is achieved over the lifetime of a ship's operation [24]. Photovoltaic penetration is a measure of how efficient a photovoltaic is at converting available power.

Photovoltaics are being investigated for applications providing all of a ship's power. In 2010, the MS Turanor was launched as a 530 m<sup>2</sup> catamaran and uses lithium ion batteries to store

electrical energy [25]. This was the also the first photovoltaic powered ship to circumnavigate the world.

However, with current application of technology, this method will only subsidise the power requirements for a large ship. The MS Turanor is made from composite materials and is a catamaran design [25], which reduces the drag significantly compared with a large ship such as a container ship. Therefore, the power requirements are much smaller, and so it is yet to be proven if the efficiency of photovoltaics could be improved to produce the power requirements for a large ship, such as the Emma Maersk propulsion requirement of 81 MWe [26].

### 1.3.4 Kites

A further method for cutting emissions is to return back to the ancient concept of a sail. There are different concept implementations of the sail, such as with traditional masts. However, a Hamburg based company called SkySails GmbH, is the market leader on adapting a large kite like device attached to the bow end of a ship for propulsion, Figure 1.4. These kites propel the ship forward, and depending on the wind strength and size of vessel, the company claims they can save on fuel consumption from anywhere between 10 % to 35 % [27].



**Figure 1.4 – SkySails kite attached to a cargo ship [28].**

Again, similar to photovoltaics, the use of a kite or other device to harness wind power would make a useful contribution to a civil marine reactor system and should be considered in the future to complement once a viable civil marine reactor system has operating experience.

### **1.3.5 Ship design**

Different techniques on the paint used for a ship have been considered. Firstly, paint has been evaluated to reduce the drag that a ship makes through the water. Work with a riblet painted surface applied has been shown to last several years and reductions of 5.2 % in fuel consumption have been measured [29]. The riblet surface is a non-smooth surface that is applied so that the direction of flow of water is unaffected, an example would be a corrugated surface.

A second method of applying an anti-fouling paint to the bottom of ships' hulls is a long standing method which has had improvements over the years. This paint prevents barnacles and other marine life from sticking to the hull, thus keeping the ship streamlined, thus reducing fuel consumption and also CO<sub>2</sub> emissions. The improvements in recent years have had environmental implications by introducing tributyltin based compounds into the paint formulations, which have a high toxicity to marine species [30].

The speed and power required for a ship is an exponential relationship, with going from 10 to 20 knots might require 3-4 times more power depending on ship weight and design, so in times when oil price is high and to reduce emissions, merchant ships run at reduced speeds known as slow steaming from 25 knots to 20 knots (28.8 mph and 23.0 mph respectively). Some have reduced further and coined the name "super slow speeds" travelling at 12 knots (14 mph) [31].

The different paint techniques and slow steaming are again methods to help mitigate and improve the efficiency of existing oil powered ships. All of these methods can be combined

into a civil marine reactor ship in order for it to operate at high efficiency, but they do not provide a credible alternative on their own.

## **1.4 Other issues around a marine reactor**

There are many issues related to this project that need to be tackled, with this thesis concentrating on the technical issues surrounding the operation and nuclear fuel of a civil marine reactor. However, other issues such as social, political, and general considerations are discussed in brief to acknowledge and appreciate the amount of work and thought that will need to be undertaken if a civil marine reactor were to be built and operated.

### **1.4.1 Political**

Nuclear powered ships are not a recent innovation, but they have been mainly deployed in the naval sector. Naval ships operate in their own territorial water, international waters or partner countries. The aim of a civil marine reactor is to be used in shipping, such as container ships, which operate in multiple countries, and therefore agreement would be required for a country to allow a civil nuclear vessel to operate in its waters.

Proliferation is another contentious area, as more civil nuclear vessels means more mobile nuclear material. This would be an area to further investigate and to determine what the scope of the problem would be, and possible mitigations.

### **1.4.2 Crew training**

The crew that would operate and run a civil marine reactor would have to be highly trained and vetted. The crew that operated the first ever nuclear ship, NS Savannah had 15 months of training before they began operating on the ship [32]. In the naval area, submariners involved in running the nuclear plant can take decades to be qualified up to the rank of chief engineer. Therefore, hiring, training, and maintaining a skilled crew would need to be investigated.

### **1.4.3 Security issues**

The security of a civil nuclear vessel would be a high priority to develop beyond this thesis. Civil nuclear vessels have, and do, operate in the world currently so similar practices would have to be implemented. The most concerning threats to consider would be terrorist attacks and modern day pirating. There could be fail safe mechanisms such as ways to render the reactor and nuclear material unusable, as well as placing conventional armed security personnel on board these ships to deter and protect.

These ships may have to avoid certain designated high risk areas and may have some standard of higher monitoring than other merchant ships.

### **1.4.4 Owner considerations**

Usually, big shipping companies finance, run, and operate a new ship for the transportation of goods. After a period of time they replace the vessel with another new ship, and therefore sell the substandard vessel onto a smaller shipping company. Therefore, a ship may pass through many owners over its years of service before being scrapped. In the case of a civil nuclear ship a different ownership model of cradle-to-grave would need to be implemented. This might be similar to current LNG ships that are specially designed to carry cargo and only a smaller number of shipping companies employ this type of ship, and hence generally own the ship for its entire life.

### **1.4.5 Insurance**

Every part of a ship's life has some form of insurance, from the owner and personnel, to the operator and ship builder. With a nuclear reactor in a civil ship and the risk of an environmental accident, how the costs might change and affect each party has to be considered.

## **1.5 Other potential uses of a ship's reactor**

The following are some other potential ideas that have been proposed in the past as side benefits of a marine nuclear reactor.

Homes F Crouch in 1962 discerned that chemical tankers can be required to keep their cargo at certain viscosities, so heating in the form of pressurised steam can be required. This is an energy intensive process but harnessing the by-product heat from the reactor could bring efficiency savings. Similarly, on a smaller scale, general heating for the ship could be provided for the manned rooms and spaces [33].

Homes F Crouch also proposed that the reactor in a bulk carrier could be used for sterilisation of food goods such as meats, grain, potatoes, fruit and milk. This would make use of the gamma rays from the reactor to kill off any foreign bodies such as bacteria, microorganisms and insects, thus limiting the need of refrigeration [33].

A further use could be that a production or refining process could be carried out on the ship, so that it would load up the raw material at one port, and then in the time it has taken to reach its intended destination, convert the raw product into a useful product.

There are Russian designs for floating nuclear power plants (FNPP) that make use of a nuclear reactor and will be able to connect to land to provide power to remote locations [34]. Similarly, when a merchant ship is in port there could be an application to connect to land to sell electrical power to the shore. Navy ships are able to connect cables to another ship that have had a failure so a similar technique could be applied, thus bringing in more revenue for the ship owner. As a marine nuclear reactor is aimed at reducing GHG emissions, it also solves the problem of a ship having to turn off its engine by having its energy needs met by another method, such as a shore to ship connection proposed [35] to reduce port CO<sub>2</sub> emissions.

## **1.6 Sponsoring organisation**

This project is being industrially collaborated with Rolls-Royce. They have been involved with the design and fabrication of nuclear marine reactors for naval use for the UK submarine fleet since 1960. This, so far, has not been a commercial business area they have been involved in, so with a general industry interest in the area of civil marine reactors they are exploring if their current skills and expertise could contribute to the design and implementation of a civil marine reactor. For this project they have contributed assistance in being a sounding wall for how certain aspects might work in practice, guidance on manufacturing, and to get a gauge on problems and requirements in the marine setting for a reactor.

## **1.7 Scope of the project**

This project is starting out with a blank canvas approach. Therefore, the focus of the project could have considered many different aspects related to the technical topic of a civil marine reactor. Initial limits of investigation were set related to nuclear reactor: the type such as a BWR, PWR, and gas cooled reactor, operation behaviours including operating temperature, pressure, size and shape of reactor fuel rods, enrichment of fuel, and nuclear fuel to be used be it uranium, plutonium, or thorium. Elements such as the naval architecture, emergency power systems, and refuelling procedures are left for future investigation.

The project has investigated the past use of civil marine reactors and other connected research to set out a base design criteria for such a system. The project has focused on one area of interest of the reactor, which is the fuel type to be used for such a system, how the reactor will operate and how it will behave based on the type of fuel and reactor system that is chosen.

## **1.8 Aims and objectives**

The initial work was to understand what relevant research had been undertaken previously in order to narrow down the area for detailed investigation. This information was used to assist in deciding the design criteria for a civil marine reactor. The main objectives of this project are:

- Investigate which civil marine reactors have been used in the past to assess requirements for this project.
- Set out a design criteria for a marine reactor, including how it will operate to power requirements and reactor mechanical and thermal conditions.
- Establish the fuel type that will be used in a civil marine reactor, its composition and how it will behave over its life time.
- Simulate how a fuel rod will behave in the designs set out for a civil marine reactor, and what if any fuel failure mechanisms come into play.
- Investigate the use of an improved fuel type that a civil marine reactor could use and help extend the lifetime of a core between refuelling.

## **1.9 Thesis structure**

The thesis is made up of 6 chapters with each one detailing the following:

Chapter 1 – Provides a brief introduction to the topic of the thesis, a background of why the work has come about, with aims and objectives and, in brief, other issues of interest for the project that are not covered in the main work of the thesis.

Chapter 2 – Investigation into what research has previously been carried out in relation to civil marine reactors and how they were operated. It also details the investigation work done on different fuel types for light water reactors that could be options for a civil marine reactor.

Chapter 3 – This is the first results chapter and details the simulation work using the software Enigma investigating the behaviour with regards to thermal and mechanical properties of a fuel rod set in the conditions for a civil marine reactor. Different designs for the fuel rod were undertaken in order to improve its operating lifetime.

Chapter 4 – The second results chapter details the fabrication and characterisation of simulant cermet fuel pellets using the method of spark plasma sintering and summarises the experimental methods used. The main area of interest is to determine the improvement on the thermal conductivity of the cermets to determine the most suitable combination of metallic and ceramic components.

Chapter 5 – Details the simulation work carried out using finite element software to simulate fuel pellets thermal behaviour and to look at different ways in which the metallic component can be implemented in order to increase thermal conductivity.

Chapter 6 – Provides a summary and conclusion of all work carried out in this thesis as well as areas for further investigation.

## 1.10 References

- [1] K. T. H.S. Eggleston, L. Buendia, K. Miwa, T. Ngara, “2006 IPCC guidelines for national greenhouse gas inventories, Prepared by the National Greenhouse Gas Inventories Programme,” 2006.
- [2] N. H. Stern and Great Britain. Treasury., “The economics of climate change : the Stern review,” 2007.
- [3] Ø. Buhaug, H. Corbett, J.J., Endresen, Ø., Eyring, V., Faber, J., Hanayama, S., Lee, D.S., Lee, D., Lindstad, and K. Markowska, A.Z., Mjelde, A., Nelissen, D., Nilsen, J., Pålsson, C., Winebrake, J.J., Wu, W., Yoshida, “Second IMO GHG study 2009,” *Int. Marit. Organ.*, pp. 1–3, 2009.
- [4] T. Smith, E. O’Keeffe, L. Adams, S. Parker, C. Raucci, M. Traut, J. J. Corbett, J. J. Winebrake, J.-P. Jalkanen, L. Johansson, B. Anderson, A. Agrawal, S. Ettinger, S. Ng, S. Hanayama, J. Faber, D. Nelissen, M. Hoen, D. Lee, S. Chesworth, and A. Pandey, “Third IMO GHG Study 2014,” *Int. Marit. Organ.*, 2014.

- [5] EU, “Directive 2001/80/EC of the European Parliament and of the Council of 23 October 2001 on the limitation of emissions of certain pollutants into the air from large combustion plants,” *Off. J. Eur. Communities*, pp. 1–21, 2001.
- [6] European Commission, “Flagging and ship registration background briefing note,” *Eur. Comm. Rep.*, 2012.
- [7] J. Hoffmann, W. Juan, and J. M. Rubiato, “Review of maritime transport,” in *Proc. United Nations Conference on Trade and Development*, 2014, pp. 56–59.
- [8] E. Nissan and A. Galperin, “Refueling in nuclear engineering: the FUELCON project,” *Comput. Ind.*, vol. 37, no. 1, pp. 43–54, 1998.
- [9] EPA, “Global Greenhouse Gas Emissions,” *EPA Rep.*, pp. 1–6, 2014.
- [10] D. Lee, “Aviation’s contribution to climate change,” *ICAO Environ. Rep.*, 2010.
- [11] ICS, “Shipping, World Trade and the Reduction of CO<sub>2</sub>,” p. 6, 2013.
- [12] S. B. Dalsøren, M. S. Eide, Ø. Endresen, A. Mjelde, G. Gravir, and I. S. A. Isaksen, “Update on emissions and environmental impacts from the international fleet of ships. The contribution from major ship types and ports,” *Atmos. Chem. Phys. Discuss.*, vol. 8, no. 5, pp. 18323–18384, 2008.
- [13] International Maritime Organization, “MARPOL ANNEX VI and NTC 2008 with guidelines for implementation,” vol. 258, pp. 1–24, 2013.
- [14] N. Molloy, “The IMO’S 2020 Global Sulfur Cap - What a 2020 Sulfur-Constrained World Means For Shipping Lines, Refineries and Bunker Suppliers,” 2016.
- [15] U. S. E. I. Administration, “Spot prices for crude oil and petroleum products,” 2015.
- [16] T. Tezdogan, A. Incecik, O. Turan, and P. Kellett, “Assessing the impact of a slow steaming approach on reducing the fuel consumption of a containership advancing in head seas,” *Transp. Res. Procedia*, vol. 14, no. 0, pp. 1659–1668, 2016.
- [17] H. N. Psaraftis and C. A. Kontovas, “Ship speed optimization: Concepts, models and combined speed-routing scenarios,” *Transp. Res. Part C Emerg. Technol.*, vol. 44, pp. 52–69, 2014.
- [18] Maersk Line, “Emma Maersk Schedules,” 2012. [Online]. Available: <https://my.maerskline.com/schedules>.
- [19] O. Schinas and M. Butler, “Feasibility and commercial considerations of LNG-fueled ships,” *Ocean Eng.*, vol. 122, pp. 84–96, 2016.
- [20] S. Jafarzadeh, N. Paltrinieri, I. B. Utne, and H. Ellingsen, “LNG-fuelled fishing vessels: A systems engineering approach,” *Transp. Res. Part D Transp. Environ.*, vol. 50, pp. 202–222, 2017.

- [21] N. Paltrinieri, A. Tugnoli, and V. Cozzani, "Hazard identification for innovative LNG regasification technologies," *Reliab. Eng. Syst. Saf.*, vol. 137, pp. 18–28, 2015.
- [22] K. B. Medlock, A. M. Jaffe, and M. O'Sullivan, "The global gas market, LNG exports and the shifting US geopolitical presence," *Energy Strateg. Rev.*, vol. 5, pp. 14–25, 2014.
- [23] M. Zetterdahl, J. Moldanova, X. Pei, R. K. Pathak, and B. Demirdjian, "Impact of the 0.1% fuel sulfur content limit in SECA on particle and gaseous emissions from marine vessels," *Atmos. Environ.*, vol. 145, pp. 338–345, 2016.
- [24] K. J. Lee, D. S. Shin, J. P. Lee, D. W. Yoo, H. K. Choi, and H. J. Kim, "Hybrid photovoltaic/diesel green ship operating in standalone and grid-connected mode in South Korea - Experimental investigation," *2012 IEEE Veh. Power Propuls. Conf. VPPC 2012*, vol. 49, pp. 580–583, 2012.
- [25] Reinforced Plastics, "Solar boat launched," *Reinf. Plast.*, p. 6, 2010.
- [26] Maersk Line, "Efficient propulsion : the Triple-E ' s ' twin-skeg ,", *Maersk Line Publ.*, 2013.
- [27] M. Schmitz and R. Madlener, "Economic viability of kite-based wind energy powerships with CAES or hydrogen storage," *Energy Procedia*, vol. 75, pp. 704–715, 2015.
- [28] "US Navy uses kite-powered cargo ship to deliver equipment," 2011. [Online]. Available: <http://www.hightech-edge.com/skysails-systems-wind-power-saves-fuel-costs-us-navy-mv-beluga/2482/>.
- [29] V. Stenzel, Y. Wilke, and W. Hage, "Drag-reducing paints for the reduction of fuel consumption in aviation and shipping," *Prog. Org. Coatings*, vol. 70, no. 4, pp. 224–229, 2011.
- [30] F. Azemar, F. Faÿ, K. Réhel, and I. Linossier, "Development of hybrid antifouling paints," *Prog. Org. Coatings*, vol. 87, pp. 10–19, 2015.
- [31] C. Guan, G. Theotokatos, P. Zhou, and H. Chen, "Computational investigation of a large containership propulsion engine operation at slow steaming conditions," *Appl. Energy*, vol. 130, pp. 370–383, 2014.
- [32] New York Shipbuilding Corporation, "Technical Press Information N.S. Savannah Personnel Training," 1957.
- [33] F. Crouch, Holmes, *Chapter 2 Commercial Advantages*. Cambridge, MD: Cornell Maritime Press, 1962.
- [34] W. J. F. Standring, M. Dowdall, I. Amundsen, and P. Strand, "Floating nuclear power plants: Potential implications for radioactive pollution of the northern marine environment," *Mar. Pollut. Bull.*, vol. 58, no. 2, pp. 174–178, 2009.

- [35] T. Coppola, M. Fantauzzi, D. Lauria, C. Pisani, and F. Quaranta, “A sustainable electrical interface to mitigate emissions due to power supply in ports,” *Renew. Sustain. Energy Rev.*, vol. 54, pp. 816–823, 2016.

## **Chapter 2 Previous marine reactors and potential fuel types**

## **2.1 Introduction**

This Chapter reviews the past use of marine reactors in a civil context, the types of reactors explored and why they were used. This review developed an understanding of existing knowledge to prioritise the most promising civil marine reactor concepts for development and optimisation.

The second half of this Chapter reviews nuclear fuel concepts in order to determine the optimum fuel type for use in a new civil marine reactor design. It is envisaged that any reactor will have to operate for long periods of time, as well as in a marine environment. Therefore, an understanding of different uranium based fuel types is required to identify the most suitable type for these requirements.

## **2.2 Past civil marine reactors**

Nuclear merchant ships began development in the 1950s, but since that time only four have been built and operated. These are discussed individually:

### **2.2.1 NS Savannah**

The Nuclear Ship (NS) Savannah (Figure 2.1) was the first civil marine merchant ship to be powered by a nuclear reactor, named after the SS Savannah being the first steam powered ship to cross the Atlantic. Proposed by President Eisenhower in 1955, it launched in 1959, was commissioned in 1962 and was operational for five years between 1965-1970, with a total of 89,818 miles completed using nuclear power [1], [2]. The ship was considered a technical success as it operated as designed without incident.



**Figure 2.1 – NS Savannah [1].**

The design brief was to demonstrate the use of a marine reactor for merchant shipping. The vessel was leased to American Export-Isbrandtsen Lines during its service time for cargo transportation [2]. The ship made an operating profit of \$12,000,000 but cost \$46,900,000 to be produced, with two thirds of the cost just for the reactor produced by Babcock & Wilcox [1]. The ship also had government subsidies in order to balance the operating budget.

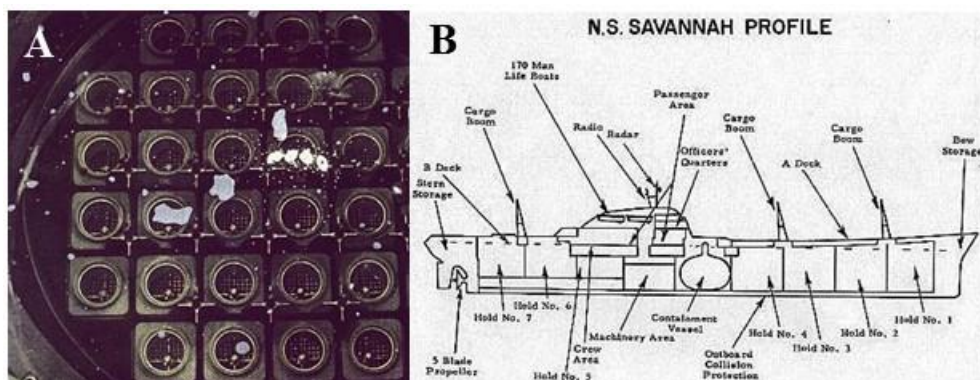


**Figure 2.2 – A – Top view of the reactor core for the NS Savannah showing fuel bundles in a circular lattice, B – Side schematic of the NS Savannah showing the reactor compartment in the middle of the ship [3].**

**Table 2.1 – NS Savannah ship and reactor specifications [1].**

<b>Overall length</b>	182 m
<b>Width</b>	24 m
<b>Crew</b>	124
<b>Displacement</b>	20,000 tonnes
<b>Load carrying capacity</b>	12,500 tonnes
<b>Passengers</b>	60
<b>Fuel type</b>	UO <sub>2</sub>
<b>Reactor power</b>	74 MWth
<b>Enrichment</b>	4.4% U-235
<b>Fuel cladding material</b>	Stainless steel
<b>Reactor vessel height</b>	8.23 m
<b>Reactor vessel diameter</b>	2.44 m
<b>Number of elements</b>	32
<b>Top speed</b>	21 knots

The reactor design of the ship was a PWR with a power of 74 MWth and a top speed of 21 knots [1]. In the ship specification, Table 2.1, it had a crew size of 124, although not all crew were for running the ship and reactor, as crew members were required for the hospitality of the passengers. The ship was a hybrid design, operating as a cargo carrier whilst also a cruise liner, which meant that it was not particularly efficient at either. External and internal aesthetics designed to appeal to paying passengers as a sleek yacht ran against the ship's ability to run efficiently to load and unload cargo. However, it was ultimately built to demonstrate that a marine nuclear reactor could operate in a civil capacity, and so was a "national showpiece" [4]. It showed the world that a marine reactor could power a merchant vessel and that nuclear energy could be used in peaceful ways.

There were 32 fuel elements in the reactor, as shown in Figure 2.2, with an average enrichment of 4.4 % U-235, which is similar to a civil on shore nuclear power plant for electrical generation. The reactor vessel, pressuriser, heat exchanger and other critical reactor

components were able to be housed inside a containment vessel 15.4 m long and 10.67 m in diameter in the middle of the ship, Figure 2.2 [1]. All of the components appear to be arranged and stacked as tightly as possible, which is different to conventional on-shore reactors being more spaced out for easier installation and servicing. The ship also had emergency diesel generators which provided electricity to get the ship to port and power systems on board.

The economics appear to have proved unfavourable due to high capital and running costs, such as extra crew, as well as the cheap price of oil. This resulted in the vessel being decommissioned in 1972. However, the adaption of PWR technology available at the time appears to have been a technical success. The ship currently is moored in Baltimore as a museum.

### **2.2.2 NS Otto Hahn**

The NS Otto Hahn, shown in Figure 2.3, was a German built nuclear ship named after the German chemist Otto Hahn due to his pioneering work in nuclear fission. She commercially operated for nine years (1970-1979). The reactor was built by Deutsche Babcock & Wilcox [5].



**Figure 2.3 – NS Otto Hahn [6].**

The NS Otto Hahn like the NS Savannah, was designed to carry both passengers and cargo, which in this case was ore [7]. The ship ran for four years before the first refuel, after covering 250,000 nautical miles using approximately 22 kilograms of U-235. After the first refuelling, the ship operated for another seven years before the reactor was decommissioned over a two year period and replaced with a conventional diesel drive [7]. Her reactor accomplished a total distance of 650,000 nautical miles over a 10 year period, sailing 126 voyages without any technical problems [5].

**Table 2.2 – NS Otto Hahn ship and reactor specifications [5].**

<b>Overall length</b>	172 m
<b>Width</b>	23.2 m
<b>Displacement</b>	23,900 tonnes
<b>Load carrying capacity</b>	12,700 tonnes
<b>Crew</b>	63
<b>Research personnel</b>	35
<b>Top speed</b>	17 knots
<b>Fuel type</b>	UO <sub>2</sub>
<b>Reactor power</b>	38 MWth
<b>Enrichment</b>	3.5-6.6% U-235
<b>Operating Temperature</b>	300°C
<b>Operating Pressure</b>	83 Bar
<b>Endurance under full load</b>	900 days
<b>Fuel rod diameter</b>	11.4 mm
<b>Fuel cladding thickness</b>	0.8 mm
<b>Fuel cladding</b>	Zircaloy-4
<b>Number of elements/fuel rods</b>	12/2810

NS Otto Hahn design specifications of interest are shown in Table 2.2. The reactor was a derivation of the NS Savannah PWR design, which was about half the size in power at 38 MWth, compared with the Savannah's 74 MWth [1]. This undoubtedly limited the top speed to just 17 knots. There is a difference in the cladding material with NS Otto Hahn using

Zircaloy-4 and the NS Savannah using stainless steel. This is assumed to be from innovation of materials at the time of construction as a report considered future use of Zircaloy-4 for the NS Savannah before it was decommissioned; one notable reason to improve the neutron economy [8] as Zircaloy-4 has a lower neutron absorption cross section than stainless steel. The NS Otto Hahn was crewed by 36 fewer personnel including researchers, which reduced the ship's operating costs when compared to the NS Savannah.

### **2.2.3 NS Mutsu**

The NS Mutsu, Figure 2.4, was a Japanese experimental research nuclear ship. Construction of the ship began in 1968 in Japan [9] and it was put to sea for the first time in 1974 [10]. The ship was used as a research vessel to evaluate utility nuclear power for shipping, as well as transportation of nuclear fuel [9]. Therefore, she was not built to carry commercial cargo or passengers like the NS Savannah and NS Otto Hahn were.

The NS Mutsu reactor design, Table 2.3, used  $\text{UO}_2$  fuel, the same as the NS Savannah and NS Otto Hahn, and had a reactor power of 36 MW<sub>th</sub>, similar to the NS Otto Hahn [11]. The reactor is a two loop primary coolant system PWR, Figure 2.5, with the reactor containment vessel located in the middle of the ship.

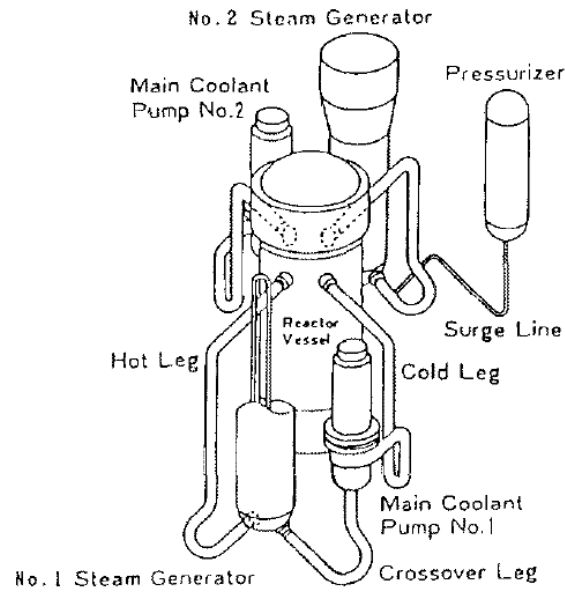
The ship encountered technical problems of radiation leaks due to inadequate shielding resulting from a design flaw. An investigation determined that neutrons were streaming through an air gap that was located between the primary shield and pressure vessel [10]. This was discovered on the first start-up of the reactor. Negative media reports led to the ship being held in port until 1991, where it then completed one year of sea experiments [7].



Figure 2.4 – NS Mutsu [12].

Table 2.3 – NS Mutsu ship and reactor specifications [9], [10], [11], [13].

<b>Overall length</b>	130 m
<b>Width</b>	19 m
<b>Displacement</b>	8240 tonnes
<b>Crew</b>	59
<b>Research personnel</b>	20
<b>Top speed</b>	17 knots
<b>Fuel type</b>	UO <sub>2</sub>
<b>Reactor power</b>	36 MWth
<b>Enrichment</b>	3.24-4.44% <sup>235</sup> U
<b>Fuel cladding material</b>	Stainless steel
<b>Active fuel length</b>	1.04 m
<b>Number of elements</b>	32



**Figure 2.5 – NS Mutsu PWR reactor two loop configuration [13].**

The reactor of the NS Mutsu was decommissioned and the ship was converted in a similar fashion as the NS Otto Hahn to a diesel drive system in 1992. As of 1996, after being retrofitted, the Mutsu was renamed the Mirai and is used as an ocean research ship.

#### **2.2.4 NS Sevmorput**

The Russian built NS Sevmorput, Figure 2.6, was the fourth merchant nuclear ship to enter service. Construction work began in 1982 at a shipyard in Kerch, Crimea and it was commissioned in 1988. The ship was built under the codes, conventions and norms of the time with regard to the nuclear materials, reactor and shipping such as the international convention on the safety of nuclear powered freight vessels [14].



**Figure 2.6 – The Russian nuclear merchant ship NS Sevmorput [15].**

The NS Sevmorput was designed as an icebreaker and operated as a merchant ship in the Arctic. Conventional ships can only operate during seasonal times in this region due to the ice unless accompanied by an ice breaker. This means that the NS Sevmorput had a longer window of operation during the year as it was designed to sail through ice up to 1 m thick. The process of sailing through ice is very energy intensive, which can limit the operation of conventional merchant ships.

Having a nuclear reactor gives the NS Sevmorput the advantage from a fuel perspective of having unlimited range over the short term, which is beneficial as there are limited places to refuel while traversing the Arctic. The Sevmorput has made 302,000 miles carrying 1.4 million tonnes of cargo. The reactor has only been refuelled once, which was carried out in 2003 [14] and this process takes about 1.5 months to complete [4].

The ship uses twin PWR reactors giving a total power of 135 MWth. The reactor is enriched to 90 % U-235, Table 2.4. This would not be acceptable for a future civil ship due to composition of low enrichment limits of <20 %. However, this setup works economically for

operation in the Arctic Ocean, due to power requirements for ice breaking and conventional diesel ships having logistic problems of needing to be refuelled [17].

**Table 2.4 – NS Sevmorput ship and reactor specifications [14], [16], [17].**

<b>Overall length</b>	260 m
<b>Width</b>	32 m
<b>Displacement</b>	61000 tonnes
<b>Top speed</b>	20 knots
<b>Reactor type</b>	PWR
<b>Reactor</b>	135 MWth
<b>Fuel type</b>	U-Zr alloy
<b>Enrichment</b>	90% U-235
<b>Fuel rod diameter</b>	5.8 mm
<b>Fuel cladding</b>	Zircaloy alloy
<b>Number of elements/fuel rods</b>	241/53
<b>Coolant inlet temperature</b>	278 °C
<b>Coolant outlet temperature</b>	318 °C

The NS Sevmorput has an emergency cooling system and is able to run via natural circulation at 25-30 % of full power [17]. Information about the NS Sevmorput was made available due to the Russian government submission of a safety report to the Norwegian authorities in 1991 to allow it to operate in Norwegian ports [17]. Similar to other nuclear ships, the NS Sevmorput has emergency diesel generators to provide power in the result of a reactor failure.

The NS Sevmorput is currently still in operation. The demonstration of this type of ship operating in a specific role leads to the possibility for other merchant ships to be designed in a similar way with a nuclear reactor to operate between East Asia and Europe via the Arctic route safely. However, the ship is using highly enriched fuel of 90 % U-235, which would not be acceptable by modern non-proliferation and safeguarding expectations.

#### **2.2.4 Russian ice breakers**

There have also been nine Russian nuclear ships that have served only as ice breakers. The first, the Lenin, was built in 1959 and was the world's first nuclear powered surface vessel. Similar to the NS Sevmorput in the need for a high amount of power to carry out the function of breaking ice, the use of a reactor served this purpose well. These ships, similar to the NS Sevmorput, used highly enriched U-235 fuel and had a similar model of PWR reactor [18].

#### **2.2.5 Naval marine reactors**

The first use of a naval nuclear reactor was in the USS Nautilus submarine commissioned by the US navy. Naval marine reactors have been used in many platforms from submarines to surface fleets, such as aircraft carriers and cruisers. These have subsequently been built and operated by US, Russian, British and French navies.

Naval reactors similar to the Russian ice breakers were not considered in detail here due to difficulties in obtaining meaningful declassified information. As well, most of these reactors run with high enrichment, which is not within the scope of the design to be developed in this project.

#### **2.2.6 Civil marine reactors summary and discussion**

Both the NS Savannah and NS Otto Hahn were built to demonstrate the technical feasibility of a nuclear ship, which they succeeded in. Neither suffered any problems with regards to the operation of the nuclear reactor, sunk or experienced any other reportable incident. However, the economic model appears to have failed in both cases due to factors including: high one-off design costs, the cheap price of oil, and the need for skilled operators, which can be mostly be attributed to them being prototypes. If more of the same design had been produced then the cost may have fallen, due to economies of scale. These are important aspects that will need to be considered for a potential civil marine reactor to come to market, but not for the main scope

of this project. However, the capital cost of the reactor for these ships was one of the biggest costs, so a new reactor design must be simple and cost-effective to manufacture and operate.

The NS Mutsu was a Japanese experimental research ship, carrying special cargos and training crew. The ship was used as a research vessel into using nuclear power for shipping and, unlike the Savannah and Otto Hahn, it was not built solely to carry cargo or passengers. The NS Mutsu also suffered setbacks from design flaws creating a negative public image leading it to be docked for a long period of time. Therefore, public perception for a future civil marine nuclear ship will need to be carefully managed.

The civil marine reactors were all PWR types and used low enriched fuel unlike Russian vessels that used high enrichment. The use of low enrichment would be of higher preference as it would be able to satisfy proliferation agreements. As the reactors and fuel were all prototypes, any new lines of fuel could come from existing main stream designs and supply to limit costs.

### **2.3 Reactor placement and type**

This section discusses two different concepts of how a civil marine reactor could be implemented in a merchant ship as well as the proposal of the reactor type to be used.

One third of world reactors built have been marine based and predominantly of a PWR configuration, with a large majority being naval submarine reactors. Therefore, this project proposes that any future civil marine reactor use this type. If new technology is used instead it will take a longer lead time to commercialise. Also, the safety record for PWR reactors is seen as high.

A PWR design shown in Figure 2.7 operates by having fuel rods grouped together in fuel assemblies inside a water filled cylindrical reactor core. The water, which acts as the primary coolant, is held at high pressure in order to raise the boiling point so that at designed

temperatures of 320°C, it does not turn into steam. As fissions take place inside the fuel rods, energy is released which is transferred to the primary coolant water. Conventionally there can be a number of primary coolant loops, between 1 and 4, inside a reactor core that are separate from each other. Once heated, the primary coolant passes through the reactor and enters a heat exchanger to transfer this heat to a secondary coolant loop. This is done to prevent radiological contamination in other equipment down the line and also allows the secondary coolant to convert to steam as it is not held under pressure. The steam in the secondary coolant loop is fed through turbines in order to either directly power a drive shaft in a ship or provide electrical power via a generator.

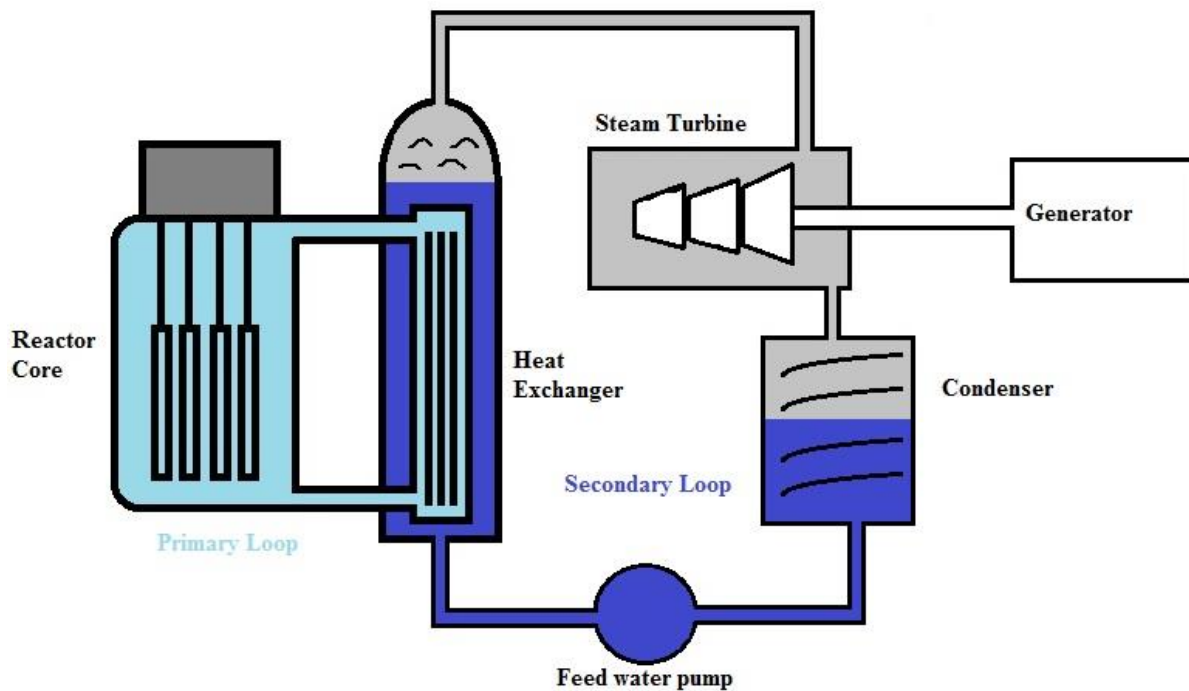


**Figure 2.7 – Typical PWR design layout.**

Other reactor types that were considered but not taken forward were; boiling water reactors (BWR) which is similar to the PWR configuration but only has one coolant loop. The water is not kept at pressure and so turns into steam in the reactor core and heads directly to the steam turbine providing higher thermal efficiency gains over a PWR. There are higher lifetime capital

costs with this configuration due to potential radiological contamination of the steam turbine and condenser equipment. As well, the control equipment required for a BWR for potential coolant loss requires a larger footprint than a PWR. Due to space being limited on a civil ship this was one of the main reasons it was not taken forward.

CANDU and pebble bed reactors were two other designs that were considered. The CANDU reactor design allows online refuelling which has the advantage of not having to shut down the reactors to replace fuel, for a ship this would work well as it could replace fuel while at sea or at dock. The CANDU is similar to a PWR configuration in that it has a primary and secondary loop but the fuel bundles are horizontal rather than vertical for online refuelling to occur at either end. The primary coolant used is heavy water which absorbs fewer neutrons than light water making it a more efficient moderator. The CANDU however requires more space and plant than a PWR due to online refuelling, as well, no CANDU have ever been used in a marine environment. Pebble bed reactors were considered as they are designed to be highly proliferation resistant and also less accident prone than compared with a PWR and BWR. Instead of fuel bundles they are small round pebbles of uranium encased in graphite with gas cooling in a primary loop that can be run direct to a steam turbine. It has the advantages of higher thermal efficiency and reduced equipment than a PWR as no water pumps are required. However the pebble bed is still a new reactor design with limited experience and so would create a long lead time to commercialisation for one to be used as a marine reactor compared with a PWR.

### **2.3.1 Reactor in the ship**

The placement of the reactor will be an important consideration. If positioned in the middle, as was the case for the four civil nuclear merchant ships previously built, wave dynamic effects will be minimised, explained below. However, the drive for the propeller would either require a long shaft, steam pipe down the ship to a turbine or an electrical driven system. Having a

large drive shaft would use more ship space and be a greater engineering challenge due to the length. Using a steam pipe to travel down the ship would provide a simpler engineering solution, while converting to electrical energy would mean efficiency losses but more control in propeller speed.

If the reactor were to be positioned at the stern of the ship then this would suit ships such as oil tankers, so as to not break up the cargo space area. However, the reactor would be subject to higher wave loading, meaning that the bow of a large ship would be in the trough of a wave while the stern would be at the crest. Depending on the amplitude of the wave this could create disruption to the power of the reactor due to the fluctuating water levels in a secondary loop of a PWR.

### 2.3.2 Mothership

Another concept that could be used is for a ship to be able to split into two, figure 2.8. This would require that all of the engineering plant, including the reactor, be in the stern of the ship and the cargo section be in the front section of the ship. This would offer the advantage of being able to dock in countries that have nuclear free zones that ordinarily would not allow such a ship to enter. Here, the ship could separate in international waters and a tug could take the cargo section of the ship in to port.

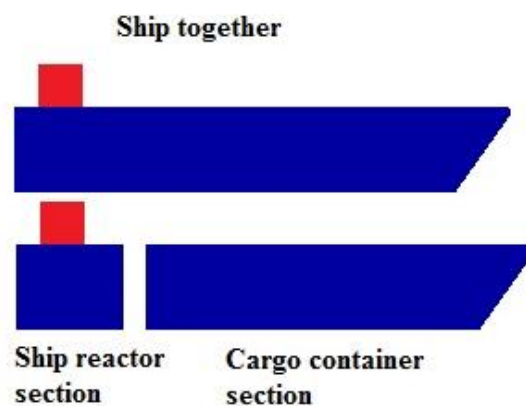


**Figure 2.8 – Mothership configuration showing the rear section of the ship would split from the cargo section.**

However, this idea would require a great deal of marine architecture, since, so far it is only a concept. As the hull of a ship is subject to longitudinal bending stresses from the combination of load displacement and sea conditions, as well as other factors [19], the effects to be considered are greater with larger ships such as container vessels. Therefore, any mothership concept would require work to understand if a hull can stay together, as well as the mechanisms involved in separating.

### **2.3.3 Reactor placement and type summary and discussion**

Having the reactor placed as central as possible is deemed to be the best option for a civil marine reactor, based on previous civil marine ships using a similar concept. In addition the envisaged design layout for the potential use of a reactor in a container ship would not take up valuable cargo space and could be housed below the bridge.

An electric drive system would be the most beneficial. This is based on keeping water systems located in one section, rather than having large steam pipes or a drive shaft running down the ship. Having the drive shaft electrically controlled would have efficiency losses but would be beneficial in providing more direct control of speed, as opposed to having to wait for a steam turbine to spin up or slowdown. Also, if a backup system of electrical batteries could be integrated into the system, it would allow the ship to sail off without having to wait for the reactor to come to temperature in order to provide power. This would be expected to be a few hours as the reactor would not have cooled significantly.

## **2.4 Different nuclear fuel types**

This section reviews different nuclear fuels types that could be used in a civil marine reactor for fuel to last an extended period of time in operation of greater than 10 years.

An investigation was carried out into different solid uranium fuel types in order to determine suitable fuel for a civil marine reactor using a PWR system. The following are the main findings from suitable fuel candidates.

Material properties that are important for this application are:

- Density
- Thermal conductivity
- Melting point
- Mechanical behaviour

The higher the density of a nuclear fuel material, the more fissile material that can be packed into the same volume, and thus a low enrichment/high density fuel is targeted. This is important because the size of the reactor vessel is to be as small as possible. The thermal conductivity and heat capacity are also important as higher values of these will improve the life of the fuel; the rate at which fuel rods deteriorate is mainly a temperature dependant function. It is also important to consider industrial scale reproduction so that a potential fuel could easily be scaled up if required for commercial production.

#### **2.4.1 Uranium dioxide**

UO<sub>2</sub> is the most extensively used nuclear fuel type for past and present world reactors. Past experience with it and its current ready availability make it a suitable candidate. However, there are characteristics that make it potentially unsuitable, such as the length of time required in the core for this civil marine reactor.

UO<sub>2</sub> fuel has a low relative thermal conductivity (Table 2.5) that creates a high temperature gradient across the fuel. This can cause the fuel to behave differently from the centre to the edge with regards to swelling, and the introduction of thermal stresses [20]. UO<sub>2</sub> fuel also has a relatively low density to other uranium based fuels, which is a disadvantage for achieving a low enriched high density fuel type.

The material does, however, have a high melting temperature that is an advantage for higher fuel failure limits and is a strong material, giving it high mechanical strength. These are desirable material properties.

**Table 2.5 – UO<sub>2</sub> material properties at standard conditions [20], [21].**

<b>Molecular formula</b>	UO <sub>2</sub>
<b>Density</b>	10.96 g/cm <sup>3</sup>
<b>Young's modulus</b>	194.2 GPa
<b>Thermal conductivity</b>	7.614 W/m/K
<b>Melting point</b>	3120 K
<b>Poisson's ratio</b>	0.32

#### **2.4.2 Uranium nitride**

Uranium nitride fuel has desirable characteristics such as high relative density and good thermal conductivity, providing high power density [22], a high melting point, and a higher young's modulus than UO<sub>2</sub> giving it an increased mechanical behaviour; Table 2.6 refers. It is compatible with existing production and reprocessing methods carried out for oxides [23]. Uranium nitride fuel has been considered for space nuclear power applications, mainly due to the high material properties discussed [24].

As expected, uranium nitride has some disadvantages. Firstly, the absorption cross-section of natural isotopic nitrogen for thermal neutrons is high enough to reduce the breeding ratio, which simplistically means less fuel, as more neutrons are absorbed by nitrogen and thus less to generate fissions and so there is a reduction in fissile material produced. Secondly, a higher proportion of carbon-14 is a biological hazard that is produced through a route from nitrogen-14. Both of these problems can be overcome by enriching natural nitrogen to obtain nitrogen-15 which is around 20% abundant in natural nitrogen [23]. However, this would require greater process energy and cost to achieve.

Uranium nitride reacts violently with water, and therefore a water coolant is not suitable. Thus a lead bismuth type coolant would have to be utilised. With these reactors operating on the oceans, it is a rational decision not to use a fuel type that behaves in this way with water.

**Table 2.6 – Uranium nitride material properties at standard conditions [20], [25].**

<b>Molecular formula</b>	UN
<b>Density</b>	14.33 g/cm <sup>3</sup>
<b>Young's modulus</b>	220 GPa
<b>Thermal conductivity</b>	20.9 W/m/K
<b>Melting point</b>	3123 K
<b>Poisson's ratio</b>	0.3

### 2.4.3 Uranium silicide

Uranium silicide was first used as a high-enriched fuel in a research reactor in Oak Ridge USA [26] and is a metallic material. Since then, it has been utilised in many research reactors over the years. The benefit is that the fuel type has a higher density than a conventional UO<sub>2</sub> fuel form, which means it can accommodate more uranium per unit volume and hence more fissile U-235. Therefore, a reduction in enrichment is possible as the fuel has the properties of low enrichment/high density.

The disadvantages that a silicide fuel form can face are high irradiation induced swelling at temperatures above 500 °C, and a higher thermal expansion coefficient than that of zirconium alloys for cladding not observed with other fuels considered [27]. Uranium silicide also has a relatively low melting point compared with UO<sub>2</sub> of 1570 K, Table 2.7, and less than half the value of young's modulus than compared with UO<sub>2</sub> giving weaker mechanical strength.

However, analysis of higher burn up levels of uranium silicide in the advanced neutron source reactor in the US, found that the fuel swells less, has better thermal conductivity and displays greater retention of fission products [26].

The material properties of uranium silicide, summarised in Table 2.7, relate to the composition  $U_2Si_3$  but other compositions that have been used are  $U_3Si$  with a density of  $15.2 \text{ g/cm}^3$  and  $U_3SiAl - Al$  with density  $14.2 \text{ g/cm}^3$  [28]. These compositions show good advantages with their higher densities when compared to  $UO_2$  at  $10.96 \text{ g/cm}^3$  [20], but they also come with some disadvantages related to their swelling behaviour. Investigations found that one of the reasons is due to the fact that the fission gases in both of these migrate together to form larger bubbles.

At the Argonne national laboratory, it was found that  $U_3Si_2$  reacts with aluminium cladding forming a shell of aluminide around the fuel particles, enhancing their stability [26]. This discovery was investigated further to create  $U_3Si_2$  with an excess loading of uranium to gain a higher take up in the element. This excess would combine with Al to form  $UAl_x$  to create an irradiation stable fuel form free from swelling; this has been achieved in part [29]. Therefore,  $U_3Si_2$  shows promise of being a good potential fuel form for a marine civil reactor.

**Table 2.7 – Uranium silicide material properties at standard conditions [28], [30], [31], [32].**

<b>Molecular formula</b>	$U_3Si_2$
<b>Density</b>	$12.2 \text{ g/cm}^3$
<b>Young's modulus</b>	77.91 GPa
<b>Thermal conductivity</b>	15 W/mK
<b>Melting point</b>	1570 K
<b>Poisson's ratio</b>	0.17

#### 2.4.4 Uranium carbide

Uranium carbide is a fuel type that has been considered mainly for fast reactor applications in Russia, France, India, and China [33], [23], as well as high temperature gas cooled reactors [34]. The fuel is 1.3 times more dense and its thermal conductivity is 2.6 times higher than that of  $UO_2$  [20], Table 2.8. There is less restructuring of the microstructure compared to oxide fuel

[23], giving a more stable fuel form and good characteristics for a marine civil reactor fuel. The fuel has a high melting point over 2000 K and a good mechanical strength of 208 GPa.

This fuel has proven fabrication processes that could be commercialised, such as reacting metallic uranium with graphite by heating pressed powders of both to produce a very hard ceramic [20], [35].

Uranium carbide fuels of small particle size are found to be pyrophoric, igniting in air instantaneously [35] and must be manufactured in an environment free from oxygen and water [23]. This would add extra challenges and costs to any potential mass fabrication.

**Table 2.8 – Uranium carbide material properties at standard conditions [20], [36].**

<b>Molecular formula</b>	UC
<b>Density</b>	13.63 g/cm <sup>3</sup>
<b>Young’s modulus</b>	208 GPa
<b>Thermal conductivity</b>	25.3 W/m/K
<b>Melting point</b>	2350 K
<b>Poisson’s ratio</b>	0.269

#### **2.4.5 Uranium molybdenum alloy**

Uranium molybdenum alloy has been developed in the same way as uranium silicide to obtain a low enriched/high density fuel. Molybdenum, when alloyed with uranium, improves the overall swelling resistance, mechanical properties and oxidation resistance. Depending on the application of required burnup, it is found that different alloying weights of molybdenum are favoured, ranging between 4.7-8 w.t.% [37].

Uranium molybdenum alloys are prone to stress corrosion cracking more so than other fuel types considered here from hydrogen embrittlement [38]. The most common application of this fuel type has been in research and fast reactors and so experience is limited for high temperature thermal reactors for this fuel is intended for [37]. Table 2.9 shows that uranium molybdenum

has a high density and good thermal conductivity, however it has a low relative melting point which would be of concern. No reliable young's modulus could be found for this material to make an assessment on its mechanical strength.

**Table 2.9 – Uranium molybdenum material properties at standard conditions [38], [39], [40].**

<b>Molecular formula</b>	UMo
<b>Density</b>	18.2 g/cm <sup>3</sup>
<b>Thermal conductivity</b>	13 W/mK
<b>Melting point</b>	1407 K

#### **2.4.6 Uranium metal**

Uranium metal is heavier, ductile, and softer than steel. It has a high relative density to UO<sub>2</sub>, Table 2.10, and therefore makes it an ideal material for being low enrichment/high density. This material has the highest thermal conductivity of all the fuels considered at 35 W/m/K, and has a good mechanical strength with a young's modulus of 190 GPa. However, uranium metal is found to be less stable than UO<sub>2</sub> due to surface oxidation when exposed to air. Water rapidly attacks it at high temperature and it will spontaneously ignite in air at ambient temperature, when in powder or chip form [41]. The material also has a very low relative melting point of 1130 K which would be a very large causes for concern for fuel failure if temperatures inside a reactor unexpectedly heated up quickly.

There is experience of using uranium metal as a reactor fuel in research reactors as well as in naval applications.

Severe swelling occurs in uranium metal after long irradiation due to fission gas build-up which could bring about problems in a 15 year fuelling cycle. Uranium metal also has three prominent crystalline structures that change from alpha to beta at 690°C and beta to gamma at 769°C. There is a volume increase between each of these phases most notably 1 % from alpha to beta.

Therefore, problems can occur of sudden temperature changes causing volume changes and potential ruptures of the fuel elements [42].

**Table 2.10 – Uranium metal material properties at standard conditions [41], [42].**

<b>Molecular formula</b>	U
<b>Density</b>	18.9 g/cm <sup>3</sup>
<b>Young's modulus</b>	190 GPa
<b>Thermal conductivity</b>	35 W/m/K
<b>Melting point</b>	1130 K
<b>Poisson's ratio</b>	0.22

#### **2.4.7 Uranium Zirconium Hydride**

Uranium zirconium hydride fuel has been used in test reactors in the USA and also in the space auxiliary power programme in the 1960's, but has had relatively little research carried out on it since [43]. During the space programme it was found that uranium zirconium hydride operated very well with low concentrations of uranium at approximately 10 w.t.% of the fuel. However, this would not be appropriate for this application and the uranium would need to be scaled up to increase either the weight percent content, or a larger volume of fuel material would be required taking up more space. Table 2.11 lists the fuel material properties showing a good thermal conductivity of 18 W/m/K, but only relatively good density, young's modulus, and melting points at 10.95 g/ cm<sup>3</sup>, 130 GPa, and 1800 K respectively which does not make it a strong candidate compared with other fuels already discussed.

**Table 2.11 – Uranium zirconium hydride material properties at standard conditions [43].**

<b>Molecular formula</b>	U <sub>0.3</sub> ZrH <sub>1.6</sub>
<b>Density</b>	10.95 g/cm <sup>3</sup>
<b>Young’s modulus</b>	130 GPa
<b>Thermal conductivity</b>	18 W/m/K
<b>Melting point</b>	1800 K
<b>Poisson’s ratio</b>	0.32

#### **2.4.8 Mixed oxide fuel**

Mixed oxide fuel (MOX) is a combination of two fissile nuclear fuel elements UO<sub>2</sub> and PuO<sub>2</sub>. The material properties, Table 2.12, are similar to UO<sub>2</sub>. This is for compatibility with UO<sub>2</sub> fuelled reactors so they can be interchanged easily when compared to previously discussed fuel types. One of the main reasons for using MOX has been to reuse plutonium used in light water reactors extracted by reprocessing. MOX fuel has a high burnup potential and relative ease of commercial manufacture [23]. Using fuel rods with more initial Pu in might be more of a proliferation issue than other pure U based fuels. Similar to UO<sub>2</sub> the material has a high melting point but low thermal conductivity. No reliable young’s modulus could be found but it is assumed to be in the same magnitude of UO<sub>2</sub> so providing good mechanical strength.

**Table 2.12 – Mixed oxide material properties at standard conditions [20].**

<b>Molecular formula</b>	U <sub>0.92</sub> Pu <sub>0.08</sub> O <sub>2</sub>
<b>Density</b>	11.07 g/cm <sup>3</sup>
<b>Thermal conductivity</b>	7.82 W/m/K
<b>Melting point</b>	3023 K

#### **2.4.9 Rod/plate design**

Nuclear fuel is commonly fabricated in two design types, a fuel rod and a plate style, Figure 2.9. The plate type of design is less common but was used more in the early years of reactor designs. Typically such a design would be a thin rectangular plate with the fuel in the middle

surrounded by a metal cladding material. Typically fuel plates are very good from a safety aspect. As the fuel meat can be kept quite thin, this reduces the core temperature and, due to the plate design, high mechanical strength is maintained. A fuel rod, by comparison, is made smaller to reduce core temperature and loses its mechanical strength [44]. The most common use these days is in research of high enrichment type of reactors where a high neutron flux might be desired.

A fuel rod design is the most commonly used type of fuel concept, and as already noted, has been used in civil marine reactors in the past. The typical design of a fuel rod is to have the fuel made as small pellets and then stacked one on top of each other in a metal cylindrical tube which acts as the cladding. Varying diameters of fuel rods have been used over the years to increase improvements in thermal efficiency and burnup. Depending on the size of the reactor, fuel rods can be in such lengths as 3.8 m or 4.0 m in what is considered the active fuel rod length for onshore reactors [45]. A set of fuel rods are normally bundled into a fuel element which can be of square or hexagonal shape in order to move and position them easily into a reactor.

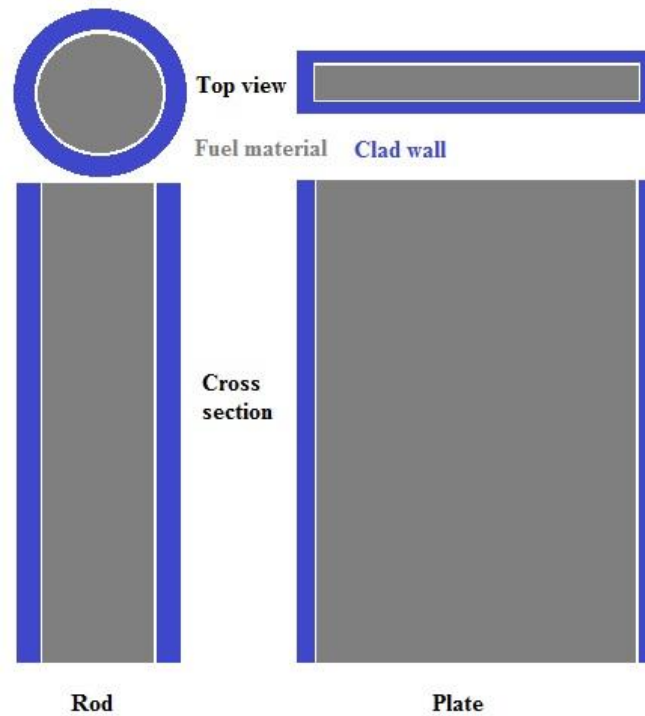


**Figure 2.9 – Design of a fuel rod and fuel plate**

#### **2.4.10 Cermet fuels**

A way to design the fuel to be more thermally efficient is to induce a metallic element into the fuel meat. If a fuel discussed previously, such as  $\text{UO}_2$ , is combined with a metallic element into the fuel design, then it is called a cermet. This is the name used to describe a material that is a ceramic and metallic composite.

The amount of each component is determined by what is required of the fuel. As the metallic component increases, so too does the thermal conductivity and generally density. However, this is offset by the loss of fissile material, shortening the life of the fuel or requiring a larger reactor to have more fuel elements to accommodate for this loss. As well, an increase of the metallic component will also lower the melting point and young's modulus.

There are different ways in which the metallic element can be combined with the fuel material. One way would be to fabricate the fuel and metal components separately. If using a rod design,

then the metal component could be made as small disks to be placed in between fuel pellets. Another method would be to incorporate them both into a pellet. This would be done by fabricating them together from powder form by mixing the powders together and then pressing and sintering. Thus, there would be no need to change the shape or design of a fuel rod itself.

No material properties are listed for cermets as depending on the metallic and ceramic material used it would vary widely. However, what is considered here would be using  $\text{UO}_2$  with a metallic material that would not lower too much its melting point and young's modulus so to keep it above ideally 2000 K and 180 GPa respectively and then raise the thermal conductivity and density to values that would be required for a civil marine reactor.

Cermets have been produced in a varying amount of metallic components, from studies using uranium metal of 15 wt% and 30 wt% with  $\text{UO}_2$  [46]. To using W at 60 wt% - 90 wt% with  $\text{UO}_2$  and also the same loading content with UN [47] with both examples giving a high return on thermal conductivity then compared with  $\text{UO}_2$ . This shows that there is experience working with cermets and using  $\text{UO}_2$  as the ceramic fuel material.

#### **2.4.11 Other fuels types not being considered**

There are many styles, types or designs that could be investigated as a potential option for this civil marine reactor. However, to constrain this investigation, conventional uranium based options were considered. Therefore, options such as thorium based reactors and advanced reactors such as a pebble bed were not investigated.

#### **2.4.12 Summary and discussion of fuel investigation**

From the fuel investigation, all the fuels researched possess advantages and disadvantages to their use as a potential fuel type for a civil marine reactor, these have been summarised in Table 2.13. They have been weighed against the benefits they would provide to a civil marine reactor from a material perspective, as well as the research required to be able to implement.  $\text{UO}_2$  has

a large amount of operating experience but low thermal and mechanical properties when compared to other fuel types considered. MOX fuel also has similar low materials properties, but the fabrication process has a higher degree of complexity than UO<sub>2</sub>, as well the proliferation consideration of a higher Pu content with MOX would need to be justified if it was taken forward.

Uranium carbide and uranium nitride both have high thermal conductivity and density values which make them suitable for a civil marine reactor. However, they both come with the disadvantage of being highly pyrophoric when exposed to water which makes them a less attractive proposition.

Uranium zirconium hydride is a fuel type has high thermal conductivity but has had limited research carried out on it. Therefore, to implement it into a civil marine reactor is not a feasible option due to the considerable basic development still required.

Uranium metal has been used in a marine environment in the Royal Navy for its fleet of nuclear powered submarines for 50 years, so there is a vast operating experience, but this has been at high enrichment levels. Uranium metal offers the best option for low enrichment/high density but due to corrosion and swelling issues it is not the favoured option.

Uranium molybdenum takes the best of the pure uranium metal of high density and alloys to give it more stable properties, however it suffers a lower melting point. The data available shows it to be a very suitable option but with stress corrosion cracking tendencies that could pose challenges.

Uranium silicide has been presented in this report in three different compositions. Further work would be needed to determine the minimum density in order to hold enough uranium to provide power for a 15 year period and at an enrichment <20 %. With the initial investigation from obtained data, the lower density uranium silicide U<sub>3</sub>Si<sub>2</sub> would be the most favourable option of

the three silicide's. Uranium silicide does have a low relative melting point in its favoured form but does have good thermal conductivity and density values reported.

Cermet fuels are seen as one of the most promising fuel types to be taken forward using the vast operating experience of  $UO_2$  and combining that with a metallic that would not reduce the melting point and mechanical strength too much while increase the thermal conductivity firstly and density secondly.

**Table 2.13 – Summary of advantages and disadvantages to taking forward the discussed fuel types for a civil marine reactor.**

	<b>Advantage</b>	<b>Disadvantage</b>
<b>Uranium dioxide</b>	High melting point Vast experience High mechanical strength	Low thermal conductivity
<b>Uranium nitride</b>	High thermal conductivity High density	Neutron economy reduction Reacts violently with water
<b>Uranium silicide</b>	Good thermal conductivity Good density	Low melting point Limited experience in proposed environment
<b>Uranium carbide</b>	Very high thermal conductivity Good density	Manufacturing challenge
<b>Uranium molybdenum alloy</b>	High density	Low melting point Limited experience
<b>Uranium metal</b>	Very high thermal conductivity High density Good mechanical strength	Very low relative melting point Stability issues
<b>Zirconium hydride</b>	High thermal conductivity	Limited experience Other fuel properties only good relatively
<b>MOX</b>	Good experience	Low thermal conductivity Proliferation concern
<b>Cermet</b>	Potentially high thermal conductivity and density Able to combine $UO_2$ vast experience	Low operational experience

## 2.5 Conclusions

This Chapter has considered several areas of interest to develop the blank canvas approach for a civil marine reactor design. The first area investigated civil marine vessels that have used a nuclear reactor in the past. From this, an understanding of the reactor types used, predominantly PWR variants of each other and a background into why they did not succeed. This was mainly due to them all being one off designs or prototypes.

The nuclear fuel type of beneficial use in civil marine reactor was considered from a thermal mechanical perspective and to be used in a PWR. Fuels that would have a high thermal efficiency and high density were preferred, as well as fuels that have had extensive use, rather than novel fuels that would take decades to research and implement on a new civil marine reactor.  $\text{UO}_2$ , MOX, and uranium silicide are fuel type materials that show promise for having the desirable material properties, as well as being able to operate in a civil marine PWR without the need for extensive research compared to the other fuels considered. For the next section of work of simulation of a fuel rod in Chapter 3, with  $\text{UO}_2$  taken forward as the fuel material of choice due to its wide experience and in developing a basis for a marine reactor as long term experience has been conducted with this material.

Cermets fuel was taken forward in the experimental fabrication research in Chapter 4, and simulation work of Chapter 5 due to its ability to link in with  $\text{UO}_2$  fuel without having to develop another fuel type further, as well, it is determined to provide the best improvement of thermal conductivity that can be developed while keeping a large amount of operating experience of  $\text{UO}_2$  which will be important for providing a safety cases.

## 2.6 References

- [1] G. T. Seaborg, J. T. Ramey, G. F. Tape, and W. E. Johnson, "Nuclear Power and Merchant Shipping," *United States At. Energy Comm.*, 1964.

- [2] New York Shipbuilding Corporation, “Technical press information N.S. Savannah.” pp. 1–9, 1980.
- [3] “The World’s First Nuclear Merchant Ship – NS Savannah,” 2010. [Online]. Available: <http://gcaptain.com/the-worlds-first-nuclear-merchant-ship-ns-savannah/>.
- [4] M. Ragheb, “Nuclear Naval Propulsion,” in *Nuclear power - deployment, operation and sustainability*, Dr. Pavel ., vol. 10, 2011, pp. 323–328.
- [5] D. Bunemann, M. Kolb, H. Henssen, E. Muller, and W. Rossbach, *Advances in nuclear science and technology - the core design of the reactor for the nuclear ship “Otto Hahn.”* New York: Academic Press, 1972.
- [6] “NS Otto Hahn - Germany’s Nuclear Powered Cargo Ship,” 2010. [Online]. Available: <http://www.radiationworks.com/photos/nsottohahn5.htm>.
- [7] L. O. Freire and D. A. De Andrade, “Historic survey on nuclear merchant ships,” *Nucl. Eng. Des.*, vol. 293, pp. 176–186, 2015.
- [8] C. L. Whitmarsh, “Review of zircaloy-2 and zircaloy-4 properties relevant to N.S. Savannah reactor design,” *Oak Ridge Natl. Lab.*, pp. 1–2, 1962.
- [9] S. Sasaki, “General description of the first nuclear ship ‘MUTSU,’” *Nucl. Eng. Des.*, vol. 10, pp. 123–125, 1969.
- [10] A. Yamaji and Y. Sakamoto, “Comparison between measured and design dose rate equivalents on board of nuclear ship MUTSU,” *J. Nucl. Sci. Technol.*, vol. 30, pp. 926–945, 1993.
- [11] H. OI and K. Tanigaki, “The ship design of the first nuclear ship in Japan,” *Nucl. Eng. Des.*, vol. 10, no. April, pp. 211–219, 1969.
- [12] “Ship Spotting Mirai,” 2011. [Online]. Available: <http://www.shipspotting.com/gallery/photo.php?lid=1345614>.
- [13] Y. Takada and T. Yokomura, “Thermo-hydraulic model test of the first nuclear ship reactor in Japan,” *Nucl. Eng. Des.*, vol. 10, pp. 126–147, 1969.
- [14] N. S. Khlopkin and A. P. Zotov, “Merchant marine-nuclear powered vessels,” *Nucl. Eng. Des.*, vol. 173, pp. 201–205, 1997.
- [15] “Rosatom Flot,” 2011. [Online]. Available: <http://www.rosatomflot.ru/index.php?menuid=34&lang=en>. [Accessed: 01-Jan-2011].
- [16] N. A. Isakov, A. M. Kovalenko, and E. E. Tyuremnov, “Radiation conditions in the region of the construction and the integrated mooring tests of the nuclear cargo container ship Sevmorput,” *At. Energiya*, vol. 72, pp. 599–604, 1992.
- [17] O. Reistad and P. L. Olgaard, “Russian nuclear power plants for marine applications,” *Nor. Radiat. Prot. Auth.*, 2006.

- [18] P. L. Olgaard, "The potential risks from Russian nuclear ships," *Riso Natl. Lab.*, pp. 1–61, 2001.
- [19] E. Alfred Mohammed, S. D. Benson, S. E. Hirdaris, and R. S. Dow, "Design safety margin of a 10,000 TEU container ship through ultimate hull girder load combination analysis," *Mar. Struct.*, vol. 46, pp. 78–101, 2016.
- [20] International Atomic Energy Agency, *Thermophysical properties of materials for nuclear engineering: A tutorial and collection of data*. IAEA, 2008.
- [21] T. R. G. Kutty, K. N. Chandrasekharan, J. P. Panakkal, and J. K. Ghosh, "Fracture toughness and fracture surface energy of sintered uranium dioxide fuel pellets," *J. Mater. Sci. Lett.*, vol. 6, pp. 260–262, 1987.
- [22] R. B. Matthews, "Irradiation Performance of Nitride Fuels," in *Specialist conference on space nuclear power and propulsion technologies - materials and fuel*, 1993.
- [23] D. E. Burkes, R. S. Fielding, D. L. Porter, M. K. Meyer, and B. J. Makenas, "A US perspective on fast reactor fuel fabrication technology and experience. Part II: Ceramic fuels," *J. Nucl. Mater.*, vol. 393, no. 1, pp. 1–11, Aug. 2009.
- [24] S. B. Ross, M. S. El-Genk, and R. B. Matthews, "Thermal conductivity correlation for uranium nitride fuel between 10 and 1923 K," *Nucl. Mater.*, vol. 151, pp. 313–317, 1988.
- [25] D. Rafaja, L. Havela, R. Kužel, F. Wastin, E. Colineau, and T. Gouder, "Real structure and magnetic properties of UN thin films," *J. Alloys Compd.*, vol. 386, pp. 87–95, Jan. 2005.
- [26] J. L. Snelgrove, G. L. Hofman, M. K. Meyer, C. L. Trybus, and T. C. Wiencek, "Development of very-high-density low-enriched-uranium fuels," *Nucl. Eng. Des.*, vol. 178, no. August, pp. 119–126, 1997.
- [27] V. I. Kolyadin, K. P. Dubrovin, V. I. Pavlenko, and A. V. Kruglov, "Research on uranium-silicide nuclear fuel," *IAEA*, pp. 93–99, 1989.
- [28] L. Hofman, J. Rest, and T. Reactors, "Comparison of irradiation behavior of different uranium silicide dispersion fuel element designs," in *International meeting on reduced enrichment for research and test reactors*, 1994.
- [29] A. Suripto, S. Soentono, I. R. Subki, G. L. Hofman, and Prayoto, "High density uranium silicide with excess uranium," in *International meeting on reduced enrichment for research and test reactors*, 1999.
- [30] H. Shimizu, "The properties and irradiation behavior of  $U_3Si_2$ ," *At. Int.*, pp. 1–44, 1965.
- [31] International Atomic Energy Agency, *Research reactor core conversion guidebook*, vol. 1. IAEA, 1992.

- [32] K. Yanagisawa, T. Fujishiro, O. Horiki, K. Soyama, H. Ichikawa, and T. Kodaira, "Dimensional stability of low enriched uranium silicide plate-type fuel for research reactors at transient conditions," *J. Nucl. Sci. Technol.*, vol. 243, no. 1, pp. 233–243, 1992.
- [33] D. V. Zverev, S. N. Kirillov, K. N. Dvoeglazov, A. Y. Shadrin, M. V. Logunov, A. N. Mashkin, O. V. Schmidt, and L. V. Arsenkov, "Possible options for uranium-carbide SNF processing," *Procedia Chem.*, vol. 7, pp. 116–122, 2012.
- [34] M. Virost, S. Szenknect, T. Chave, N. Dacheux, P. Moisy, and S. I. Nikitenko, "Uranium carbide dissolution in nitric solution: sonication vs. silent conditions," *J. Nucl. Mater.*, vol. 441, pp. 421–430, 2013.
- [35] H. Matzke, *Science of advanced LMFBR fuels solid state physics, chemistry, and technology of carbides, nitrides, and carbonitrides of uranium and plutonium*. Amsterdam: Elsevier Science Pub. Co., 1986.
- [36] T. Autoren, C. Jacques, L. Mats, L. Yacine, K. P.- Asq, I. Icam, W. Wagner, F. Groeschel, L. Zanini, L. Tecchio, E. Brun, and E. Task, *Detail thermal stress analysis of EURISOL fission targets - first concept*. Paul Scherrer institute, 2006.
- [37] D. E. Burkes, R. Prabhakaran, J.-F. Jue, and F. J. Rice, "Mechanical properties of DU-xMo alloys with x = 7 to 12 weight percent," *Metall. Mater. Trans. A*, vol. 40, pp. 1069–1079, Mar. 2009.
- [38] D. E. Burkes, R. Prabhakaran, T. Hartmann, J.-F. Jue, and F. J. Rice, "Properties of DU–10wt% Mo alloys subjected to various post-rolling heat treatments," *Nucl. Eng. Des.*, vol. 240, no. 6, pp. 1332–1339, 2010.
- [39] J. M. Fackelmann, A. A. Bauer, and D. P. Moak, "Literature Survey on Dilute Uranium Alloys," *Battelle Meml. Inst.*, 1969.
- [40] V. P. Sinha, G. J. Prasad, P. V. Hegde, R. Keswani, C. B. Basak, S. Pal, and G. P. Mishra, "Development, preparation and characterization of uranium molybdenum alloys for dispersion fuel application," *J. Alloys Compd.*, vol. 473, no. 1–2, pp. 238–244, 2009.
- [41] U . S . Department of Energy Office, "Characteristics of uranium and its compounds," *U.S. Dep. energy Off. Environ. Manag.*, pp. 1–4, 2001.
- [42] A. F. Kaufman, *Nuclear Reactor Fuel Elements: Metallurgy and Fabrication*. New York: Interscience Publishers, 1962.
- [43] D. Olander, E. Greenspan, H. D. Garkisch, and B. Petrovic, "Uranium–zirconium hydride fuel properties," *Nucl. Eng. Des.*, vol. 239, pp. 1406–1424, Aug. 2009.
- [44] Y. Ronen and A. Sharon, "Plate vs rod fuel elements in a tight-lattice water reactor," *Ann. Nucl. Energy*, vol. 10, pp. 277–280, 1982.
- [45] International Atomic Energy Agency, "Structural behaviour of fuel assemblies for water cooled reactors," *Proceedings*, p. 324, 2005.

- [46] S. Mishra, P. S. Kutty, T. R. G. Kutty, S. Das, G. K. Dey, and A. Kumar, "Cermets for fast reactor - Fabrication and characterization," *J. Nucl. Mater.*, vol. 442, no. 1–3, pp. 400–407, 2013.
- [47] J. a. Webb and I. Charit, "Analytical determination of thermal conductivity of W–UO<sub>2</sub> and W–UN cermet nuclear fuels," *J. Nucl. Mater.*, vol. 427, no. 1–3, pp. 87–94, 2012.

## **Chapter 3 Civil marine reactor design and thermo-mechanical fuel rod simulation**

### **3.1 Introduction**

This Chapter covers the research undertaken using the software ENIGMA 78, which is a fuel performance code that simulates a nuclear fuel rod over its lifetime, predicting the changes in the thermal and mechanical properties. One of the key criteria set out for the design of this civil marine reactor is to operate for long periods of time between refuelling, with the target being 15 years. An understanding is needed of how a fuel rod will operate and behave in the given environment for this length of time.

### **3.2 ENIGMA**

The simulation work was carried out using the fuel performance code ENIGMA 78. The software was originally designed and operated by BNFL, with this particular version licensed through Westinghouse. The software predicts the lifetime behaviour of a single fuel rod inside a reactor with respect to its thermal and mechanical properties. The ENIGMA source code is written in the FORTRAN language, and “consists of house-keeping modules which perform input, output, initialisation, updating, and processing (including sub-division) of the supplied irradiation history” [1]. ENIGMA is currently used in the UK for commercial licensing of current and future fuel [2].

ENIGMA runs as an .exe file and is able to be run on a desktop or laptop computer without the need for any external research computer power.

Essentially, the software calculates changes in material properties working from the bottom of the fuel rod up to the top during one timestep using a finite difference technique [3]. The fuel rod is divided into even axial zones [4] defined by the user with each zone simulated in order, with the results of each zone influencing the next zone. A simulation requires a data file containing essential information about the fuel rod to run. These are properties such as the

geometry, material type such as UO<sub>2</sub>, MOX, coolant conditions and power rating of the fuel rod. During each time step the software updates the material properties of each component.

Once the simulation has run, the software generates an output file that contains information for each iteration. This records such things as temperatures at different points in the fuel rod, oxidation thickness on the cladding, coolant temperatures, fission gas release (FGR) from the fuel pellets, internal pressure inside the fuel rod, power rating, stress and strains on the cladding, as well as the fuel clad gap. From this information, a picture can be generated of how the fuel rod is behaving over its lifetime and what the final conditions are. This information is particularly useful to determine if the fuel rod will fail.

Heat flow is assumed only in the radial direction and not axially or circumferentially [4] and the same axial strain is subjected to fuel annuli, allowing shear stresses to be ignored [4]. As heat is generated throughout the length of the fuel rod, the path favoured for conduction is in the radial direction and that axially and circumferentially is a marginal effect relatively.

Thermal conductivity is one material property that is the focus of this Chapter and thesis. In ENIGMA the basic thermal conductivity formulation that is used is described below:

$$k = \frac{1}{a + bT} + \text{electronic term}; a = a_0(1 + \infty B)$$

In the above equation, T is the absolute temperature, k is the thermal conductivity, a is a phonon scattering term which is from impurities and lattice defects scattering, b is the phonon-phonon scattering constant, and  $\infty$  is the thermal conductivity degradation with burnup rate [4].

The ENIGMA code has been validated against a database of over 500 rod irradiations with burnups as high as 90 MWd/kgHM, with all rods from light water reactors [3].

There are other fuel performance codes that could have been used for this simulation work. FRAPCON is a US fuel performance code developed by the Nuclear Regulatory Commission.

The code is used for modelling light water reactors [5], [6]. The Advanced MultiPhysics (AMP) fuel performance code is a more recent code developed in the last 10 years to assist with modelling of generation 4 reactors. This code is run at Oak Ridge National Laboratory and is designed to provide a 3D simulation software and enhanced user interfaces when compared older codes such as FRAPCON [7]. The availability of these codes and licensing were the biggest draw backs to using them as the main simulation software or even to using them in parallel with ENIGMA.

### **3.3 Fuel failure mechanisms**

The ENIGMA code provides data on different properties that can show conditions of fuel failure. There are different ways a fuel rod could fail in a thermal mechanical way and the following conditions can be predicted by ENIGMA.

#### **3.3.1 Cladding corrosion failure**

Oxidation occurs on the outer wall of fuel rod cladding in a light water reactor. This is a process that is managed rather than trying to engineer its prevention. Over long periods of time, there is the potential that the corrosion will reach a point that makes the rod brittle or weak in certain areas that could cause it to rupture. It is the time frame of this failure that is of interest for this investigation.

To monitor this condition by using ENIGMA, the code provides a value for the thickness of the oxidation that has occurred on the cladding at each axial section of the fuel rod, with it assuming a homogenous oxidation growth radially and axially in each section. Regulatory practices in this area set a limit for the oxidation thickness not to exceed 10 % of the wall thickness. ENIGMA provides a data value of the thickness in  $\mu\text{m}$  of the oxidation. As the oxide material has different material properties to the original cladding material, the Pilling Bedworth ratio is used. This ratio compares the metal oxide volume to the original metal volume [8]. In

this situation the percentage of wall thickness lost is determined by dividing the thickness of oxidation by the Pilling Bedworth ratio.

The ENIGMA model for cladding corrosion assumes that the oxidation occurs using a cubic rate growth until a thickness of 2.2  $\mu\text{m}$ , after which a linear rate is applied and is based upon a review of PWR clad corrosion behaviour. The oxidation is calculated at each given time step [1].

### **3.3.2 Fuel rod swelling, ballooning**

If the pressure build up inside, the fuel rod becomes greater than the coolant pressure, the fuel cladding will expand outwards away from the fuel pellets. The pressure build up is caused by fission gas release (FGR), where by gaseous fission products that are produced in the fuel material manage to escape out of the fuel material grains, work their way along the grain boundaries, and thus are release out of the fuel material into the void between the fuel material and clad wall. When this happens the fuel-clad gap, if present, will increase and heat transfer will decrease thereby raising the temperature inside the fuel. One of the contributory factors to the increase in internal rod pressure is due to the FGR from the fuel pellets. This rate of release is a function of temperature. Therefore, as the fuel becomes hotter, the rate of FGR increases which, in turn, increases the pressure further causing the fuel-clad gap to expand. This feedback loop continues, referred to as a ballooning effect, until the melting of the clad wall material or fuel.

In ENIGMA, to record this fuel failure, the rod internal pressure can be monitored over the lifetime of the fuel rod. As the coolant pressure is a constant and known value, it can be compared with the internal pressure and a limit set below the coolant pressure not to be surpassed, which would be a value lower than the coolant pressure.

### 3.3.3 Pellet clad interaction

At the start of the life of a fuel rod, there is a gap between the fuel pellets and the clad wall. Initially this gap increases as the fuel pellets heat up and increase in density as porosity is removed. As time progresses, the rate of creation of fission products overtakes the increases in density, the fuel pellets increase in volume, and so the rod swells. The thermal expansion of  $UO_2$  is greater than the zirconium clad. Thus, thermal expansion makes a contribution in closing the pellet clad gap [9]. Once the pellet clad gap closes, the pellet interacts with the cladding thereby causing pellet clad interaction (PCI); simplistically the pellet is in contact with the wall and applying radial stress. This occurs at certain points on the pellet, and it takes on the appearance of an hour glass shape or wheat sheaf, Figure 3.1, due to the difference in temperature across the pellet and varying thermal expansion. Point loads can occur at the top and bottom of the pellet where the PCI occurs. The top parts of the pellet can also break off and form a chip and can fall down to the middle of the pellet creating a point load. This can result in a rupture of the clad wall and potential failure of the fuel rod, depending on the size of the rupture.

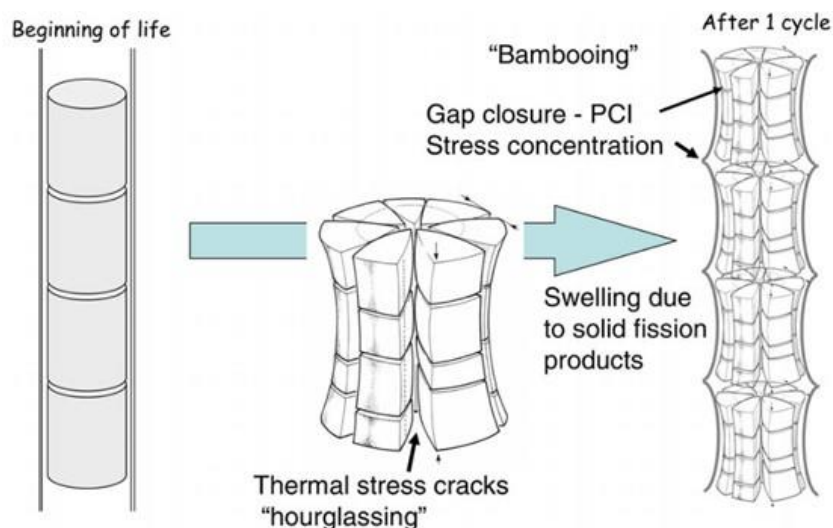


**Figure 3.1 – Representation of fuel pellets and cladding to demonstrate pellet clad interaction [10].**

ENIGMA can simulate the point at which the PCI begins, as it is a reasonably well understood phenomenon, and predict where the stress will occur at different sections on the clad wall. The safe industry limit for the stress applied on the cladding is less than 1 % of the yield stress of the clad material. Therefore, the 1 % yield stress value can be determined and monitored against outputs by ENIGMA to determine if it goes above a set safe limit.

### **3.3.4 Fuel/clad melting**

ENIGMA predicts the temperature in axial zone of the fuel rod for the fuel pellet centreline temperature, fuel pellet surface temperature, average fuel pellet temperature and the rod/outer clad wall surface temperature. All of these are able to be monitored through the life of the rod and compared with the melting temperature of the relevant material. To give an example, the melting temperature of UO<sub>2</sub> is at 2865°C [11]. The centreline and fuel edge temperatures can be monitored in ENIGMA to determine if they get close to the melting temperatures.

## **3.4 Marine reactor design criteria**

### **3.4.1 Marine reactor type and fuel**

The reactor type for this design is a pressurised water reactor (PWR). Several reasons have influenced the justification for this decision. Firstly, PWR reactors have been the predominant reactor design for civil merchant ships to date as discussed in Chapter 2. This provides a wealth of knowledge and experience with regards to designing and operating in this environment. Secondly, large PWR reactors are one of the most widely used for national electricity generation in many countries. This is true for currently operating, currently under construction, and future planned reactors as established from an IAEA report [12]. Therefore, this provides for a vast amount of experience over different reactor types such as boiling water or gas cooled reactors. As well, the supply chain to manufacture such reactors is established due to the ongoing investment worldwide in these reactors.

As this project is started with a blank canvas approach, having such a wealth of knowledge and experience with PWR reactors provides confidence in the design chosen for this civil marine reactor. In the future, if civil marine reactors are implemented into merchant ships, and an operating knowledge base built up, it would then allow the potential for other reactor types to be further considered.

Similar to the reactor type chosen, the fuel choice will be uranium dioxide ( $\text{UO}_2$ ). Again there is a large knowledge base on the use of this type of fuel; it is the most used fuel type for marine reactors. The ENIGMA fuel performance code is setup to use several fuel types but the most common one is  $\text{UO}_2$ . From the fuel investigation conducted in Chapter 2, uranium silicide and MOX fuel also show interest to be developed at a later stage.

One consideration for manufacturing is that the maximum core diameter should not be greater than 3.5 m. This was a suggestion by Rolls-Royce, because at this size the reactor would be able to be transported by rail.

### **3.4.2 Operating behaviour of proposed reactor**

The proposed use for this reactor is to operate on large civil ships; other uses could be for large platforms or land based sites. However, the main goal for this work is designing it for one of the larger container vessels that currently operate in the world, such as the Emma Maersk, which is one of a class of eight ships of similar size. The Emma Maersk requires a total power of 110 MWe [13]. Originally, simulations were going to base the power load of the reactor on the actual requirements of the Emma Maersk. This would have assumed a typical route that the ship undertakes and the operating days in and out of port [14]. This assumption would dictate the high and low power levels required. However, for simplification, this work has focused on considering the reactor to operate at a constant power level for a period of 15 years. Therefore, the fuel rod simulations will not cycle through ramp ups and downs in power level, these effects

are considered to be marginal to the length of the simulation. Future simulations will look into a more detailed power cycle loading.

Collaborative work on this project with Aiden Peakman at the University of Manchester has determined that the power level requirement per rod for this reactor should be between 7 kW/m and 9 kW/m using the MONK Monte Carlo reactor physics analysis software. Therefore simulations will be conducted using power ratings in this range.

### 3.4.3 Fuel rod and reactor design

The initial simulations carried out used fuel rod designs that are commonly used in civil reactors; that being of cylindrical shape and using UO<sub>2</sub> fuel and Zircaloy-4 as a cladding material. All other geometry conditions for the fuel rod and other reactor conditions used in the simulations are specified in Table 3.1.

**Table 3.1 – Design criteria used for ENIGMA simulations.**

Property	Value	Units
Reactor type	PWR	
Cladding material	Zircaloy-4	
Power	110	MWe
Efficiency	33	%
Core diameter	3.5	m
Refuelling period	15	years
Cladding radius inner/outer	4.1707/4.7422	mm
Coolant Pressure	15.513	MPa
Coolant inlet temperature	281	°C
Target coolant exit temperature	310	°C
Fuel type	UO <sub>2</sub>	
Enrichment of fuel	10	%
Fuel stack length	2.7	m
Fuel pellet radius	4.94	mm
Fuel pellet length	13.691	mm
Plenum length	0.14	m
Internal gas composition	97.09 He, 2.91 N	%
Average grain size of fuel	11	µm

## 3.5 Results and discussions

### 3.5.1 UO<sub>2</sub> simulation

The first set of simulations were conducted basing the operating conditions on a land civil nuclear reactor. This analysis was conducted to set a base line of what an existing reactor design could achieve. The simulations were carried out to evaluate the rods behaviour and to determine if life-limiting or failure mechanisms would occur.

Error bars have been calculated for each result by varying three key elements for each simulation. These were the power rating by 2 %, clad wall thickness by 2 %, and coolant inlet temperature by 5°C. The variations used are possible expected values that might occur due to the acceptable tolerance of key parameters. These variations were determined through conversations with Westinghouse. Simulations were carried out for each element varied above and below the given conditions. The error was calculated by taking the root mean square of the individual positive and negative errors of each element. Where the error is too small to represent on the plot error bars have not been included on the data points.

**Table 3.2 – Fuel rod key criteria design safety limits.**

<b>Fuel rod criteria</b>	<b>Safety limit</b>	<b>Units</b>
<b>Final rod internal pressure</b>	13	MPa
<b>Total fission gas release</b>	2	%

Design safety limits that are used through this Chapter are shown in Table 3.2. A safe limit of 13 MPa for the final rod internal pressure which is below 10 % of the coolant pressure was set with the intention to not reach the coolant pressure and to protect against the possibility of a variation of the coolant pressure. A 2 % safety limit on FGR release was used from advice by Westinghouse as they use it as their industry standard. Generally past 2 % break away FGR release occurs.

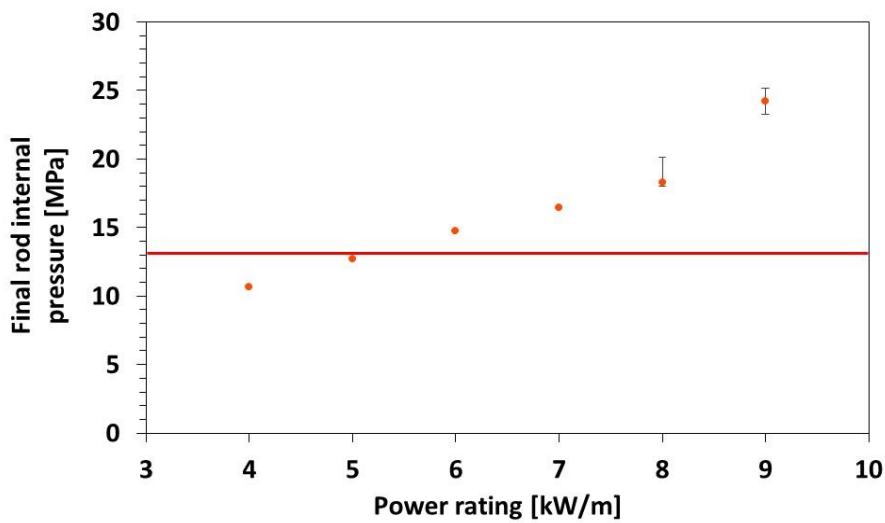


**Figure 3.2 – Final rod internal pressure or varying power ratings of initial UO<sub>2</sub> fuel rod conditions. The red line indicates the maximum safe limit. Error bars that can be represented are shown.**

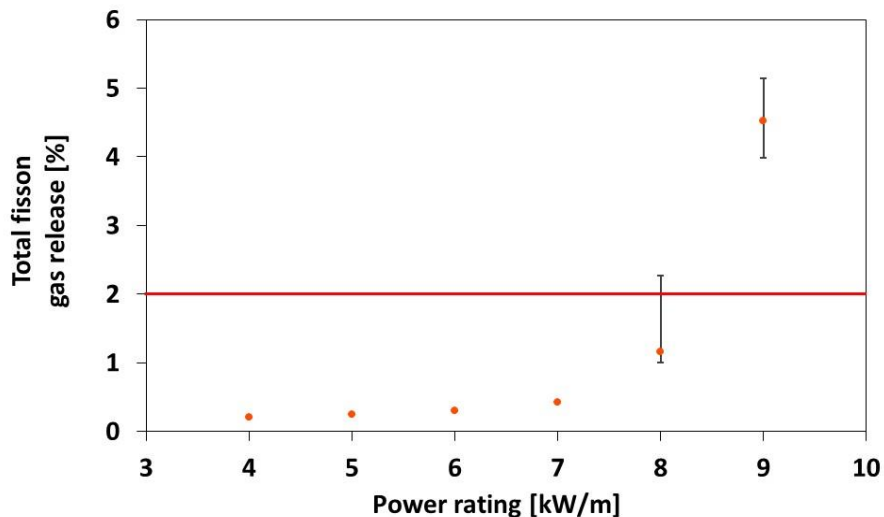


**Figure 3.3 – Total FGR from the pellet at varying power ratings of initial UO<sub>2</sub> fuel rod conditions. Error bars that can be represented are shown.**

The first set of simulations conducted showed that there was one main failure mechanism occurring after running for 15 years. The power rating in kW/m is used as this is the average power produced across the length of the fuel rod. Figure 3.2 shows that as the power rating of the fuel rod increases, the internal fuel rod pressure also increases and from 6 kW/m rating and up, the internal fuel rod pressure goes above the 13 MPa safe limit set. The total FGR, Figure 3.3, shows an exponential release of fission gases as the power rating is increased. These two factors lead to the fuel rod failure by possible ballooning and eventually rupturing.

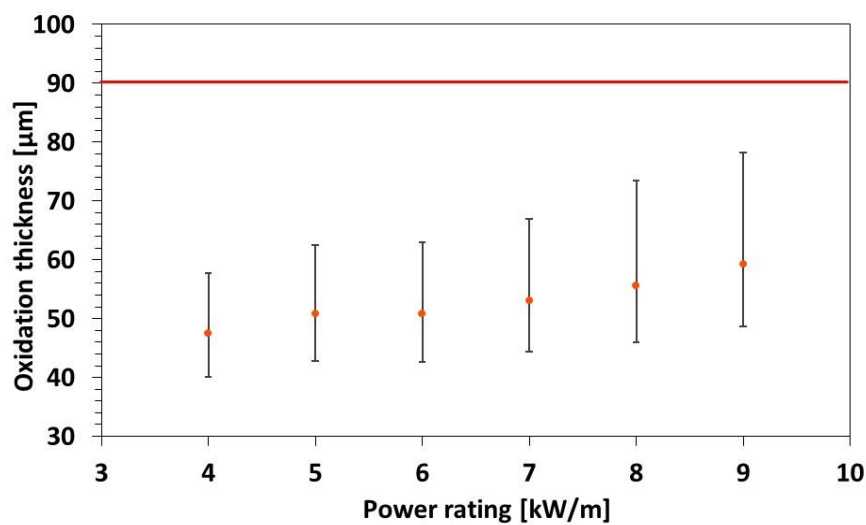


**Figure 3.4 – The oxidation accumulation for each power rating at the end of each 15 year simulation. Error bars that can be represented are shown.**

**Table 3.3 – Calculation for the oxidation limit of the clad wall.**

Clad wall thickness [µm]	10% wall thickness [µm]	Pilling Bedford ratio for Zircaloy-4	Oxidation limit [µm]
572	57.2	1.56	89

Other fuel failure mechanisms do not appear to be of concern. Figure 3.4 shows the oxidation thickness that has accumulated over the lifetime. The data here shows the greatest amount of oxidation accumulation on each fuel rod section at each power rating. As indicated on Figure 3.4 the red line is the safe limit set for oxidation occurring; this is 10 % of the cladding wall material that is then converted into oxidation thickness by using the Pilling Bedford ratio for Zircaloy-4 from Table 3.3, as the oxidised cladding material has a reduced density and thus

larger volume, this is also demonstrated in Figure 3.5 to show the 10 % maximum limit. Therefore, for the rest of the simulations carried out, oxidation is not apparently a cause for concern and so will not be investigated further.

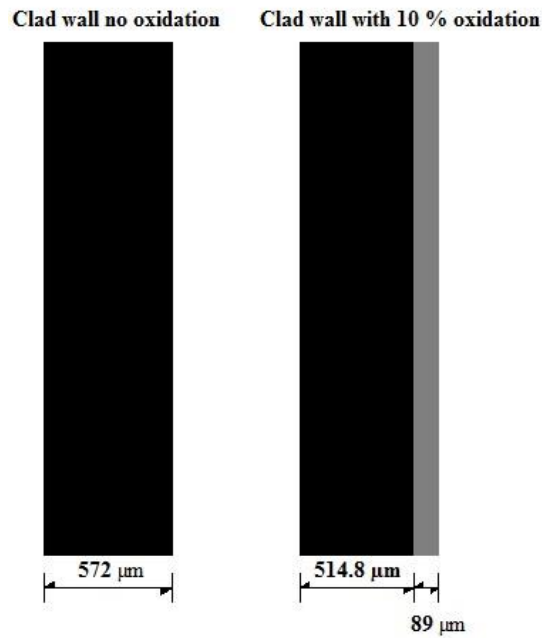


**Figure 3.5 – Cladding wall cross section to demonstrate the loss of 10 % wall material to oxidation.**

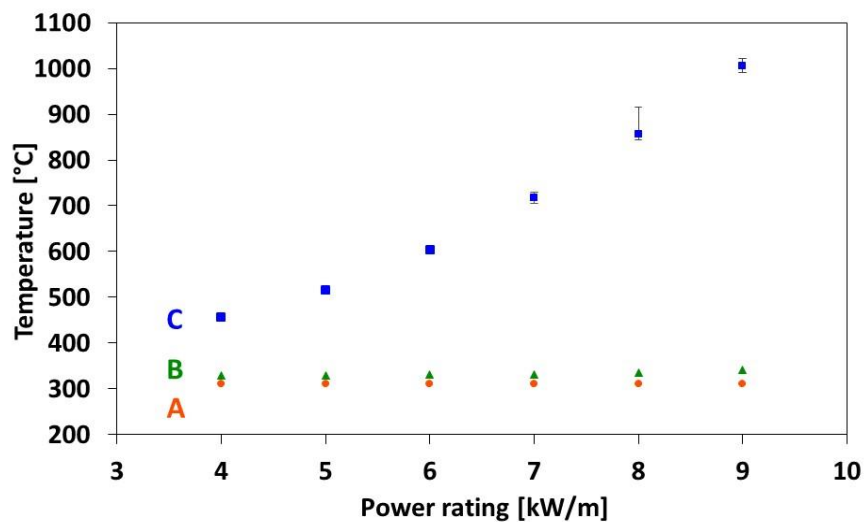


**Figure 3.6 – Final rod temperature from the hottest section of the fuel rod, A Clad surface temperature, B fuel surface temperature, C fuel centreline temperature.**

Another aspect considered from the ENIGMA simulation data with regards to fuel failure is the temperature in the fuel rod. ENIGMA is able to show the temperature at key points in the fuel rod. Shown in Figure 3.6 are the temperatures in the centre of the fuel and on its surface at the hottest section of the fuel rod. With the melting temperature of  $\text{UO}_2$  of  $2865^\circ\text{C}$  [11] and Zircaloy-4  $\sim 1760^\circ\text{C}$  [9], the temperatures shown in the simulation do not show cause for concern of the fuel or cladding melting. However, the simulations show that the difference in the centreline to the surface temperature increases exponentially as the power rating is increased. This will cause a more prominent hour glass effect of the fuel pellet due to its small diameter of 9.88 mm and the change in thermal expansion. This effect is linked to the internal rod pressure increasing, due to heat not being able to conduct out of the rod as effectively from the ballooning fuel failure condition. Therefore, the main focus of reactor design concept should be to prevent the internal rod pressure increase.

### 3.5.2 Annular $\text{UO}_2$ fuel pellets

With the findings from the first set of simulations showing high fuel rod internal pressure and FGR, the geometric design of the fuel rod and pellets was refined as an option to mitigate this problem.

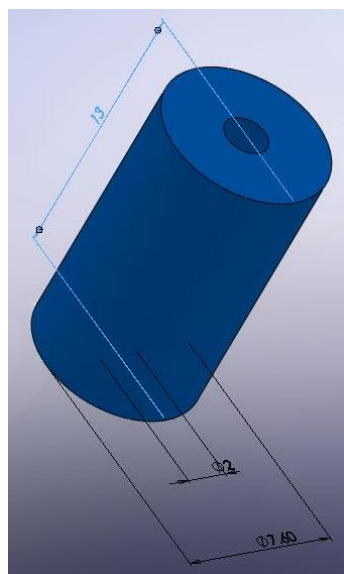


**Figure 3.7 – Computer aided design drawing using Solidworks of the geometry of an annular pellet.**

The use of annular fuel pellets with the same fuel rod cladding geometry was considered, with Figure 3.7 showing a representative geometry for a 2 mm diameter annular pellet. Six annulus sizes from 1 mm to just under 6 mm were used, and all other conditions kept the same.

The annular fuel pellets simulated here are single cooled. Meaning that the coolant is only on the outer wall of the fuel cladding. Dual-cooled annular fuel pellets are not simulated in this investigation where a second coolant channel runs through the middle. Such fuel rod designs have a clad material on the outside and through the middle of the fuel pellet and were first proposed in 2006 [15]. This fuel type design presents the possibility for increasing the reactor power [16]. However, ENIGMA is not validated or coded for such a fuel design and such an undertaking falls outside the scope of this research. This is proposed for a future area of investigation if required.

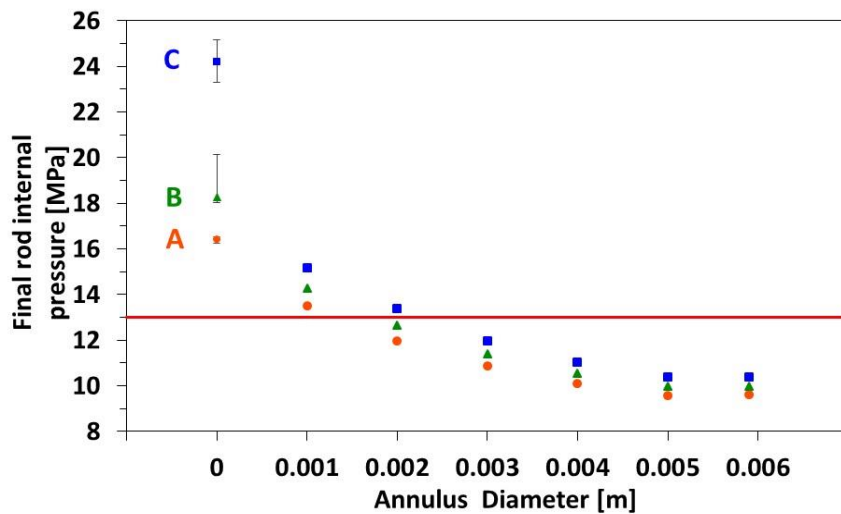


**Figure 3.8 – Final rod internal pressure for varying annulus diameters at power ratings A 7 kW/m, B 8 kW/m, C 9 kW/m. The red line indicates the maximum safe limit.**

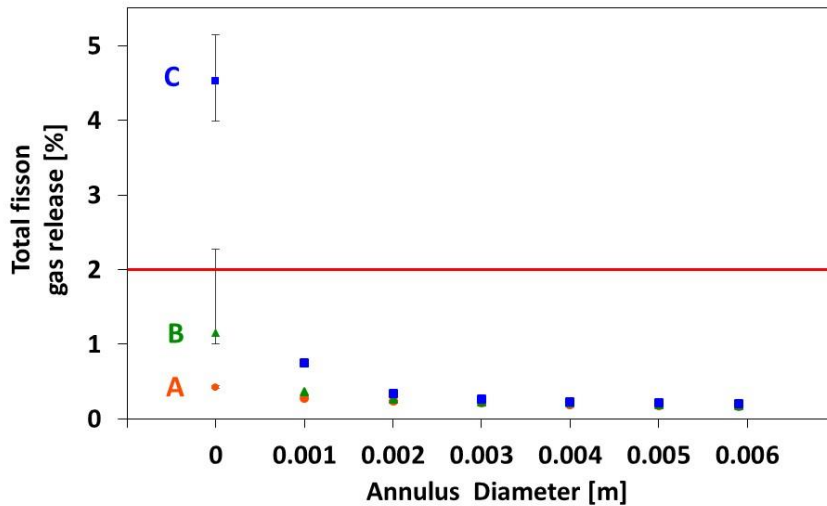


**Figure 3.9 – Total FGR from varying annulus diameters and at power ratings A 7 kW/m, B 8 kW/m, C 9 kW/m.**

Only power ratings of 7 kW/m, 8 kW/m and 9 kW/m were used for the simulation of the design of this civil marine reactor. These power ratings were based on collaborative work on this project that carried out simulations on the entire core. The final rod pressure, Figure 3.8, shows that from an annulus diameter of 3 mm and above, the final internal pressure was kept below the limit set of 13 MPa. This is explained by a greater free volume for gases to occupy and thus a reduced pressure, and also a reduced amount of fission gases that are released, Figure 3.9. The annular pellet is able to run cooler and thus less fission gas is released, as FGR is a temperature dependant process [17].

### 3.5.3 Plenum increase of fuel rod

A second geometric parameter investigated was to increase the plenum volume of the fuel rod. This was done by increasing the height at the top of the fuel rod, thus providing more free space. Simulations were carried out again at 7 kW/m, 8 kW/m and 9 kW/m power rating settings and the plenum length varied from 0.14 m to 0.50 m.

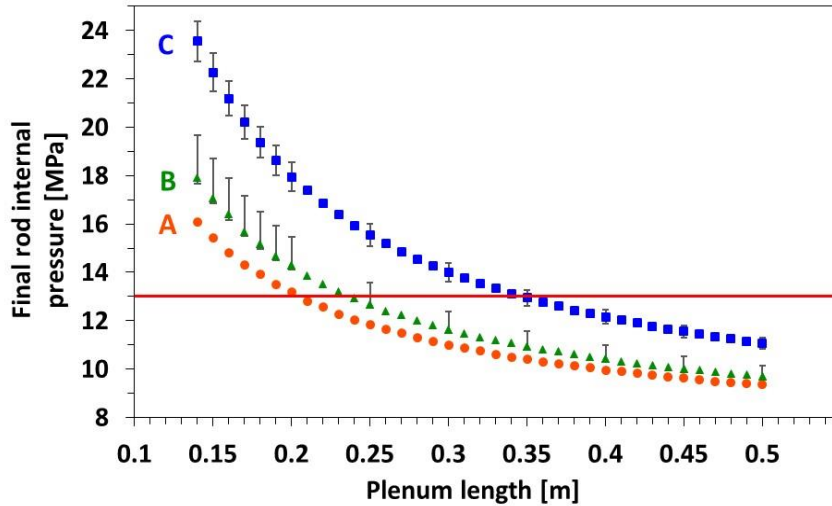


**Figure 3.10 – Final rod internal pressure for varying plenum length at power ratings A 7 kW/m, B 8 kW/m, C 9 kW/m. The red line indicates the maximum safe limit.**

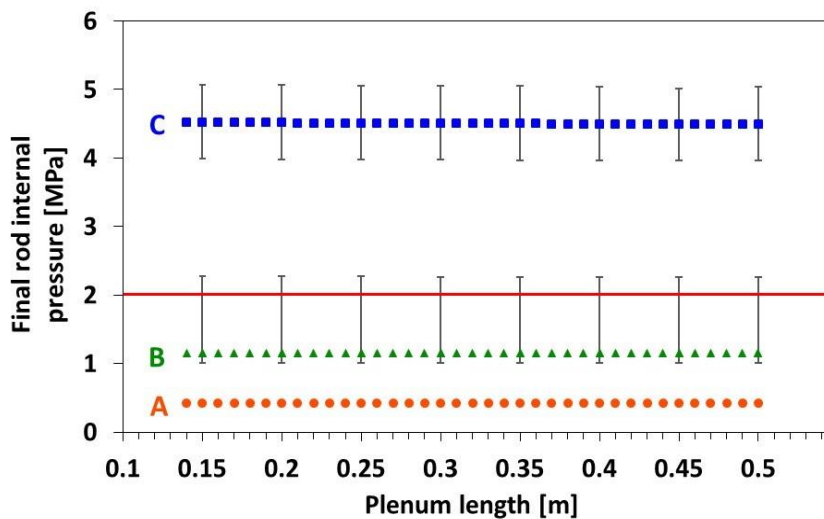


**Figure 3.11 – Total FGR from varying plenum length and at power ratings A 7 kW/m, B 8 kW/m, C 9 kW/m.**

The final rod internal pressure from the increase of plenum simulations, Figure 3.10, shows the minimum height of the plenum required at each power rating to keep the pressure below the safe limit. This is 0.21 m for 7 kW/m, 0.24 m for 8 kW/m, and 0.36 m for 9 kW/m. The plenum length increase is simply a geometry change to the cladding of the rod, and does not affect the fuel itself, and the FGR, Figure 3.11, remains constant throughout the simulation. Therefore,

the plenum increase can help mitigate the problem of the increased FGR, but it does not address the underlying cause.

### 3.5.4 Plenum and annulus hybrid

Having a larger plenum has a disadvantage of an increased length to the fuel rod and reactor, thereby resulting in higher costs. A larger annulus means the fissile fuel has to carry out more work and to compensate for this, a wider diameter pellet would be necessary. Therefore, simulations were undertaken on a fuel rod with a plenum height of 0.25 m and a varying annulus diameter of greater than 0.004 m. Current annulus manufacturing has focused on annulus sizes of 0.012 m, as the manufacture of a annulus of 0.004 m or smaller is more technical to carry out to keep to accurate tolerances [18].

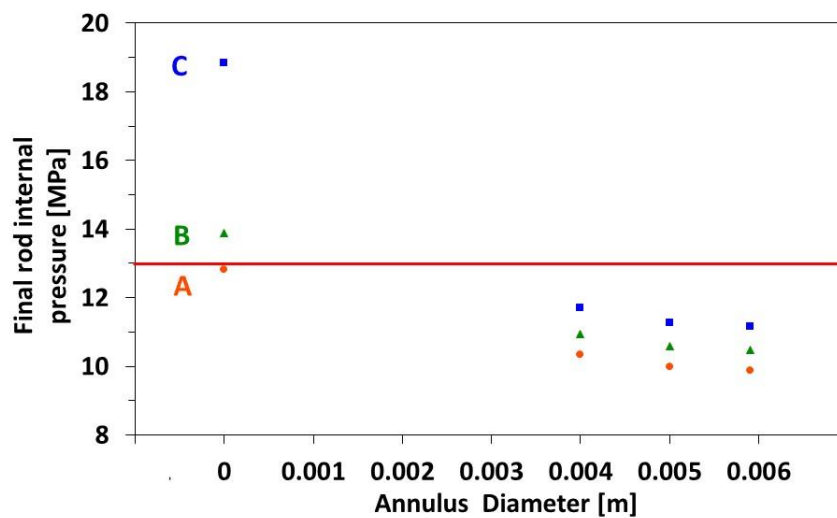


**Figure 3.12 – Final rod internal pressure for varying plenum length at power ratings A 7 kW/m, B 8 kW/m, C 9 kW/m. The red line indicates the maximum safe limit.**

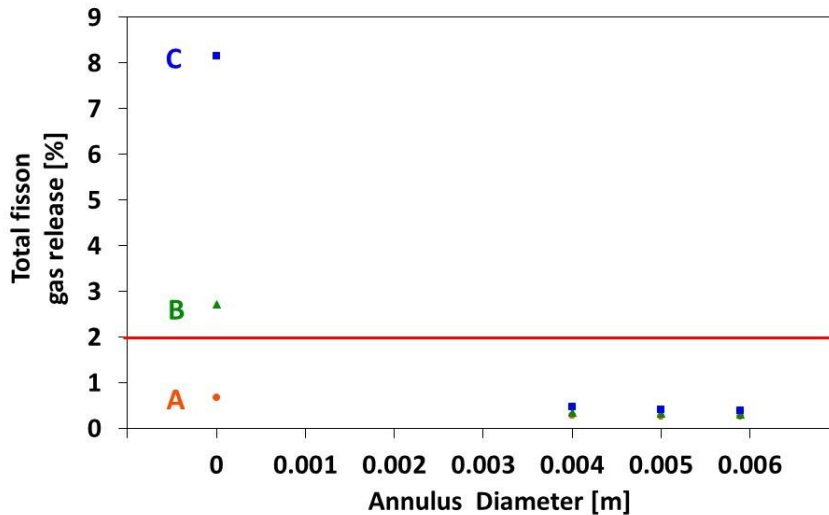


**Figure 3.13 – Total FGR from varying plenum length and at power ratings A 7 kW/m, B 8 kW/m, C 9 kW/m.**

The hybrid simulations with a constant plenum length and varying annulus size, Figure 3.12, show that, with an annulus diameter of 0.004 m and above, the total rod pressure is below the safe limit and that there is little variance between the different annulus sizes. The FGR, Figure 3.13, also shows a large drop in the fission gas released with all three annulus sizes being approximately the same.

### 3.5.5 Increase grain size of pellets

A second direction studied to overcome the problem of high pressure and FGR was to simulate changes in the fuel material properties itself. If these material properties could be adequately optimised, it would be beneficial to manufacturing costs.

The first material property considered was the grain size of the  $\text{UO}_2$  fuel. With the grain size for all previous simulations set at an average of 11  $\mu\text{m}$ , simulations were undertaken for increasing and decreasing the grain size for power ratings of 7 kW/m, 8 kW/m, and 9 kW/m. A plenum length of 0.14 m and no annulus was used for all.

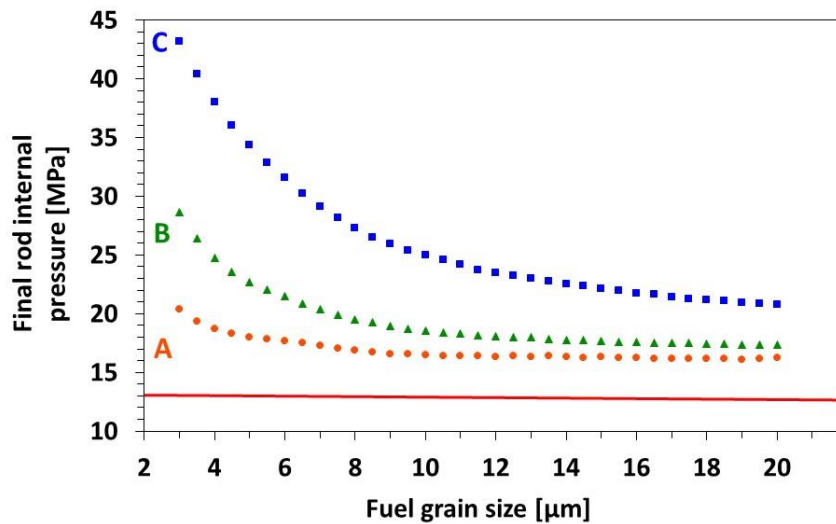


**Figure 3.14 – Final rod internal pressure for varying grain size at power ratings A 7 kW/m, B 8 kW/m, C 9 kW/m.**

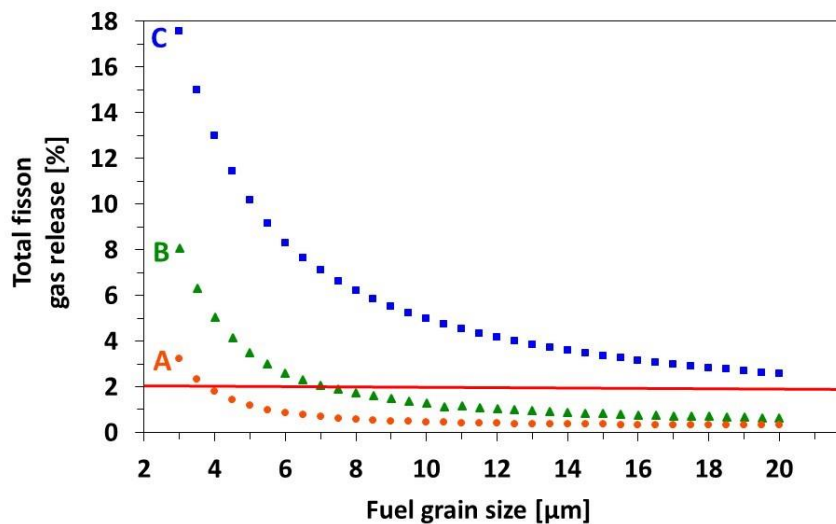


**Figure 3.15 – Total FGR from varying grain size at power ratings A 7 kW/m, B 8 kW/m, C 9 kW/m.**

A decrease in the final rod pressure, Figure 3.14, and FGR, Figure 3.15, is observed for an increase to the grain size for a power rating of 9 kW/m. Marginal decreases are observed for 7 kW/m and 8 kW/m power ratings. Decreasing the grain size resulted in the internal rod pressure and fission gas release to increase at an exponential rate. This would agree with the general understanding of the effect of grain size, that the smaller the grain, the rate of release of fission

gases from the grain increases due to the shorter distance to find the grain edge [17]. Thus, more fission gas being released contributes to an increase in the rod internal pressure.

Increasing the grain size appears to have some merits for the 9 kW/m power rating but little improvement for the 7 kW/m and 8 kW/m ratings. However, increasing the grain size does not remove the fuel failure mechanism due to increased internal pressure but could be considered with fuel design improvements previously discussed.

### **3.5.6 Improved UO<sub>2</sub> thermal conductivity pellets**

A second material property of interest was to improve the thermal conductivity of the fuel, here a percentage increase to the thermal conductivity value is defined by the user that Enigma applies. If the heat can be transferred more quickly from the fuel then this should reduce the centreline temperatures of the fuel. This would help reduce the FGR as it is a temperature dependant mechanism, the higher the temperatures, the faster the release rate.

Simulations were carried out on power ratings of 7 kW/m, 8 kW/m, and 9 kW/m using ENIGMA to increase the UO<sub>2</sub> thermal conductivity data values by a percentage amount. Simulations were conducted up to a 50 % increase as values plateaued above this. This is a percentage that is applied to the thermal conductivity at all temperatures.

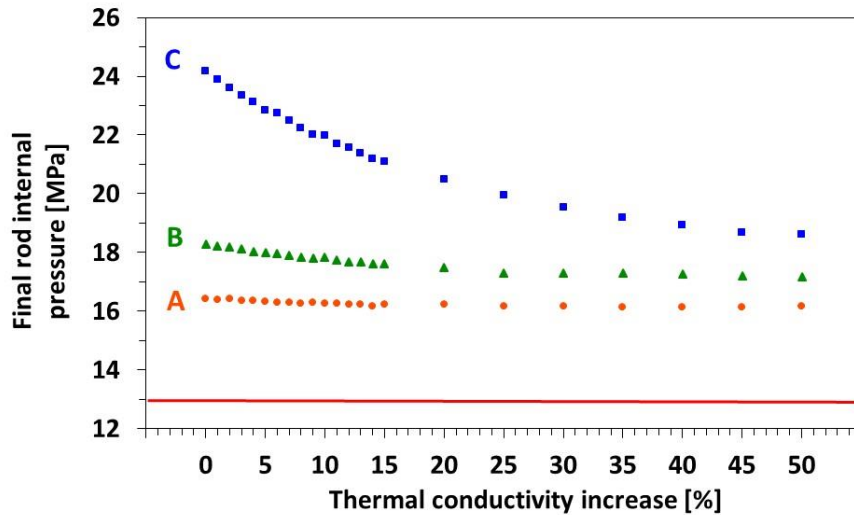


**Figure 3.16 – Final rod internal pressure for increasing thermal conductivity of UO<sub>2</sub> at power ratings A 7 kW/m, B 8 kW/m, C 9 kW/m.**

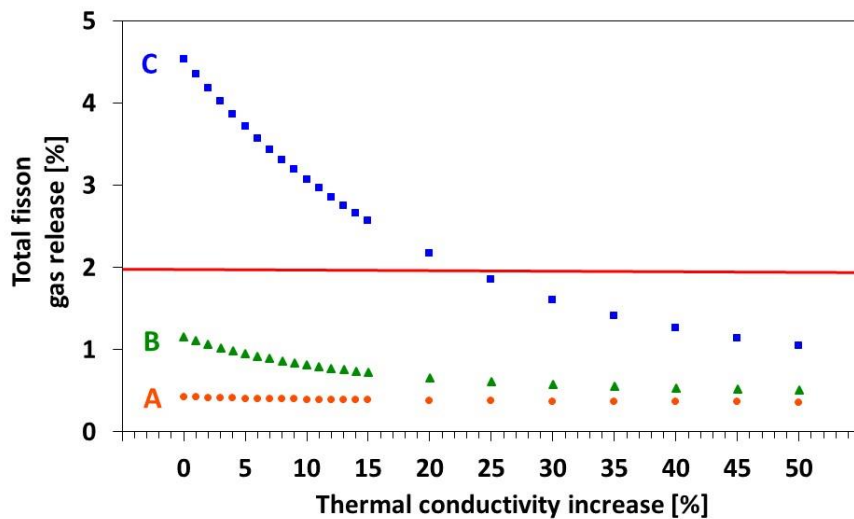


**Figure 3.17 – Total FGR for increasing thermal conductivity of UO<sub>2</sub> at power ratings A 7 kW/m, B 8kW/m, C 9 kW/m.**

There is a large improvement for the 9 kW/m power rating from increasing the thermal conductivity from 0 % to 50 %, Figure 3.16, with similar improvements in the reduced FGR observed as well, Figure 3.17. Similar to the results from varying the grain size, the 7 kW/m and 8 kW/m power ratings show only marginal decreases when compared with the 9 kW/m power rating. The 9 kW/m power rating simulations are initially at a state of exponential fuel failure, and so improvements to the design or material properties are able to influence it

significantly. Although all of these simulations are above the 13 MPa design limit for final rod internal pressure, they show that improving the thermal conductivity can help reduce the final pressure, and so will be considered to work in conjunction with other design improvements.

The simulation data shows a large decrease in centreline temperatures for the fuel in the rod. For 7 kW/m, the decrease is on average 100°C through the rod from 0 % to 50 % thermal conductivity increase, and for 9 kW/m it is 200°C shown in Figure 3.18. These decreases are due to the increase in thermal conductivity and underline that running the fuel cooler reduces the FGR and pressure build up. Another advantage of running cooler is that there will be less cracking observed in the fuel, as the thermal expansion values will be closer together across the diameter and length of the fuel stack due to the difference in centreline and surface temperatures being reduced.

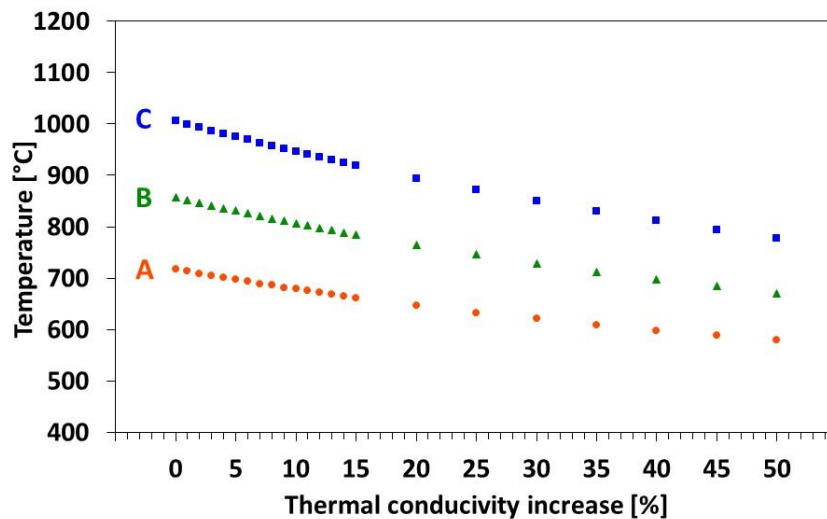


**Figure 3.18 – Centreline end of life temperature with increasing thermal conductivity values at power ratings A 7 kW/m, B 8kW/m, C 9 kW/m.**

### 3.5.7 Improved UO<sub>2</sub> thermal conductivity pellets and annulus

Simulations combining geometrical changes to the fuel by using an annular fuel pellet and increasing the thermal conductivity were also undertaken. This was done for fuel pellets of

annulus diameter of 0.002 m and 0.004 m, both while improving the conductivity between 20 % and 50 %, and while not improving the thermal conductivity for comparison.

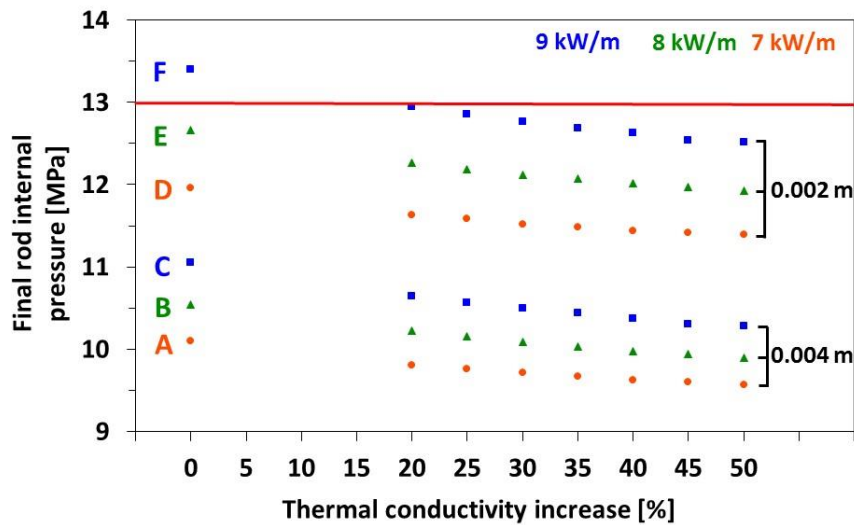


Figure 3.19– Final rod internal pressure for increasing thermal conductivity of UO<sub>2</sub> at power ratings A 7 kW/m, B 8 kW/m, C 9 kW/m all with an annulus diameter of 0.004 m and D 7 kW/m, E 8 kW/m, F 9 kW/m with an annulus diameter of 0.002 m.

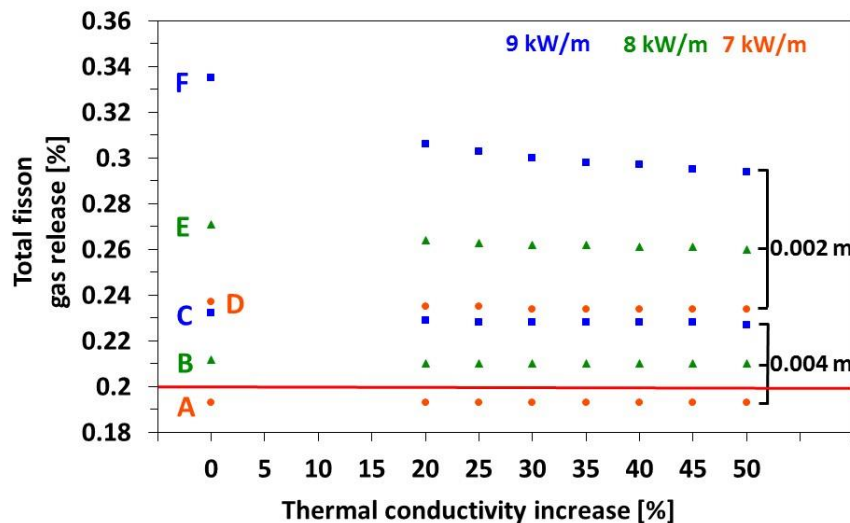


Figure 3.20 – Total FGR for increasing thermal conductivity of UO<sub>2</sub> at power ratings A 7 kW/m, B 8 kW/m, C 9 kW/m all with an annulus diameter of 0.004 m and D 7 kW/m, E 8 kW/m, F 9 kW/m with an annulus diameter of 0.002 m.

The effect of the annulus in decreasing the internal pressure (Figure 3.8) and the FGR, (Figure 3.9) is quite significant. Compared to increasing the thermal conductivity, Figure 3.19, for the

rod internal pressure, and the FGR, Figure 3.20, the improvement is marginal, with the 9 kW/m at 0.002m diameter annulus only reducing by 1 MPa of final rod pressure with a 30 % increase in thermal conductivity.

### 3.5.8 Improved UO<sub>2</sub> thermal conductivity pellets and increased plenum

The combination of increasing the plenum height while increasing the thermal conductivity was also investigated. As with the annulus/plenum hybrid simulations, a plenum height of 0.25 m was used for varying power ratings of 7 kW/m, 8 kW/m, and 9 kW/m, no annulus was used.

The improvement for 9 kW/m, as in previous simulations, is more significant than 7 kW/m and 8 kW/m (Figure 3.21 and Figure 3.22). For 9 kW/m the drop in internal pressure is approximately 3.5 MPa and 3.5 % for the FGR when increasing the thermal conductivity from 0 to 50 %. For a thermal conductivity improvement of above 40 %, the internal pressure falls below the safe limit of 13 MPa for 9 kW/m. For 7 kW/m and 8 kW/m the level was below this for all thermal conductivity values.

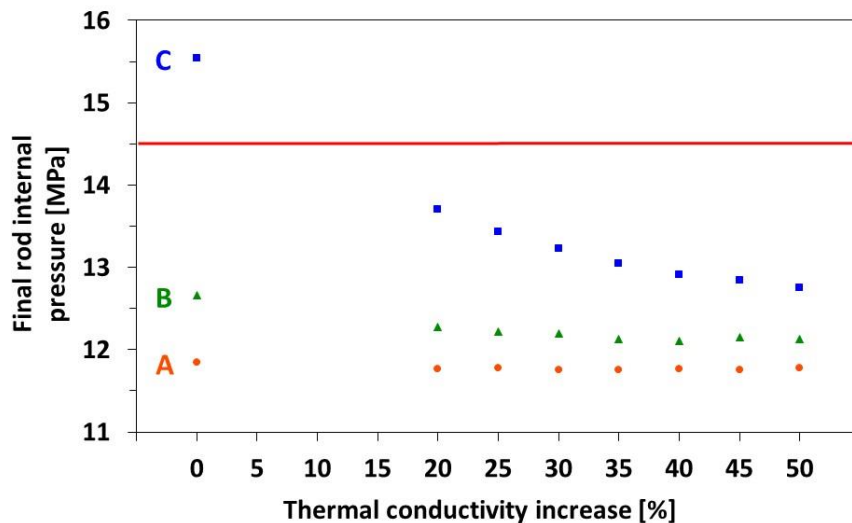


**Figure 3.21 – Final rod internal pressure for increasing thermal conductivity of UO<sub>2</sub> at power ratings A 7 kW/m, B 8 kW/m, C 9 kW/m all at a plenum height of 0.25 m.**

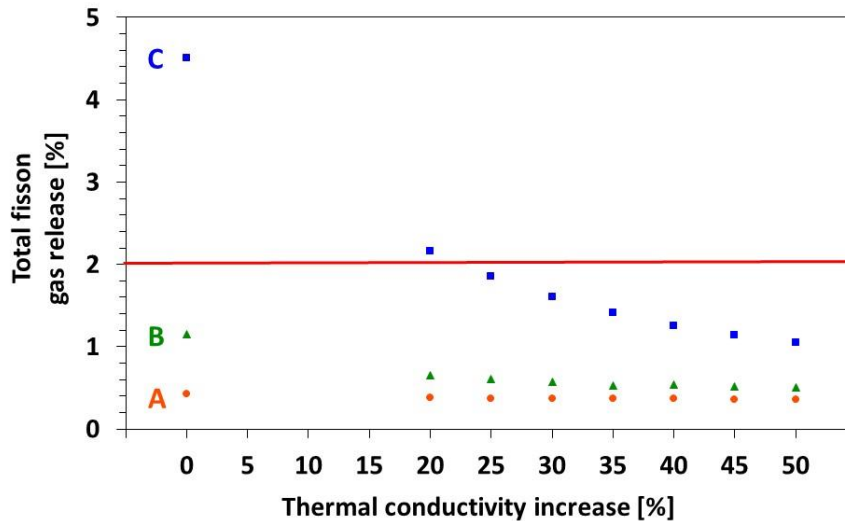


**Figure 3.22– Total FGR for increasing thermal conductivity of UO<sub>2</sub> at power ratings A 7 kW/m, B 8 kW/m, C 9 kW/m all at a plenum height of 0.25 m.**

### 3.5.9 Other literature studies

There have been few long term, 10-15 year, light water reactor UO<sub>2</sub> pellets studies undertaken. Mainly due to the length of testing time required. However, an evaluation was undertaken by R. Restani et al. of a PWR UO<sub>2</sub> fuel pellet that underwent a burn-up of 115 MWd/kgHM, and spent 10 years in the reactor [19]. Table 3.4 shows a comparison of the burn-ups for each of the linear power ratings at 10 and 15 years of the simulations presented in this Chapter. The results from the Restani study showed an average linear power rating of 20 kW/m and the UO<sub>2</sub> fuel pellet was intact with a FGR of 43 %. Restani study provides confidence in the simulated results obtained in this results Chapter as the linear power rating used in this research was half of what was used in the Restani study, and therefore be assumed that the FGR would be lower, this is due to the to the FGR being a temperature dependant value, so as it will run cooler, there will be a reduction in the FGR. Furthermore the 15 years burn-ups are of similar magnitude of 107 MWd/kgHM, 122 MWd/kgHM, and 137 MWd/kgHM compared to the Restani study of 115 MWd/kgHM for 10 years in the reactor.

**Table 3.4 – 10 year and 15 year burn-up for each linear power rating simulated.**

Power rating	10 year Burn-up MWd/kgHM	15 year Burn-up MWd/kgHM
7 kW/m	71	107
8 kW/m	81	122
9 kW/m	91	137

Another study by S. Holcombe et al. analysed the FGR release of fuel rods with burn-ups of 51 MWd/kgHM and 26 MWd/kgHM and high linear power rate of 70 kW/m. FGR releases for the high burn-up were 24 % and 17 % for the lower burn-up. The design of the fuel rods were UO<sub>2</sub> fuelled but appeared to be twice the diameter, 10.51 mm, of the fuel pellets simulated in this results Chapter. And again, a high linear power rate was used. In comparison, the results obtained by the simulated work done in this results Chapter would fall in line with the experimental findings of the literature.

### **3.6 Conclusions**

The initial simulations, Figures 4.2 and 4.3, show that the fuel rod design for rod power ratings of 7 kW/m, 8 kW/m and 9 kW/m on a 15 year refuelling cycle are limited by the failure mechanism of high internal pressure, which leads to break away swelling, overheating, and fuel rod rupture. This high pressure comes mainly from the build-up of FGR inside the fuel rod, this mechanism is also found in literature to be the main limiting factor for safe operation of UO<sub>2</sub> fuel in a PWR [19]

Two methods of altering the geometrical design of the fuel rod were investigated. Firstly, to use fuel pellets of an annular design, and secondly, to increase the height of the plenum. The annular pellet design provided a large reduction in the fuel rod internal pressure and FGR with an annulus diameter of 0.003 m and a greater reduction of the internal pressure below the safe limit of 13 MPa. The use of an annular pellet contributes in two ways to reducing the pressure.

Firstly, the creation of the annulus provides more free volume for the fission gas to reside in. Secondly, the fuel pellet runs cooler due to heat dissipating from the fuel into the annulus, thus reducing the FGR rate.

The second geometrical design change investigated was varying the height of the plenum length. This has the effect of increasing the height of the fuel rod at the top and providing more free volume for the released fission gases to occupy. This does not address the issue of reducing the rate at which fission gases are released, but it does reduce the internal pressure by providing a larger free volume inside the rod.

Varying the grain size of the fuel appears to give some benefit in the production of FGR but only by a small amount. Therefore, it could be done in combination with other approaches to help reduce the FGR, but it is not a significant enough change to be the main direction forward.

The second fuel material property that was investigated was the thermal conductivity. Here, ENIGMA was used to manipulate the thermal conductivity by increasing it by a given percentage for all temperatures. As the power rating increased, the effect of increasing the thermal conductivity was greatly enhanced, but was not able to reduce the internal pressure below the safe limit. However, this was achieved in combining the thermal conductivity with use of an annular pellet and also increasing the plenum. The contribution of the thermal conductivity to the reduction in internal pressure was greater with the plenum increase than with using an annular pellet, as the effect of the annular pellet had already reduced the pressure.

Assumptions discussed in this Chapter such as how the heat is considered to be transferred in the radial direction only and not in the axial will not have any impact on the results produce here as their effect would be marginal at best. The variation limits to calculate error bars for the power rating, clad wall thickness, and inlet temperature are all considered to be appropriate

and that the variations expected in reality would not be any higher. Therefore, a good confidence is associated with the variation shown in the results.

The aim of this work was to evaluate the potential use of a fuel rod not too dissimilar to conventional PWR designs and determine when operated under the conditions set out, if any problems would occur. The main problem identified was the build-up of FGR inside the pellet, which contributed to the rise in internal rod pressure and the main cause of a fuel failure mechanism. The simulations carried out took different approaches to combat this problem. The use of annular pellets looks to be a good solution, yet the foreseeable extra manufacturing costs make this option unattractive. The most interesting route appears to be to increase the thermal conductivity of the fuel pellet while providing more free volume by increasing the height of the plenum.

The work undertaken here has investigated long term fuel rod behaviour for a reactor designed for a civil marine reactor which has not been undertaken before. The combination of using geometry and material properties to reduce the FGR release and internal pressure for fuel rods on this time scale is an area of work that has been done in order to evaluate the potential for using  $\text{UO}_2$  with Zircaloy-4 cladding in a PWR for a civil marine reactor.

In summary, the design to take forward would be to keep the criteria in Table 4.1 the same, apart from increasing the plenum length from 0.14 m to 0.25 m. This would undoubtedly add extra cost to manufacture due to a longer fuel rod and hence taller reactor core. The thermal conductivity of the fuel should be targeted to be increased by at least 50 % in order to achieve the improvement of reducing the FGR and internal fuel rod pressure. The research in Chapter 4 has investigated fabricating cermets with two different metallic materials of molybdenum and tungsten in order to increase the thermal conductivity by 50 %.

## References

- [1] I. D. Palmer and G. D. Rossiter, *The ENIGMA fuel rod performance code, code manual: Version 7.8*. Nexia Solutions Ltd, 2007.
- [2] I. Palmer, G. Rossiter, and R. J. White, "Development and Validation of the Enigma Code for Mox Fuel Performance Modelling," *Int. Symp. MOX Fuel Cycle Technol. Mediu. Long-Term Deploy.*, pp. 271–281, 1999.
- [3] G. Rossiter, I. Palmer, and R. Gregg, "Development of the ENIGMA fuel performance code," *NNL Sci.*, pp. 24–27, 2013.
- [4] I. Palmer and P. Morris, "IAEA FUMEX-III co-ordinated programme : NNL final report," 2012.
- [5] H. S. Aybar and P. Ortego, "A review of nuclear fuel performance codes," *Prog. Nucl. Energy*, vol. 46, pp. 127–141, 2005.
- [6] L. E. Herranz, I. Vallejo, G. Khvostov, J. Sercombe, and G. Zhou, "Assessment of fuel rod performance codes under ramp scenarios investigated within the SCIP project," *Nucl. Eng. Des.*, vol. 241, pp. 815–825, 2011.
- [7] K. T. Clarno, B. Philip, W. K. Cochran, R. S. Sampath, S. Allu, P. Barai, S. Simunovic, M. a. Berrill, L. J. Ott, S. Pannala, G. a. Dilts, B. Mihaila, G. Yesilyurt, J. H. Lee, and J. E. Banfield, "The AMP (Advanced MultiPhysics) nuclear fuel performance code," *Nucl. Eng. Des.*, vol. 252, pp. 108–120, 2012.
- [8] N. Pilling and R. Bedworth, "The oxidation of metals at high temperatures," *J. Inst. Met.*, vol. 29, pp. 529–582, 1923.
- [9] P. Hofmann and D. Kerwin-peck, "UO<sub>2</sub>/Zircaloy-4 chemical interations from 1000 to 1700 ° C under isothermal and transient temperature conditions," *J. Nucl. Mater.*, vol. 124, pp. 80–105, 1984.
- [10] D. R. Olander, "Nuclear Fuels: Present and Future," *Eng. J.*, vol. 13, no. 1, pp. 1–28, 2009.
- [11] International Atomic Energy Agency, *Thermophysical properties of materials for nuclear engineering: A tutorial and collection of data*. IAEA, 2008.
- [12] IAEA, "Nuclear Power Reactors in the World," no. 2, pp. 14–86, 2010.
- [13] Maersk Line, "Efficient propulsion : the Triple-E ' s ' twin-skeg ,," *Maersk Line Publ.*, 2013.
- [14] Maersk Line, "Schedules for EMMA MAERSK," 2012. [Online]. Available: <https://my.maerskline.com/schedules/vesselresults?b.vesselName=EMMA+MAERSK&b.vesselFromDate=18%2F01%2F2015&b.vesselToDate=15%2F03%2F2015&b.vesselCode=766>.

- [15] H. G. Kim, I. H. Kim, B. K. Choi, J. Y. Park, and M. S. Kim, "Parameter study for manufacturing an inner and outer cladding tube used in dual-cooled annular fuel," *Nucl. Eng. Des.*, vol. 248, pp. 35–41, 2012.
- [16] C. Y. Lee, C. H. Shin, and W. K. In, "Pressure drop in dual-cooled annular and cylindrical solid fuel assemblies for pressurized water reactor," *Nucl. Eng. Des.*, vol. 250, pp. 287–293, 2012.
- [17] D. A. Macinnes, P. T. Elton, and P. E. Coleman, "A Mechanism for Fission Gas Release from High Temperature Fuel," *J. Nucl. Mater.*, vol. 135, pp. 63–67, 1985.
- [18] Y. W. Rhee, D. J. Kim, J. H. Kim, J. H. Yang, K. S. Kim, K. W. Kang, and K. W. Song, "Minimization of inner diametric tolerance of annular pellet for dual cooled fuel," in *Advanced Fuel Pellet Materials and Fuel Rod Design for Water Cooled Reactors*, 2009, pp. 191–199.
- [19] R. Restani, M. Horvath, W. Goll, J. Bertsch, D. Gavillet, a. Hermann, M. Martin, and C. T. Walker, "On the condition of UO<sub>2</sub> nuclear fuel irradiated in a PWR to a burn-up in excess of 110 MWd/kgHM," *J. Nucl. Mater.*, vol. 481, pp. 88–100, 2016.

## **Chapter 4 Fabrication of simulant cermet nuclear fuels**

## 4.1 Introduction

This Chapter describes the highlighted experimental techniques used and data gathered in the fabrication of simulant cermet fuel pellets for use in a long life civil marine reactor, further techniques are found in the Appendix 1. The Chapter is split into four sections: the first presents the highlighted experimental techniques used for fabrication and characterisation; the second presents justification for the materials used for the fabrication of simulant fuel pellets and their characterisation; the third section presents the characterisation data from the fabrication of the molybdenum yttria-stabilised zirconia cermet pellets and; the fourth section presents the characterisation data from the fabrication of tungsten yttria-stabilised zirconia cermet pellets.

The aim of this work was to evaluate different metallic cermet components for their potential use as a fuel in a civil marine reactor. Evaluation of the data was undertaken to determine what metallic fraction would deliver the optimal improvement in the thermal conductivity of a simulant fuel pellet. Analysing the literature review, Chapter 2, of potential materials to be used with regards to having high thermal conductivity and high density, a cermet was seen as a good way to develop a fuel type to provide the benefits of having these properties without moving away from  $\text{UO}_2$  as the fuel.

The experimental work focused on the optimisation of the fabrication conditions for simulant cermet fuels using spark plasma sintering (SPS), as well as determining the optimal metallic content. The characterisation techniques were used to determine that a stable cermet had been produced while also evaluating each one for their thermal conductivity.

## 4.2 Experimental techniques

### 4.2.1 Powder preparation

Raw powders of cubic yttria stabilised zirconium (YSZ) ( $Y_2O_3ZrO_2$ ), molybdenum metal (Mo), and tungsten metal (W) were acquired from Alfa Aesar. These were used to produce green powders in different compositions for use in the fabrication of simulated fuel pellets. YSZ powder was first dried for 24 hours in an 800°C furnace. Batches of 30 g powders were then made by weighing the appropriate amounts of each material using a glass shielded balance depending on the desired composition. The next stage involved the powders being ball milled to obtain a homogenous powder and then mixed with isopropanol to produce a slurry to aid the mixing process. This was done with a planetary mill for 4 mins at 200 rpm. Once milled the pot lids were opened and placed inside a drying oven set at 80°C for 20 mins, Figure 4.1.



**Figure 4.1 – Dried milled powder before being removed for sieving.**

Powders were sieved through a 250  $\mu$ m sieve and then a 125  $\mu$ m sieve inside a fume cupboard, Figure 4.2, to obtain a consistent powder size. They were then stored in vials before use.



**Figure 4.2 – Sieve apparatus for uniform powder size.**

#### 4.2.2 Spark Plasma Sintering (SPS)

SPS is a sintering technique in which a pulsed direct current, low voltage and pressure are utilised [1]. This technique is also termed field assisted sintering technique (FAST), pulsed electric current sintering (PECS) and current-activated pressure-assisted densification [2]. A review of literature indicates that SPS is the most common term used [3].

One of the main advantages of SPS is the shorter sintering time required for powders to obtain the required density compared to other methods, such as hot pressing [2], which provides the heating source from an element that surrounds the die of the material being sintered [4]. The main process involved for SPS is applying a current to a material while at the same time having uniaxial pressure applied. The application of the current provides the heat to the material and allows for fast heating rates [2]. Although it has been termed spark plasma sintering, no evidence exists of a spark or plasma [5], [6].

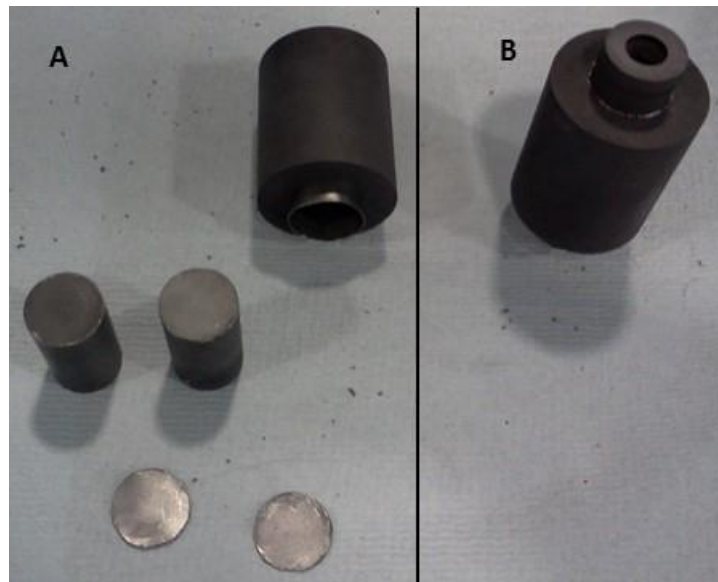


**Figure 4.3 – A – Graphite die with graphite paper lining inside, graphite plungers and graphite disks. B – Graphite die assembled with plungers and green powder inside.**

SPS was used as the main fabrication process for manufacturing simulant cermet fuel pellets for this research. The material powder to be sintered by SPS was loaded into a graphite die

lined with graphite paper and had two graphite plungers top and bottom in between, on which the green powder sat. Graphite paper disks were set onto the plungers as well, Figure 4.3. The purpose of the graphite paper was to prevent powder contaminating the dies and plungers. After fabrication, the graphite paper was discarded, while the graphite die set was reused.

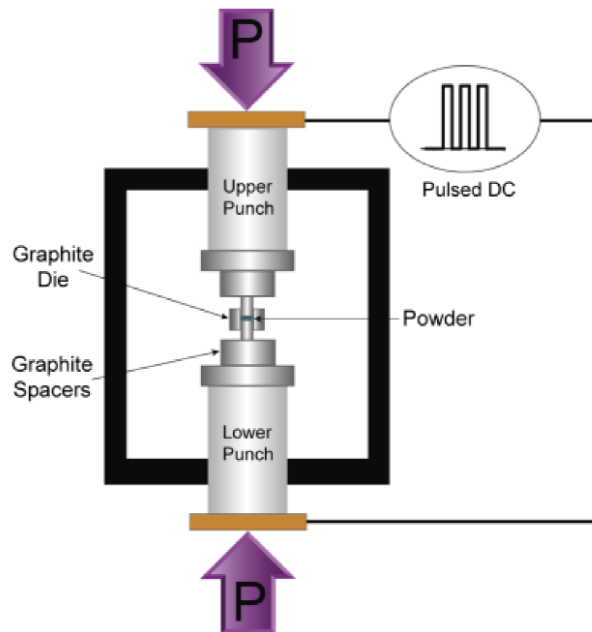


**Figure 4.4 – Schematic of an SPS main equipment [2].**

Once assembled, the die arrangement was mounted in a Specac manual hydraulic press under one tonne of pressure for 10 seconds. This was to achieve maximum density at room temperature for the powder, and thus minimise an automatic shutoff event with the SPS. If pre-pressing is not carried out, then the pressure applied to the plungers might cause them to displace rapidly. To the SPS equipment, this might mean a failure event of a broken plunger and shutoff. The die arrangement was then mounted inside the SPS on the lower punch, with the upper punch lowered on top, and put under an initial load, Figure 4.4, with the pressure and current applied during operation through the punches.

The chamber was evacuated and backfilled with argon gas. Four soak temperatures were used of 1300°C, 1400°C, 1500°C, and 1600°C. Other soak temperatures were also investigated at 800°C, 900°C, 1000°C, 1100°C, and 1200°C but did not either form a complete solid or provide

a high enough density. The ramp rate was investigated and found to have no effect on the final product; this was set at 300°C/min. A soak time of 5 min was used with a pulse ratio of 12/2; this was 12 pulses with the current on, 2 pulses with the current off, with a pulse lasting 3.3 ms. A voltage of 5 V, a current of 1.5 A and a maximum force of 16 kN were used. A picture of the equipment in use is shown, Figure 4.5.



**Figure 4.5 – SPS equipment during a run, with the main chamber right, control panel left.**

After each run the equipment power was turned off and the die left to cool naturally. Once the die arrangement was removed, the pellets were taken out and graphite paper removed, Figure 4.6.

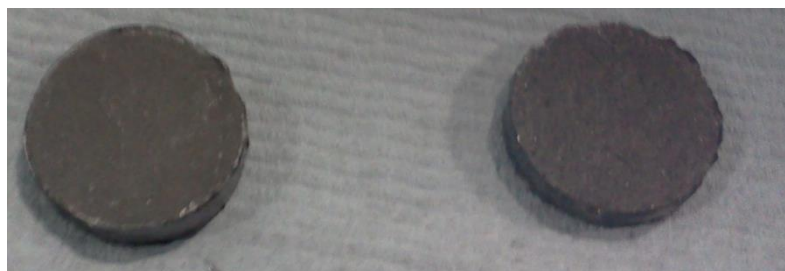


**Figure 4.6 – Two pellets sintered by SPS after graphite paper removed.**

#### **4.2.4 Sample preparation**

Pellets fabricated via SPS required finishing before they could be used in characterisation methods. The use of graphite foil between the dies and the powder/pellet creates a rough surface due to some of the graphite foil remaining. Therefore, a manual grinding wheel was used with a high grit count of 100 to remove the foil, with water being used as a lubricant between the paper and pellet. Subsequent grit papers of 200 and 400 were used to get a smoother finish.

The core drilling process on the bottom side of the pellet created chips. This end of the pellet was sectioned using a slow saw to create a smooth finish with the end portion saved for SEM preparation. Once an adequate finish was produced the pellet was core drilled to obtain a 12.2 mm diameter pellet for use with a laser flash.

From the tails remaining after the core drilling process, a large piece was selected for hardness testing. The rest were gathered up and a percussion motor was used to turn them into a powder, which was then sieved to less than 250  $\mu\text{m}$  for use in XRD.

#### **4.2.5 Laser flash**

Laser flash technique is one of the most common methods used for measuring the thermal conductivity of different types of materials [7] and has been used for the analysis in this research to determine the thermal conductivity at 100°C intervals from 100°C to 1000°C for all fabricated pellets.

Samples were coated with a thin graphite film, with nitrogen gas flow inside the chamber to prevent any oxidation. Samples were heated from room temperature to 1000°C at a ramp rate of 5°C/min to 400°C and then at 10°C/min to 1000°C with testing at 100°C and then at 100°C intervals. Further details on this technique are described in the Appendix 1.

#### **4.2.6 Vickers hardness**

The Vickers hardness was analysed for each fabricated pellet to determine if there was any variation between the holding temperatures on the fabrication process. The hardness of a material is a characterisation of a material ability to resist indentation, from this a yield stress can be inferred [8]. Further details of this technique are contained in the Appendix 1.

#### **4.2.7 XAS spectroscopy**

X-ray absorption spectroscopy (XAS) characterisation was conducted utilising the technique of X-ray absorption near edge spectroscopy (XANES) to test molybdenum samples at known oxidation states and Mo fabricated pellets to determine their absorption edge pattern. Samples at different oxidation states produce different absorption edge patterns and so the known samples are compared against the fabricated samples in order to determine the oxidation state of the Mo in the sample. Further discussion on this technique is contained in the Appendix 1.

### **4.3 Yttrium stabilised zirconia as a UO<sub>2</sub> fuel simulant**

This work set out to fabricate a matrix of cermet pellets to conduct a systematic study of different sintering temperatures and metallic loading content to determine optimum fabrication conditions. A non-radioactive simulant material for UO<sub>2</sub> was required, with similar crystal structure and comparable thermal conductivity behaviour. Two candidate materials were considered, cerium oxide (CeO<sub>2</sub>) and yttria-stabilised zirconia (YSZ, (Y<sub>2</sub>O<sub>3</sub>ZrO<sub>2</sub>)). Both materials have been used as an non-radioactive analogue/simulant materials for UO<sub>2</sub> [9], [10], [11], [12]. They have the same fluorite structure as UO<sub>2</sub> with space group Fm $\bar{3}$ m, however YSZ chemical composition is slightly more oxygen rich than UO<sub>2</sub>. Initial fabrication tests using cold pressing in air and inert condition furnace work was undertaken for both materials. This identified reduction of CeO<sub>2</sub> to Ce<sub>2</sub>O<sub>3</sub> which is not a stable oxidation state, and caused swelling oxidation of the metallic fraction component, thus ruling out CeO<sub>2</sub> as an effective UO<sub>2</sub>

simulant. This issue was not apparent for YSZ, so this material was selected as the UO<sub>2</sub> simulant.

The thermal conductivity of YSZ and UO<sub>2</sub> at room temperature are reported in the order of 2.5-3.2 W/m/K [13] dependent on yttria content and 7.5-8.5 W/m/K [14], [15], [16], respectively. The thermal conductivity decreases as temperature increases up to 500°C for YSZ and to 1500°C for UO<sub>2</sub> after which an increase in thermal conductivity occurs for both [13], [14]. Therefore, the two materials are not exact match for each other, but they do both exhibit broadly similar behaviour and thermal conductivity is of the same order of magnitude.

#### **4.4 Cermets choice and SPS past work**

With different fuel types that had been identified previously in Chapter 2, it was decided that the best route forward for a fuel type to be used in a civil marine reactor would be a cermet. The key reasons are discussed as follows. It has been understood that there is a vast amount of knowledge and operational experience with UO<sub>2</sub> fuel; therefore keeping UO<sub>2</sub> would shorten the lead time of any civil marine reactor being licensed. The requirement for fuel to operate for a long period of time in the conditions envisaged, having improved thermal conductivity to enable the fuel rods to run cooler, makes using a cermet a relatively simple solution compared with investigating other uranium compounds, and it believed that it can deliver a 50 % or greater increase in thermal conductivity set out by the modelling work in Chapter 3

Increasing the metallic loading content of a cermet will reduce the ceramic component and hence the fuel content. Therefore, metallic materials were considered not just for a high thermal conductivity but also for high density.

Molybdenum and W were identified as being of particular interest as they both have good thermal properties and high density. Also, they have both been used previously as cermets with UO<sub>2</sub> in different scenarios. Tungsten with 50 % UO<sub>2</sub> loading was fabricated successfully as a

cermet via SPS [17]. This study by O'Brien and Jerred was the first reported investigation of using SPS to form a cermet using W and U, this was confirmed using SEM and EDS mapping to show the different elemental regions. They produced several samples of 12.5mm diameter using SPS soak times of 10 minutes and a hold temperature of 1500°C with a ramp rate of 100°C/min. Tungsten / UO<sub>2</sub> cermets have also been fabricated to produce a continuous metal network throughout the cermet pellet in order to improve the thermal conductivity [18]. Investigations have also considered using SPS to produce near full densification of pure Mo samples [19]. Uranium molybdenum cermet fuel has also been used widely in the application for research reactors with high loading of the Mo content [20]. Fully dense YSZ has been fabricated using SPS in different studies [21], [22], [23]. There has also been a successful study of CeO<sub>2</sub>/W simulant cermets with 40 % W and 60 % CeO<sub>2</sub> by volume achieving above 90 % of theoretical density [24].

SPS is a desirable technique to use for material consolidation due mainly to the short sintering time achievable. This is due to quick ramp rates of 10 minutes or less, hold times at temperature of 5 minutes and natural cool down. In comparison a muffle furnace is a time intensive process due to slow heating ramp rates of 5°C/min, long hold times of 2-6 hours, and then, cool down ramp rates the same as heating. SPS also uses axial pressing during sintering, which is one of the main drivers in the shortening of the sintering time in order to reach high densification of a pellet.

There is experience in using W, Mo and YSZ in different fabrication techniques to produce fuel cermets. There appears to have been no attempt to produce UO<sub>2</sub> Mo or YSZ Mo pellets via SPS and, as discussed above, limited work on UO<sub>2</sub> W pellets, but nothing in regards to YSZ W pellets via SPS. Therefore, the work that has been undertaken in this Chapter is the first study looking into YSZ Mo and W simulant fuel pellets to be fabricated using the method of SPS.

## 4.5 Furnace work

Initial work, before using SPS, made use of fabricating pellets using a muffle furnace and tube furnace. YSZ pellets were able to be sintered with 85 % theoretical densification by using an open air muffle furnace with a hold temperature of 1700°C for 4 hours with a ramp rate of 5°C/min. Under the same conditions, cermets of YSZ with 10 % Mo are believed to have oxidised as shown in Figure 4.7.



**Figure 4.7 – YSZ 10 % Mo fabricated pellet sintered in an open air muffle furnace.**

After several attempts at reducing the temperature to confirm that the Mo could not remain in metallic form using an open air muffle furnace, the work switched to using a tube furnace with an argon atmosphere. This was conducted at a hold temperature of 1300°C for 4 hours with a ramp rate of 5°C/min. The limit in the maximum temperature was imposed by the equipment. Densification was able to be achieved of 85-90 % of theoretical density. However the metallic Mo pellets still believed to have reacted in the furnace through oxidation by trace oxygen with the argon gas, Figure 4.8.

Table 4.1 lists the results of testing using CeO<sub>2</sub> 10 % Mo and YSZ 10 % Mo using either open air muffle furnace or tube furnace with different gases used in order to achieve a stable high density pellet.



**Figure 4.8 – YSZ with 10% Mo pellets sintered in a tube furnace with argon atmosphere held at 1300°C for 4 hours.**

**Table 4.1 – Summary table of different methods tried to sinter CeO<sub>2</sub> 10 % Mo and YSZ 10 % Mo.**

	Hold temperature [°C]	Hold time [Hours]	Gas used	T.D. %
CeO <sub>2</sub> 10 % Mo	1400	4	None	67.6
CeO <sub>2</sub> 10 % Mo	1500	4	None	64.7
CeO <sub>2</sub> 10 % Mo	1600	6	None	60.5
CeO <sub>2</sub> 10 % Mo	1700	6	None	67.0
CeO <sub>2</sub> 10 % Mo	1300	6	Argon	80.0
CeO <sub>2</sub> 10 % Mo	1300	10	Argon	80.0
CeO <sub>2</sub> 10 % Mo	1300	20	Argon	77.8
YSZ 10 % Mo	1300	4	Argon	81.7
YSZ 10 % Mo	1300	4	Hydrogen	86.4

As the results that were obtained showed that this work was not able to achieve stable cermets, with high density and so it gave emphasis to conducting further work via the route of SPS. Furthermore with only achieving 85-90 % theoretical density another method was needed to achieve high density pellet of at least 95 % as this is the standard for new fuel pellets.

Discussed in this Chapter are the results from SPS testing that was done under conditions identified to form stable solid pellets after trial testing of YSZ and YSZ 10 % Mo pellet shown in Table 4.2. Testing for density was not carried out on them as they did not stay solid.

**Table 4.2 – Summary of YSZ and YSZ 10 % Mo testing conditions via SPS that did not form a stable solid pellet.**

	<b>Hold temperature [°C]</b>	<b>Hold time [Hours]</b>
<b>YSZ</b>	800	3
<b>YSZ</b>	1000	3
<b>YSZ</b>	1100	5
<b>YSZ</b>	1200	5
<b>YSZ 10 % Mo</b>	900	2
<b>YSZ 10 % Mo</b>	900	5
<b>YSZ 10 % Mo</b>	1000	2
<b>YSZ 10 % Mo</b>	1000	20
<b>YSZ 10 % Mo</b>	1100	10
<b>YSZ 10 % Mo</b>	1200	10

## 4.6 Materials used

This section details the characterisation of the green powders of YSZ, metallic Mo and metallic W used for the fabrication of simulant cermets.

### 4.6.1 Powder characterisation

#### 4.6.1.1 Density of powder

**Table 4.3 – Powder density of material measured by a gas pycnometer.**

<b>Powder</b>	<b>Density [g/cm<sup>3</sup>]</b>	<b>Standard deviation [g/cm<sup>3</sup>]</b>	<b>Density from literature [g/cm<sup>3</sup>]</b>
YSZ	5.867	0.020	5.85-6.1 [25]
Molybdenum	10.517	0.207	10.18-10.22 [26], [27], [28]
Tungsten	19.424	0.106	19.3 [26], [27], [29]

The densities of all three green powders were measured by a gas pycnometer, Table 4.3. The YSZ result has a low standard deviation and falls in line with other literature sources obtained and therefore a good degree of confidence is held in this value. The Mo and W are both in line with other literature based values. Though both slightly on the high side, they have a higher

standard deviation than obtained from the YSZ material. However, the values are determined to be in agreement with literature values and so will be accepted.

#### 4.6.1.2 Particle size analysis PSA of powder

**Table 4.4 – Particle size analysis of green powders.**

Powder	Average particle size [ $\mu\text{m}$ ]	Standard deviation [ $\mu\text{m}$ ]
YSZ	16.3	0.210
Molybdenum	14.1	0.228
Tungsten	13.1	0.129

Table 4.4 shows the average particle size of each of the three green powders for simulant fuel pellet fabrication. The data shows that the bulk content of the powders are all in the same size range. This was intentional so that when mixed a homogenous distribution of particles could be achieved.

#### 4.6.1.3 XRD of powder

The XRD patterns for each green powder are presented:

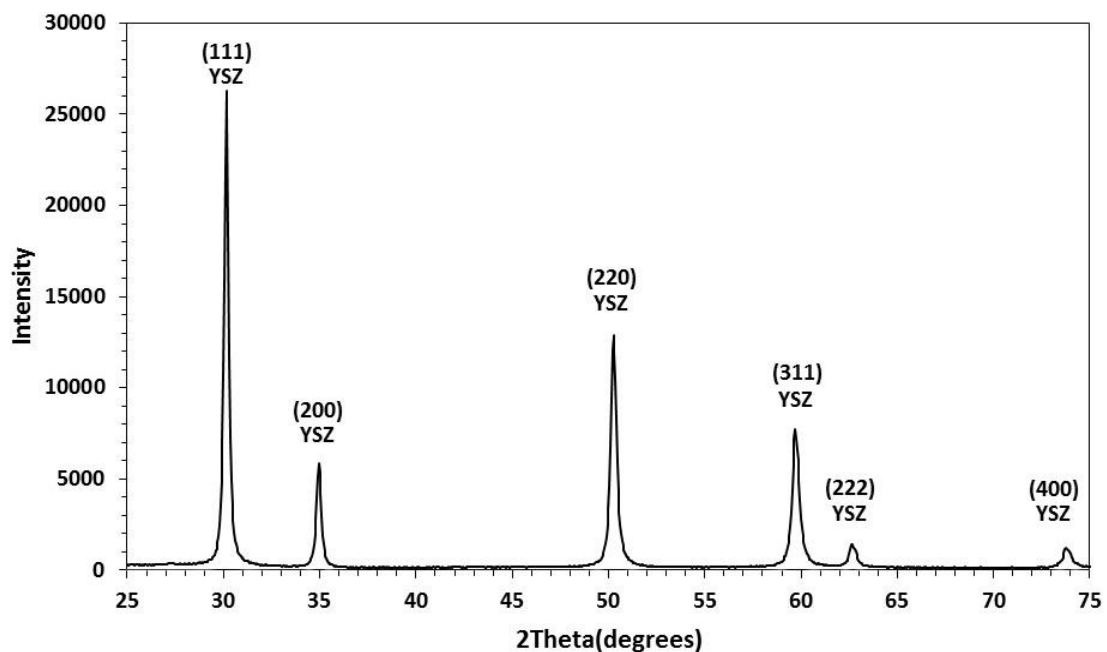


**Figure 4.9 –XRD pattern of green YSZ powder used for pellet fabrication.**

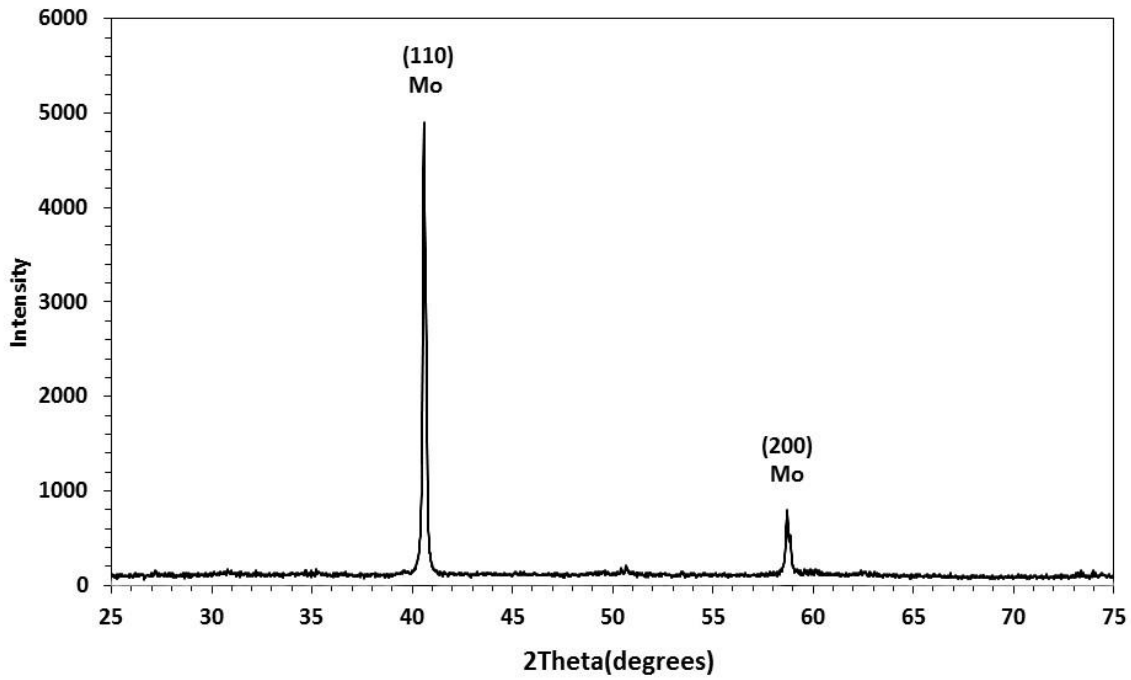


**Figure 4.10 –XRD pattern of green metallic Mo powder used for pellet fabrication.**

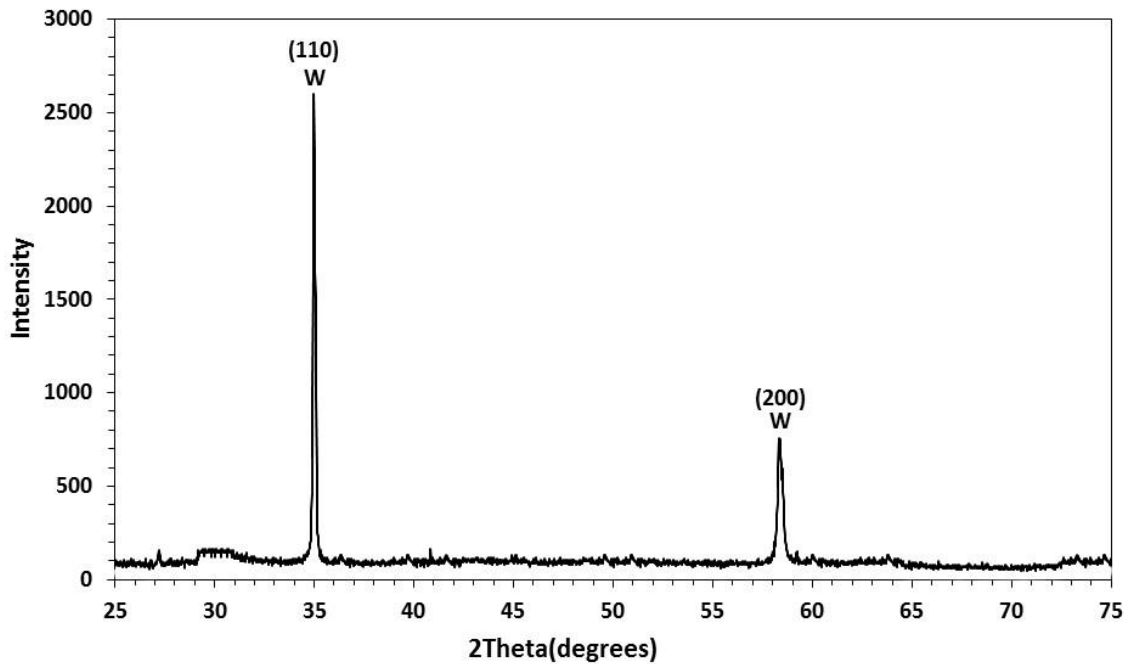


**Figure 4.11 –XRD pattern of green metallic W powder used for pellet fabrication.**

Each green powder was characterised by XRD to confirm that YSZ was in its stable cubic form and that both metals were not oxidised. This was essential to ensure that any new reflections arising on the XRD patterns of the cermet, from reaction between YSZ/metal, were not

impurities present in the reagents. The XRD pattern for YSZ is shown in Figure 4.9. The peaks in the pattern were compared with those in the PDF4 material database and are a match for YSZ (PDF 04-010-3271).

Figure 4.10 and 4.11 show the XRD patterns of the metallic Mo and W, respectively. Two single peaks are observed on both these patterns and are matches in the database Mo (PDF 04-014-7435) and W (PDF 04-004-7097) confirming that they are metallic and that they are not in an oxide form. Additional peaks would be observed if a metal oxide contaminate was present.

#### **4.7 Matrix of pellets**

As discussed, the aim of this work was to assess the use of SPS for fabrication of simulant cermet fuels, to determine the optimal cermet processing conditions, as well as comparing the difference between the loading content of W and Mo with regards to overall density and thermal conductivity.

The matrix of all pellets fabricated via SPS are listed in Table 4.5. In total 28 different pellets were fabricated at 4 temperatures. These temperatures were selected from previous work found in the literature of YSZ pellets fabricated with SPS [23], [30], [31], [32] and an initial study of fabrication of pure YSZ at these temperatures and lower. It was found in this initial work that below 1300°C high densification was not able to be achieved and that the pellets were only poorly sintered. Table 4.5 also list the density values and the percentage of theoretical density (T.D.) that was achieved. All pellets achieved >90 % T.D. with the majority being >95 % which is the ideal density for fuel pellets.

**Table 4.5 – List of pellets fabricated with their volume percentage content of each material and heating conditions.**

	Temperature [°C]	YSZ [vol. %]	Mo [vol. %]	W [vol. %]	Density [g/cm <sup>3</sup> ]	T.D. [%]
YSZ	1300	100	0	0	5.963	97.8
YSZ/Mo	1300	90	10	0	6.218	97.8
	1300	80	20	0	6.495	97.8
	1300	70	30	0	6.768	97.4
YSZ/W	1300	90	0	10	6.384	97.5
	1300	80	0	20	6.391	90.4
	1300	70	0	30	7.450	97.1
YSZ	1400	100	0	0	5.962	97.6
YSZ/Mo	1400	90	10	0	6.242	98.2
	1400	80	20	0	6.507	98.0
	1400	70	30	0	6.807	98.0
YSZ/W	1400	90	0	10	6.395	97.7
	1400	80	0	20	6.898	97.5
	1400	70	0	30	7.484	97.5
YSZ	1500	100	0	0	5.961	97.9
YSZ/Mo	1500	90	10	0	6.188	97.3
	1500	80	20	0	6.462	97.3
	1500	70	30	0	6.746	97.1
YSZ/W	1500	90	0	10	6.385	97.5
	1500	80	0	20	6.848	96.8
	1500	70	0	30	7.355	95.9
YSZ	1600	100	0	0	5.944	97.8
YSZ/Mo	1600	90	10	0	6.189	97.4
	1600	80	20	0	6.488	97.7
	1600	70	30	0	6.771	97.4
YSZ/W	1600	90	0	10	6.416	98.0
	1600	80	0	20	6.775	95.8
	1600	70	0	30	7.519	98.0

#### **4.8 Yttria stabilised zirconia molybdenum cermets**

This Section details the characterisation of the fabricated YSZ Mo cermets. In total there were 14 samples fabricated at 4 different sintering temperatures and 4 different compositions at each temperature.



**Figure 4.12 – YSZ 10 % Mo sample after grinding wheel has removed graphite paper and interaction layer. A – Whole SPS pellet, B – Top part after core drilling, C – Bottom part after core drilling with chips on the side.**

After pellets had been fabricated via SPS, an interaction layer between the graphite paper and the sample material was observed. This has also been reported in other SPS investigations [17]. This layer was removed by using a grinding wheel on both sides of the pellet, Figure 4.12. In this figure can also be seen a pellet after it has been core drilled in order to have an appropriate size sample for laser flash measurements. The bottom part of the core drilled sample edges break off during this process. To accommodate for this, the bottom section was slow sawed off and this sample used for SEM. The outer ring of the SPS sample left over after the core drilling was half used for hardness testing and the other half was crushed for powder XRD.

#### **4.8.1 Density**

The density of each sample was measured geometrically and by Archimedes method. These are shown in Figure 4.13 on plots for each sintering temperature. The density of pellets increases with loading content of Mo through all sintering temperatures, and there is good agreement in most cases between the two methods of measurement, especially at the higher Mo loading. The increase in density also appears to be a linear relationship.

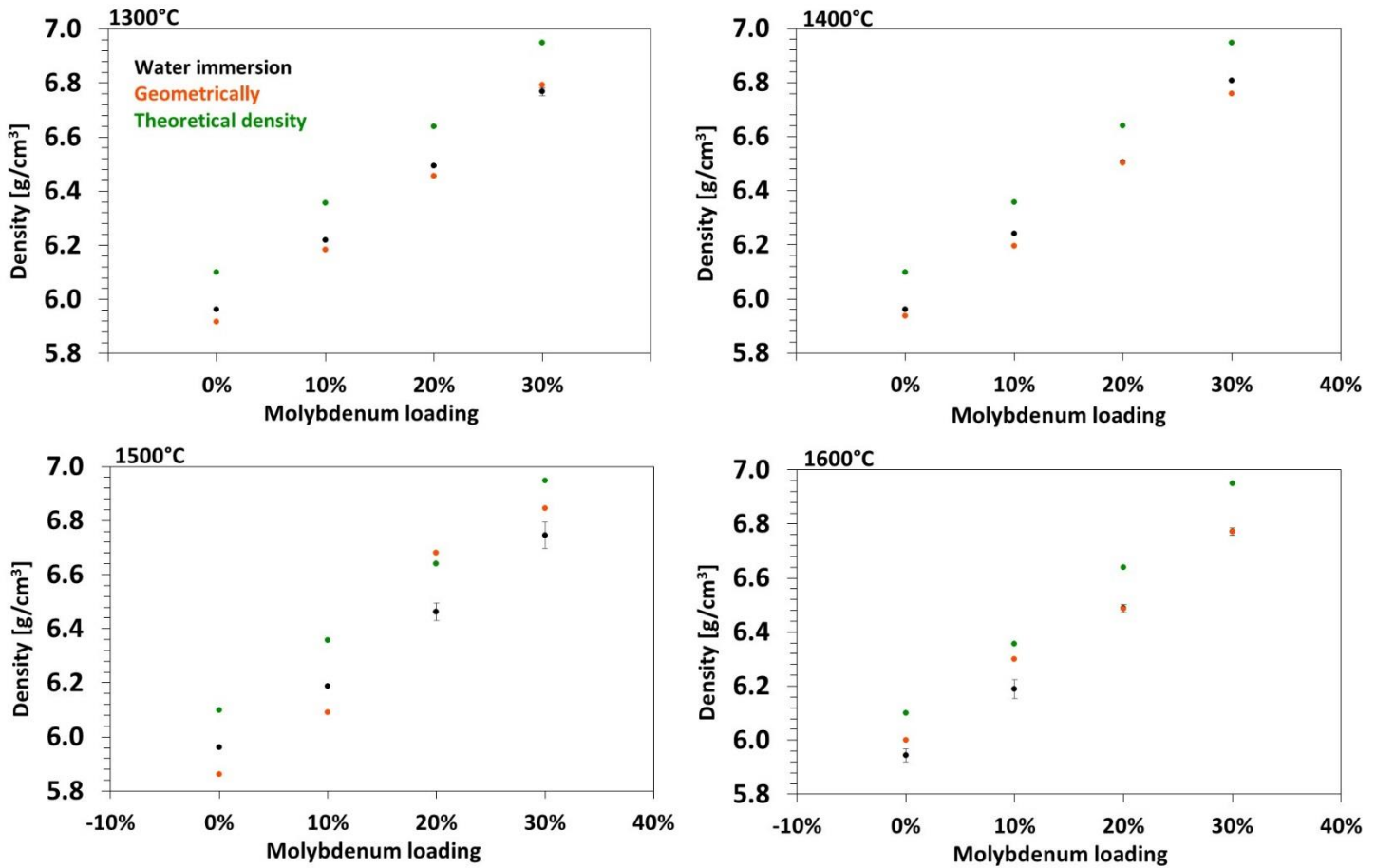


**Figure 4.13 – Density of fabricated YSZ Mo cermet at each temperature by Archimedes method, geometrically, and theoretical density error bars with standard deviation of greater than 0.01 shown.**

The density of Mo loading content was plotted at each temperature for the water immersion method, Figure 4.14. Here there appears to be no strong correlation to suggest that any one of the sintering temperatures can achieve a greater densification of the simulant cermet materials. Especially with the pure YSZ samples (e.g. 0 % Mo loading), strong correlation of results are shown.

Therefore, the data presented suggests no appreciable difference in the densification across these temperatures and that any one of them would be suitable for effective fabrication. High T.D. have been achieved across the pellets of >95 %.

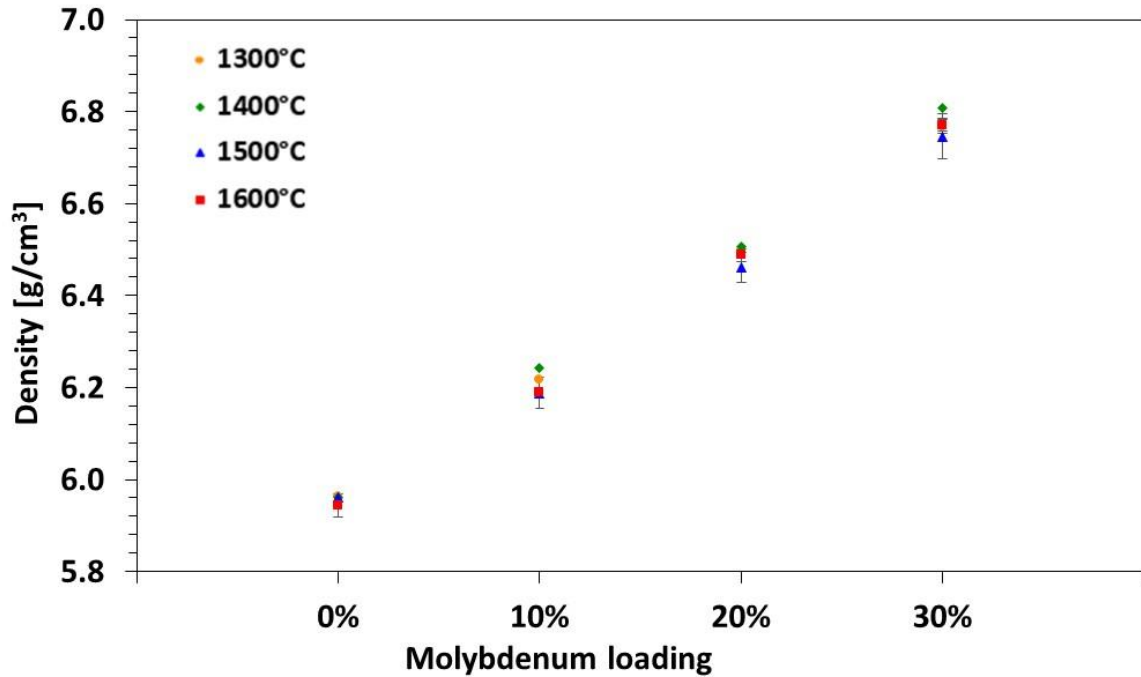


**Figure 4.14– Density of fabricated Mo pellets at each temperature by water immersion method, error bars with standard deviation of greater than 0.01 shown.**

#### 4.8.2 XRD

Powder XRD was conducted on all samples with each pattern shown in Figures 4.15-4.18. The patterns have been normalised relative to the highest intensity peak for comparison of each sample at each sintering temperature.

From the XRD data several trends are apparent across the matrix of samples. As anticipated, there is an increase in intensity of Mo peaks as the Mo loading increases. This confirms that there is higher content of Mo in the higher loaded samples.

All diffraction patterns can be interpreted as a mixture of YSZ and Mo metal. By reference to the XRD patterns of the reagent materials, no additional peaks were detected which would be an indication of reaction between YSZ and Mo. This is the first piece of evidence to confirm that the sintering process has produced a ceramic metallic i.e. a cermet.

Comparing the samples across the different temperatures there is no noticeable observed difference between each sample. This again would suggest that between the 4 sintering temperatures there is no appreciable benefit. In other words, the cermets are remarkably insensitive to processing conditions.

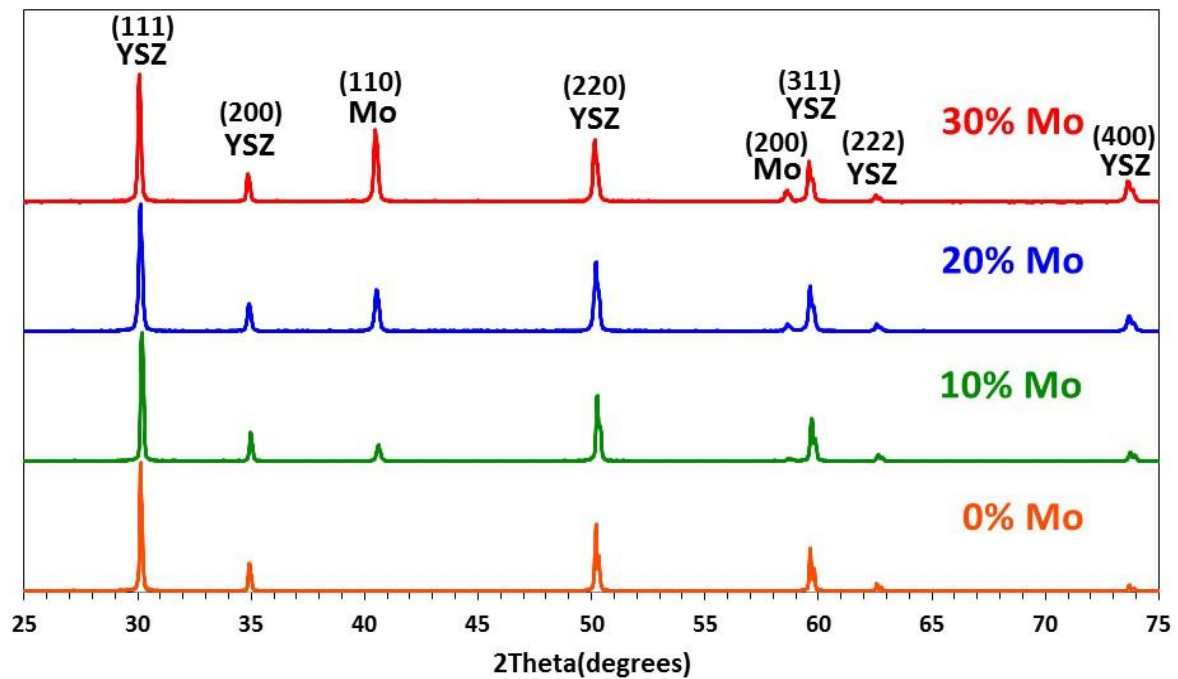


**Figure 4.15 – Normalised XRD patterns of Mo samples heated at 1300°C.**

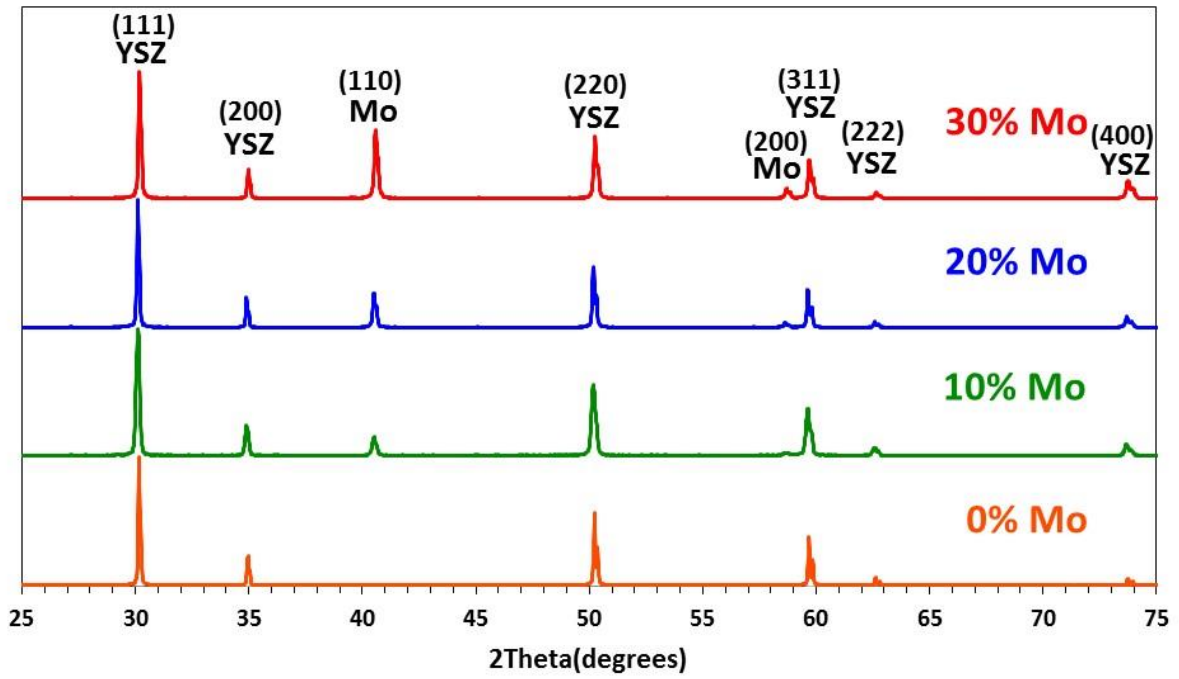


Figure 4.16 – Normalised XRD patterns of Mo samples heated at 1400°C.

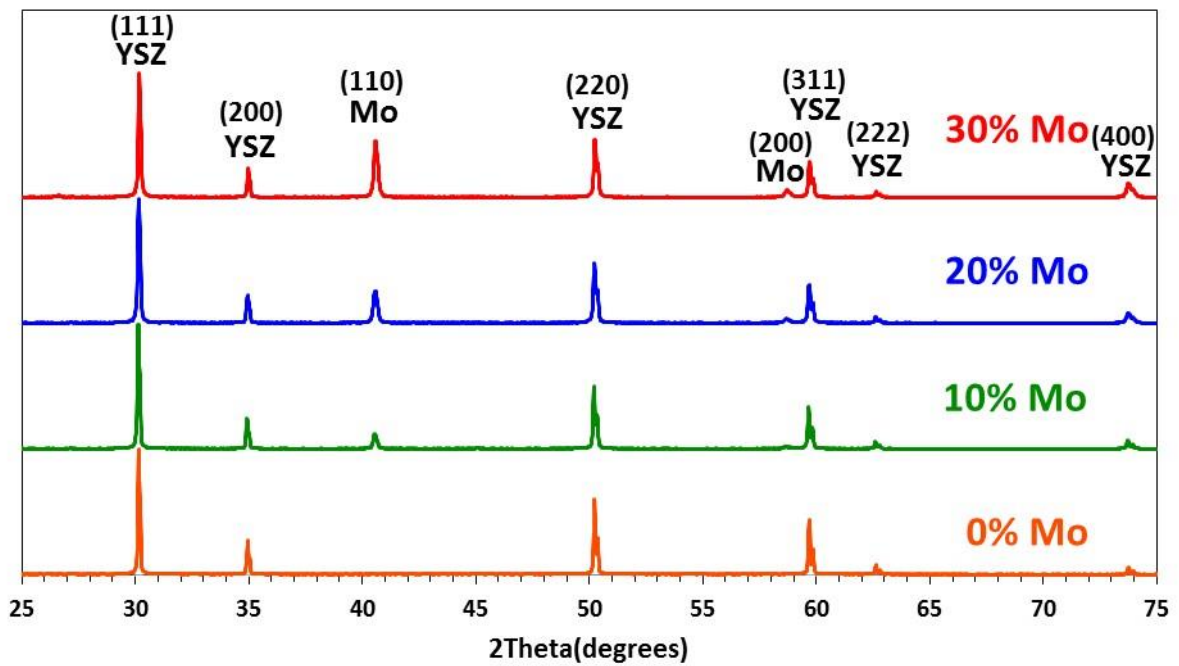
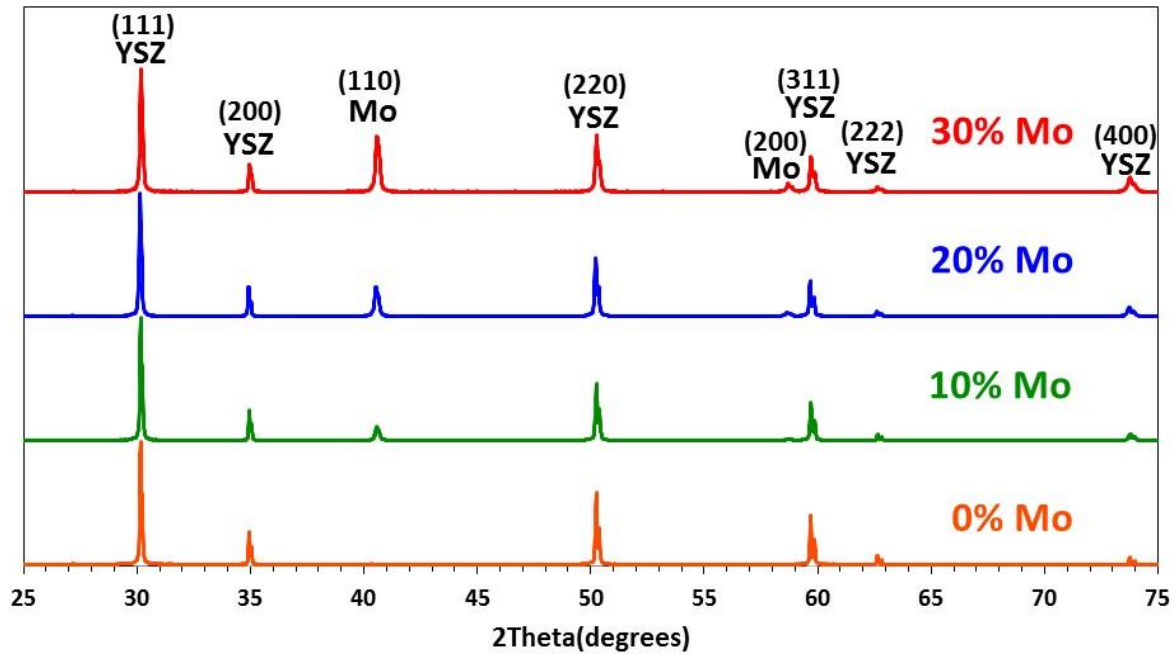


Figure 4.17 – Normalised XRD patterns of Mo samples heated at 1500°C.



**Figure 4.18 – Normalised XRD patterns of Mo samples heated at 1600°C.**

### 4.8.3 SEM analysis

Fabricated cermet pellets were prepared for inspection by scanning electron microscopy as described in Appendix 1. Figures 4.19, 4.20, 4.21, and 4.22 show all the pellets with loading content of 0 %, 10 %, 20 %, and 30 % Mo, respectively. Mo material appears as a white feature on the images due to its higher electron conductivity when compared to YSZ.

From initial viewing at 100x magnification of all the pellets, the Mo content is evenly distributed across the pellet in each loading across all 4 temperatures. There does appear to be some areas of larger Mo content in a few samples, Figure 5.15 A, and D. However, overall, the Mo content appears to be distributed evenly.

There is no evidence that any of the Mo in the samples has formed completely interconnected channels or paths through the pellets. This shows that the YSZ has encapsulated the Mo. If there were channels of Mo through the pellets this would possibly make for improved thermal conductivity.

Clear defined boundaries between the Mo and the YSZ are shown with no evidence of any interaction area between the two that the Mo has not oxidised and that a cermet has been produced. This in agreement with interpretation of X-ray diffraction data.

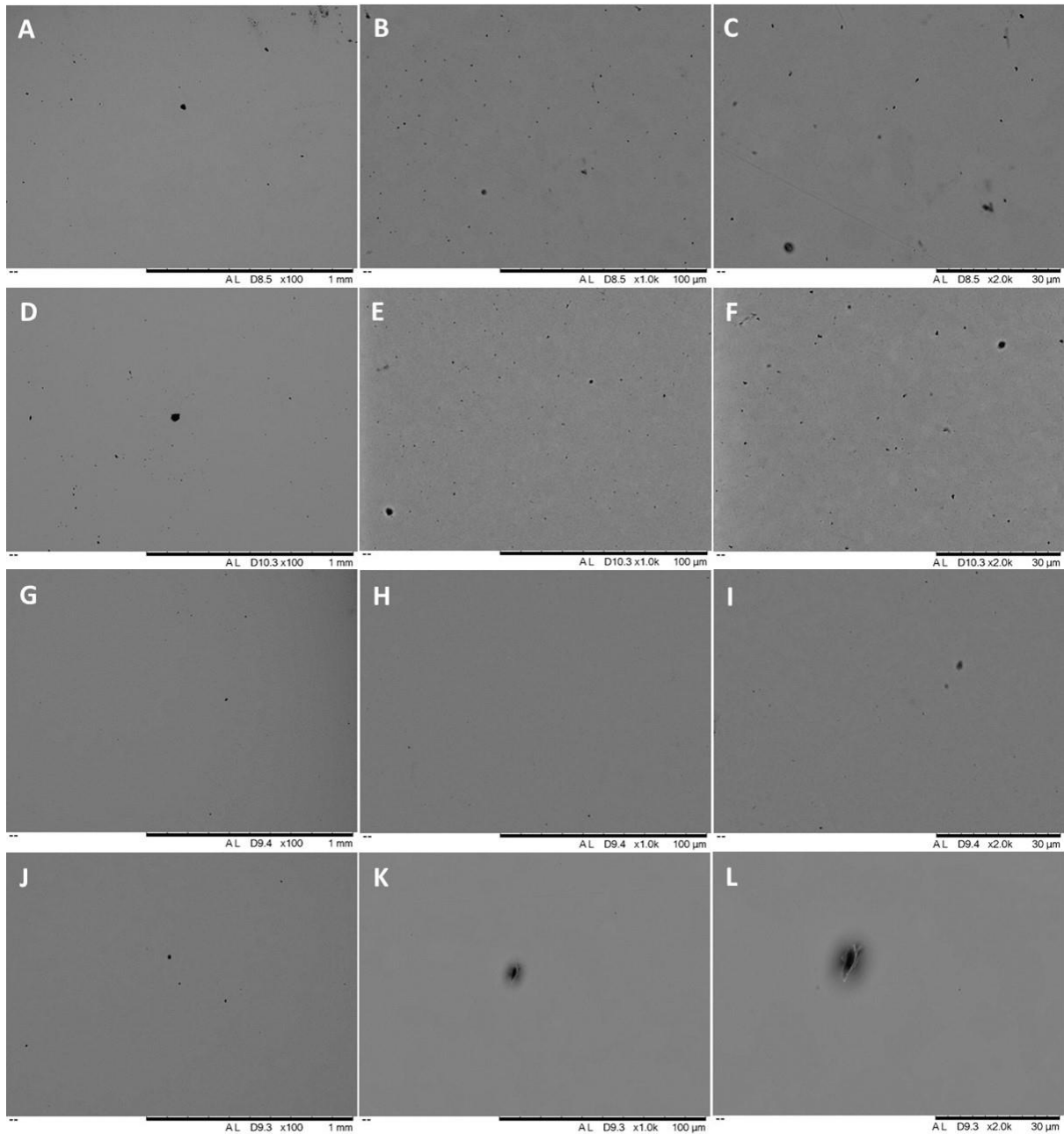


**Figure 4.19 – SEM backscattered micrographs are control samples of YSZ at magnifications 100x, 1000x, and 2000x; A, B, C heated at 1300°C; D, E, F heated at 1400°C; G, H, I heated at 1500°C; J, K, L heated at 1600°C.**

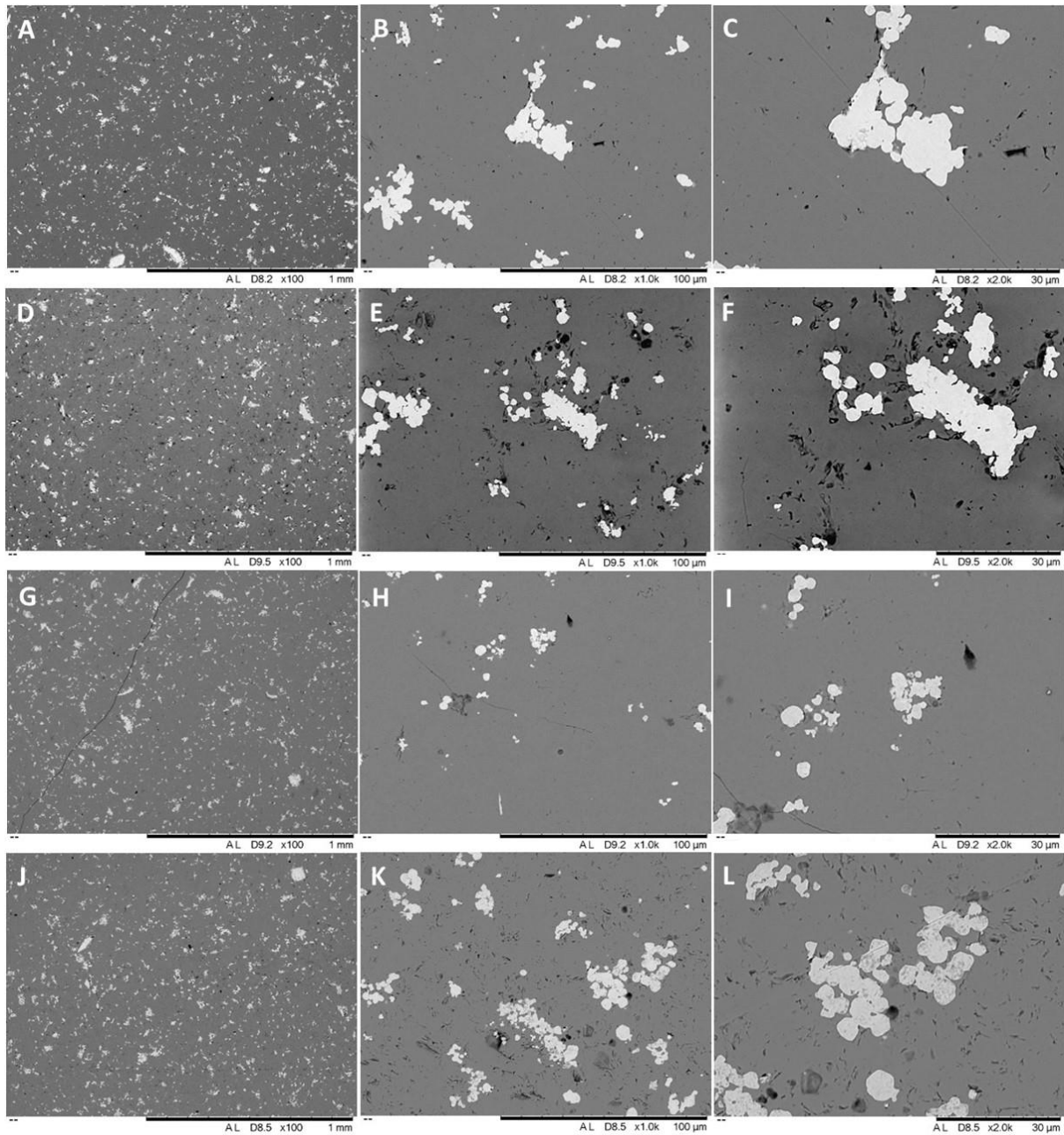


**Figure 4.20 – SEM backscattered micrographs of 10 % Mo sample at magnifications 100x, 1000x, and 2000x; A, B, C heated at 1300°C; D, E, F heated at 1400°C; G, H, I heated at 1500°C; J, K, L heated at 1600°C.**

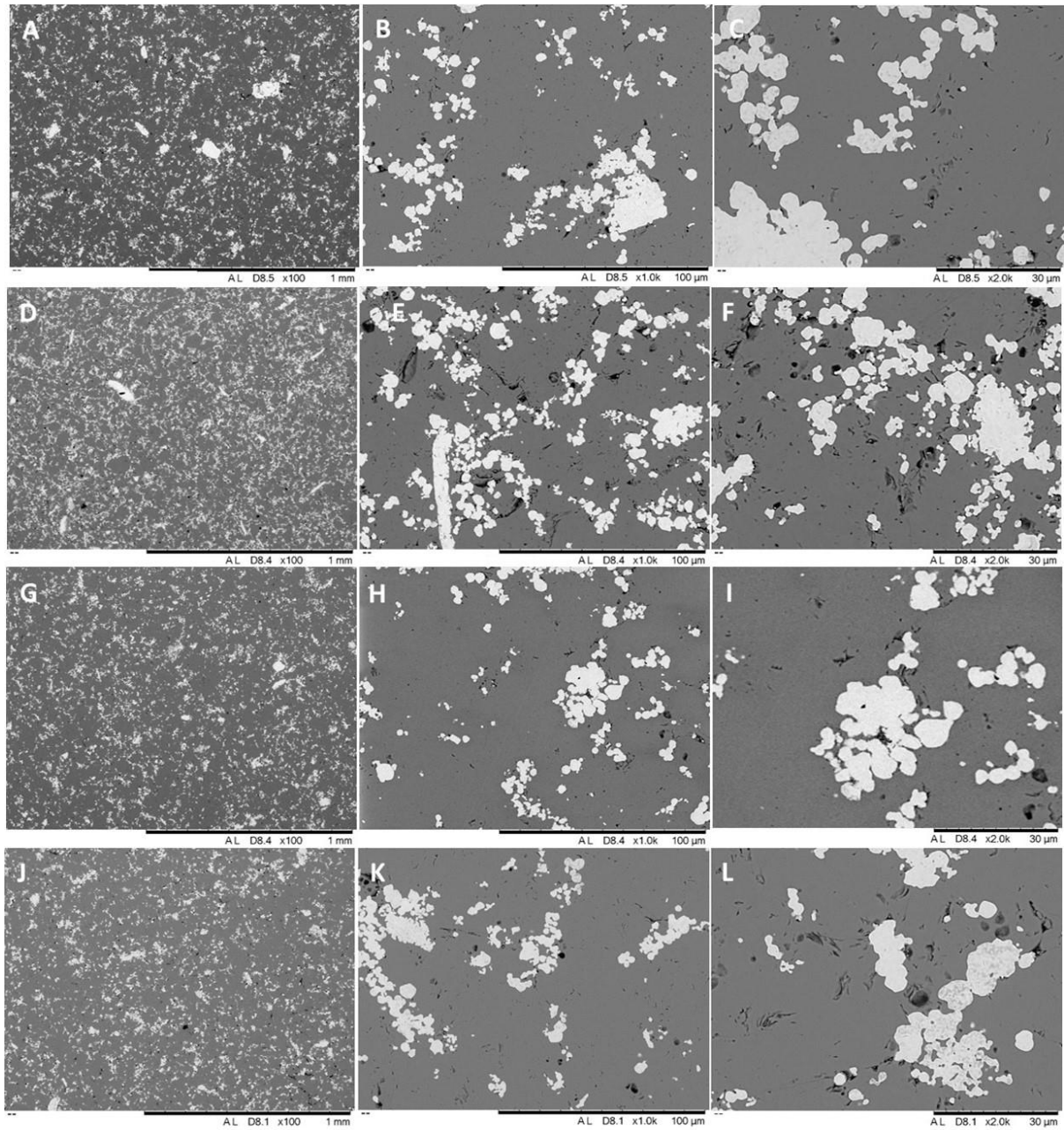


**Figure 4.21 – SEM backscattered micrographs of 20 % Mo sample at magnifications 100x, 1000x, and 2000x; A, B, C heated at 1300°C; D, E, F heated at 1400°C; G, H, I heated at 1500°C; J, K, L heated at 1600°C.**

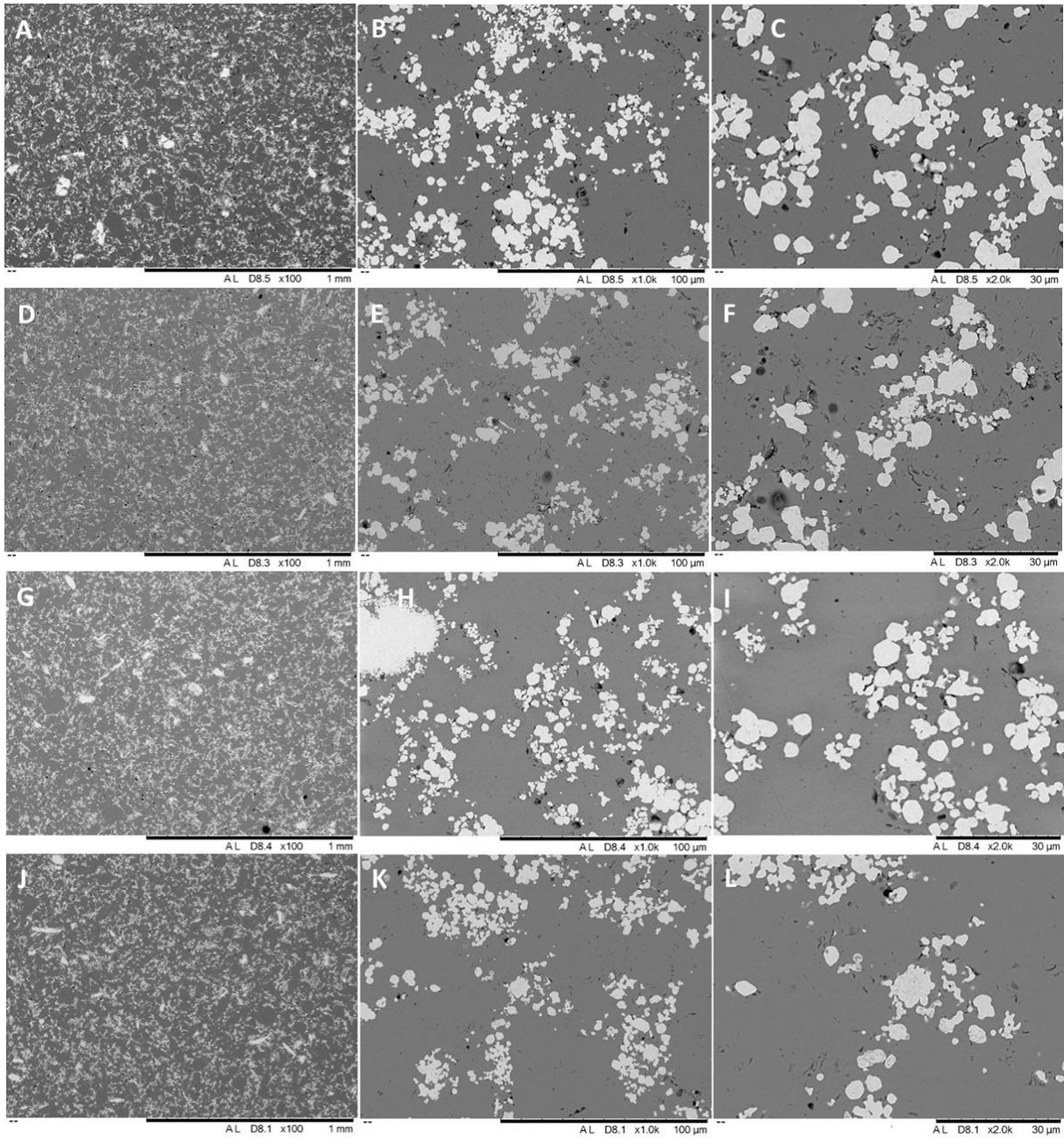


**Figure 4.22 – SEM backscattered micrographs of 30 % Mo sample at magnifications 100x, 1000x, and 2000x; A, B, C heated at 1300°C; D, E, F heated at 1400°C; G, H, I heated at 1500°C; J, K, L heated at 1600°C.**

#### **4.8.4 SEM EDX**

EDX maps were acquired from each pellet as shown in Figure 4.23-4.26, with each figure comparing the loading content of Mo. Elements present in each sample with Mo loading are Y, Zr, Mo, and O. With the 100 % YSZ samples just having Y, Zr, and O present. This confirms that no other trace element has contaminated the samples.

The 100 % YSZ samples, Figure 5.17, show that there is an even distribution of each element present other than areas where porosity occurs. For samples with Mo content, Figures 5.18-5.20, there is clear definition between area of Mo to areas of yttria, zirconium, and oxygen. This shows that the Mo has remained separate to the YSZ material and not reacted.

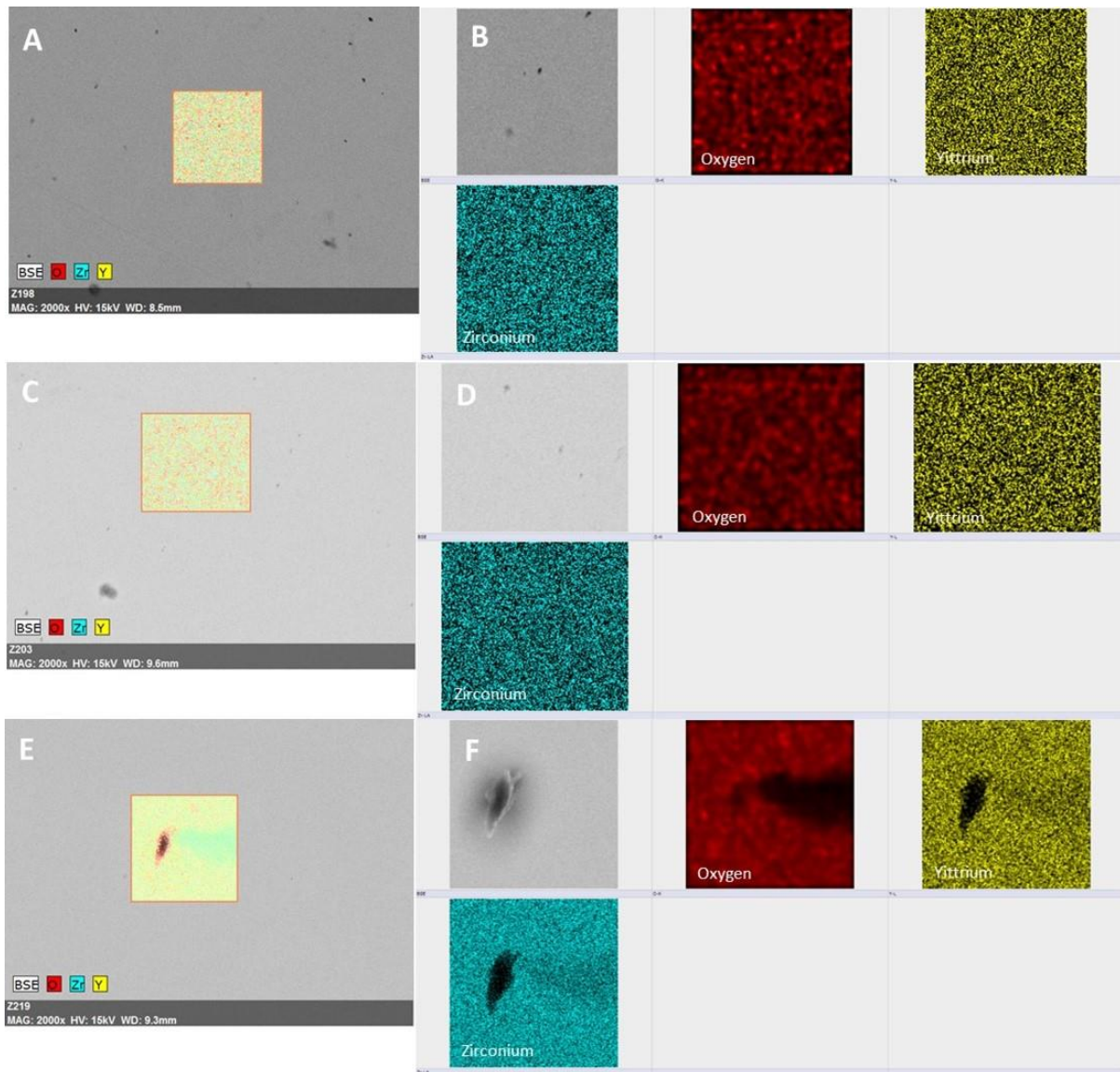


**Figure 4.23 –SEM micrograph of EDX scanned area and EDX scans of each element composition present. Samples are control samples of YSZ; A, B heated at 1300°C; C, D heated at 1400°C; E, F heated at 1600°C.**

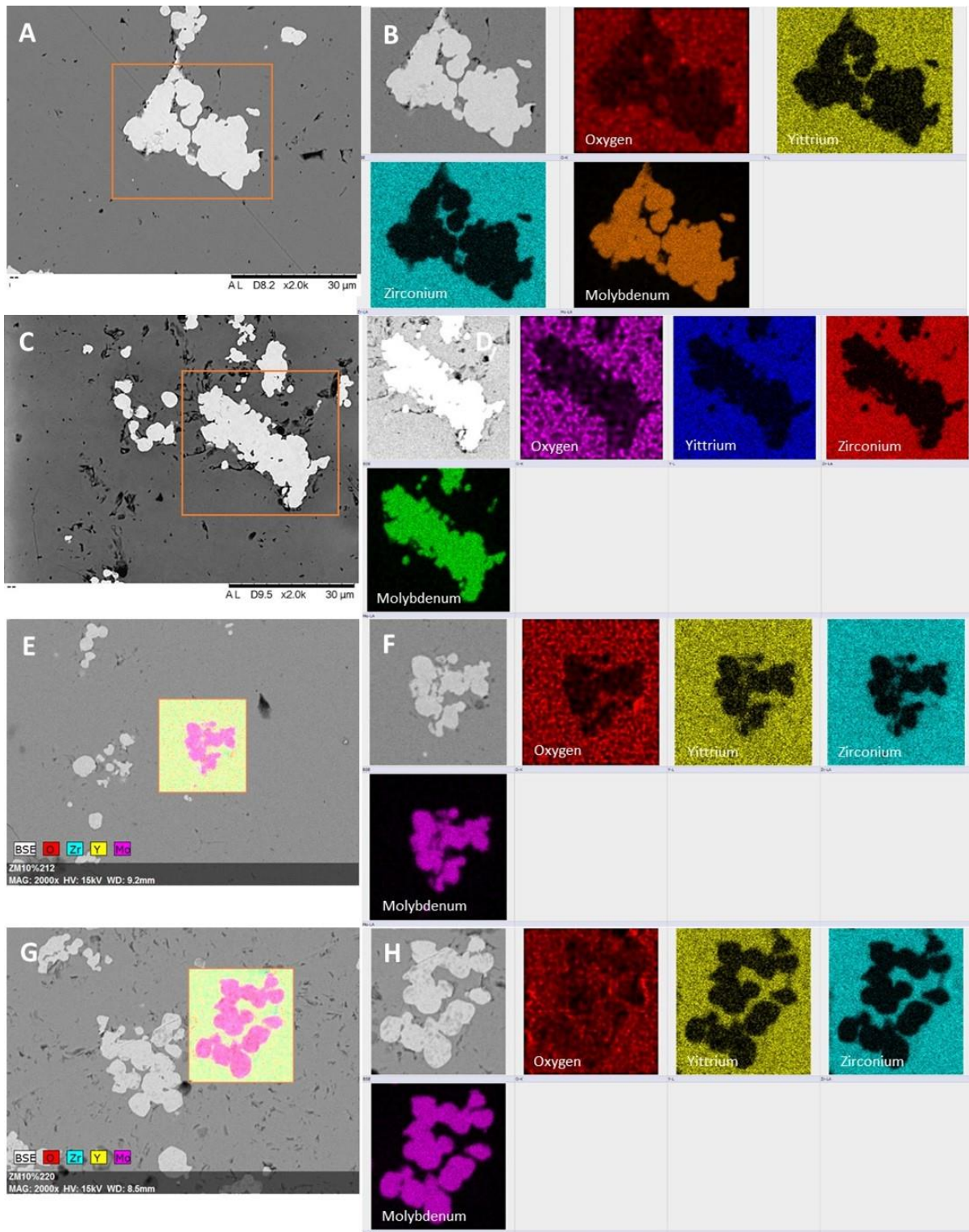


**Figure 4.24 –SEM micrograph of EDX scanned area and EDX scans of each element composition present. Samples are 10 % Mo; A, B heated at 1300°C; C, D heated at 1400°C; E, F heated at 1500°C; G, H heated at 1600°C.**

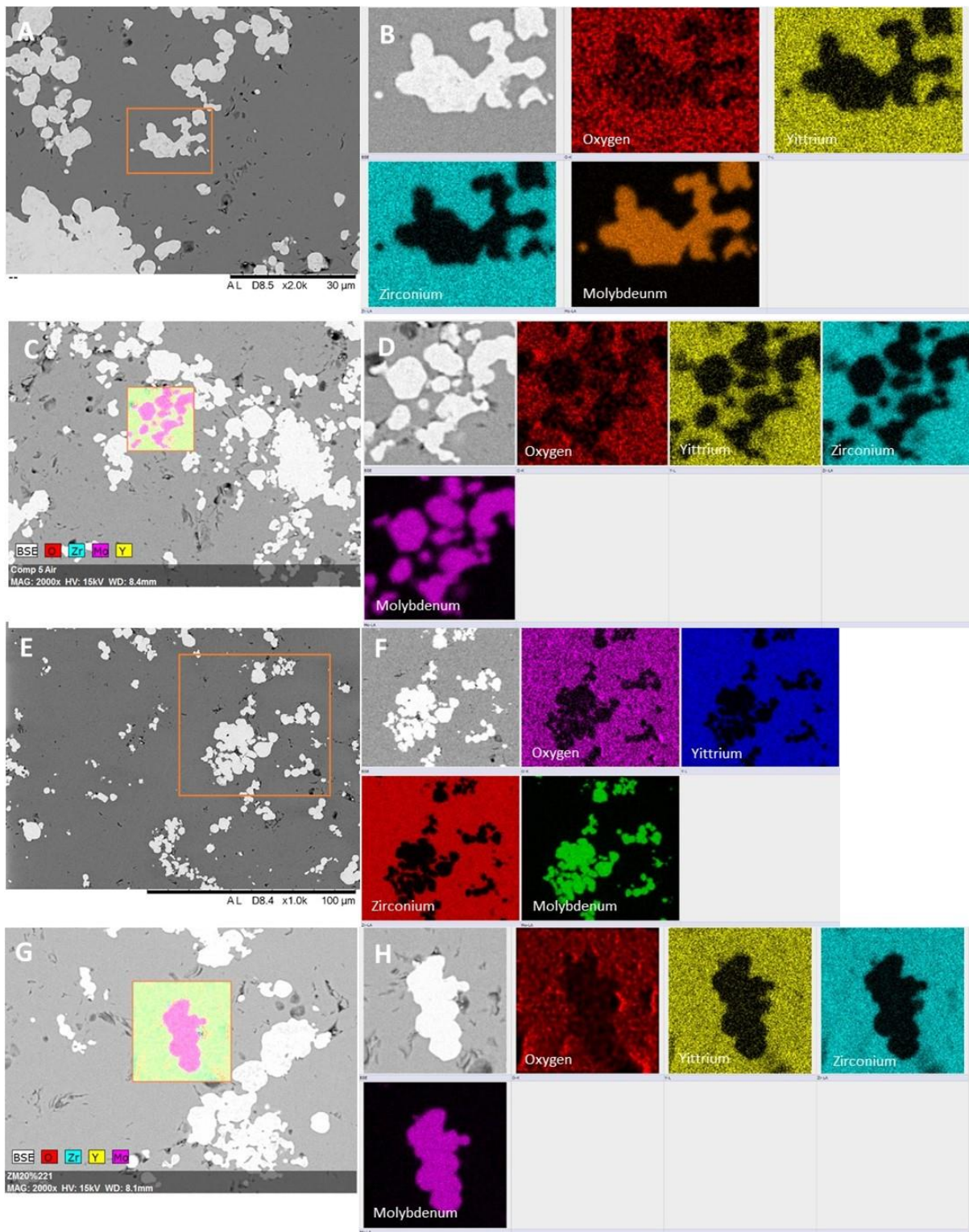


**Figure 4.25 –SEM micrograph of EDX scanned area and EDX scans of each element composition present. Samples are 20 % Mo; A, B heated at 1300°C; C, D heated at 1400°C; E, F heated at 1500°C; G, H heated at 1600°C.**

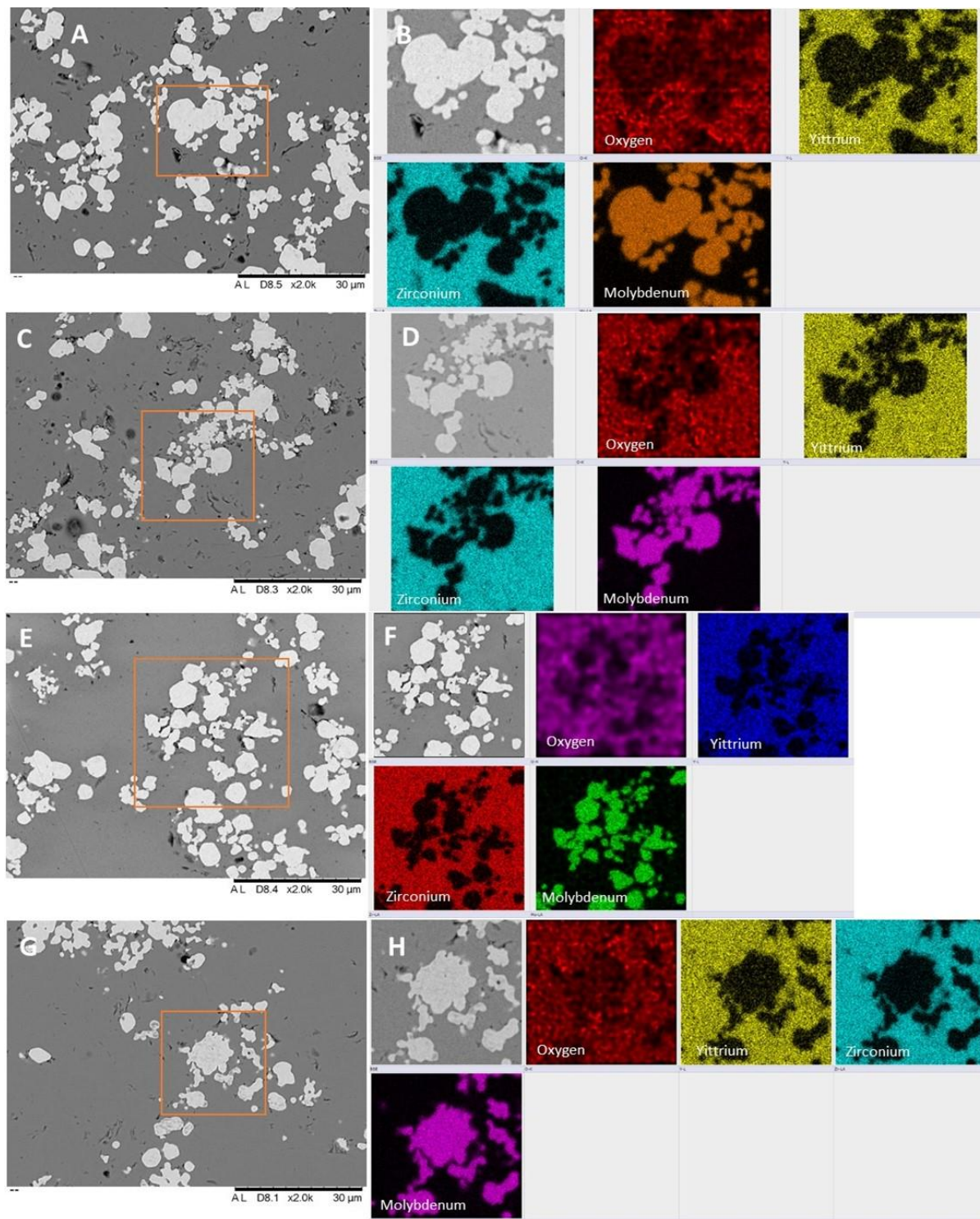


**Figure 4.26 –SEM micrograph of EDX scanned area and EDX scans of each element composition present. Samples are 30 % Mo; A, B heated at 1300°C; C, D heated at 1400°C; E, F heated at 1500°C; G, H heated at 1600°C.**

#### 4.8.5 XAS spectroscopy

Another technique used to determine that a cermet was produced and that the Mo remained unoxidised was the use of X-ray absorption spectroscopy (XAS), Mo is stable at oxidation state +4, and +6. Samples of 10 %, 20 %, and 30 % Mo loading fabricated at 1600°C were analysed. As well, samples of Mo foil and Mo in its two stable oxide forms of MoO<sub>2</sub> and MoO<sub>3</sub> were analysed for comparison.

Figure 4.27 shows the XAS data of the samples. The data from the fabricated cermet samples are identical to that of the Mo foil. This is in contrast to the two Mo oxide samples which produced different traces. This therefore shows that the Mo in the cermets have remained metallic.

For comparison, other literature studies using XAS for Mo metal, MoO<sub>2</sub>, and MoO<sub>3</sub> patterns were compared to confirm these materials. These patterns, Figure 4.28, show a good match with the data in Figure 4.27. The K-edge occurs at the same energy for each of the materials, and the absorption patterns are very similar. This further confirms that the fabricated simulant samples are stable cermets.

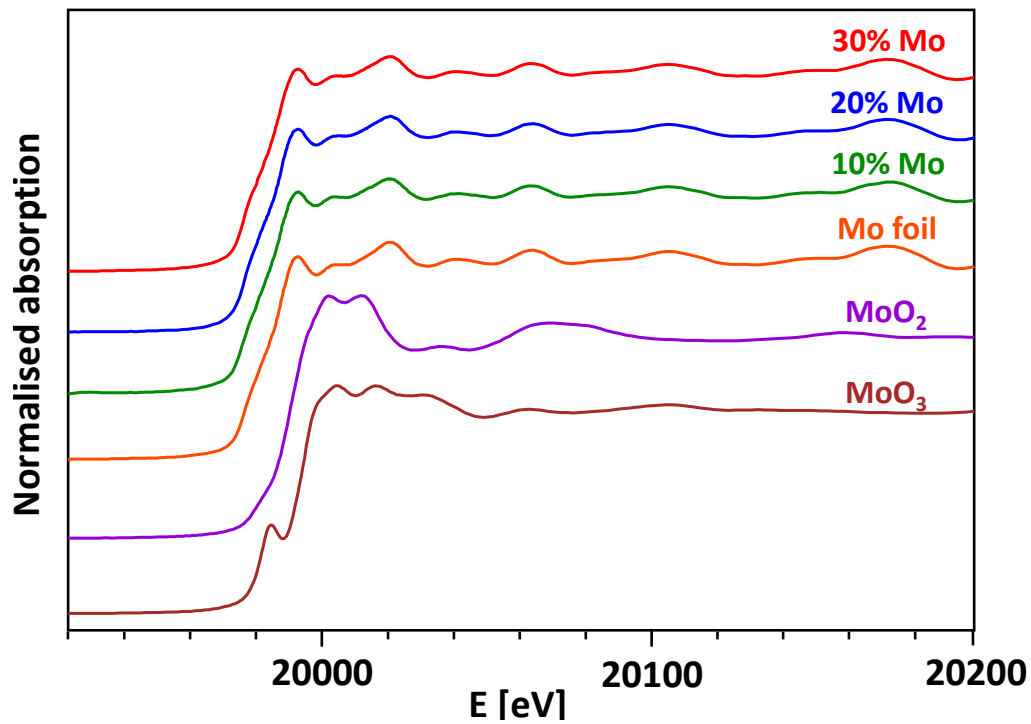


Figure 4.27 – XAS patterns of the 10 %, 20 %, and 30 % Mo pellet compositions, Mo foil, MoO<sub>2</sub>, and MoO<sub>3</sub>.

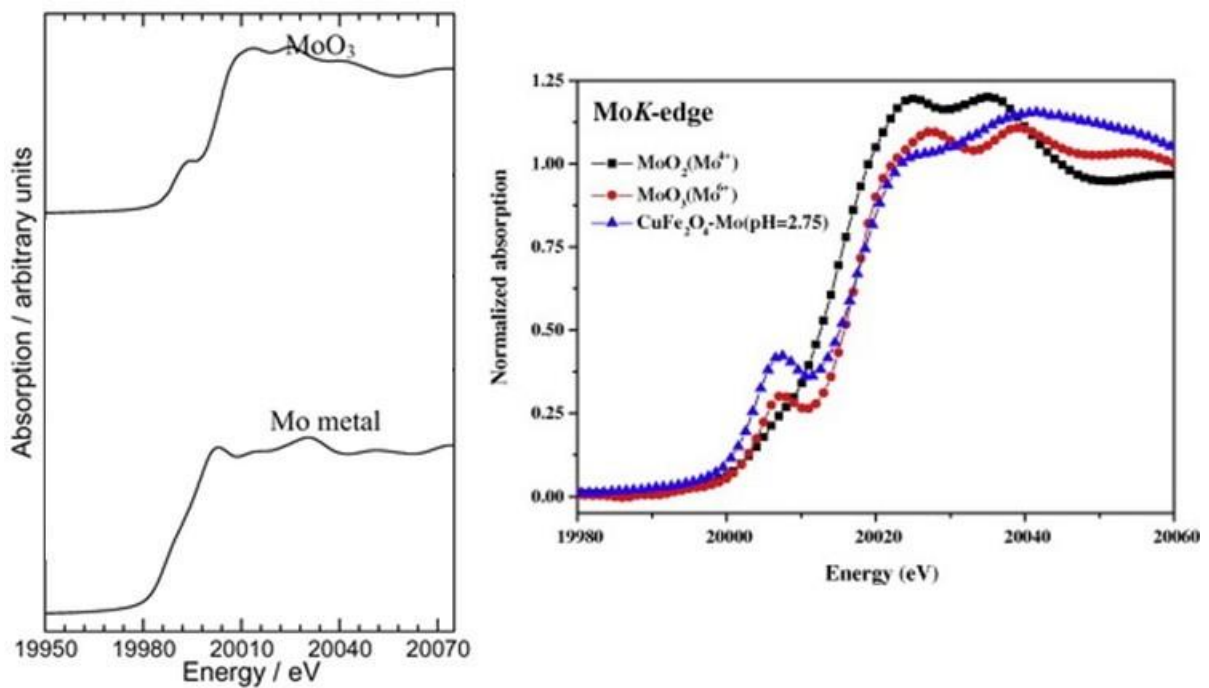


Figure 4.28 – XAS patterns from the literature of other studies done using Mo metal, MoO<sub>2</sub>, and MoO<sub>3</sub> samples [33], [34].

#### 4.8.6 Laser flash thermal conductivity

One of the main experimental characterisations for this work was the measurement of thermal conductivity values across the temperature range 100-1000°C of each cermet. Figures 4.29-4.32 show the thermal conductivity curves over the temperature range for pellets sintered at each temperature.

The thermal conductivity of the YSZ in each case decreases slightly in value in the range 100-400°C and then increases in the range 500-1000°C. This trend agrees with other YSZ materials at lower yttria content found in the literature [13], [35] and is a similar pattern observed with UO<sub>2</sub>. There is also a trend of an increase in thermal conductivity values as the YSZ sintering temperature increases. This is interesting as no other benefit of the sintering temperature has so far been shown. Although the grain size has not been investigated, by increasing sintering temperature there could be an increase in grain size, with larger grains improving the thermal conductivity. This is shown in simulation results in Chapter 3.

The cermets with 10 %, 20 % and 30 % Mo loading all have improved thermal conductivity compared to the YSZ sample as was the aim of this work, the exception to this that at >500°C the YSZ does have higher thermal conductivity than some Mo pellets, but this is not seen to be an issue as the operating design of the fuel would be at temperatures of <500°C. There is roughly a 60 % increase in thermal conductivity for the 10% Mo samples, with 100 % for the 20 % Mo loading and 200 % increase in the 30% Mo samples. This increase in thermal conductivity using only low metallic content is very promising. When compared with fuel rod simulations from Chapter 3, having just a 50 % increase in thermal conductivity would make a significant difference in the length of life for a fuel rod with regards to thermal mechanical conditions. Referring to Chapter 3, this would allow the fuel to operate for 15 years. Therefore, if this same process can be applied to UO<sub>2</sub> then improved thermal efficiency will be achieved for the fuel in a civil marine reactor.

There was to be expected a greater increase in thermal conductivity as the Mo content was increased, due thermal conductivity value of pure Mo at 138 W/mK [36] at room temperature. However there only appears to be an order of magnitude of 200 % increase for the 30 % Mo simulant fuel pellet. It is proposed that the low ceramic thermal conductivity behaviour of the YSZ material is a strong limiting factor. In that the advantage of the Mo is limited as the YSZ is still the main material in the fuel pellets.

A sintering temperature advantage between the three loadings does not appear as it does with the YSZ samples. As shown in Table 4.6 the thermal conductivity values of Mo loading content when compared at similar temperatures are all in the same ball park.

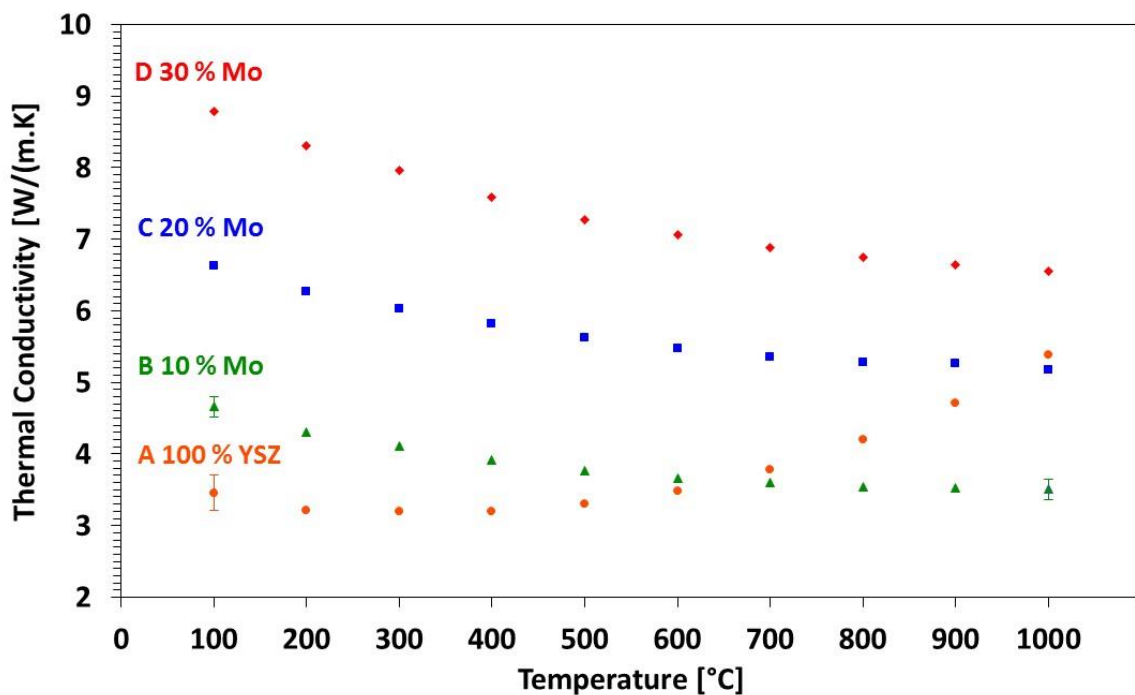


**Figure 4.29 – Thermal conductivity of Mo samples fabricated at 1300°C of composition; A 100 % YSZ, B 10 % Mo, C 20 % Mo, D 30 % Mo. Error bars on data with a standard deviation of greater than 0.1.**

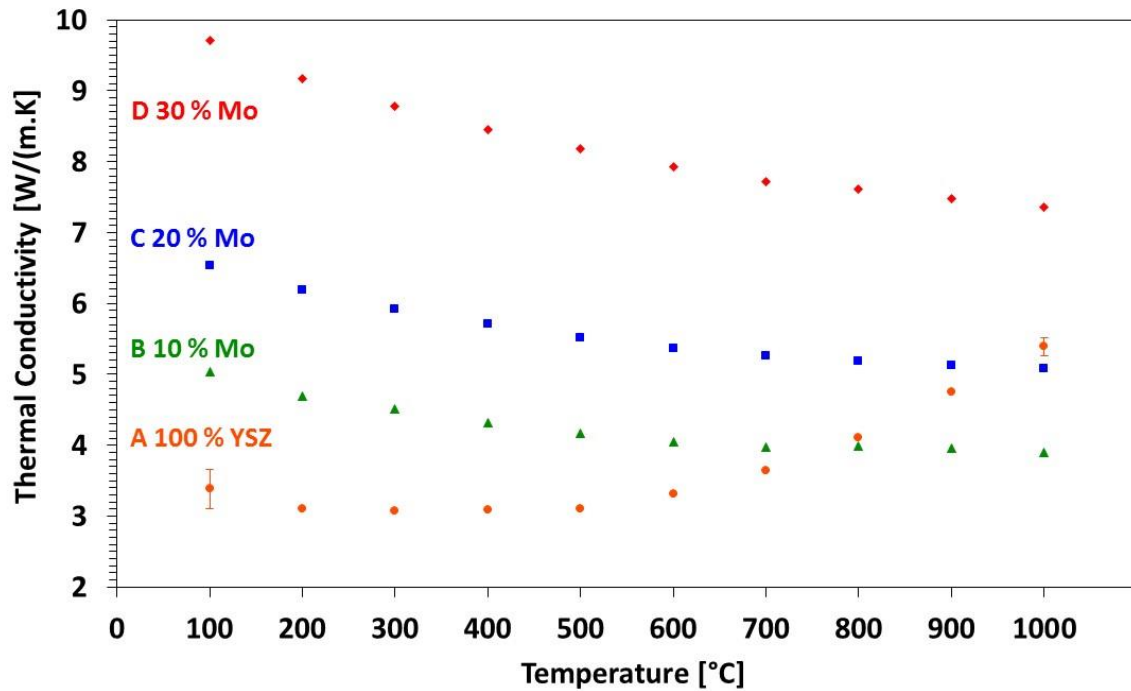


Figure 4.30 – Thermal conductivity of Mo samples fabricated at 1400°C of composition; A 100 % YSZ, B 10 % Mo, C 20 % Mo, D 30 % Mo. Error bars on data with a standard deviation of greater than 0.1.

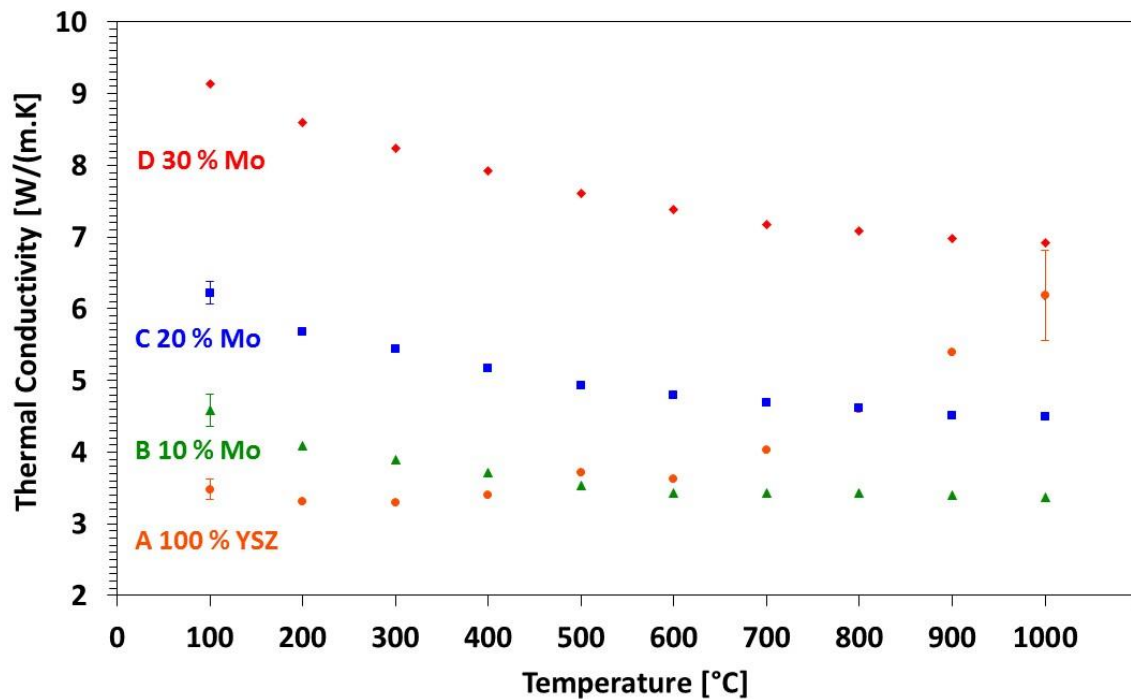


Figure 4.31 – Thermal conductivity of Mo samples fabricated at 1500°C of composition; A 100 % YSZ, B 10 % Mo, C 20 % Mo, D 30 % Mo. Error bars on data with a standard deviation of greater than 0.1.

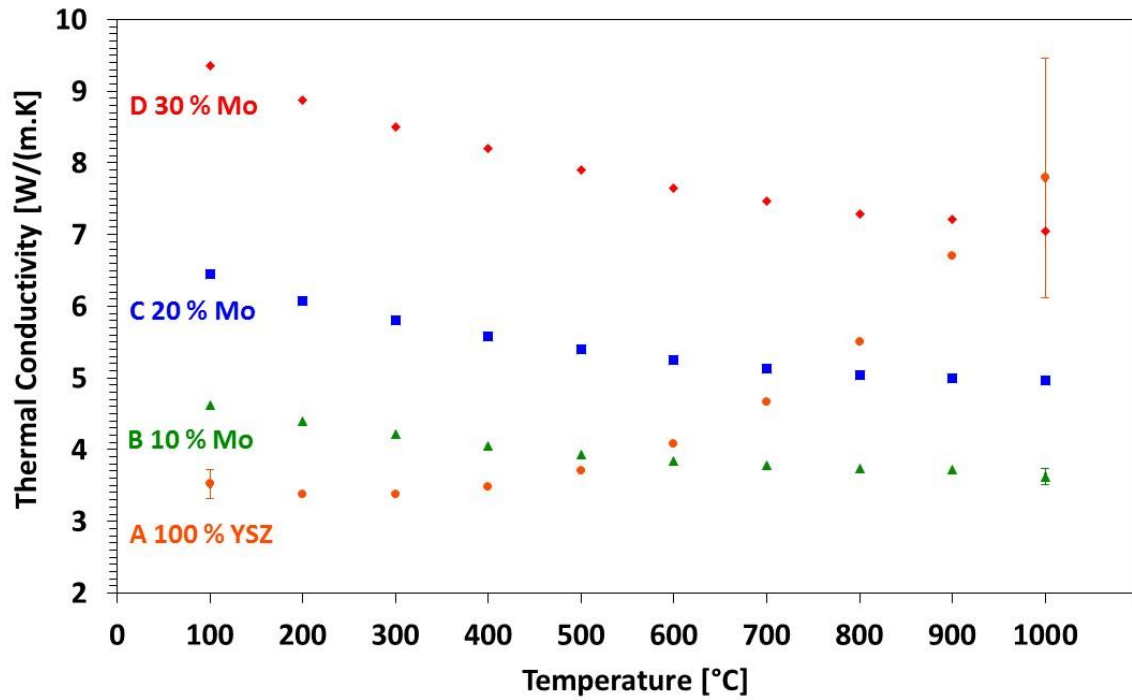


Figure 4.32 – Thermal conductivity of Mo samples fabricated at 1600°C of composition; A 100 % YSZ, B 10 % Mo, C 20 % Mo, D 30 % Mo. Error bars on data with a standard deviation of greater than 0.1.

Table 4.6 – Tabulated values from laser flash testing of all Mo fabricated samples.

		Thermal conductivity [W/(m.K)]									
Temperature		100	200	300	400	500	600	700	800	900	1000
1300°C	100 % YSZ	3.46	3.21	3.20	3.20	3.30	3.48	3.79	4.20	4.72	5.38
	10 % Mo	4.66	4.30	4.11	3.92	3.76	3.66	3.60	3.54	3.53	3.51
	20 % Mo	6.62	6.28	6.02	5.81	5.63	5.48	5.36	5.27	5.26	5.18
	30 % Mo	8.78	8.30	7.96	7.59	7.27	7.06	6.89	6.74	6.65	6.56
1400°C	100 % YSZ	3.39	3.11	3.07	3.08	3.11	3.32	3.65	4.10	4.75	5.39
	10 % Mo	5.03	4.69	4.51	4.32	4.16	4.05	3.98	3.99	3.97	3.89
	20 % Mo	6.53	6.19	5.92	5.71	5.52	5.37	5.26	5.18	5.13	5.08
	30 % Mo	9.71	9.17	8.79	8.45	8.18	7.93	7.72	7.61	7.49	7.35
1500°C	100 % YSZ	3.48	3.31	3.29	3.41	3.72	3.62	4.04	4.60	5.39	6.19
	10 % Mo	4.58	4.09	3.89	3.72	3.54	3.43	3.42	3.43	3.40	3.37
	20 % Mo	6.22	5.68	5.43	5.17	4.93	4.80	4.68	4.62	4.51	4.50
	30 % Mo	9.13	8.60	8.24	7.92	7.61	7.38	7.18	7.08	6.99	6.92
1600°C	100 % YSZ	3.52	3.38	3.38	3.48	3.71	4.08	4.67	5.50	6.70	7.79
	10 % Mo	4.62	4.39	4.22	4.05	3.93	3.84	3.78	3.74	3.73	3.62
	20 % Mo	6.45	6.08	5.81	5.58	5.40	5.25	5.13	5.05	5.00	4.96
	30 % Mo	9.36	8.87	8.51	8.21	7.90	7.64	7.46	7.29	7.21	7.05

#### 4.8.7 Hardness testing

Vickers hardness testing was carried out on all samples with an average taken from 5 results. From Figure 4.33, the loading at each sintering temperature shows a general downward trend in hardness value the higher the metallic loading. This would agree with expectations due to ceramic material YSZ having an increased hardness of literature values of 1350-1500 GPa [37] with the metallic Mo 230 GPa [28]. The values of YSZ measured, 1458 GPa, 1414 GPa, 1356 GPa, and 1430 GPa are in the range of values from the literature.

Figure 4.34 compares the results for each metallic loading. There does not seem to be any strong evidence that the sintering temperature produces a material with a higher or lower hardness. This shows that the sintering temperature does not appear to have an important impact on the hardness.

The hardness of the material for future fuel samples is important to understand, as its behaviour in a fuel rod will change depending on the hardness. Due to swelling and hydrostatic pressures put upon fuel pellet in a PWR reactor, being more ductile would be a benefit as less cracking of the pellet would be expected. This would reduce fuel failure incidents and lower fission gas release as just a number of benefits.

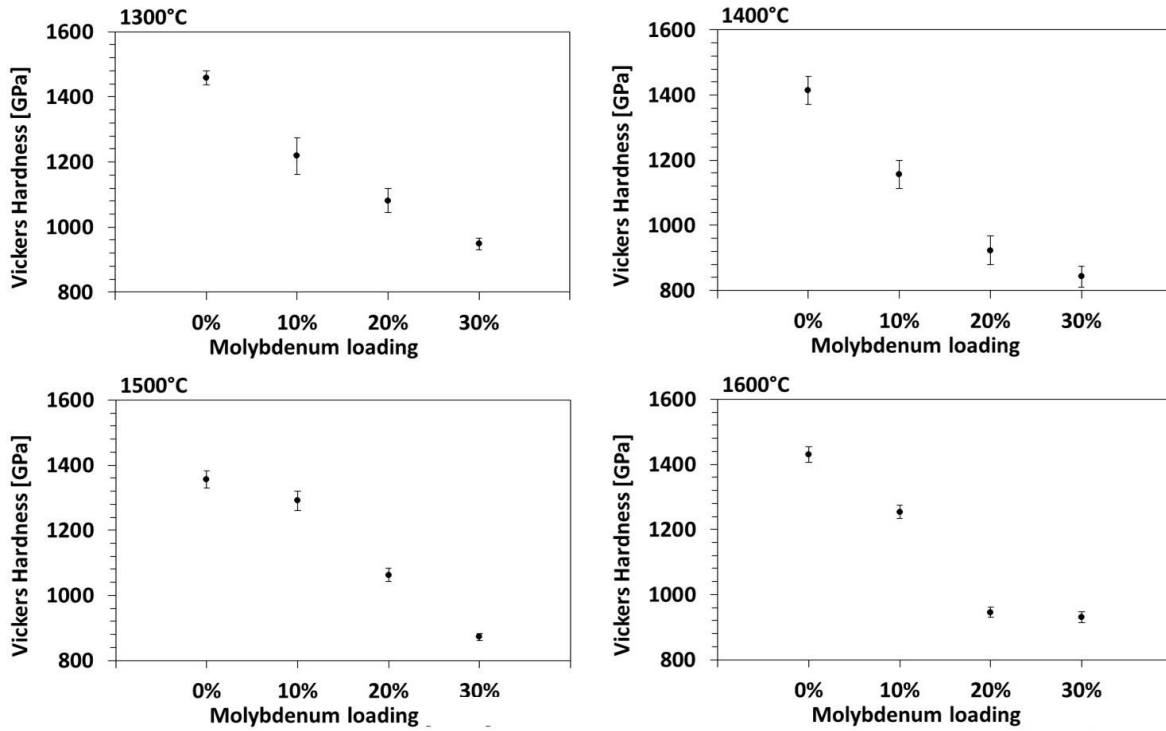


Figure 4.33 – Vickers hardness of YSZ Mo samples for each sintering temperature.

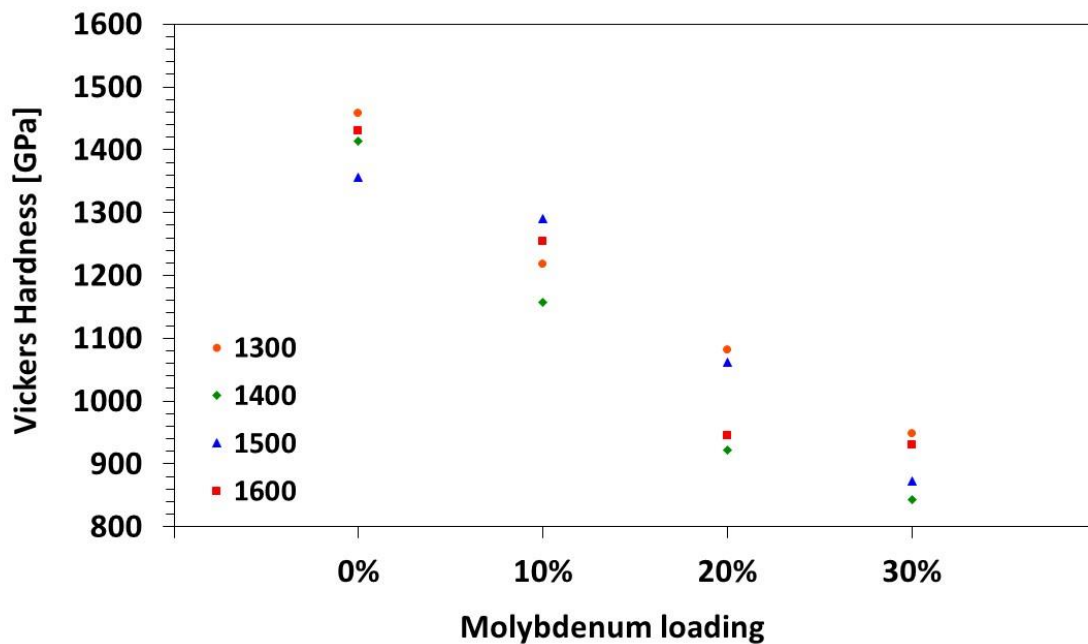


Figure 4.34 – Vickers hardness of YSZ Mo samples for each sample comparatively shown for each Mo loading. Error bars have been removed for clarity.

## 4.9 YSZ W pellets

This section details all the characterisation work carried out on all fabricated YSZ W samples. The 100 % YSZ samples here are the same used for comparison as with the Mo samples.

### 4.9.1 Density

The density of the YSZ W pellets was carried out by the water immersion method and geometrically. These results at each sintering temperature, Figure 4.35, show the density increasing with the W content, similar to the Mo pellets. However, an increase in the density in the W samples compared with the Mo is apparent. This was expected as the initial density of W being significantly higher than Mo, Table 4.3.

The agreement between the two techniques shows consistency in the same linear trend of increasing density as W content is increased. Comparing the actual values obtained from each method, there is some discrepancy for the 1300°C, 1400°C, and 1600°C as half of the values are a close match, whilst there is a difference in agreement shown in the other half. The 1500°C simulant pellets show the same difference for all 4 results. These difference are attributed to unconnected porosity in the simulant pellets that is not accounted for in the water immersion method.

When compared against sintering temperature, Figure 4.36, there is shown to be consistency, excluding the 1300°C 20 % result, of similar measurements of density for each fabrication temperature. Similar again to the Mo samples there does not appear to be any trend suggesting a benefit due to the sintering temperature. As the pure YSZ simulant pellets are the same used for comparison with the Mo samples, the same agreement for all 4 temperatures is shown again.

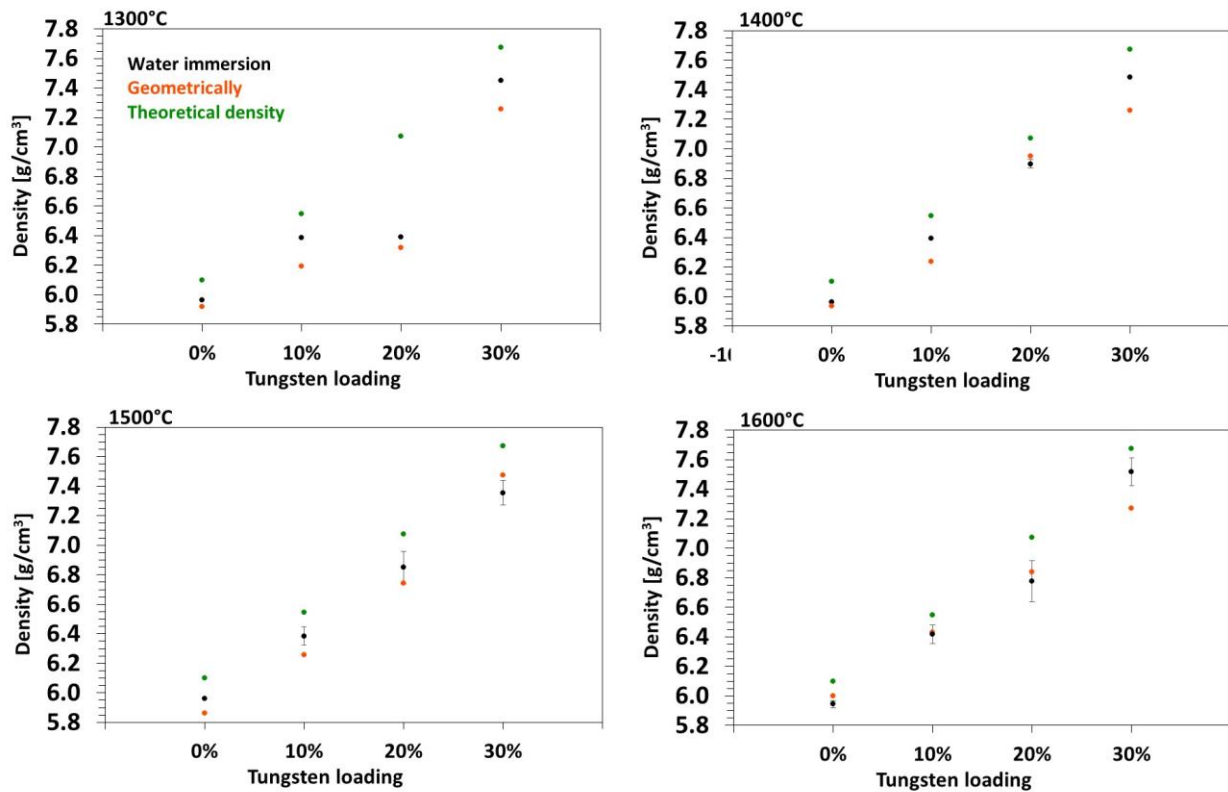


Figure 4.35 – Density of fabricated YSZ W cermet at each temperature by Archimedes method and geometrically, error bars with standard deviation of greater than 0.01 shown.

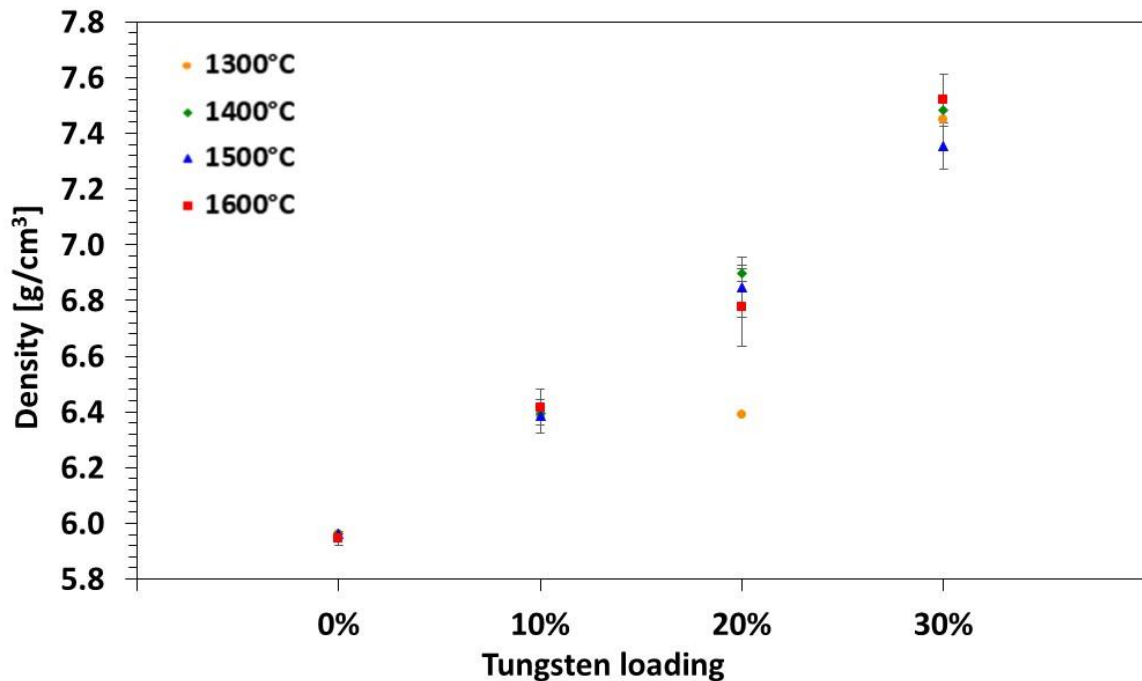


Figure 4.36 – Density of fabricated W pellets at each temperature by water immersion method, error bars with standard deviation of greater than 0.01 shown.

#### **4.9.2 XRD**

The XRD patterns were taken on crushed powder from the fabricated pellets of all W samples. Figures 4.37 – 4.40 show these traces at each of the sintering temperatures. Each of these sample results have been normalised for comparison. For all 4 sintering temperatures, there is a good agreement shown that in the increase of W content the stronger the trace of the XRD pattern for that element.

The diffraction patterns Figures 4.37 – 4.40 can be interpreted as YSZ and W metal material. Referring back to the reagent green powder XRD patterns, no further peaks are shown providing evidence that no reaction has taken place between the two materials, giving support that a stable cermet has been fabricated.

As well, similar to the Mo test results, these does not appear to be any evidence that there is a difference between the 4 different sintering temperatures from the XRD pattern data shown. There is also a clear increased intensity for the W material as the content is increased for all the temperatures, as was to be expected.

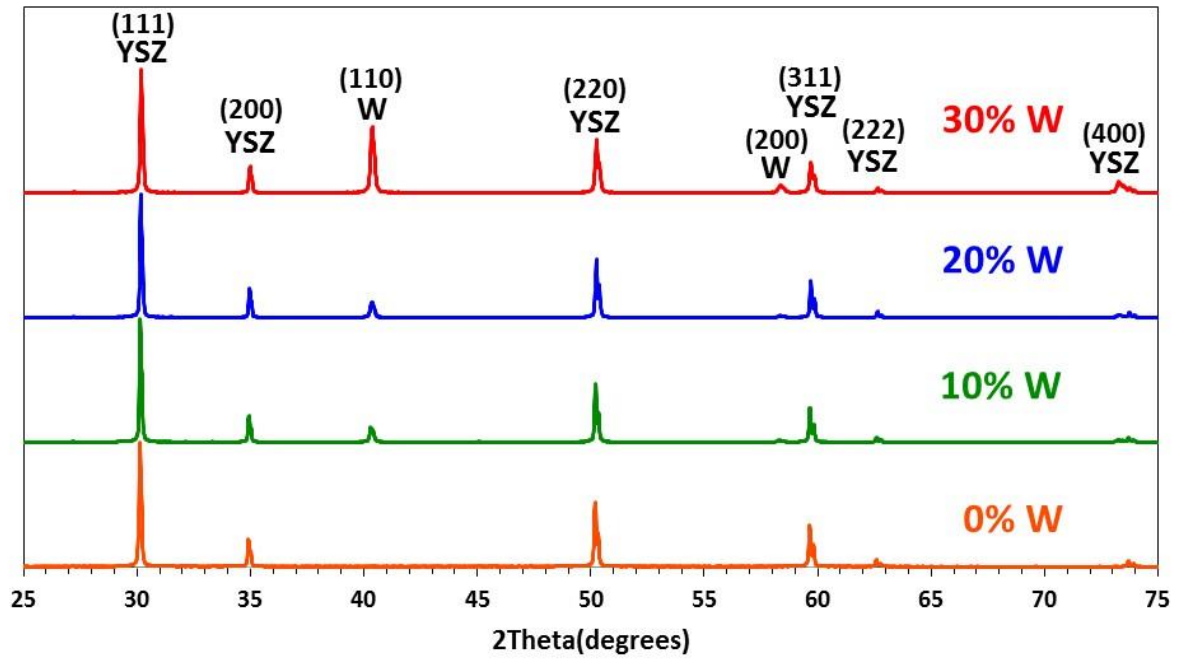


Figure 4.37 – Normalised XRD patterns of W samples heated at 1300°C.

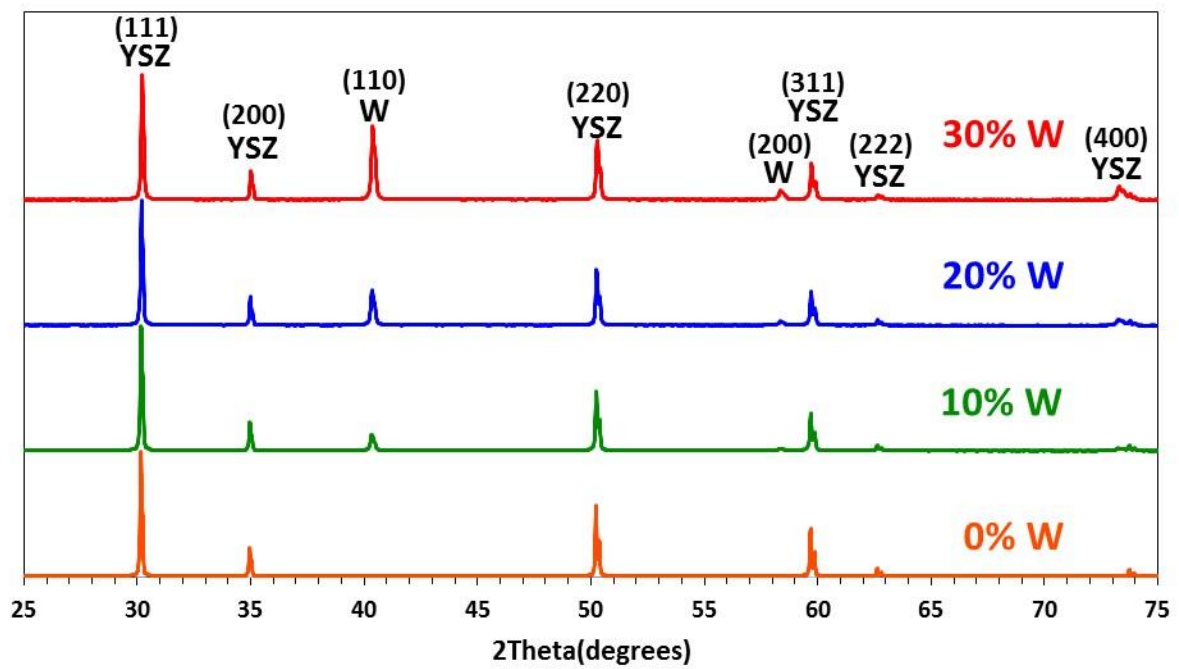


Figure 4.38 – Normalised XRD patterns of W samples heated at 1400°C.

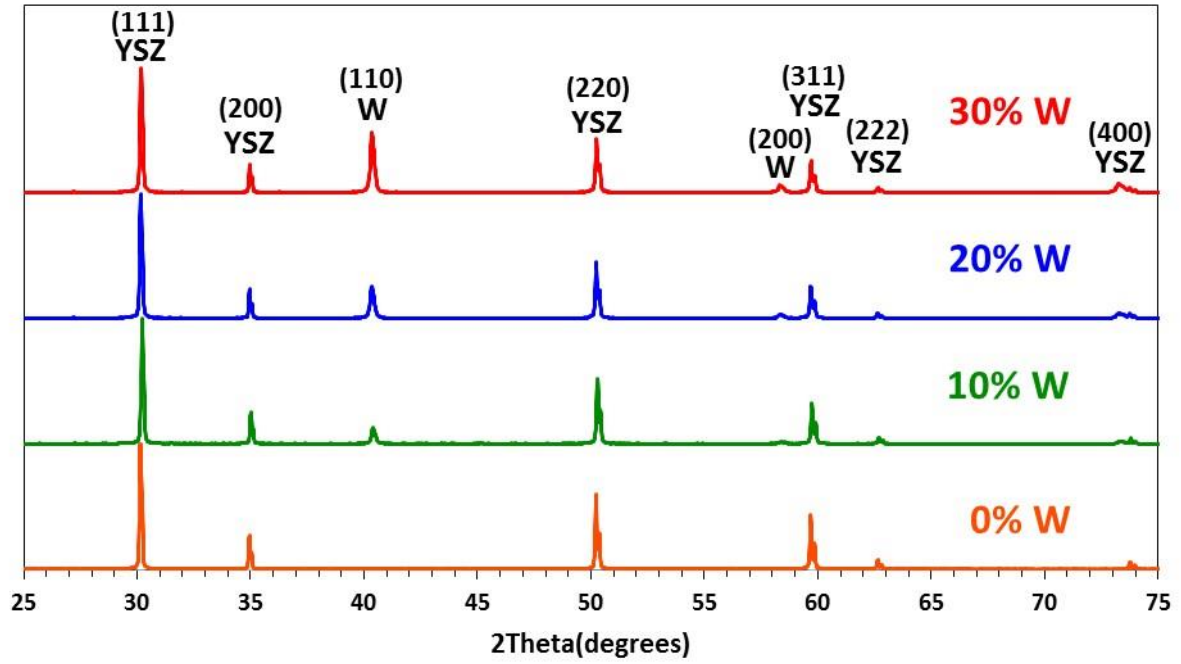


Figure 4.39 – Normalised XRD patterns of W samples heated at 1500°C.

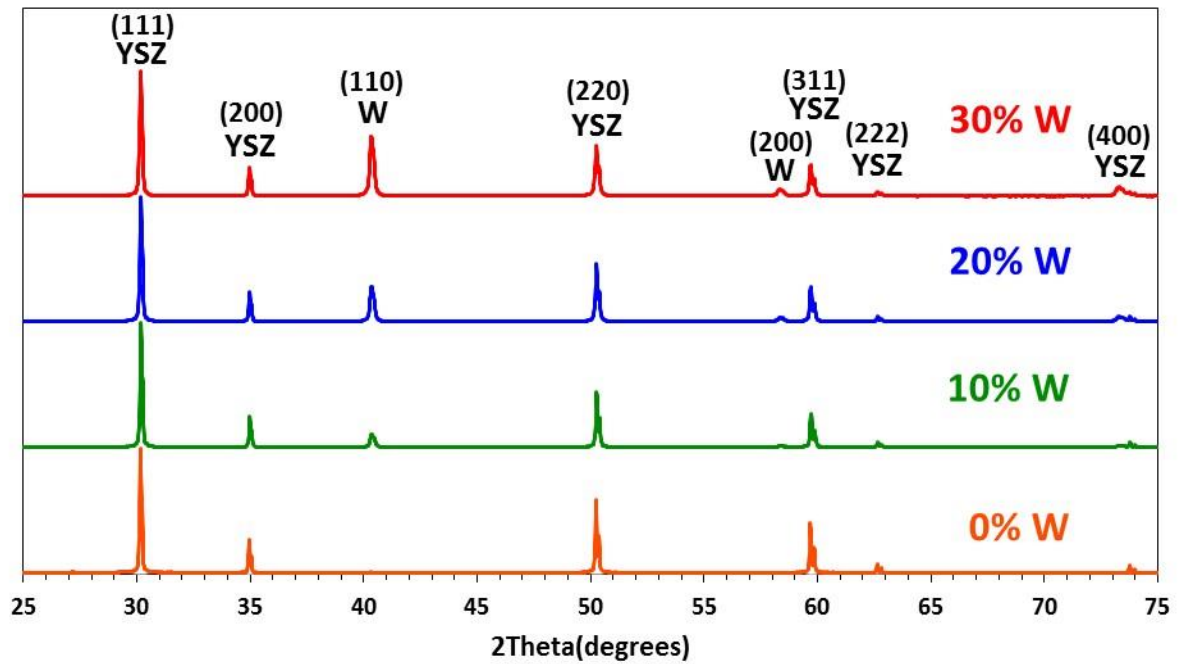
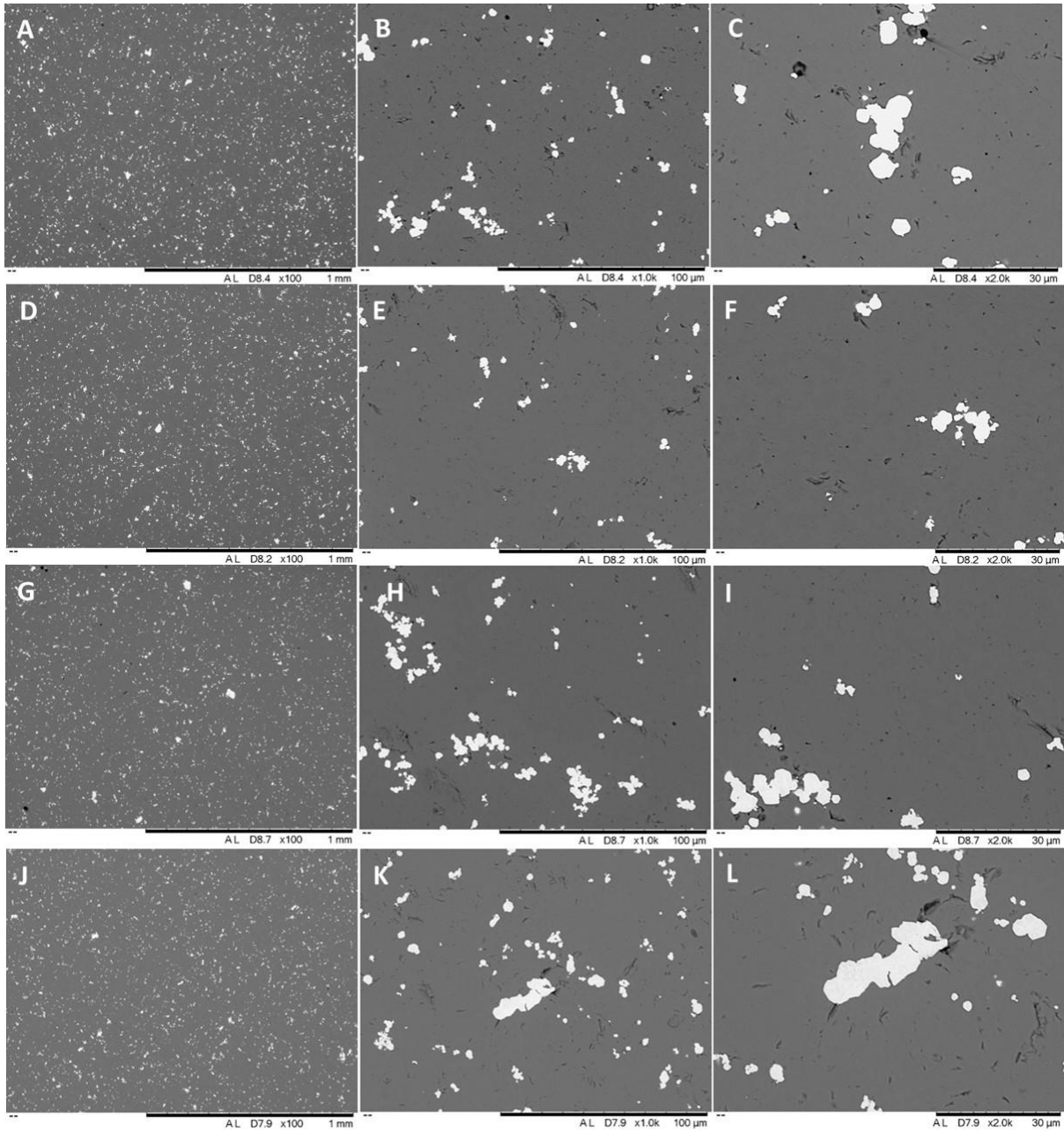


Figure 4.40 – Normalised XRD patterns of W samples heated at 1600°C.

### **4.9.3 SEM analysis**

The SEM backscattered micrographs of all W samples at each sintering temperatures can be seen across Figures 4.41-4.43. With the W samples appearing brighter due to their higher atomic number and electron conduction, and thus producing greater electron scattering, there appears to be a good distribution of the metallic material across each of the samples.

Noticeable is also the amount of W material shown in each loading content and that it is distributed evenly in each one. There also does not appear to be much porosity, which is confirming the T.D. achieved listed in Table 4.5, in the samples assuming that each of the dark areas on the images is a mix up of material that has been removed during the grinding/polishing process and actual porosity in the sample.



**Figure 4.41– SEM backscattered micrographs of 10 % W sample at magnifications 100x, 1000x, and 2000x; A, B, C heated at 1300°C; D, E, F heated at 1400°C; G, H, I heated at 1500°C; J, K, L heated at 1600°C.**

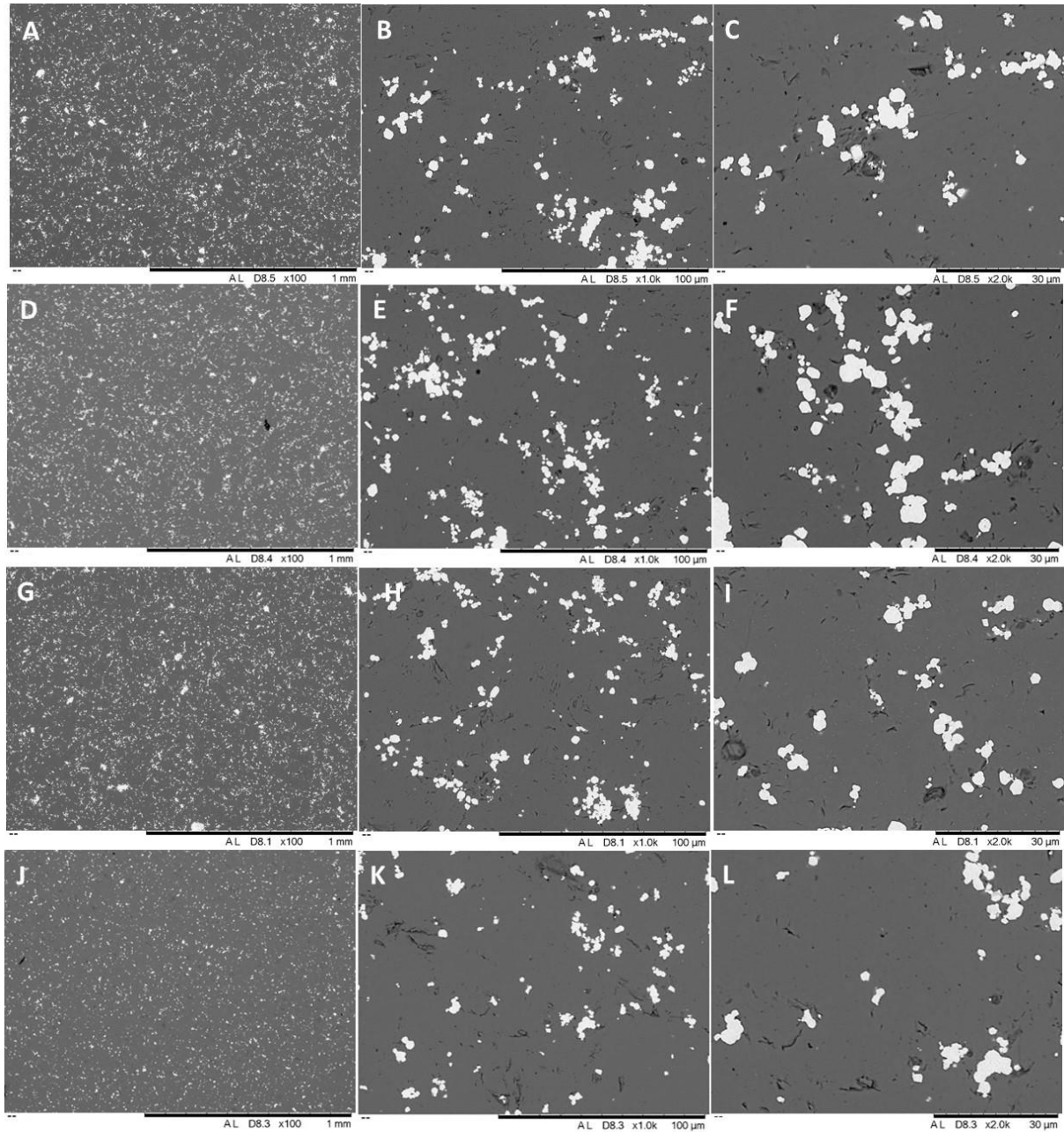


**Figure 4.42 – SEM backscattered micrographs of 20 % W sample at magnifications 100x, 1000x, and 2000x; A, B, C heated at 1300°C; D, E, F heated at 1400°C; G, H, I heated at 1500°C; J, K, L heated at 1600°C.**

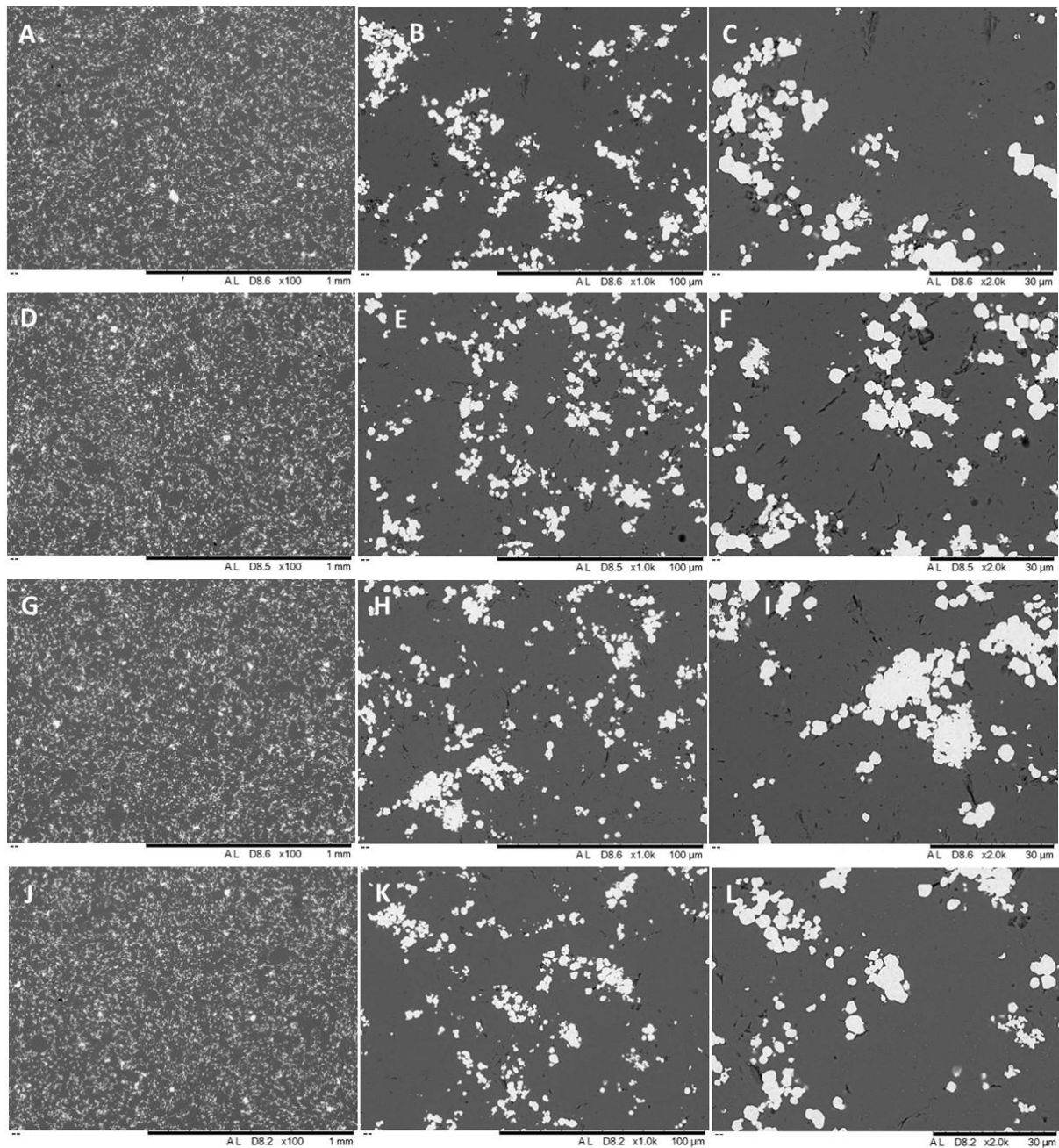


**Figure 4.43 – SEM backscattered micrographs of 30 % W sample at magnifications 100x, 1000x, and 2000x; A, B, C heated at 1300°C; D, E, F heated at 1400°C; G, H, I heated at 1500°C; J, K, L heated at 1600°C.**

#### **4.9.4 SEM EDX**

The SEM EDX scans of each W sample were also conducted, these shown in Figures 4.44-4.46. The elements present in each sample are O, Y, Zr, and W. What can be observed across all samples at each temperature is a good definition of the W material to the YSZ regions. There

is shown to be small amounts of oxygen present in the W regions but due to the presence of yttrium too, this is either due to material being lifted and deposited from the grinding and polishing process or more likely the depth of EDX electrons into the sample might be penetrating Y below the W regions.

The definition of the YSZ and W regions gives further proof that a complete cermet has been produced and that there are no boundary regions in the sample between the YSZ and W material to suggest any oxidation has occurred.

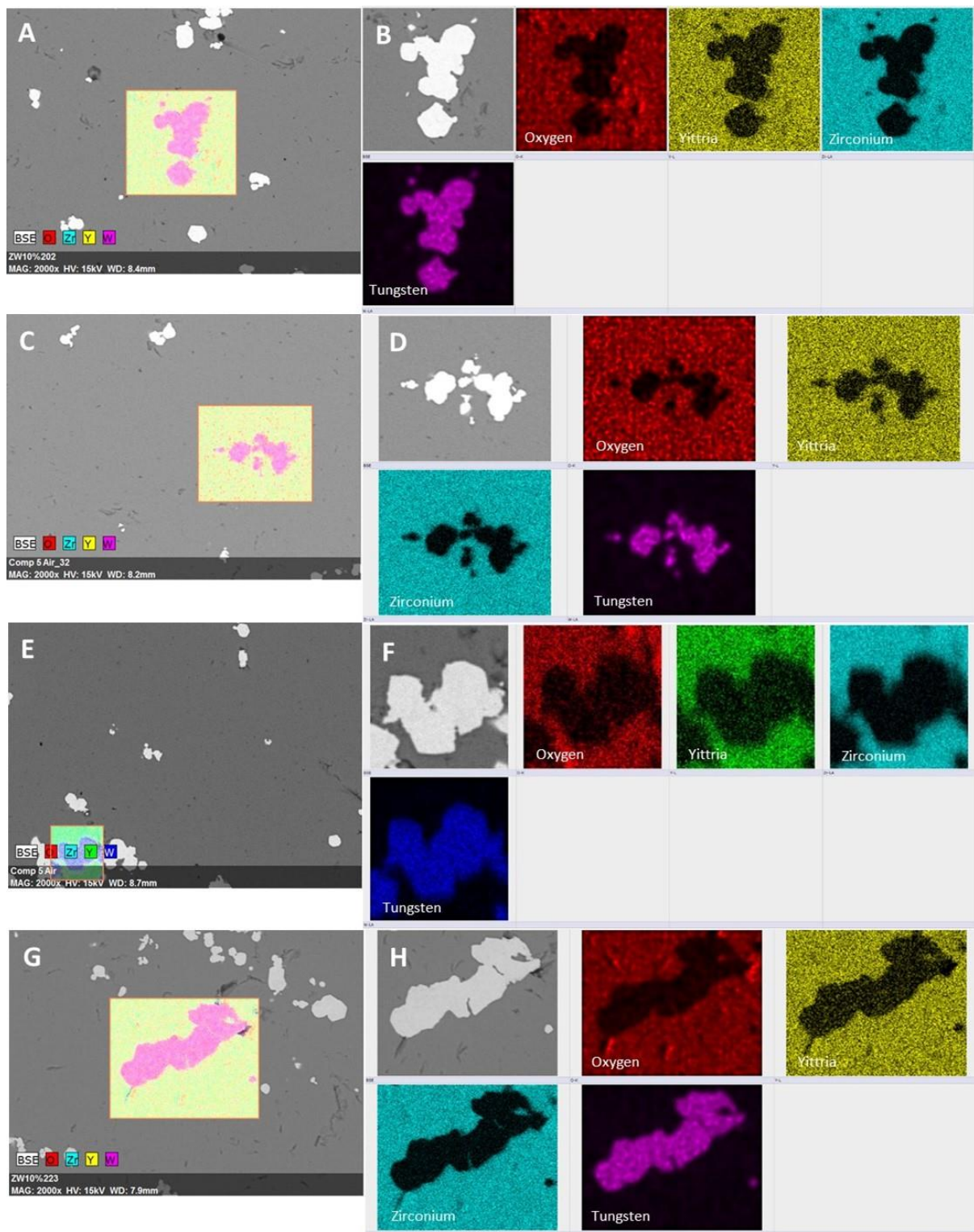


**Figure 4.44 –SEM micrograph of EDX scanned area and EDX scans of each element composition present. Samples are 10 % W; A, B heated at 1300°C; C, D heated at 1400°C; E, F heated at 1500°C; G, H heated at 1600°C.**

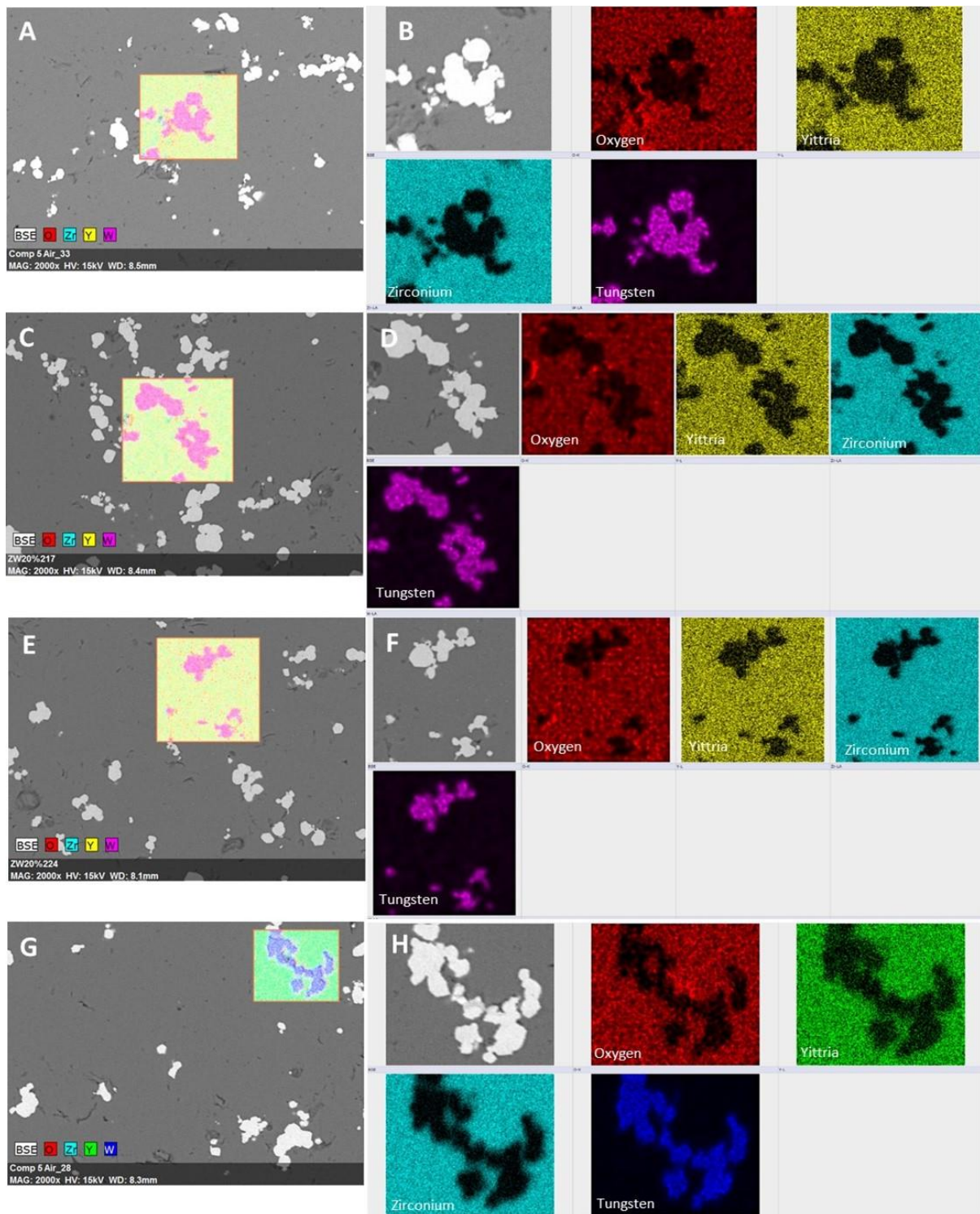


**Figure 4.45 –SEM micrograph of EDX scanned area and EDX scans of each element composition present. Samples are 20 % W; A, B heated at 1300°C; C, D heated at 1400°C; E, F heated at 1500°C; G, H heated at 1600°C.**

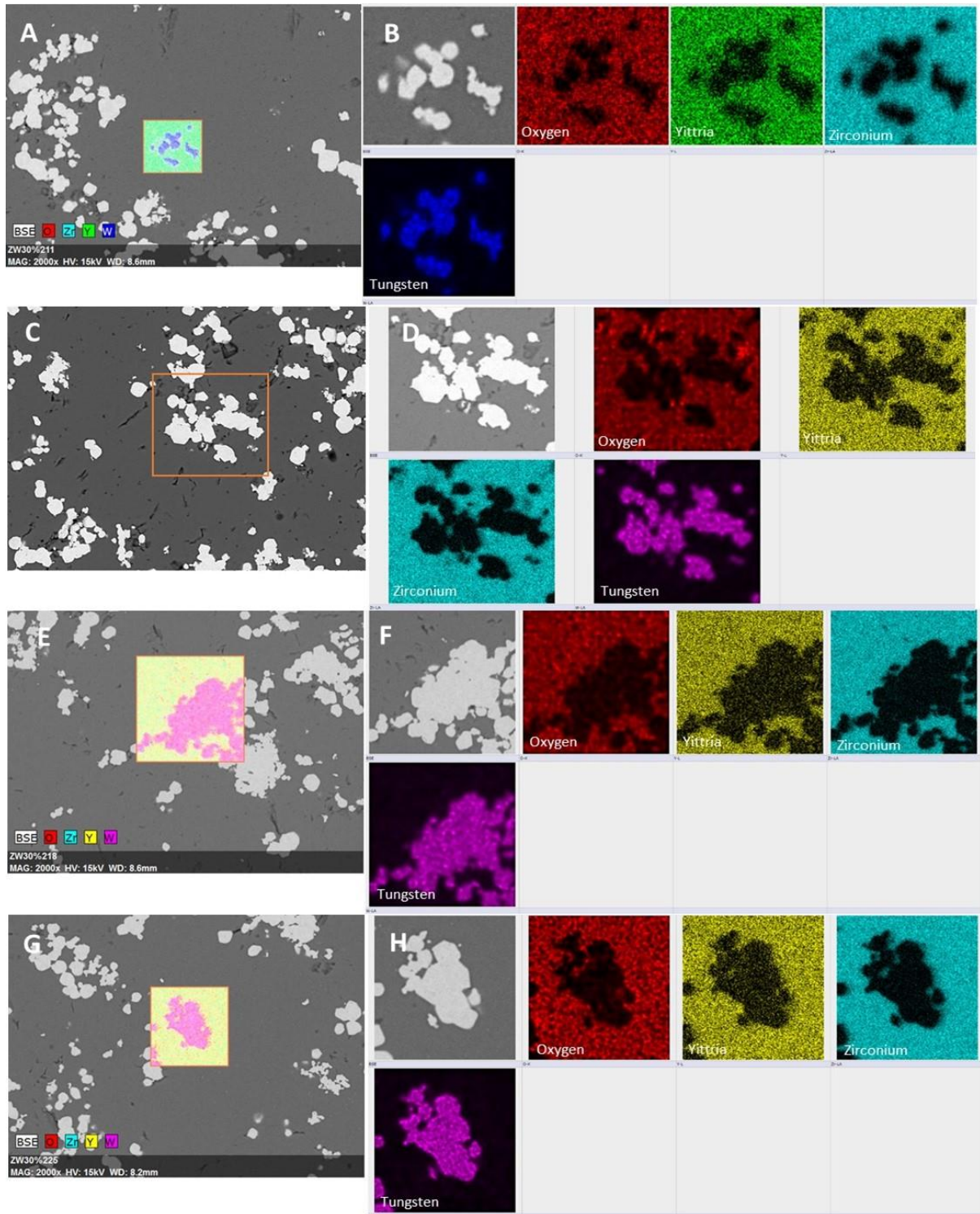


**Figure 4.46 –SEM micrograph of EDX scanned area and EDX scans of each element composition present. Samples are 30 % W; A, B heated at 1300°C; C, D heated at 1400°C; E, F heated at 1500°C; G, H heated at 1600°C.**

#### 4.9.5 Laser flash thermal conductivity

Laser flash testing was carried out on all W samples to determine the thermal conductivity of each sample over the temperature range 100°C to 1000°C. Figures 4.47-4.50 show these results for each sintering temperature. The same results are shown for the 100 % YSZ samples as in the Mo comparison, since the same sample is used.

The general trend shown is that there is an increase in the thermal conductivity of the samples as the loading content is increased, for 10 %, 20 %, and 30 % W samples. An average increase of the 4 sintering temperatures of 34 %, 68 %, and 127 % was observed respectively at 100°C.

Similar to findings with the Mo samples, no discernible differences in the sintering temperatures effect on the thermal conductivity values of the samples were observed. Shown in Table 4.7 are all the tabulated thermal conductivity values of all W fabricated pellets. For example the 10 % W loading thermal conductivity values at 500°C are 3.65 kW/m, 3.94 kW/m, 3.65 kW/m, and 3.86 kW/m for the 1300°C, 1400°C, 1500°C, and 1600°C sintering temperatures respectively. The 1400°C result is the highest value and could be due to variation in results but they are all in the same region, and does not suggest any bias to sintering temperature.

Interestingly, when the 100°C values of the W samples are compared with the Mo counterparts, the Mo samples at 20 % and 30 % loading have significantly higher thermal conductivity values, with 10 % loading being equal in value. The room temperature thermal conductivity value of W is 169 kW/m [36] which is higher than that of Mo previously listed as 138 kW/m.

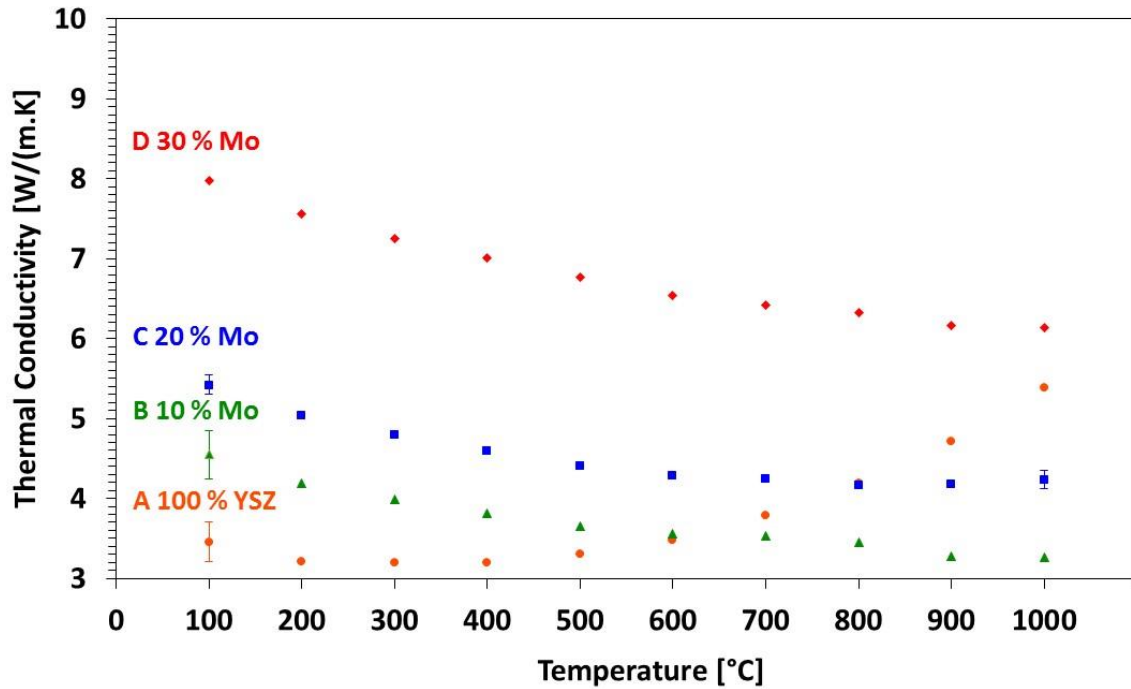


Figure 4.47 – Thermal conductivity of W samples fabricated at 1300°C of composition A 100 % YSZ, B 10 % W, C 20 % W, D 30 % W. Error bars on data with a standard deviation of greater than 0.1.

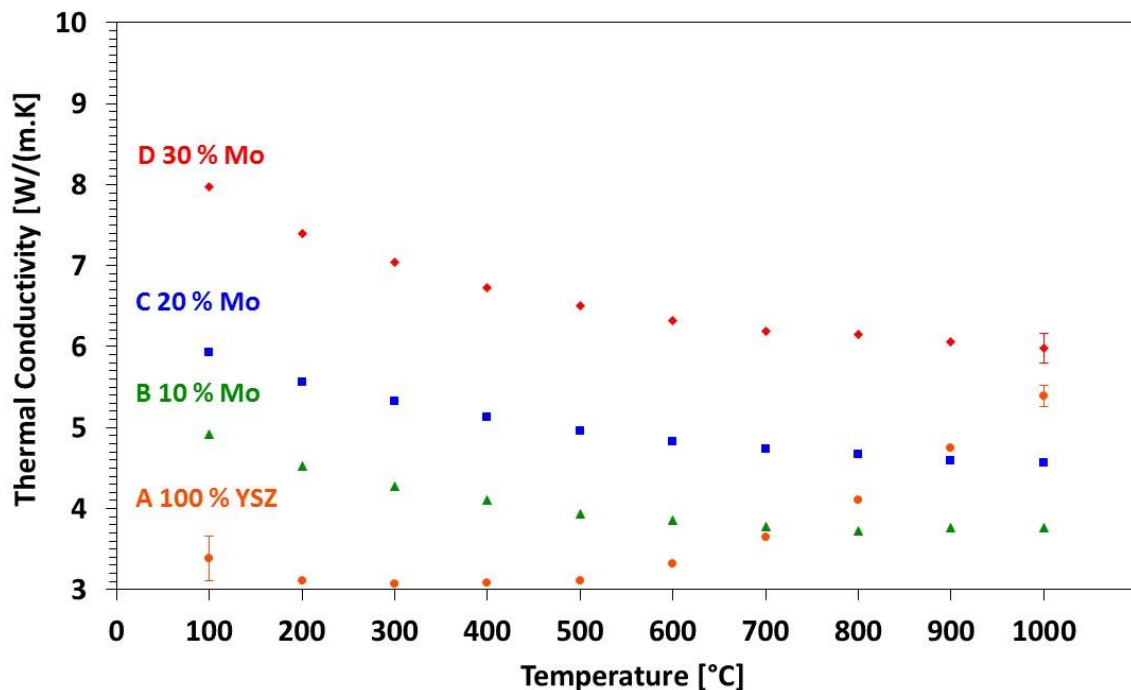


Figure 4.48 – Thermal conductivity of W samples fabricated at 1400°C of composition A 100 % YSZ, B 10 % W, C 20 % W, D 30 % W. Error bars on data with a standard deviation of greater than 0.1.

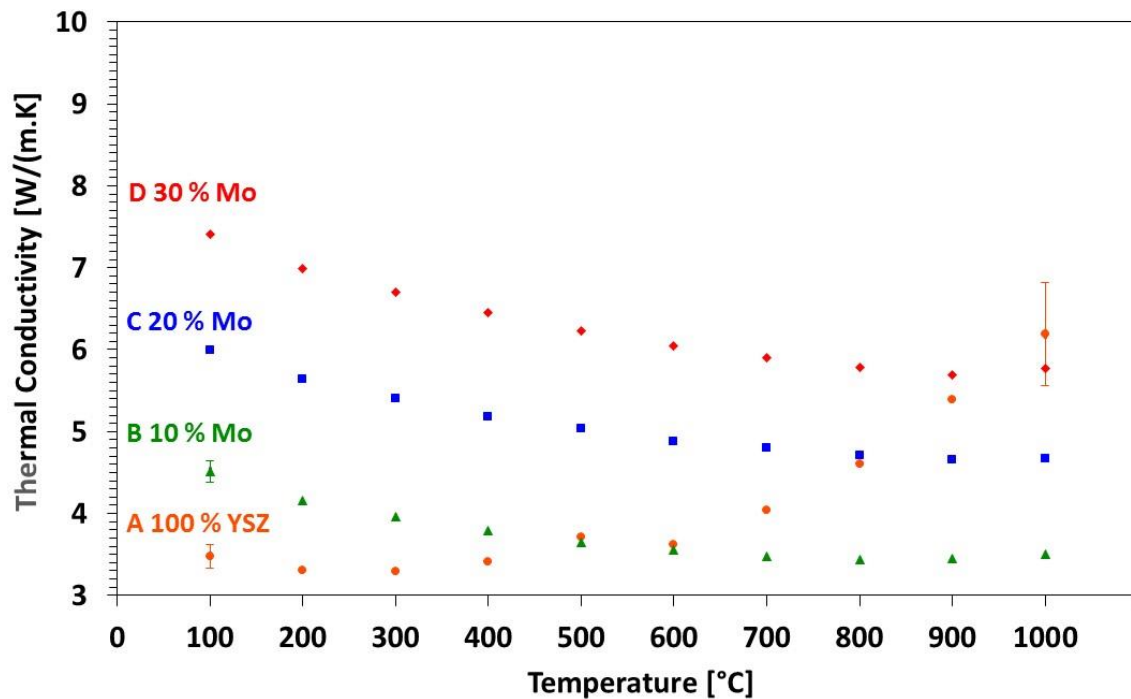


Figure 4.49 – Thermal conductivity of W samples fabricated at 1500°C of composition A 100 % YSZ, B 10 % W, C 20 % W, D 30 % W. Error bars on data with a standard deviation of greater than 0.1.

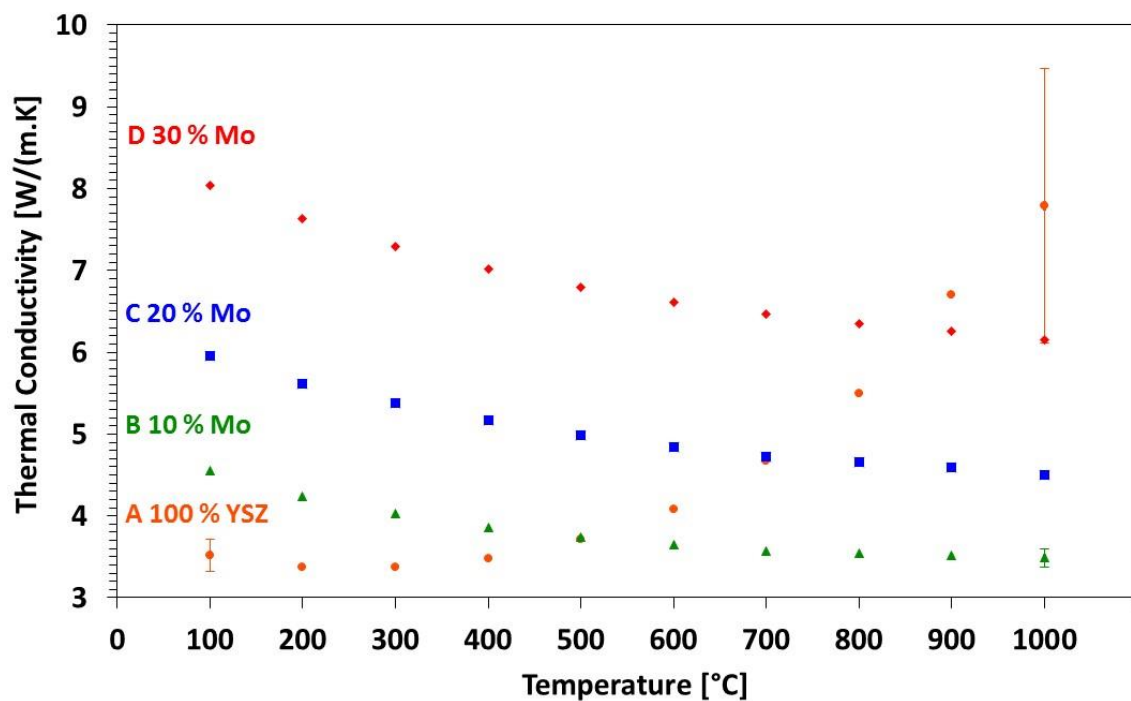


Figure 4.50– Thermal conductivity of W samples fabricated at 1300°C of composition A 100 % YSZ, B 10 % W, C 20 % W, D 30 % W. Error bars on data with a standard deviation of greater than 0.1.

**Table 4.7 – Tabulated values from laser flash testing of all W fabricated samples.**

		<b>Thermal conductivity [W/(m.K)]</b>									
	<b>Temperature</b>	<b>100</b>	<b>200</b>	<b>300</b>	<b>400</b>	<b>500</b>	<b>600</b>	<b>700</b>	<b>800</b>	<b>900</b>	<b>1000</b>
<b>1300°C</b>	<b>100 % YSZ</b>	3.46	3.21	3.20	3.20	3.30	3.48	3.79	4.20	4.72	5.38
	<b>10 % W</b>	4.55	4.19	3.99	3.82	3.65	3.55	3.53	3.45	3.28	3.26
	<b>20 % W</b>	5.41	5.03	4.79	4.60	4.41	4.29	4.24	4.16	4.17	4.24
	<b>30 % W</b>	7.97	7.56	7.25	7.01	6.76	6.54	6.42	6.32	6.16	6.14
<b>1400°C</b>	<b>100 % YSZ</b>	3.39	3.11	3.07	3.08	3.11	3.32	3.65	4.10	4.75	5.39
	<b>10 % W</b>	4.92	4.52	4.27	4.10	3.94	3.86	3.78	3.73	3.76	3.77
	<b>20 % W</b>	5.93	5.55	5.33	5.13	4.96	4.83	4.74	4.67	4.59	4.57
	<b>30 % W</b>	7.98	7.40	7.04	6.72	6.51	6.33	6.18	6.15	6.05	5.98
<b>1500°C</b>	<b>100 % YSZ</b>	3.48	3.31	3.29	3.41	3.72	3.62	4.04	4.60	5.39	6.19
	<b>10 % W</b>	4.51	4.16	3.96	3.79	3.65	3.55	3.47	3.44	3.45	3.51
	<b>20 % W</b>	5.99	5.64	5.41	5.19	5.03	4.88	4.80	4.71	4.65	4.67
	<b>30 % W</b>	7.41	6.99	6.70	6.45	6.23	6.04	5.90	5.79	5.69	5.77
<b>1600°C</b>	<b>100 % YSZ</b>	3.52	3.38	3.38	3.48	3.71	4.08	4.67	5.50	6.70	7.79
	<b>10 % W</b>	4.56	4.24	4.03	3.86	3.74	3.65	3.58	3.54	3.52	3.49
	<b>20 % W</b>	5.95	5.61	5.38	5.17	4.99	4.85	4.73	4.66	4.59	4.50
	<b>30 % W</b>	8.05	7.63	7.30	7.02	6.79	6.61	6.46	6.35	6.25	6.16

#### **4.9.6 Hardness testing**

The Vickers hardness of each W sample was determined, Figure 4.51 shows the samples at each sintering temperature. There is agreement with the Mo samples that as the loading content is increased the hardness of the material goes down. However there is shown a high variability in the results obtained, with Figure 4.52 showing this in more detail. It can be seen that there is a wide range of results obtained especially at the 30 % loading. This is not attributed to the sintering temperature and more to a variation in the measurements, since the low and high temperature results of 1300°C and 1600°C correlate together.

The variability could be due to the nature of the testing, in that when using the SEM images there are areas of larger concentration of W material. One reason for this could be that when

the indentation is carried out it might relate to a higher area of W content. However this is one reason why 5 measurements were carried out to average this error out.

W metal has a lower Vickers hardness value than YSZ of 310 GPa, but is higher than that of Mo metal 230 GPa. The higher Vickers hardness is apparent when the average measurements for the 4 loading contents from each temperature are compared between the Mo and W simulant pellets, Table 4.8. This shows a difference in the effect of Mo to W in the hardness of the simulant pellets.

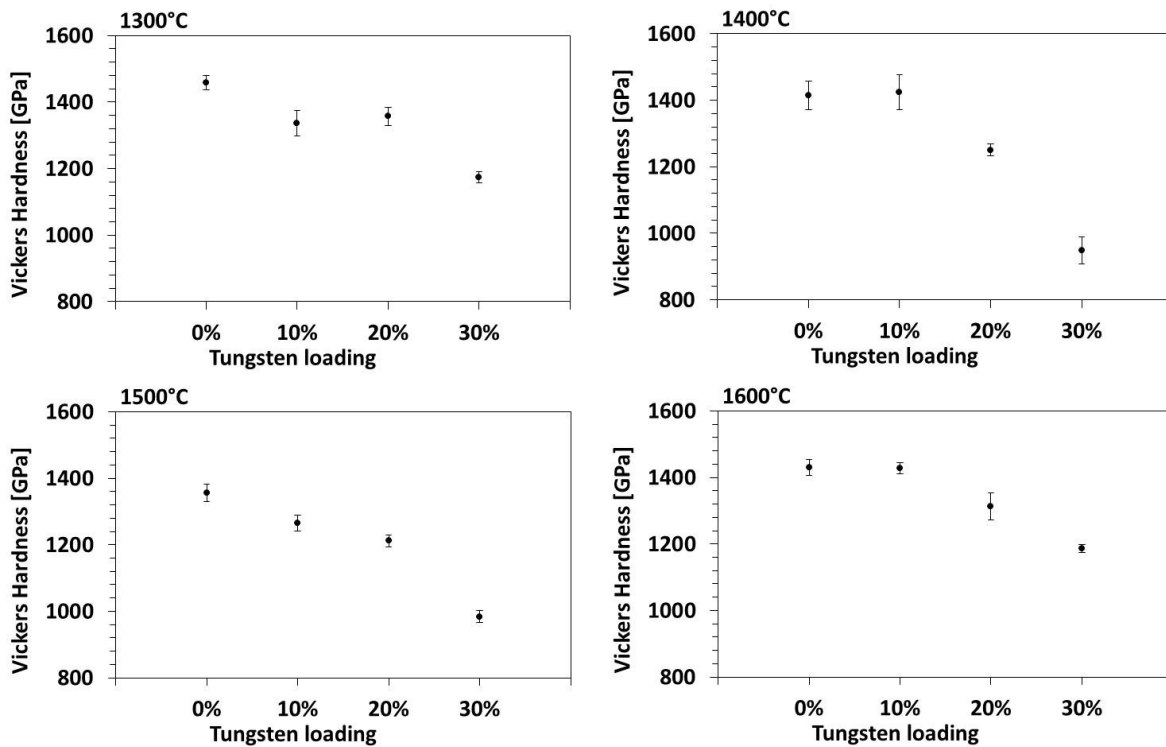
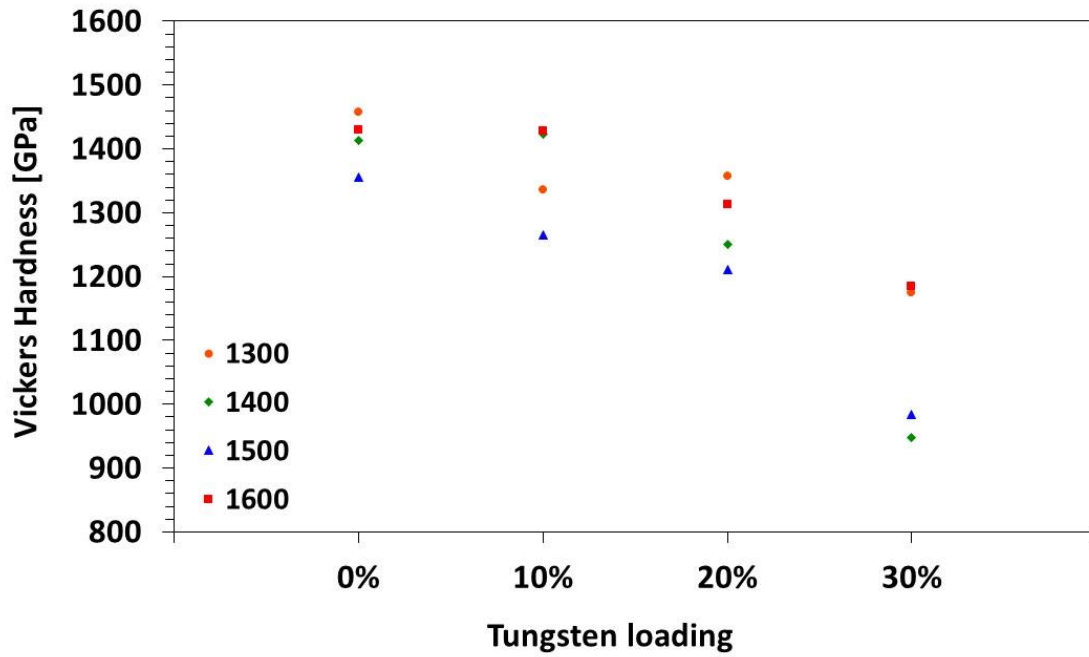


Figure 4.51 – Vickers hardness of YSZ W samples for each sintering temperature.



**Figure 4.52 – Vickers hardness of YSZ W samples for each sample comparatively shown for each Mo loading. Error bars have been removed for clarity.**

**Table 4.8 – Comparison of the averaged Vickers hardness measurements of the fabrication temperatures 1300°C, 1400°C, 1500°C, and 1600°C for each loading content of Mo and W.**

Metallic content	Vickers Hardness [GPa]	
	Mo	W
0 %	1414	1414
10 %	1230	1364
20 %	1003	1283
30 %	899	1073

#### 4.10 Conclusion

The research presented in this Chapter has detailed the fabrication of producing simulant fuel pellets using the process of SPS. Different metallic content, sintering temperature and metallic

loading content were all studied and compared, with the goal of fabrication of stable cermets, and to determine the most effective composition.

The ability to make cermets using SPS was a success. This was confirmed with several characterisation techniques described in this Chapter, such as XRD, EDS, and XAS. The XRD analysis shows that all samples have remained in their cubic structure and that no new compounds have been formulated. The EDS maps show that there is clear definition between the metallic components of either the Mo or W with the ceramic YSZ material. No boundary regions between the two are present, which confirms that there has been no reaction between the two materials. The XANES data compared fabricated Mo samples with Mo samples at different oxide states. The XANES patterns show a clear match with the Mo metallic foil sample, confirming again that the Mo material in the fabricated samples remained metallic.

The benefit of fabrication using SPS over conventional sintering is the ability to use a lower sintering temperature, as well as a reduction in sintering time. This is mainly due to the axial pressure while the pellet sinters. However, it should be noted that time is still required after sintering to remove the graphite paper from the sample and some sample material is lost. The use of silicone lubricants was trialed to determine if this reduced the ability of the graphite paper to stick, but this trial was not successful and was determined to be ineffective for this research.

Two appropriate metallic materials were studied to determine if one is more beneficial than the other. Mo and W both have good thermal properties as well as relative high density compared to YSZ and UO<sub>2</sub>. For the intended purpose of a long life civil marine reactor, both of these properties are important. Testing showed that incorporating these metallic Mo and W in the simulant fuel material greatly improved the thermal conductivity of the pellets in both cases. With the three different loadings analysed, a YSZ 20 % Mo pellet would provide a sufficient

increase in the thermal conductivity by 100 % at 100°C, that the Chapter 3 fuel simulations showed would be beneficial for the life of the fuel. The YSZ pellets did increase in thermal conductivity and in some lower metallic loading cases >500°C the YSZ pellets had a higher thermal conductivity. This however is not of concern as the designed fuel for a civil marine reactor is expected to operate at centreline temperatures at <500°C. As well, with the intended use of using UO<sub>2</sub> fuel, which has a higher thermal conductivity than YSZ, when combined with metallic material to form cermets should provide a larger percentage increase in the thermal conductivity.

The higher loading of the metallic component resulted in a reduced hardness in the simulant fuel pellet. This was to be expected because metallic Mo and W have a lower hardness than the YSZ ceramic material. This is important for fuel conditions, such as when the fuel pellets come under stress and strain from swelling from fissions, or the hydrostatic forces in a PWR are applied onto the fuel rod. The hardness testing showed a clear difference in the results between the Mo and W simulant cermets, with the latter having a higher average Vickers hardness at each metallic loading content. This result will be important to consider in the future for further mechanical simulations that focus on the strain and stress on the pellet under reactor conditions.

One focus of investigation in this research was to determine what effect the sintering temperature has on the fabricated pellet. As discussed, the minimum temperature found to have a stable monolithic pellet was 1300°C, and 3 other temperatures of 1400°C, 1500°C, and 1600°C were tested. The density data for all compositions of simulant pellets provided no evidence to suggest that the temperature has any effect on the final density. Therefore, the biggest factor for the final density comes from the force used from pressing during the sintering process, and thus future fabrication would be able to use a lower sintering temperature to obtain a dense pellet. To note, the force of 16 kN used in the experiments was the maximum allowed for the die size used.

In summation, the first known systematic study on YSZ-Mo and YSZ-W simulants cermet at varying metallic content and sintering temperature using SPS has been successfully undertaken in this thesis. For the context of a civil marine reactor, the YSZ 20 % Mo cermet sample sintered at 1300°C is the most promising sample to be taken forward for further work. This is due to W for future being a higher cost than Mo and that there appears to be not much thermal advantage when compared with Mo.

## 5.10 References

- [1] O. Guillon, J. Gonzalez-Julian, B. Dargatz, T. Kessel, G. Schierning, J. Räthel, and M. Herrmann, "Field-assisted sintering technology/spark plasma sintering: Mechanisms, materials, and technology developments," *Adv. Eng. Mater.*, vol. 16, no. 7, pp. 830–849, 2014.
- [2] Z. a. Munir, D. V. Quach, and M. Ohyanagi, "Electric current activation of sintering: A review of the pulsed electric current sintering process," *J. Am. Ceram. Soc.*, vol. 94, no. 1, pp. 1–19, 2011.
- [3] R. Orrù, R. Licheri, A. M. Locci, A. Cincotti, and G. Cao, "Consolidation/synthesis of materials by electric current activated/assisted sintering," *Mater. Sci. Eng. R Reports*, vol. 63, no. 4–6, pp. 127–287, 2009.
- [4] S. Grasso, Y. Sakka, and G. Maizza, "Electric current activated/assisted sintering (ECAS): A review of patents 1906-2008," *Sci. Technol. Adv. Mater.*, vol. 10, no. 5, p. 053001, 2009.
- [5] D. M. Hulbert, A. Anders, D. V. Dudina, J. Andersson, D. Jiang, C. Unuvar, U. Anselmi-Tamburini, E. J. Lavernia, and A. K. Mukherjee, "The absence of plasma in 'spark plasma sintering,'" *J. Appl. Phys.*, vol. 104, no. 3, p. 033305, 2008.
- [6] D. M. Hulbert, A. Anders, J. Andersson, E. J. Lavernia, and A. K. Mukherjee, "A discussion on the absence of plasma in spark plasma sintering," *Scr. Mater.*, vol. 60, pp. 835–838, 2009.
- [7] S. Min, J. Blumm, and a. Lindemann, "A new laser flash system for measurement of the thermophysical properties," *Thermochim. Acta*, vol. 455, no. 1–2, pp. 46–49, 2007.
- [8] A. E. Giannakopoulos, P. L. Larsson, and R. Vestergaard, "Analysis of Vickers indentation," *Int. J. Solids Struct.*, vol. 31, no. 19, pp. 2679–2708, 1994.
- [9] M. C. Stennett, C. L. Corkhill, L. a. Marshall, and N. C. Hyatt, "Preparation, characterisation and dissolution of a CeO<sub>2</sub> analogue for UO<sub>2</sub> nuclear fuel," *J. Nucl. Mater.*, vol. 432, no. 1–3, pp. 182–188, 2013.

- [10] A. De Bremaecker, L. Ayrault, and B. Clément, “Deterioration of yttria-stabilized zirconia by boron carbide alone or mixed with metallic or oxidized Fe, Cr, Zr mixtures,” *J. Nucl. Mater.*, vol. 451, no. 1–3, pp. 153–161, 2014.
- [11] C. Garcia-Ostos, J. a. Rodriguez-Ortiz, C. Arevalo, J. Cobos, F. J. Gotor, and Y. Torres, “Fabrication and characterization of CeO<sub>2</sub> pellets for simulation of nuclear fuel,” *Nucl. Eng. Des.*, vol. 298, pp. 160–167, 2016.
- [12] R. E. Hoggan, L. D. Zuck, W. R. Cannon, and P. a. Lessing, “Processing of surrogate nuclear fuel pellets for better dimensional control with dry bag isostatic pressing,” *J. Nucl. Mater.*, vol. 482, pp. 34–41, 2016.
- [13] K. W. Schlichting, N. P. Padture, and P. G. Klemens, “Thermal conductivity of dense and porous yttria-stabilized zirconia,” *J. Mater. Sci.*, vol. 36, no. 12, pp. 3003–3010, 2001.
- [14] International Atomic Energy Agency, *Thermophysical properties of materials for nuclear engineering: A tutorial and collection of data*. IAEA, 2008.
- [15] J. J. Carbajo, G. L. Yoder, S. G. Popov, and V. K. Ivanov, “A review of the thermophysical properties of MOX and UO<sub>2</sub> fuels,” *J. Nucl. Mater.*, vol. 299, no. 2001, pp. 181–198, 2001.
- [16] C. G. S. G. S. Pillai and a. M. M. George, “Thermal conductivity of uranium dioxide,” *J. Nucl. Mater.*, vol. 200, no. 1, pp. 78–81, 1993.
- [17] R. C. O’Brien and N. D. Jerred, “Spark Plasma Sintering of W–UO<sub>2</sub> cermet,” *J. Nucl. Mater.*, vol. 433, no. 1–3, pp. 50–54, Feb. 2013.
- [18] J. H. Yang, K. W. Song, K. S. Kim, and Y. H. Jung, “A fabrication technique for a UO<sub>2</sub> pellet consisting of UO<sub>2</sub> grains and a continuous W channel on the grain boundary,” *J. Nucl. Mater.*, vol. 353, no. 3, pp. 202–208, Jul. 2006.
- [19] B. Mouawad, M. Soueidan, D. Fabrègue, C. Buttay, V. Bley, B. Allard, and H. Morel, “Full densification of molybdenum powders using spark plasma sintering,” *Metall. Mater. Trans. A*, vol. 43, no. 9, pp. 3402–3409, May 2012.
- [20] S. H. Lee, J. M. Park, and C. K. Kim, “Thermophysical properties of U–Mo/Al alloy dispersion fuel meats,” *Int. J. Thermophys.*, vol. 28, no. 5, pp. 1578–1594, Jun. 2007.
- [21] G. Bernard-Granger and C. Guizard, “Spark plasma sintering of a commercially available granulated zirconia powder: I. Sintering path and hypotheses about the mechanism(s) controlling densification,” *Acta Mater.*, vol. 55, no. 10, pp. 3493–3504, Jun. 2007.
- [22] G. Bernard-Granger, N. Monchalain, and C. Guizard, “Comparisons of grain size-density trajectory during spark plasma sintering and hot-pressing of zirconia,” *Mater. Lett.*, vol. 62, no. 30, pp. 4555–4558, Dec. 2008.

- [23] X. . Chen, K. . Khor, S. . Chan, and L. . Yu, "Preparation yttria-stabilized zirconia electrolyte by spark-plasma sintering," *Mater. Sci. Eng. A*, vol. 341, no. 1–2, pp. 43–48, Jan. 2003.
- [24] R. C. O'Brien, R. M. Ambrosi, N. P. Bannister, S. D. Howe, and H. V. Atkinson, "Spark plasma sintering of simulated radioisotope materials within tungsten cermets," *J. Nucl. Mater.*, vol. 393, no. 1, pp. 108–113, 2009.
- [25] Matweb, "Yttria stabilised zirconia, YSZ," 2016. [Online]. Available: <http://www.matweb.com/search/DataSheet.aspx?MatGUID=4e3988dd9adb4d1ca37a1b2cbab87d9a>.
- [26] Engineering Tool Box, "Metals and Alloys - Densities," 2016. [Online]. Available: [http://www.engineeringtoolbox.com/metal-alloys-densities-d\\_50.html](http://www.engineeringtoolbox.com/metal-alloys-densities-d_50.html).
- [27] E. A. Brandes and G. B. Brook, *Smithells Metal Reference Book*, 7th ed. Oxford: Butterworth-Heinemann, 1992.
- [28] Matweb, "Molybdenum, Mo, Annealed," 2016. [Online]. Available: <http://www.matweb.com/search/DataSheet.aspx?MatGUID=ef57c33963404798ad0301a05692312a>.
- [29] Matweb, "Tungsten, W," 2016. [Online]. Available: <http://www.matweb.com/search/DataSheet.aspx?MatGUID=41e0851d2f3c417ba69ea0188fa570e3>.
- [30] G. Bernard-Granger, A. Addad, G. Fantozzi, G. Bonnefont, C. Guizard, and D. Vernat, "Spark plasma sintering of a commercially available granulated zirconia powder: Comparison with hot-pressing," *Acta Mater.*, vol. 58, no. 9, pp. 3390–3399, May 2010.
- [31] G. Bernard-Granger, C. Guizard, S. Surblé, G. Baldinozzi, and a. Addad, "Spark plasma sintering of a commercially available granulated zirconia powder—II. Microstructure after sintering and ionic conductivity," *Acta Mater.*, vol. 56, no. 17, pp. 4658–4672, Oct. 2008.
- [32] K. Rajeswari, M. B. Suresh, U. S. Hareesh, Y. S. Rao, D. Das, and R. Johnson, "Studies on ionic conductivity of stabilized zirconia ceramics (8YSZ) densified through conventional and non-conventional sintering methodologies," *Ceram. Int.*, vol. 37, no. 8, pp. 3557–3564, Dec. 2011.
- [33] D. Hara, H. Ikuta, Y. Uchimoto, and M. Wakihara, "Electrochemical properties of manganese vanadium molybdenum oxide as the anode for Li secondary batteries," *J. Mater. Chem.*, vol. 12, no. 8, pp. 2507–2512, 2002.
- [34] Y. J. Tu, C. F. You, C. K. Chang, T. S. Chan, and S. H. Li, "XANES evidence of molybdenum adsorption onto novel fabricated nano-magnetic  $\text{CuFe}_2\text{O}_4$ ," *Chem. Eng. J.*, vol. 244, pp. 343–349, 2014.
- [35] Kyong Jun An, "Assessment of the Thermal Conductivity of Yttria-Stabilized Zirconia Coating," *Mater. Trans.*, vol. 55, no. 1, pp. 188–193, 2014.

- [36] D. E. Gray, *American Institute of Physics Handbook*. New York: McGraw-Hill Book Company, 1957.
- [37] G. A. Gogotsi, S. N. Dub, E. E. Lomonova, and B. I. Ozersky, "Vickers and knoop indentation behaviour of cubic and partially stabilized zirconia crystals," *J. Eur. Ceram. Soc.*, vol. 15, no. 5, pp. 405–413, 1995.

## **Chapter 5 Fuel pellet simulation**

## **5.1 Introduction**

This Chapter analyses the data obtained with the simulation software ANSYS Mechanical. These simulations consider what effect the geometry of the metallic component of a cermet has on the heat transfer. The motivation was to understand if thermal efficiency gains could be obtained with the same percentage of metallic fuel in different orientations.

The simulations in this Chapter will help to choose the optimal concept for the orientation of the metallic component for cermet fuels to be fabricated via SPS. Several assumptions have been made in the simulation of these different cermet fuels in order to produce a set of predictions that can be easily compared under the same conditions. The main question to be answered is which geometric arrangement is the most thermally efficient and would be advantageous to be used in a fuel type for a civil marine reactor.

### **5.1.2 ANSYS software**

ANSYS Mechanical is an engineering finite element analysis (FEA) software tool that is able to model thermal transfer, fluids and structural analysis, as well as others with different software packages [1]. However, only thermal analysis was carried out in the simulations for this work.

The software utilises a model of the system under study generated in either 2D or 3D perspective. Once this model has been created, a mesh can then be applied to it. This is a series of shapes that are termed elements that cover the surface or volume of the generated model and define the material properties for it. When the software conducts the simulations, it calculates the conditions in each element by solving the relevant second order differential equations to find an approximate value [2]. Having a finer mesh, and therefore more elements, will generate a more detailed approximation. This is particularly useful in areas of high interest in a model

such as the boundary of different materials. However in a large complex model this has to be weighed up against the computing power available.

An example of meshing conducted in this study is shown in Figure 5.1. Images A and B are in reference to a pellet that is of one complete material and so the meshing is very uniform. Images C and D have two materials present, one material making the bulk of the pellet and the second material located in the circle shapes. When the same mesh setting are applied, more elements are generated especially in the interaction area between the two materials.

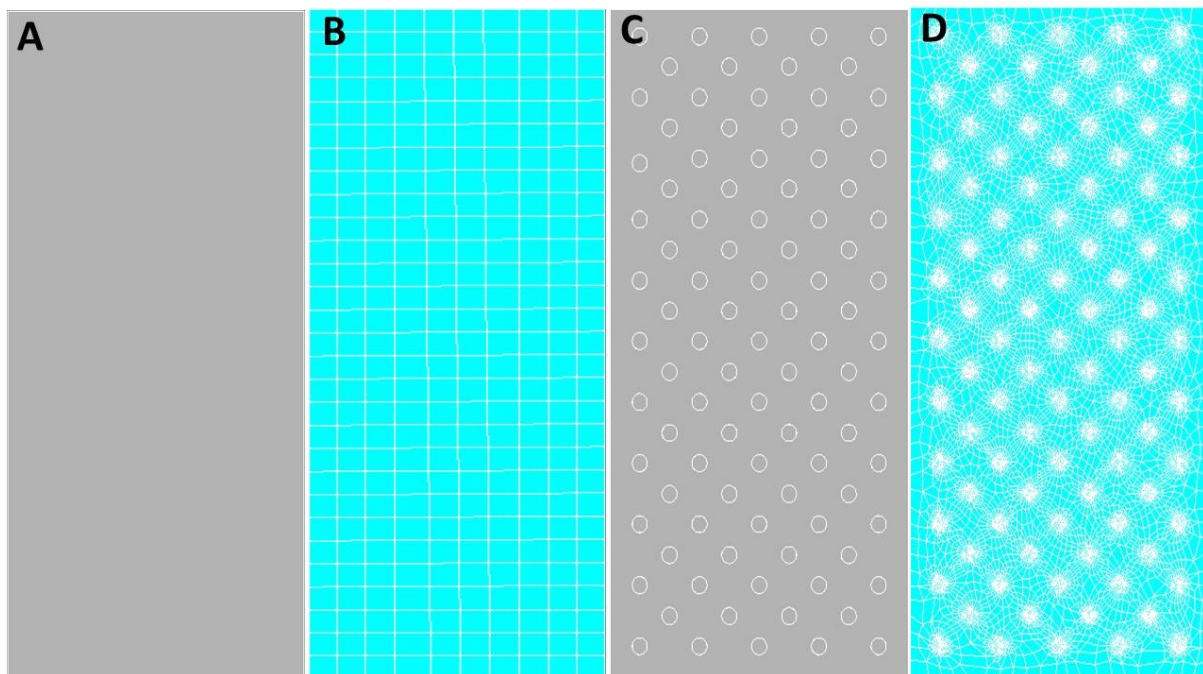


**Figure 5.1 – Example of meshing used in Ansys; A – Pellet of one material, B – Mesh applied to pellet in A, C – Pellet with two different materials, D – Mesh applied to pellet shown in C.**

In the simulations produced in this Chapter, ANSYS models have been generated with reference to only the thermal conditions, with heat being generated and conducted across the model. As the heat moves from each element, the material properties specified will be used to determine the approximation of the temperature at the boundary conditions of that element,

move to the next element, and so on, until all elements have been calculated. The temperature is then determined across the model and can be mapped.

The ANSYS Mechanical software tool was chosen for several reasons. Firstly, it has been used in a wide array of ways for research with nuclear aspects and is therefore familiar to the industry. These include areas such as creating thermal mechanical models of helium cooled pebble bed reactors [3] and in the thermal analysis of nuclear waste containers in different geological conditions [4]. Secondly the access and licencing was easier to obtain for this work than compared with a similar finite element software such as ABAQUS. There have been comparative studies between ANSYS and ABAQUS [2] that show negligible difference in the precision of the two packages in problems of this type, with the only negatives for ANSYS being a slower simulation time and larger file size. For this work these issues are not a concern.

The second order differential equations used in ANSYS are based on the Sturm-Liouville theory which is used to determine the condition inside an element given initial boundary conditions:

$$\frac{d}{dx} \left[ p(x) \frac{dy}{dx} \right] + q(x)y = -\lambda w(x)y,$$

The simulations carried out focus on the thermal analysis of each pellet with no stress or strains considered, for simplification. In ANSYS, the thermal analysis for this work is regarding heat transfer by conduction which is governed by Fourier's Law, with equation:

$$[K(T)]\{T\} = \{Q(T)\}$$

Here K is the thermal conductivity value of the material which is temperature dependant and Q is the heat flux, also temperature dependant.

The convection is also modelled from the fuel pellet wall to external ambient condition, which in ANSYS is governed by the following:

$$q = hA(T_{Surface} - T_{Ambient})$$

Here  $q$  is the convection heat flux,  $h$  is the film coefficient,  $A$  the surface area and in brackets the difference in temperature between the surface and ambient conditions.

### 5.1.3 Shape of pellet materials

Fabricating nuclear cermet fuel pellets with regards to the shape of the particles has been previously studied in some regards. In studies of W-UO<sub>2</sub> cermet fuel, it was found that the thermal conductivity of fuel can be affected by the geometry of the particles, as well as the grain size [5]. Sudhir Mishra et al. investigated the thermal properties of uranium metal-uranium oxide cermet, with two different compositions studied, highlighting the differences in the morphology of spherical particles for the metal and irregular shaped particles for the uranium oxide, but no conclusion if the effect of the shape of the particles had a role in the thermal conductivity improvement [6]. Particle size has been an interest with regards to thermal conductivity in nanofluids, with one study investigating graphene oxide with increasing particle size determined that thermal conductivity increased with particle size [7].

However, little work has been focused on novel ways into the shape and distribution of the metallic component in a cermet. This is where this study aims to identify how to distribute the metallic material in a cermet to improve the thermal conductivity.

Different designs that were analysed as part of this work considered large spherical metallic particles evenly distributed across the cermets, strips of metal, using a grid layout and then having the metallic component as a separate component to the ceramic as a disk. These concepts were chosen to compare designs that would have an easier fabrication route whilst providing large thermal conductivity increases.

#### 5.1.4 Material information for simulations

The same simulant fuel materials that were used in Chapter 4 for the SPS fabrication have been used to conduct the FEA simulations. Input material properties, Table 5.1, have been obtained from experimental data obtained in Chapter 4 at room temperature, the powder densities of the materials that were used and the average of four YSZ samples used for the thermal conductivity. An assumption made is that these values are not variable and remain constant at different temperatures, this was done to reduce the simulation size as all materials used in this work have a decreasing thermal conductivity in the temperature range used, and so a similar behaviour exhibited in these results would be expected in reality. Thermal conductivity values for Mo and W were taken from literature.

**Table 5.1 – Material properties used for FEA simulation**

Material	Thermal conductivity [w/mK]	Density [g/cm <sup>3</sup> ]
YSZ	3.46	5.867
Molybdenum	138 [8]	10.517
Tungsten	169 [8]	19.424

YSZ has been chosen as a simulant fuel type for these simulations in order to be able to tie the work of Chapter 4 together with simulations looking at using UO<sub>2</sub>. As discussed in Chapter 4, YSZ and UO<sub>2</sub> have the same crystal fluorite face centre cubic structure. Also YSZ has been used as a simulant material in the past for UO<sub>2</sub> [9] [10]. The thermal conductivity in ambient conditions for UO<sub>2</sub> is reported to be between 7.5-8.5 w/mK [11], [12], [13] and accepted density of 10.97 g/cm<sup>3</sup> [5]. Therefore, both of these material properties are higher in value than YSZ, Table 5.1, and so the results of the simulation work here will show that when applied to a UO<sub>2</sub> scenario that they have improved bulk thermal conductivity across a cermet compared to a YSZ scenario. This is discussed further in the conclusion section of this Chapter.

By choosing YSZ as an  $\text{UO}_2$  surrogate for this computational study, future experimental investigation will be able to easily verify the conclusion without the use of active materials. This would reduce the scope of future development to focus on all the most promising concepts for  $\text{UO}_2$  studies and associated modelling.

## **5.2 Reference simulation and setup**

The first simulation carried out was conducted on a pure YSZ pellet. This was done in order to have a reference simulation to compare to. All simulation setup and assumptions discussed here are carried out through the rest of the simulations.

2D simulations were carried out on a cross section of a pellet. The pellet was simplified to a 1 cm height, 0.5 cm radius and half symmetry was used of the cross section of the pellet. This was done for two reasons. Firstly, the heat generation was assumed to be from just the core of the pellet at  $500^\circ\text{C}$ , shown in Figure 5.2. This in practice would not be the case as heat generation occurs across the pellet where fissions takes place, with the thermal neutron flux distribution being a proportional relationship to the heat generation [14]. However, for a method of determining the heat conduction from one side of the pellet to the other, this was a useful approach. Secondly, the effects on one side of the fuel pellet will ideally be mirrored on the other by virtue of symmetry, so working with half the volume element would reduce the model size, in modelling this is usually taken advantage of [15]. This was helpful especially on smaller metallic components when it came to the mesh generation, which required computing power to do. The meshing of each pellet, a quadratic element, was applied to all models with a smart size of 4.

With heat generation being provided from the centre of the pellet, the outside wall was assumed, for simplification, to be in contact with ambient room temperature at  $30^\circ\text{C}$ , rather than a liquid PWR coolant, as in Chapter 3, which has an inlet temperature of  $280^\circ\text{C}$ ; the top

and bottom sides of the pellet were assumed to have closed boundary conditions with no heat transfer. This was done to determine the effectiveness of heat transfer from one side of the pellet to the other. In a nuclear fuel rod, pellets are normally stacked one on top of each other and heat is dissipated radially towards the fuel rod wall. Other simulation work has used radial heat in their models [16]. The material of the pellet was assumed to have initial conditions at 30°C.

For these simulations, plane55 element type in ANSYS was chosen as it provides a four node element with one degree of freedom of temperature at each node [17], it is used for thermal conduction in 2-D. With thermal properties being the only analysis being conducted, this was a suitable choice. Simulations were run until steady state conditions were achieved.

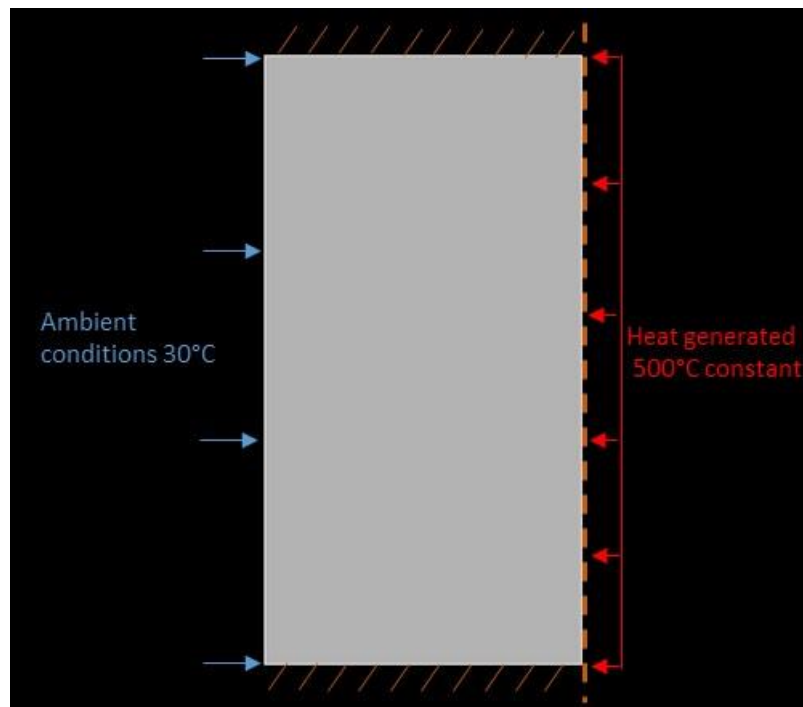


**Figure 5.2 – Representation of a 2D half axis of symmetry YSZ pellet in ANSYS for thermal simulation.**

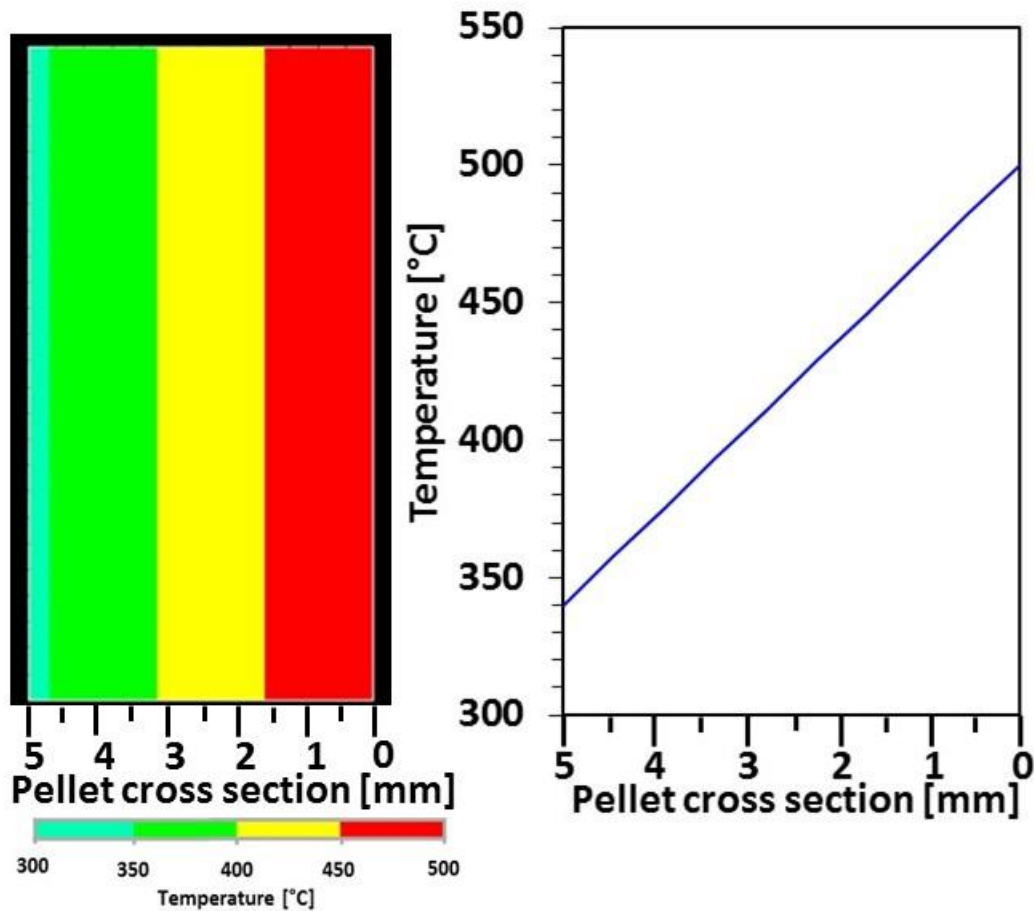


**Figure 5.3 – 2D simulation of YSZ pellet at steady state conditions with contour plot and plot of the temperature gradient across the pellet.**

The simulation for the YSZ pellet was conducted and Figure 5.3 shows the temperature gradient across the pellet. As with the assumptions made for the simulation, a uniform temperature gradient is achieved across the pellet, with a temperature drop of 161°C from the heat generation of 500°C to the outer wall of 339°C.

This reference simulation is used to compare the cermet pellet simulations to the temperature gradient across the pellet to ascertain the effectiveness of each.

### **5.3 Fuel pellet with Mo spherical particles**

The next set of three simulations considered using spherical particles of Mo evenly distributed across the pellet at different percentages of area of the pellet. The ability to fabricate particles

of consistent spherical size is a process already understood by different techniques [18], [19], and therefore, would not require a large amount of research and development to produce. As discussed, the simulated pellet bulk material is of YSZ, with metallic addition to form a cermet, for clarity, all proceeding pellet simulations will be in reference to their shape and metallic content.

### 5.3.1 Spherical 10 % Mo

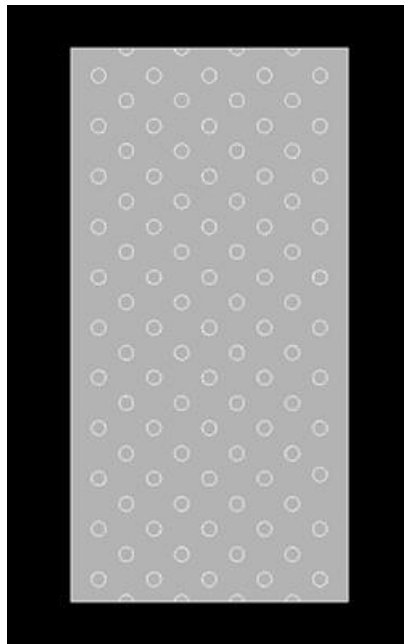


**Figure 5.4 – Representation of a 2D half axis of symmetry spherical 10 % Mo evenly distributed in ANSYS for thermal simulation.**

Mo spherical particles were distributed evenly at 10 % content as shown in Figure 5.4. These particles have a radius of 1.2 mm which represent a particle more like a ball bearing.

The simulation results are represented in Figure 5.5. The effect of having the metallic component of Mo with a higher thermal conductivity than the YSZ can clearly be seen. A wave effect of the temperature gradient is observed as it transfers across the pellet and through the Mo. This wave effect is due to the spheres having the higher thermal conductivity than the bulk YSZ material. The temperature differential of 140°C, an improvement of 5.7 %, is observed

across the pellet which confirms, as expected, an improved conduction over the pure YSZ material.

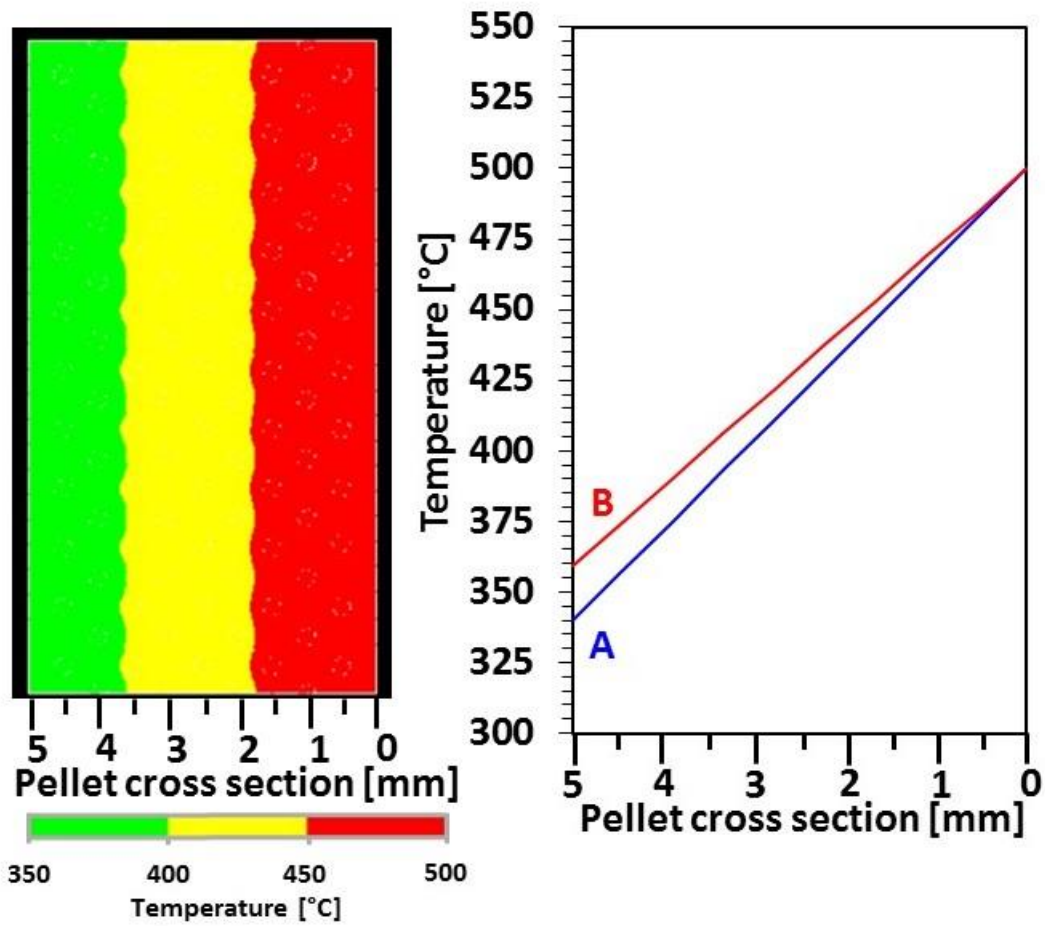


**Figure 5.5 – 2D simulation of spherical 10 % Mo at steady state conditions and temperature gradient plot of A – pure YSZ pellet, B – spherical 10 % Mo pellet.**

### 5.3.2 Spherical 20 % Mo

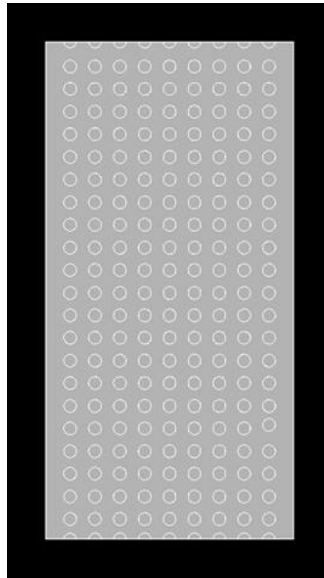


Figure 5.6 – Representation of a 2D half axis of symmetry spherical 20 % Mo evenly distributed in ANSYS for thermal simulation.

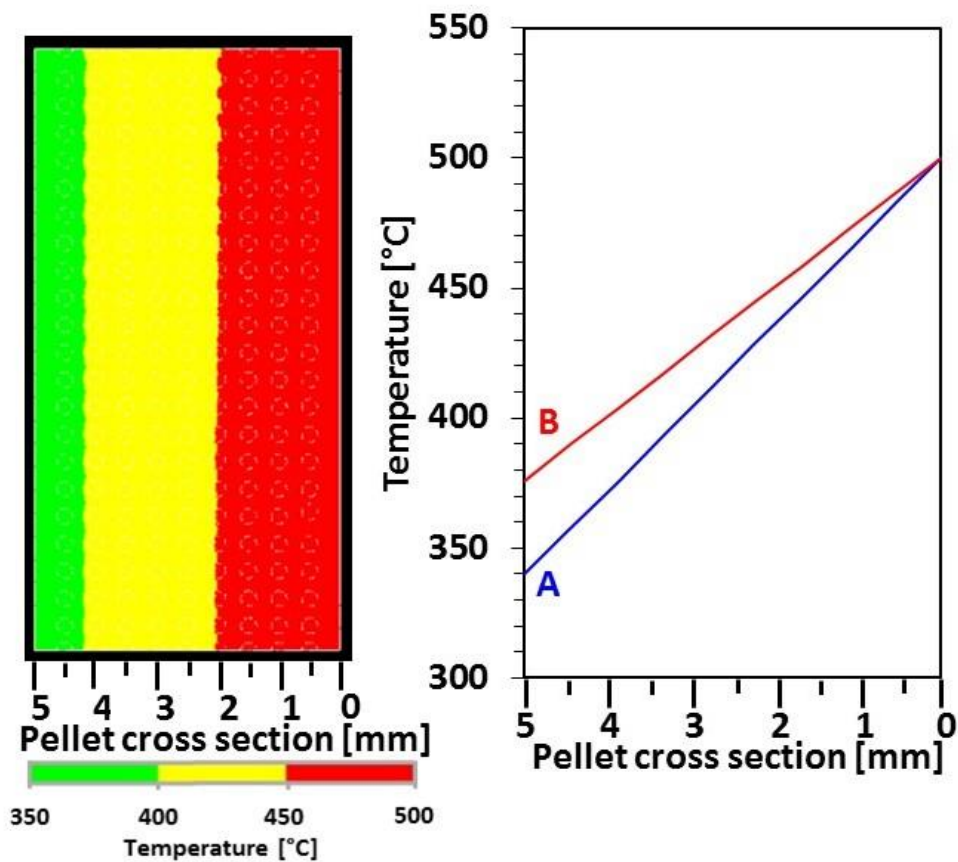


Figure 5.7 – 2D simulation of spherical 20 % Mo at steady state conditions and temperature gradient plot of A – pure YSZ pellet, B – spherical 20 % Mo pellet.

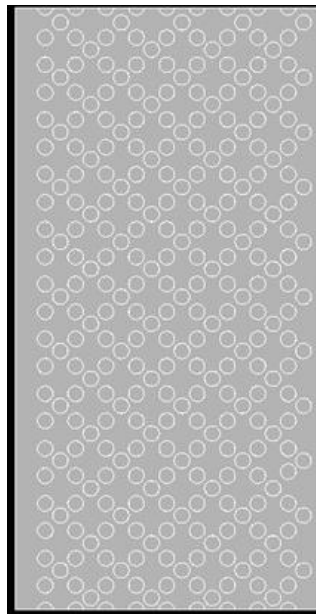
A spherical 20 % Mo particle cement generated in ANSYS, Figure 5.6, visualises that the particles were distributed uniformly and similar to the spherical 10 % Mo pellet with the same radius of 1.2 mm.

The results from this simulation, Figure 5.7, show a similar distribution of temperature in a wave appearance as the spherical 10 % Mo pellet. With a temperature differential of 124°C observed across the pellet it gives a 10.7 % improvement, over the spherical 10 % Mo pellet.

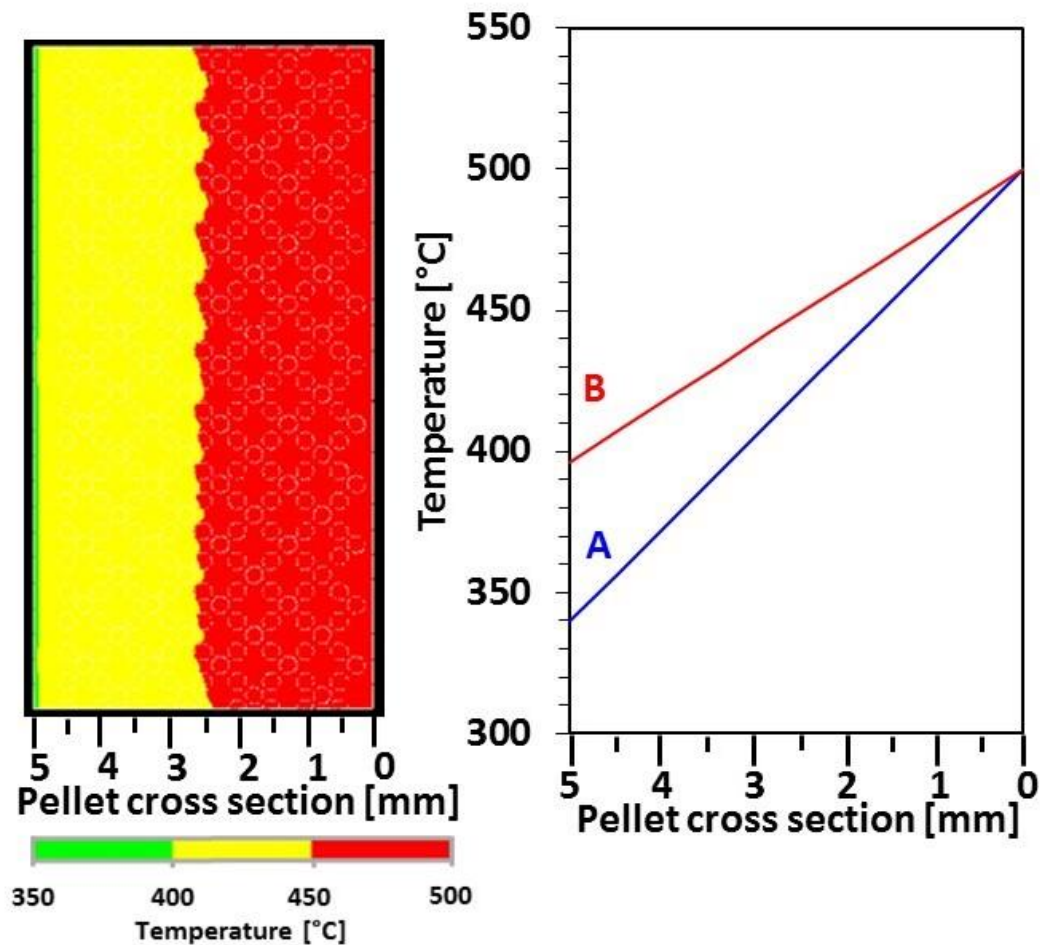
### 5.3.3 Spherical 30 % Mo

Figure 5.8 shows the layout for the cermet with 30 % Mo content as spherical particles with the same radius of 1.2 mm as for the 10 % and 20 % studies. Care was taken to make sure that no particles were touching and that each one was surrounded by the bulk ceramic YSZ.

The heat distribution, Figure 5.9, obtained from the simulation shows a more pronounced wave effect than the spherical 10 % Mo and 20 % Mo simulations due to the higher Mo content in the sample. A temperature gradient across the sample of 103°C was achieved, resulting in a 16.6 % increase in thermal conductivity compared with the YSZ pellet.



**Figure 5.8 – Representation of a 2D half axis of symmetry spherical 30 % Mo evenly distributed in ANSYS for thermal simulation.**



**Figure 5.9 – 2D simulation of spherical 30 % Mo at steady state conditions and temperature gradient plot of A – pure YSZ pellet, B – spherical 30 % Mo pellet.**

### 5.3.4 Summary

All three spherical Mo pellet simulations show an improvement on the thermal conductivity when compared with the reference sample of 5.7 %, 10.7 %, and 16.6 % efficiency increase for the spherical 10 % Mo, 20 % Mo, and 30 % Mo pellet simulations respectively. For the 30 % Mo simulation the temperature increase on the outside wall was 56.5°C when compared with the YSZ pellet. With reference to Figure 5.9, the temperature gradient is shallower for the spherical 30 % Mo pellet than the YSZ, which would lower the thermal stress across the pellet. In an actual nuclear fuel case, this would allow the pellet to be run cooler at a lower power

rating, which would help extend the life of the pellet, as the total temperature generation need not be as high to the YSZ pellet in order to dissipate the heat to the outside wall.

## **5.4 Fuel pellet with W spherical particles**

The three model layouts for the spherical 10 %, 20 %, and 30 % Mo simulations were used for the same loading content of W. This was done in order to determine the effect of having a metallic material with a higher thermal conductivity, Table 5.1, relative to the Mo simulations.

### **5.4.1 Spherical 10 % W**

Simulation for the spherical 10 % W pellet is shown in Figure 5.10. The thermal transfer across the pellet occurs in the same way as the spherical 10 % Mo pellet. The temperature at the outer wall was 359°C, this was identical to the case of the 10 % Mo pellet, and shows that there is no improvement achieved in using W. This is interesting, as the thermal conductivities of W and Mo are 173 W/mK and 138 W/mK respectively. Both values are much higher than the bulk YSZ material of 3.46 W/mK and so it appears that the metallic material has an impact in the thermal transfer, but is possibly limited by the lower thermal conductivity of the bulk YSZ material.

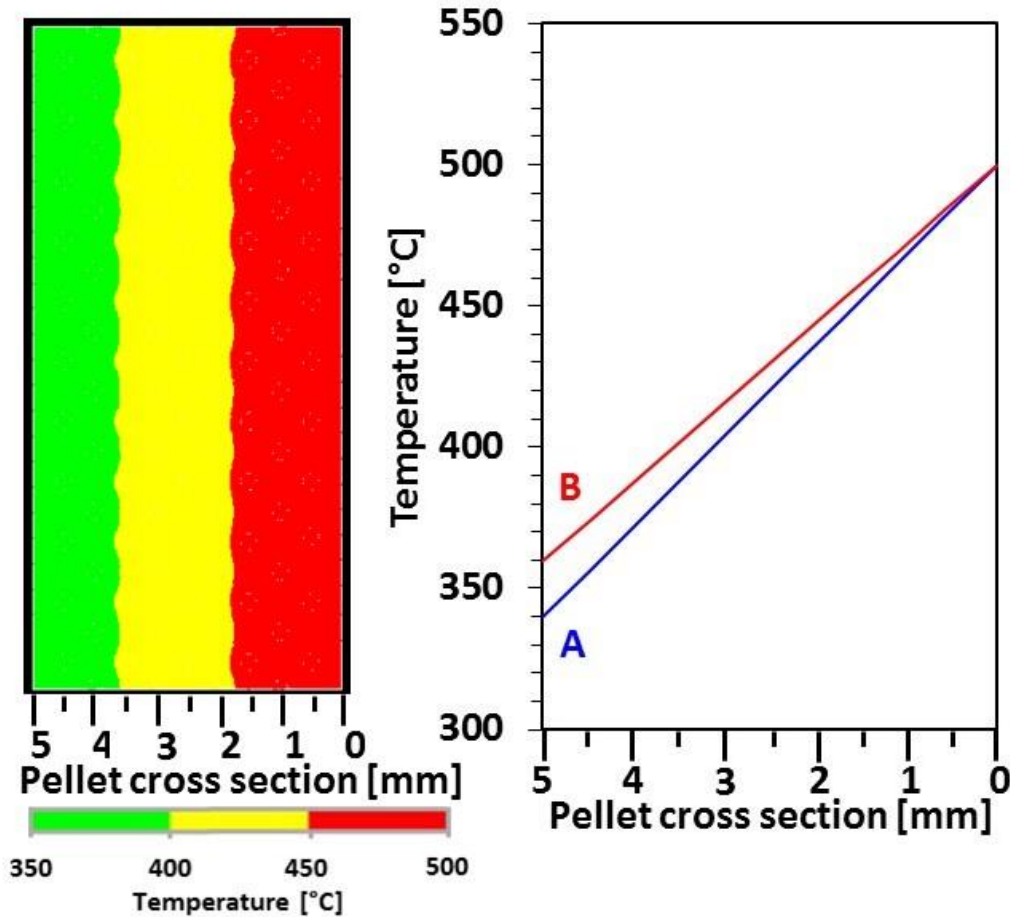


**Figure 5.10 – 2D simulation of spherical 10 % W at steady state conditions and temperature gradient plot of A – pure YSZ pellet, B – spherical 10 % W pellet.**

#### **5.4.2 Spherical 20 % W**

The spherical 20 % W simulation results, Figure 5.11, show a similar pattern to that of the spherical 20 % Mo simulation with the same wave thermal transfer across the pellet brought upon by the spherical metallic particles. This was identical again with the spherical 20 % Mo simulation, 376°C and 376°C wall temperatures for the spherical 20 % W and spherical 20 % Mo simulations respectively; with a 10 % increase in metallic loading, no improvement is achieved with the W. Across the spherical 20 % W and 20 % Mo pellets the midway temperatures are 431°C and 431°C and quarter way 458°C and 458°C respectively. This shows that across the pellet with regards to the bulk thermal conductivity, there appears to be no

advantage of utilising W over Mo, even though they are setup with their relative thermal conductivities shown in Table 5.1.

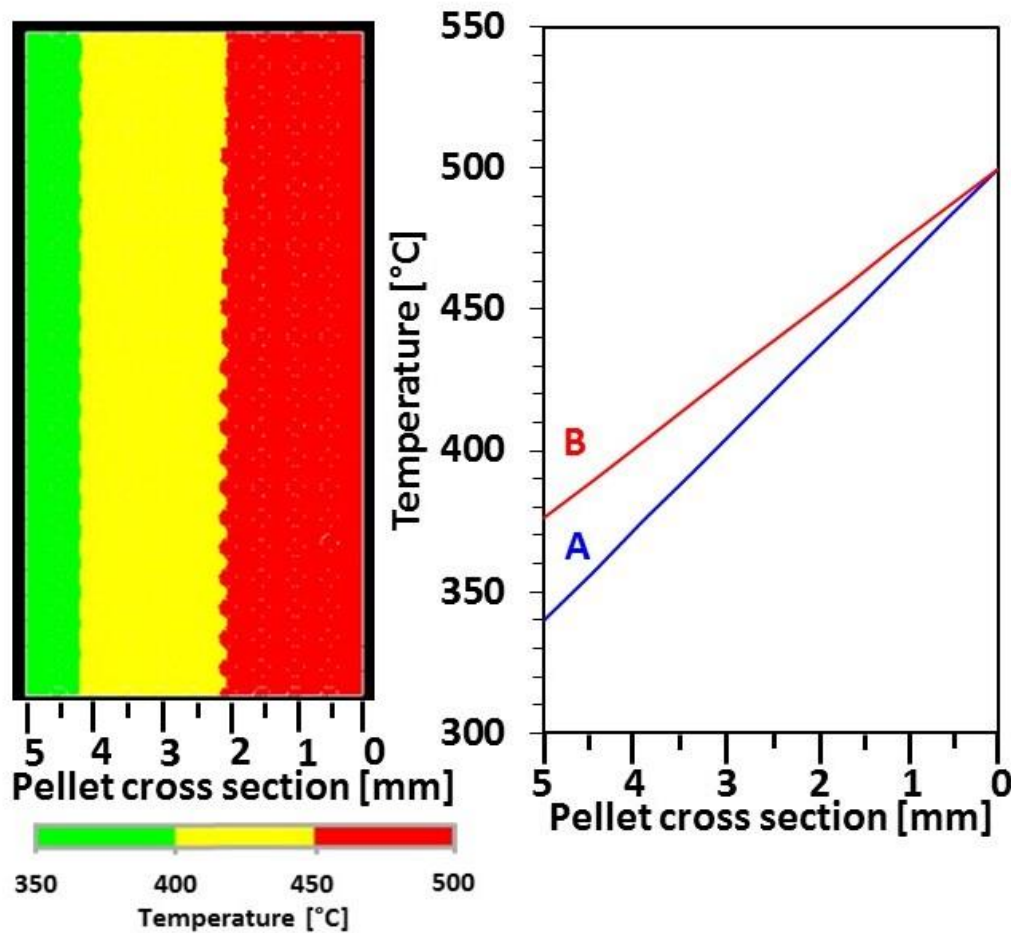


**Figure 5.11 – 2D simulation of spherical 20 % W at steady state conditions and temperature gradient plot of A – pure YSZ pellet, B – spherical 20 % W pellet.**

#### 5.4.3 Spherical 30 % W

The simulation for spherical 30 % W pellet was carried out with the results shown in Figure 5.12. Again compared with the spherical 30 % Mo pellet, the temperature gradients are both similar as the layout of the metallic components are the same. The pellet wall, midway and quarter way temperatures of 398°C, 443°C and 465°C respectively being similar for both the spherical 30 % W and spherical 30 % Mo pellets.

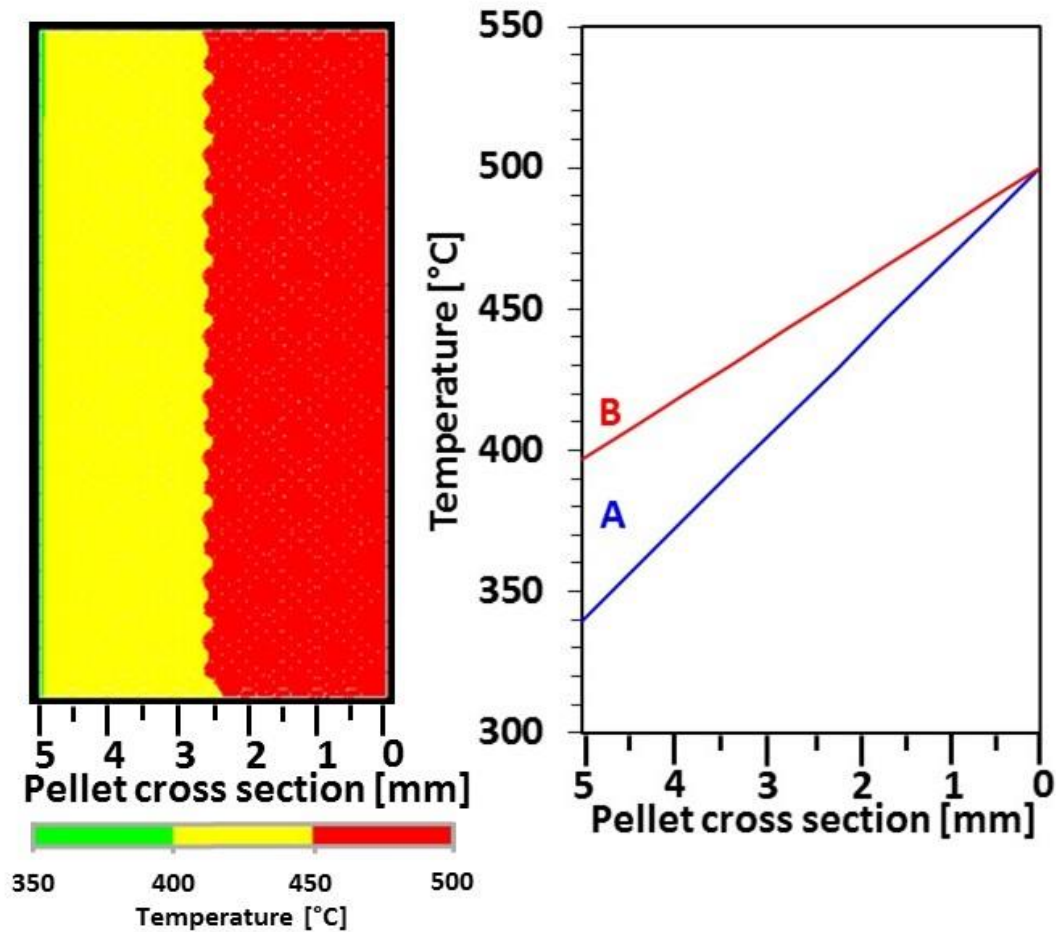


**Figure 5.12 – 2D simulation of spherical 30 % W at steady state conditions and temperature gradient plot of A – pure YSZ pellet, B – spherical 30 % W pellet.**

#### 5.4.4 Summary

The results of the three spherical W loading pellets have been compared against the three spherical Mo loading pellets. It has been shown that there is no perceivable benefit using the W material over the Mo with regards to the overall thermal conductivity of the pellet. This has been reasoned that due to the bulk material of YSZ having a much lower thermal conductivity, it nullifies the advantage provided from using metallic components of high thermal conductivity value and therefore appears to dominate the thermal conductivity of the system.

It is proposed that the advantage from the metallic thermal conductivity has a value that reaches a plateau effect for the overall thermal conductivity for the pellet. This value would be below the thermal conductivity of W and could be determined by doing iterations of simulations as discussed above. However, the investigative scope is merely focused on Mo and W materials and so would be carried out in future work.

Mo has a lower thermal conductivity than W, but if they are to be considered the same in these simulation cases, then looking at cost, Mo recently has averaged at \$7/lb [20] compared to W at \$20/lb [21]. Therefore in this situation, Mo would be more favourable to use.

## **5.5 Fuel pellet with 20 % Mo metallic in different designs**

This section of research focused on simulations in which the shape of the metallic component was changed while keeping constant the metallic material as Mo and the loading content as 20 %. These conditions were selected as it appears from the previous spherical 20 % Mo simulation there is a significant improvement of 10.6 % in the thermal conductivity of the pellet, while keeping the fissile material high, in this case with YSZ as a surrogate.

### **5.5.1 Horizontal strips**

This first simulation, keeping the Mo content at 20 % by area of the pellet, considered using cuboid shapes as the metallic content in a horizontal orientation relative to the pellet central axis. From a manufacturing point of view, it is deemed that the fabrication of uniform metallic cuboids would not pose a high level of difficulty, but evenly distributing them would require some more thought. Here the model, Figure 5.13, has the strips, of size 4 mm x 0.6 mm, in a uniformly distributed pattern with no metal strip touching another.

The results of the simulation are shown in Figure 5.14. Here, a uniform pattern of thermal transfer can be observed across the pellet. The first point of interest, is that compared with the

YSZ pellet, there is a 14 % increase in bulk thermal conductivity across the pellet, with pellet wall temperatures of 340°C and 394°C for the reference and horizontal strips pellets respectively.

Also of note, when the horizontal strips pellet is compared with the spherical 30 % Mo pellet, the results are very similar with only a 2°C pellet wall temperature difference. This is most likely due to the orientation of the strips in the direction of travel of the thermal transfer providing a network across the pellet.

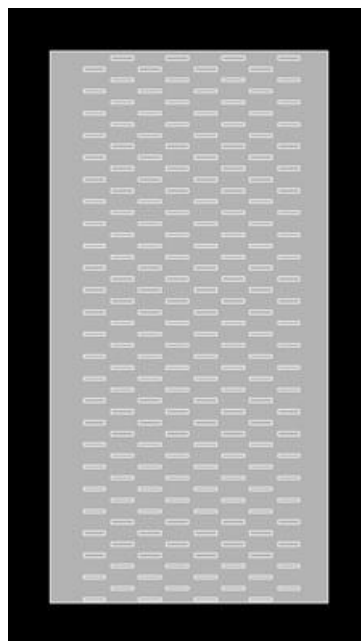


**Figure 5.13 – Representation of a 2D half axis of symmetry YSZ pellet with horizontal 20 % Mo strips evenly distributed in ANSYS for thermal simulation.**

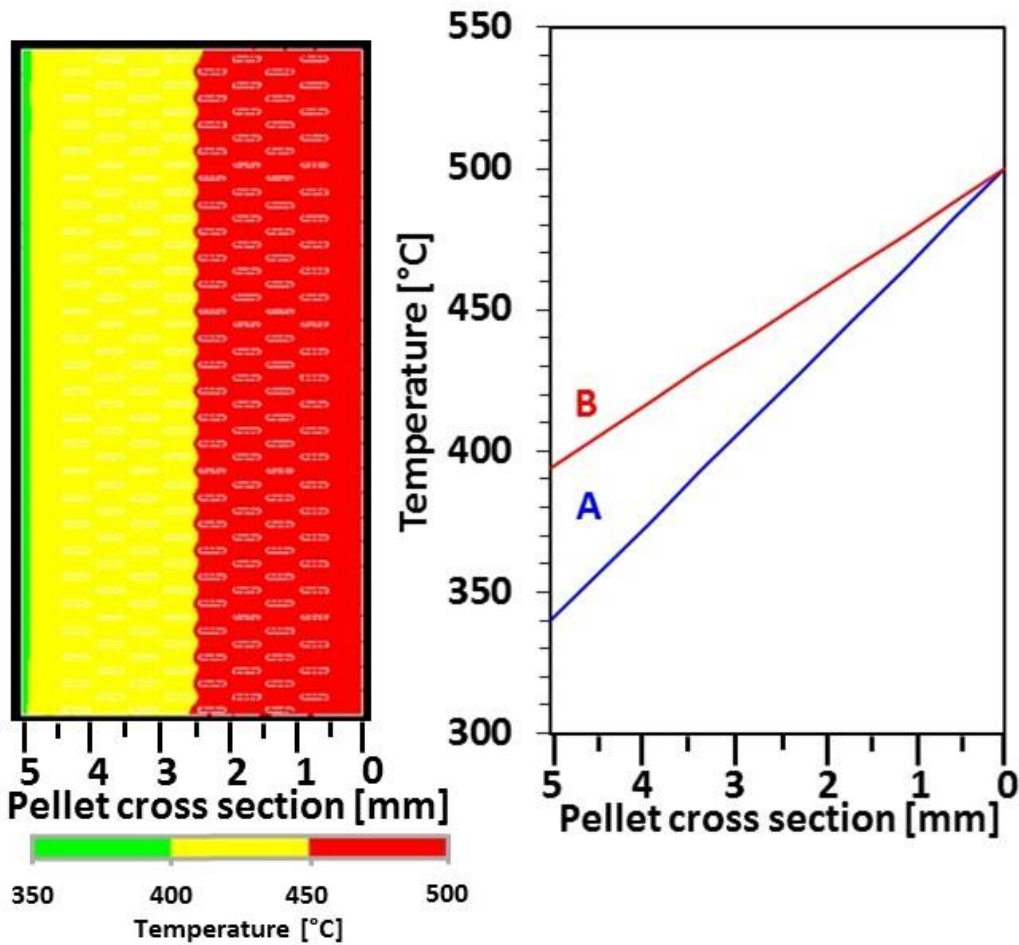


**Figure 5.14 – 2D simulation of horizontal 20 % Mo strips at steady state conditions and temperature gradient plot of A – pure YSZ pellet, B – horizontal 20 % Mo strips pellet.**

### 5.5.2 Vertical strips

The layout scenario of 0.04 mm x 0.6 mm horizontal strips was orientated 90° to the vertical direction, to compare and contrast the differences between the two. Again, the same area of Mo of 20 % was used with the layout remaining uniform and separation between each of the strips.

The simulation results are shown in Figure 5.16. The increase in bulk thermal conductivity on the pellet wall is only 3 % when compared with the YSZ pellet, this is a low increase when compared with other simulations previously discussed.

There is a stark difference with the vertical orientation pellet in comparison with the horizontal pellet, with outer wall temperatures of 353°C and 394°C respectively. The heat transfer pattern, Figure 5.16, is arguably straight between each temperature contour, when compared with the horizontal simulation which has the more pronounced wave effect, due to more thermally efficient material in the direction of heat transfer. This gives more evidence to confirm that having the metallic loading orientated in the direction of travel of the heat transfer is of huge benefit; in this case a 10 % difference between the horizontal and vertical.

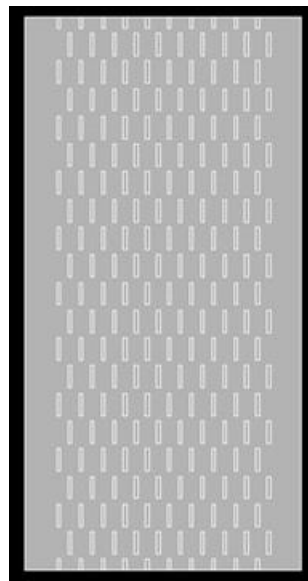


**Figure 5.15 – Representation of a 2D half axis of symmetry YSZ pellet with vertical 20 % Mo strips evenly distributed in ANSYS for thermal simulation.**

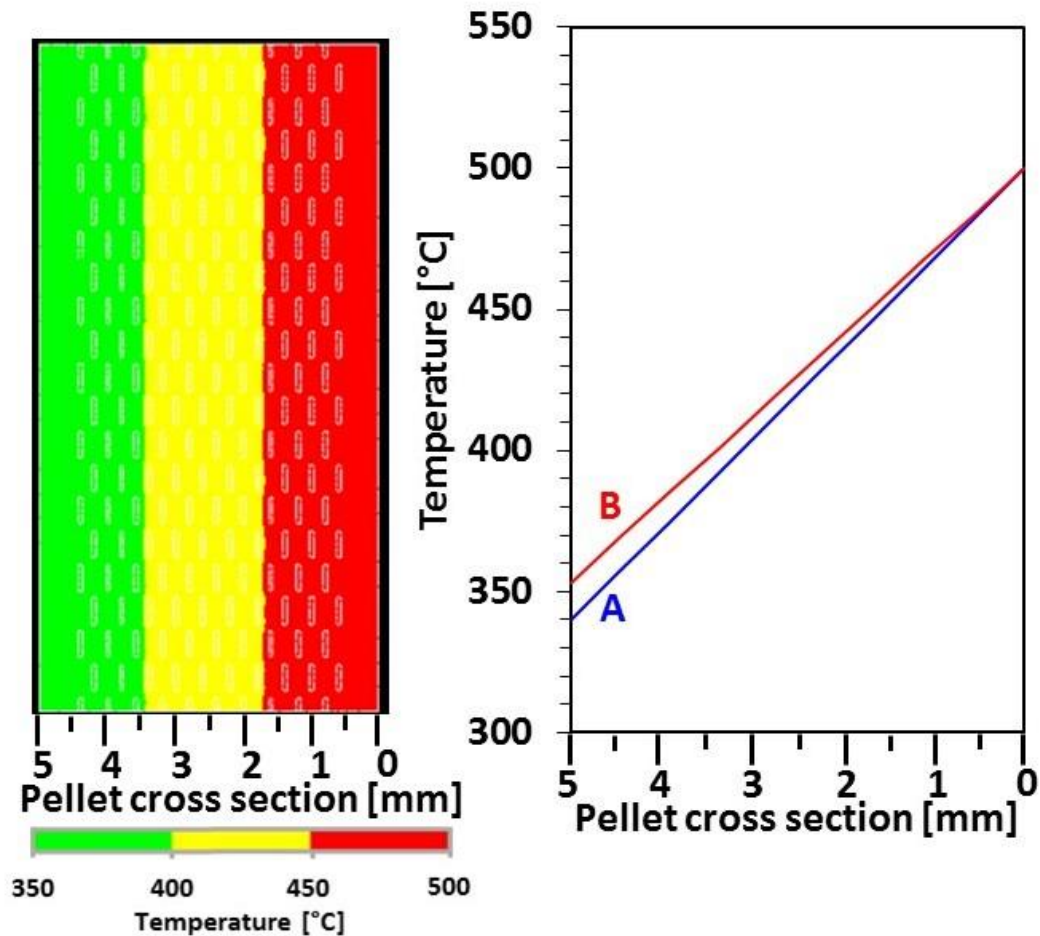


**Figure 5.16 – 2D simulation of vertical 20 % Mo strips at steady state conditions and temperature gradient plot of A – pure YSZ pellet, B – horizontal 20 % Mo strips pellet.**

### 5.5.3 Disk spacers

A way in which manufacturing a cermet pellet without the complication of having to uniformly position the metallic component would be very advantageous. What is proposed in this simulation is to have a complete fuel pellet with metallic disks top and bottom or, simply, as spacers between each fuel pellet in a rod. Technically, this would not count as a cermet as the fuel and metal components are separate to each other in the fuel rod.

For this simulation, Mo was used as the material for the disks. In effect, each disk is 10 % of the volume of the fuel pellet, with two disks being 20 % (Figure 5.17). However, as with the previous simulations the metallic loading has made a reduction in the amount of fuel

component. When scaled up to a fuel rod, there would be 20 % less fuel material if the fuel rod was kept the same length in all scenarios due to the stacking of the disks between each pellet.

Note, that heat generation was only applied on the centre line of the fuel pellet and not on the centre line of the Mo disks.

The simulation results in Figure 5.18, show a non-uniform thermal transfer map across the pellet. In this case the Mo disks are acting as pathways for the thermal transfer to use, meaning that less heat is transferred through the middle of the pellet. This creates different temperature zones on the outer wall of the pellet, with a temperature differential of 101°C from the middle of the pellet wall to the top at the Mo disk. The temperature drop however from the centre to the pellet wall of the disks is only 30°C. This is obviously due to the thermal conductivity of the Mo providing a direct pathway for the thermal transfer to the pellet. As can be seen in Figure 5.18, the middle of the Mo disk pellet, which is just YSZ, does have an improved heat transfer when compared with the YSZ pellet.

Long term, having a non-uniform heat distribution across the pellet when material properties, such as thermal expansion come into play, might have a more detrimental effect on the structural stability of the pellets. Having such a temperature differential along the vertical axis of the pellet would provide non-uniform heat transfer to the cladding wall also causing differences in thermal expansion. What could be envisaged is that the fuel rod might swell up at each metallic disk, and be more pronounced than what might normally be expected in a fuel rod.

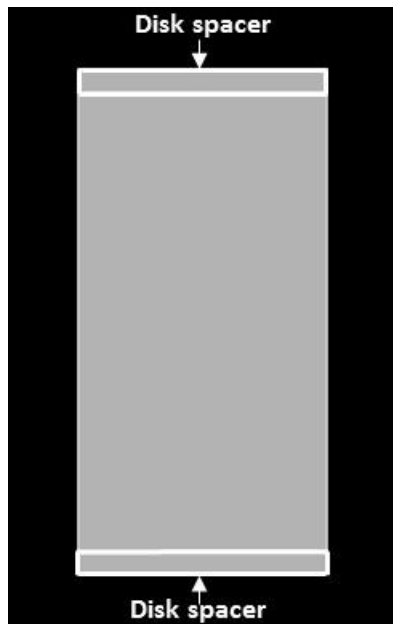


Figure 5.17 – Representation of a 2D half axis of symmetry YSZ pellet with Mo disks top and bottom in ANSYS for thermal simulation.

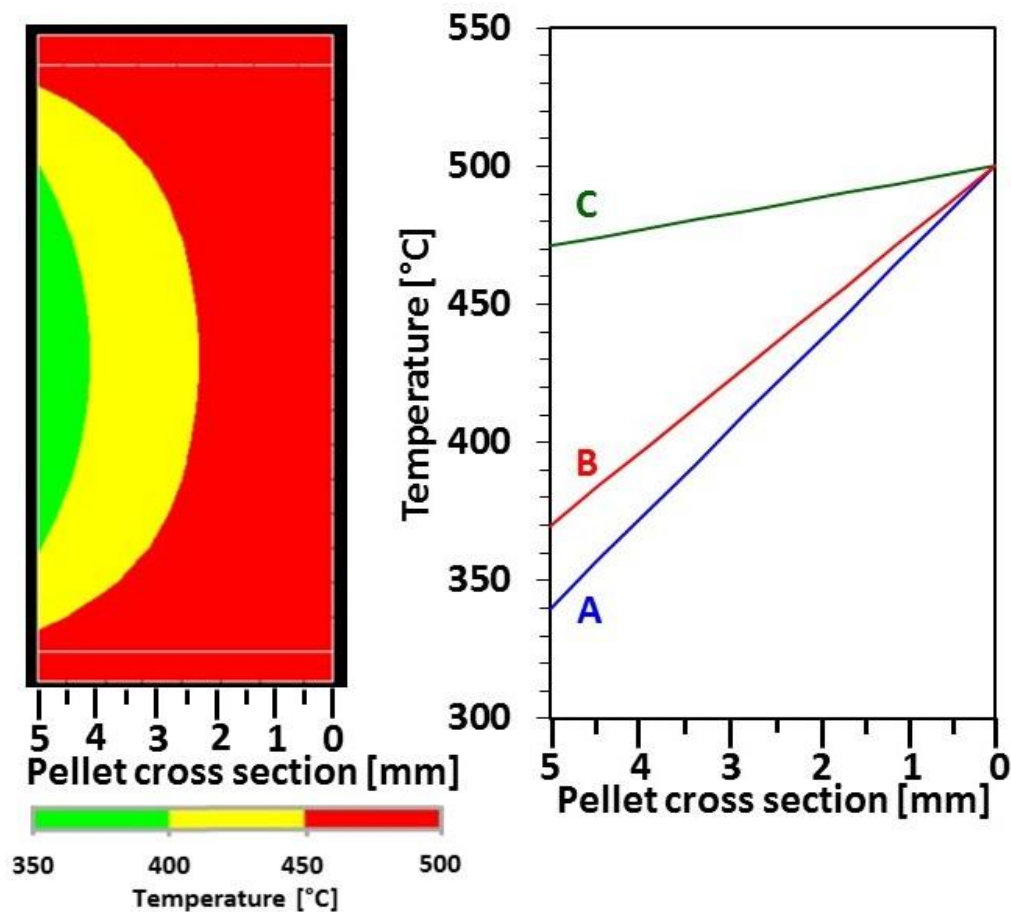
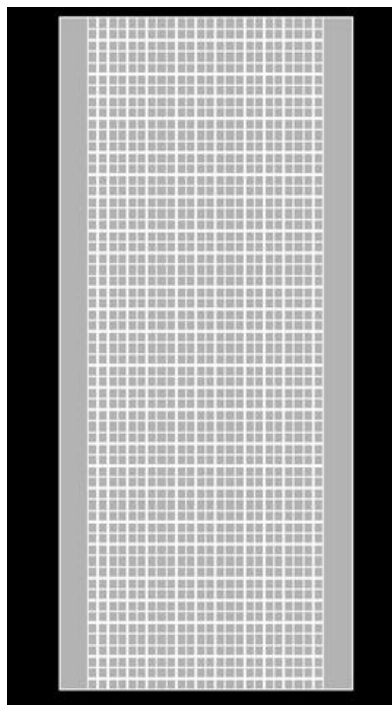


Figure 5.18 – 2D simulation of Mo disks top and bottom at steady state conditions and temperature gradient plot of A – pure YSZ pellet, B – Middle of the YSZ pellet, C – Across the Mo disks.

#### 5.5.4 Grid layout

The last simulation conducted was of a 20 % Mo in a grid arrangement inside of the YSZ pellet, Figure 5.19. Here, small wires of Mo were connected together to produce an evenly shaped grid. The idea was that this provides uniform pathways for the thermal transfer to conduct to the pellet wall. This would be a challenging pellet to manufacture with some novel techniques required. Such ways could be to use a 3D printer to layout powder material or if the wires are already formed then robotics could be used to accurately arrange a metal mesh and then YSZ powder distributed around.

The results from the simulation are shown in Figure 5.20. Here, a very uniform temperature pattern can be seen across the pellet. The pellet wall temperature is 418°C, which is the highest observed temperature uniformly across any of the simulated pellets. This shows that only an 82°C temperature drop across the pellet has occurred with it being 23 % more efficient than the YSZ pellet.



**Figure 5.19 – Representation of a 2D half axis of symmetry YSZ pellet with 20 % Mo in the form of a connect grid in ANSYS for thermal simulation.**

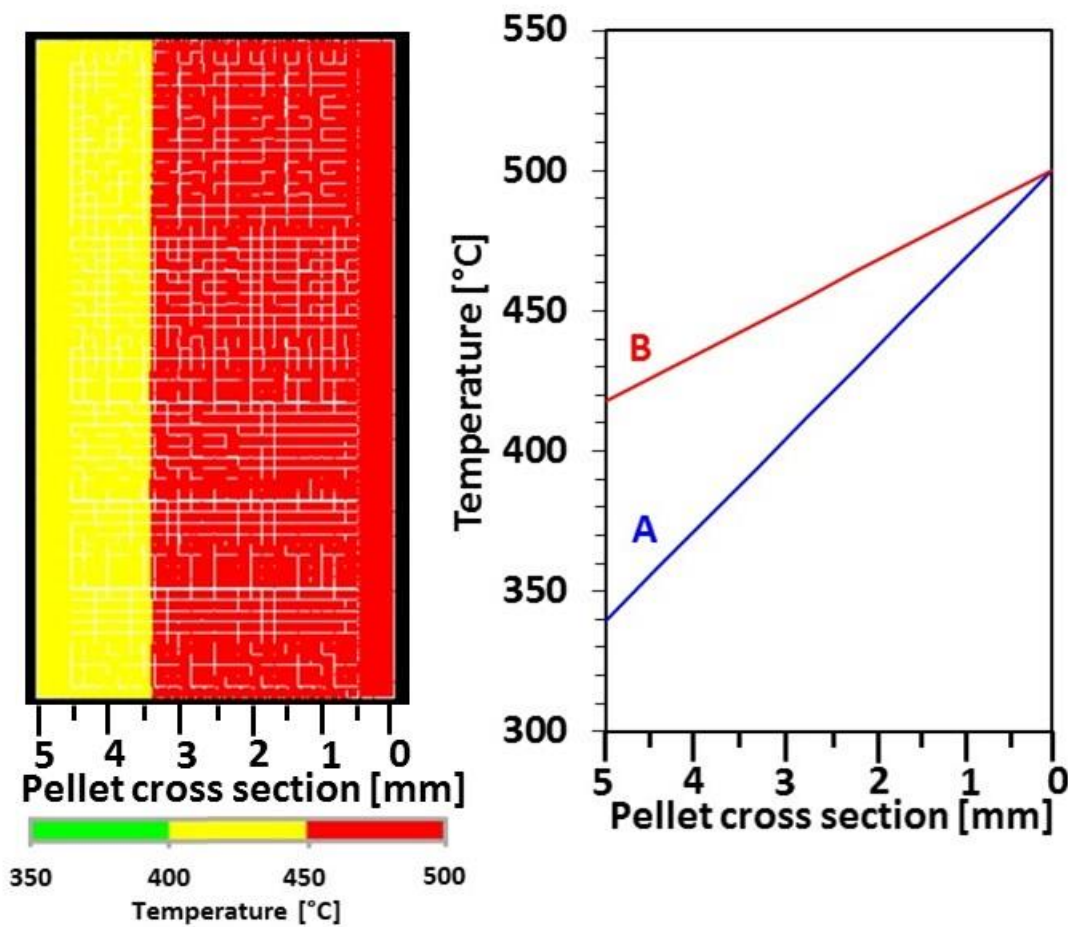


**Figure 5.20 – 2D simulation of Mo wire grid at steady state conditions and temperature gradient plot of A – pure YSZ pellet, B – Mo wire grid.**

The grid design has performed well due to Mo forming a continuous matrix through the pellet providing a higher thermal conductivity pathway, when compared with the YSZ pellet. This simulation is by far the most interesting design to take forward for further work given the uniform heat distribution across the pellet. However, one significant challenge for this design would be the construction of such a fine metallic grid as well as keeping its integrity when fabrication takes place. Namely with the fabrication route of SPS the axial pressure during the sintering process could shift the wire mesh in either direction from the vertical.

## 5.6 Comparison of simulations

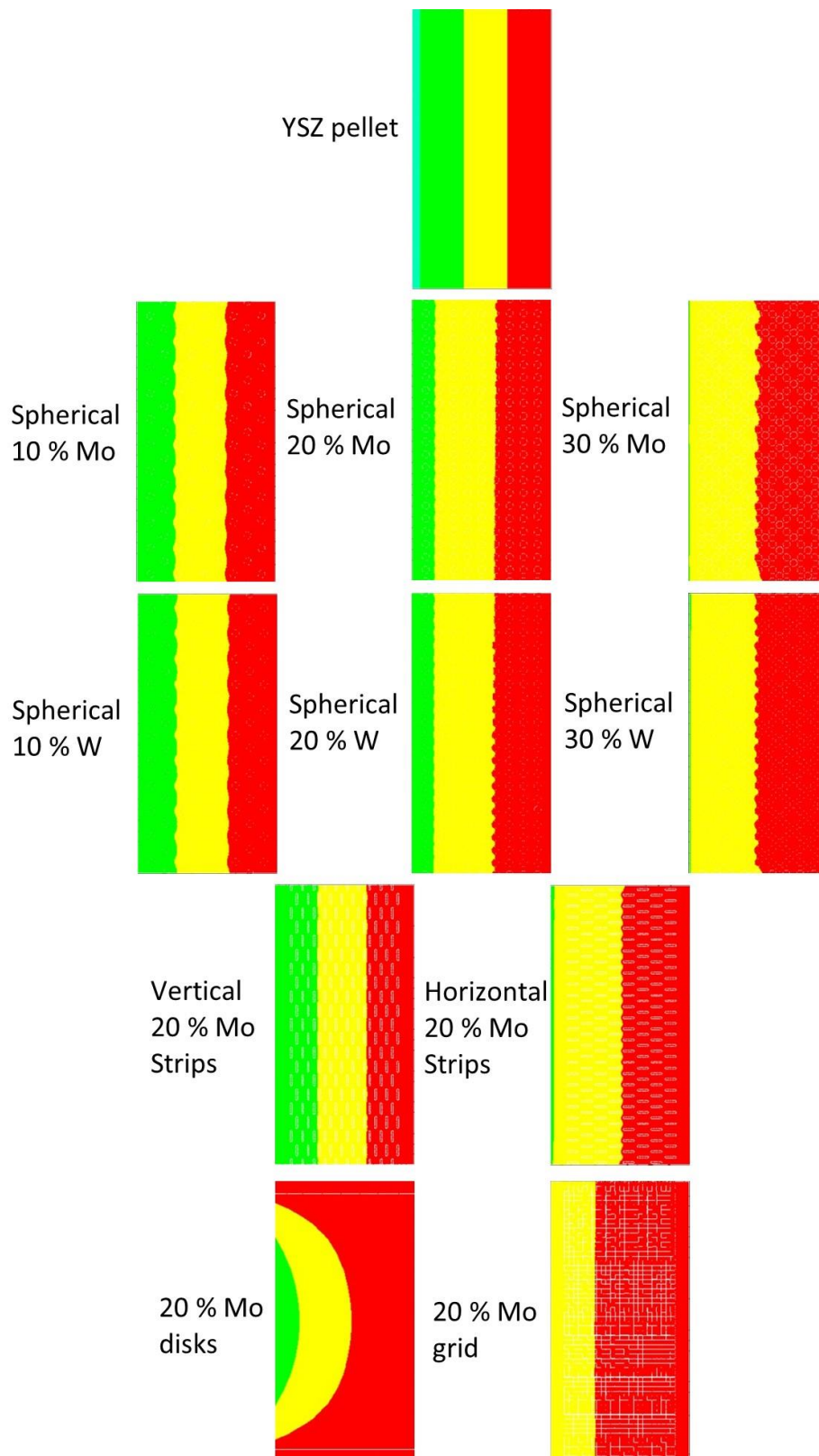


**Figure 5.21 – All simulations undertaken with a non-uniform contour plot for comparison.**

A non-uniform contour plot has been applied to all simulations carried out to obtain a visualisation comparison between them all shown in Figure 5.21. As previously discussed, the similarities between the different loading of Mo and W content in the outer wall temperature and the thermal transfer pattern across the pellet can be seen.

The vertical 20 % Mo strips simulation heat transfer is more in line with the 10% spherical simulations, and that the horizontal 20 % Mo strips arrangement is one of the most efficient designs for models with just particles.

The two most efficient thermal transfer models are of the disk design and the grid layout. These produce the highest pellet wall temperature peak and highest uniform pellet wall temperatures respectively.

One clarification is that many assumptions have been made in these simulations; however these are necessary to ensure a fair comparison of the designs of their thermal performance and not how they will truly behave through life in a reactor. Actual heat generation in a fuel pellet occurs throughout the body and not just in the centre. Therefore, these pellets would not behave exactly as demonstrated here with the thermal pattern across them, but as most of the designs are uniform patterns it shows how the heat will dissipate from the pellet no matter where the heat is generated and so the more effective designs in this work will still be most effective in reality.

Another assumption used is that the thermal conductivity is a constant value with regards to temperature for each material. This is however not the case as it decreases for the temperature ranged used. Therefore, the temperature profiles would have a steeper gradient and thus the wall temperature would be lower. However this would be the same relative to all the designs and so the ones shown to be the most effective would still be, as this work was done to compare designs, the decision on ones to take forward would still be valid.

## 5.7 Conclusions

The work in this Chapter investigated novel designs for the metallic matrix of a nuclear fuel cermet for use inside a civil marine reactor. This was conducted to determine a design that could be taken forward for further work to improve the thermal transfer across the pellet whilst keeping the metallic component as low as possible.

The metallic loading content and metallic type were studied first. Improvement in the thermal transfer was shown with increasing metallic loading, as was expected. However, more improvement between Mo and W was also expected, due to the materials having a difference in thermal conductivity of 31 W/mK, Table 6.1, and both having the same vol. % in the pellet. With no noticeable difference in the comparable simulations, it was concluded that the role of bulk material of YSZ impeded the effectiveness of the higher W thermal conductivity. Also, the arrangement of the spheres with a buffer zone on either edge could have played a role. The assumptions that have been used and discussed could also play an underlining factor in the identical results between the Mo and W simulations. Future work of more detailed simulations on the most promising designs with fewer assumption would bring to light if this has an effect. There was a noticeable difference between the vertical and horizontal orientation of the metal strips arrangement, with a 4 % and 16 % improvement between the vertical and horizontal orientations respectively. This shows that having the metallic loading in the direction of heat transfer is of significant benefit.

Metallic disks placed at the top and bottom of a pellet have immediate advantages when used for fabrication, as each component can be made separately. The results showed a good improvement of 9 % in the middle of the pellet wall and 30 % on the Mo disk wall. They also showed a nonlinear heat distribution across the pellet, which would initially be considered a negative aspect. However, a possible advantage could be achieved by the pellet clad interaction

effect, when a pellet shape resembles an hour glass or wheat sheaf, as previously discussed in fuel failure section of Chapter 3. A cooler centre would be beneficial as the top and bottom of the pellet end up having more contact with the inner clad wall of the fuel rod, due to a reduction in the hour glass effect, therefore this would reduce the effect of PCI and the risk of fuel failure.

By far, the most effective design was the use of a 20 % Mo grid across the pellet. This provided an improvement of 23 % uniformly across the pellet's outer wall compared with the YSZ pellet. The effectiveness of having the entire metallic component interconnected plays a strong role in providing pathways for the thermal transfer. The ease of fabrication of such a pellet would remain a challenge, including how to manufacture a metallic grid of such small size while also maintaining a uniform fashion during production.

Further work would include using  $\text{UO}_2$  as the bulk fuel material. The main difference seen would be the higher density and thermal conductivity values of  $\text{UO}_2$  would provide an improved temperature profile across the pellet, so not as steep, and thus for all cermet simulation would also provide an improved temperature profile than what was simulated in this work.

No account of fission products has been taken into consideration, as if  $\text{UO}_2$  was the choice fuel material, fission products would be produced through life. This would include more Mo and other elements that could either add or reduce the bulk fuel material conductivity. Therefore, work to be taken forward would be to conduct simulations that take into account the change overtime of the fuel material thermal conductivity.

In summary, this Chapter has shown how important metal morphology is to the thermal conduction of a pellet and how large gains in thermal efficiency can be achieved for the same metallic loading content. Going forward, it will be important that fuel for a civil marine reactor is required to run thermally cooler while still maintaining a high fissile loading content. The

designs of greatest interest in the future will be the metal grid for its high thermal conductivity, and the metal disk and horizontal strips due to their perceived ease of manufacture.

## 5.8 References

- [1] Y. Nakasone, S. Yoshimoto, and T. A. Stolarski, "Overview of ANSYS structure and visual capabilities BT - engineering analysis with ANSYS software," Oxford: Butterworth-Heinemann, 2006, pp. 37–50.
- [2] L. O. Alcalá, "Comparision between ANSYS and ABAQUS using ultrasonic guided waves," Ecole de Technologie Superieure, 2014.
- [3] F. Hernández, F. Cismondi, and B. Kiss, "Thermo-mechanical analyses and assessment with respect to the design codes and standards of the HCPB-TBM Breeder Unit," *Fusion Eng. Des.*, vol. 87, no. 7–8, pp. 1111–1117, 2012.
- [4] B. Bulut Acar and H. O. Zabunoğlu, "Comparison of the once-through and closed nuclear fuel cycles with regard to waste disposal area required in a geological repository," *Ann. Nucl. Energy*, vol. 60, pp. 172–180, 2013.
- [5] J. a. Webb and I. Charit, "Analytical determination of thermal conductivity of W–UO<sub>2</sub> and W–UN cermet nuclear fuels," *J. Nucl. Mater.*, vol. 427, no. 1–3, pp. 87–94, 2012.
- [6] S. Mishra, P. S. Kutty, T. R. G. Kutty, S. Das, G. K. Dey, and A. Kumar, "Cermet fuel for fast reactor - Fabrication and characterization," *J. Nucl. Mater.*, vol. 442, no. 1–3, pp. 400–407, 2013.
- [7] M. R. Esfahani, E. M. Languri, and M. R. Nunna, "Effect of particle size and viscosity on thermal conductivity enhancement of graphene oxide nanofluid," *Int. Commun. Heat Mass Transf.*, vol. 76, pp. 308–315, 2016.
- [8] D. E. Gray, *American Institute of Physics Handbook*. New York: McGraw-Hill Book Company, 1957.
- [9] M. C. Stennett, C. L. Corkhill, L. a. Marshall, and N. C. Hyatt, "Preparation, characterisation and dissolution of a CeO<sub>2</sub> analogue for UO<sub>2</sub> nuclear fuel," *J. Nucl. Mater.*, vol. 432, no. 1–3, pp. 182–188, 2013.
- [10] A. De Bremaecker, L. Ayrault, and B. Clément, "Deterioration of yttria-stabilized zirconia by boron carbide alone or mixed with metallic or oxidized Fe, Cr, Zr mixtures," *J. Nucl. Mater.*, vol. 451, no. 1–3, pp. 153–161, 2014.
- [11] International Atomic Energy Agency, *Thermophysical properties of materials for nuclear engineering: A tutorial and collection of data*. IAEA, 2008.

- [12] J. J. Carbajo, G. L. Yoder, S. G. Popov, and V. K. Ivanov, "A review of the thermophysical properties of MOX and UO<sub>2</sub> fuels," *J. Nucl. Mater.*, vol. 299, no. 2001, pp. 181–198, 2001.
- [13] C. G. S. G. S. Pillai and a. M. M. George, "Thermal conductivity of uranium dioxide," *J. Nucl. Mater.*, vol. 200, no. 1, pp. 78–81, 1993.
- [14] T. Kiguchi, *Nuclear Reactor Design*. Japan: Springer, 2014.
- [15] D. Roylance, "Finite Element Analysis," 2001.
- [16] N. Marchal, C. Campos, and C. Garnier, "Finite element simulation of Pellet-Cladding Interaction (PCI) in nuclear fuel rods," *Comput. Mater. Sci.*, vol. 45, no. 3, pp. 821–826, 2009.
- [17] ANSYS Inc., "ANSYS mechanical APDL element reference," *ANSYS Man.*, p. 267, 2012.
- [18] E. S. Bomar and H. Inouye, "Fabrication of spherical particles," 1954.
- [19] H. S. Chae, S. H. Piao, and H. J. Choi, "Fabrication of spherical Fe<sub>3</sub>O<sub>4</sub> particles with a solvothermal method and their magnetorheological characteristics," *J. Ind. Eng. Chem.*, vol. 29, pp. 129–133, 2015.
- [20] "Investment Mine Molybdenum," 2016. [Online]. Available: <http://www.infomine.com/investment/molybdenum/>.
- [21] "Investment Mine Tungsten," 2016. [Online]. Available: <http://www.infomine.com/investment/metal-prices/ferro-tungsten/>.

## **Chapter 6 Conclusions and recommendations**

## 6.1 Conclusions

### 6.1.1 Design of civil marine reactor

This thesis has investigated the design of a civil marine reactor and put forward proposals for the materials and design of the nuclear fuel for that reactor. From an examination of past uses of civil reactors for merchant shipping in Chapter 2, it was determined that a PWR reactor type would be best suited for a new civil marine reactor. This choice was primarily due to its successful past use in merchant ships and the experience and knowledge that is available for these reactor systems. As well, it was envisaged to operate the fissile fuel at low enrichment levels, <20 %, so as not to be perceived as a high proliferation risk.

The fuel type to be used in a civil marine reactor was investigated to determine the preferable composition, with the density, thermal conductivity, melting temperature, and mechanical strength all important factors considered. UO<sub>2</sub> fuel type was chosen due to the large operating experience on land and in civil marine environments. The option of using a UO<sub>2</sub> cermet was proposed in order to improve the thermal conductivity of the pellet, which was seen as an aid against fuel failure conditions.

Computational simulations of fuel rods under conditions envisaged for a civil marine reactor were conducted in Chapter 3. The fuel failure condition of fuel rod swelling was determined to be an issue if the design of the fuel rod was kept similar to current land PWR reactor systems, such as Sizewell B in the UK which is a Westinghouse design [1]. Therefore, the design of the fuel rod was investigated to prevent fuel failure mechanisms from coming into effect. Several design changes were determined to be effective. Increasing the plenum length of the fuel rod mitigated the problem of mainly FGR causing the fuel rod to swell. The use of an annular fuel pellet was also of interest as this was able to lower the FGR of the pellet. It was also shown

that increasing material properties of grain size and thermal conductivity would provide significant benefit in reducing the FGR, with an increase of 50 % showing the most potential.

Fabrication of simulant cermet fuels was undertaken in Chapter 4, with an explanation of the equipment and processes used. Data from the fuel rod simulations, Chapter 3, was used to aid the fuel design and demonstrated that improving the thermal conductivity of the fuel material would be of significant benefit. YSZ was able to be sintered using the technique of spark plasma sintering and was considered an appropriate simulant material for UO<sub>2</sub>. This was taken forward to produce two cermet types of Mo and W with three loading contents of 10 vol.%, 20 vol.%, 30 vol.% and sintering temperatures of 1300°C, 1400°C, 1500°C, and 1600°C. This technique demonstrated the ability to successfully use SPS as a method of producing stable cermets. The 4 sintering temperatures showed no difference in the material properties, such as thermal conductivity, density and hardness characterised in the research. Using SPS as the fabrication method offers rapid sintering, 5 minute temperature hold, and the ability to use lower sintering temperatures over the use of a conventional muffle furnace.

There was shown to be a 60 %, 100 %, and 200 % increase in the thermal conductivity for a 10 %, 20 %, and 30 % metallic Mo loading of the cermet samples respectively at 100°C. There was found to be lower increase for W in thermal conductivity. When compared with the simulation data from Chapter 3, a 50 % increase in the thermal conductivity would make a considerable reduction in the amount of FGR. Therefore, it is proposed that a loading content of 20 % would be a suitable option for the design of a nuclear fuel cermet for a civil marine reactor with Mo chosen as the selected metallic fuel material. This thesis is the first known systematic study of a simulant cermet fuel to be successfully studied using SPS. It has been demonstrated that stable simulant cermets of YSZ at varying metallic loading can be fabricated.

The focus of the final investigation in this thesis, Chapter 5, was to determine the extent to which the shape and design of the metal matrix in a pellet influences the thermal conductivity of a cermet. There was no applicable difference between the two metals in influencing the thermal conductivity. It was assumed that either the YSZ bulk material provides a limiting factor, or the assumptions used in the model could also have an underling effect. Having metallic material oriented in the direction of heat transfer was beneficial. This was demonstrated with metal strips in the horizontal direction, metal disks above and below the simulant fuel pellet, and having a grid arrangement inside the fuel pellets. The most promising of these options for further consideration is the use of metal strips or metal disks due to ease of fabrication.

### **6.1.2 Fuel design for civil marine reactor**

The work presented in this thesis has considered the fuel to be used in a civil marine reactor from several approaches. From the culmination of this work a determination of the requirements for a civil marine reactor has been made, as outlined in Table 6.1. A PWR reactor was used for the reasons outlined above, and in particular the large amount of operational experience available. The nuclear fuel chosen was  $\text{UO}_2$ , with an average enrichment of 10 %. The fuel type was a cermet fuel type due to the benefit of improved thermal conductivity. A cermet with  $\text{UO}_2$  and 20 % Mo by volume was chosen after evaluation of potential cermet compositions, and should be used in the form of metal strips or disks above and below the pellet.

The power requirement for the civil marine reactor was determined from the cargo container ship Emma Maersk at 110 MWe, one of the largest container ships in the world [2], and it was assumed that it would be able to meet the power levels of most of the world's fleet. The plenum length for the fuel rod was 0.25 m in order to accommodate any build up in pressure from fission gas release.

**Table 6.1 – Proposed design criteria for civil marine reactor, developed by the research conducted in this thesis.**

<b>Property</b>	<b>Value</b>	<b>Units</b>
<b>Reactor type</b>	PWR	
<b>Cladding material</b>	Zircaloy-4	
<b>Power</b>	110	MWe
<b>Efficiency</b>	33	%
<b>Core diameter</b>	3.5	m
<b>Refuelling period</b>	15	years
<b>Cladding radius inner/outer</b>	4.1707/4.7422	mm
<b>Coolant Pressure</b>	15.513	MPa
<b>Coolant inlet temperature</b>	281	<sup>o</sup> C
<b>Target coolant exit temperature</b>	310	<sup>o</sup> C
<b>Fuel type</b>	UO <sub>2</sub> /20 % Mo	
<b>Enrichment of fuel</b>	10	%
<b>Fuel stack length</b>	2.7	m
<b>Fuel pellet radius</b>	4.94	mm
<b>Fuel pellet length</b>	13.691	mm
<b>Plenum length</b>	0.25	m
<b>Internal gas composition</b>	97.09 He, 2.91 N	%
<b>Average grain size of fuel</b>	11	μm

## **6.2 Recommendations for further work**

This section discusses a few key areas that could be further explored in order to develop the fuel to be used in a civil marine reactor, as well as other areas of investigation to facilitate the design of a ship using a civil marine reactor.

### **6.2.1 Fabrication of zirconium pellets with metallic material in different forms**

The work in Chapter 5 of using metallic material in different forms would be combined with the SPS conditions that were used for the YSZ 20 % Mo simulant pellet in Chapter 4, in order to fabricate simulant cermet pellets with the metallic component in the form of metal strips, disks, and spherical particles. Although the spherical particles were not the most improved

design with regards to thermal efficiency, they are envisaged to be easy to fabricate and would be useful to validate against the simulated results.

### **6.2.2 Fabrication of uranium cermets by SPS**

The matrix of pellets fabricated and characterised in Chapter 4 provided an ideal composition and sintering condition, which was a YSZ Mo 20 % simulant pellet with a hold time of 5 minutes and hold temperature of 1300°C. Therefore, the next step would be to use these same conditions using UO<sub>2</sub> as the ceramic material in the cermet, as well as to fabricate a pure UO<sub>2</sub> pellet. These two pellets could then be characterised in the same way as the simulant pellets were in Chapter 4, with thermal analysis using laser flash, hardness and density measurements, and XRD and SEM to confirm that a cermet exists. More care would be required due to the use of an active material. All powder preparation, removal of graphite paper and cutting of the pellet would need to be done inside a glove box.

### **6.2.3 Grain size investigation**

The importance of the grain size of the fuel material in respect to fission gases being retained was discussed in Chapter 3. The process of a fission gas leaving the grain is a random event, thus the larger grain size reduced the chance of the gas particle finding a pathway out.

The grain size is a material property that is influenced by the sintering hold time. It is proposed that YSZ Mo 20 % cermets using SPS at a range of hold times be explored. Each pellet would use the same hold temperature of 1300°C to determine how effective this would be at growing the grain size. Hold time with increments of 5 mins could be used.

### **6.2.4 Ansys fuel pellet simulations**

The simulation designs with the most promise in Chapter 5, such as the spherical particles for ease of manufacturing, metallic disks, and the metallic grid design, could be taken forward to be simulated with UO<sub>2</sub> fuel material properties to further develop their behaviour. Thermal

conductivity data over the temperature range used should also be included to further improve and reduce assumptions in the model. A further step would be investigating the build-up of fission products inside the pellet and modelling that by determining what the reduction/increase in thermal conductivity might be over the lifetime of the fuel pellet.

### **6.2.5 Reactor design**

The research presented in this thesis has focused on improving the thermal efficiency of the fuel for a civil marine reactor. For this work to be taken forward, analysis regarding the neutronics of the proposed reactor core is needed to see how the improved thermally conductivity would affect the system. Having a more thermally efficient system would allow the fuel rods to deliver more energy in the form of heat to the coolant. To accommodate this, the coolant could be passed through at an increased rate, or the fuel rods could run at a lower power. This could potentially give a longer life to the fuel in the reactor.

How the reactor should be fuelled will be an important decision to be made. The options are to use a PWR reactor design that would be refuelled by removing each fuel assembly one at a time, or the use of a marine modular reactor [3], where the entire reactor core would be removed and replaced with a new one, not too dissimilar to the concept of a battery. The advantage with a modular design would be the reduced risk of accident during refuelling, as only one unit would be handled, albeit larger, rather than many smaller fuel assemblies. The modular reactor could then be stripped down in a secure location, rather than on the ship.

The ship design would need to be considered from a naval architecture view point. Firstly, an analysis of the placement of the reactor would need to be undertaken with regards to the concepts discussed in Chapter 1 of locating the reactor in the middle or stern of the ship. Secondly, the placement of the reactor, if based on the cargo ship Emma Maersk, would need

to avoid interference with the operation of the ship, as previously occurred with the NS Savannah, thereby avoiding detriment to the economic model.

### 6.2.7 Other research areas

Chapter 1 briefly discussed different research areas that could be investigated further in regards to the concept of a civil marine reactor. These areas included training and regulation of crew to operate the ship's reactor, insurance models, ownership for the lifetime of the vessel, political considerations and security. Additional areas to research would be waste disposal of the civil marine reactor, which state would take ownership of the nuclear waste, and the flag country of the ship, ship builder or ship owner? If the norms of nuclear licencing for any new reactor built in the UK are used [4], then the end of life of the fuel, reactor, and nuclear waste would also need to be planned before anything could be built and operated.

## 6.3 References

- [1] D. R. Davies, A. C. Roberts, and D. Ness, "A review of the design and construction of the Sizewell B pressurized water reactor building containment structures," *Nucl. Eng. Des.*, vol. 156, pp. 259–268, 1995.
- [2] H. N. Psaraftis and C. A. Kontovas, "Ship speed optimization: Concepts, models and combined speed-routing scenarios," *Transp. Res. Part C*, vol. 44, pp. 52–69, 2014.
- [3] S. E. Hirdaris, Y. F. Cheng, P. Shallcross, J. Bonafoux, D. Carlson, B. Prince, and G. A. Sarris, "Considerations on the potential use of Nuclear Small Modular Reactor (SMR) technology for merchant marine propulsion," *Ocean Eng.*, vol. 79, pp. 101–130, 2014.
- [4] A. Bredimas and W. J. Nuttall, "An international comparison of regulatory organizations and licensing procedures for new nuclear power plants," *Energy Policy*, vol. 36, no. 4, pp. 1344–1354, 2008.

## Appendix 1 Experimental Techniques

### A1.1 Density measurements

Density measurements were carried out on the green powder before fabrication and then on the fabricated pellets:

#### A1.1.1 Gas Pycnometer

A Micromeritics AccuPyc II 1340 gas pycnometer was used to measure the density of green powders before they were made into batches as previously described in the powder preparation. Each raw powder was measured out to 0.1 g using a glass shielded balance.

A gas pycnometer was used, as it provides a means of non-destructive technique combined with a high accuracy [1]. Helium was used as the displacement fluid for the gas pycnometer, as it is inert and easily able to penetrate all the voids in between the powder [2]. An inert fluid was used so that no reaction took place between the fluid and the material being measured. This enables the gas pycnometer to utilise the ideal gas equation to calculate the density:

$$pV = nRT$$

In the above equation,  $p$  is the pressure,  $V$  is the volume,  $n$  is the number of moles,  $R$  is the Reynolds number and is a constant, and  $T$  is the temperature in kelvin. For this application,  $n$ ,  $R$ ,  $T$ , and  $p$  are known values with the  $V$  being calculated from the amount of gas able to be held in the chamber with the powder due to the chamber size being known. Therefore the volume of the powder can be determined and with the measured mass of the powder the density can be calculated from  $\rho = \frac{m}{V}$ .

The mass of the sample was measured before it was placed into the sample chamber in the gas pycnometer using a glass shielded balance. The volume of the sample was determined by the

equipment from the displacement of the cell [3]. Measurements were repeated 25 times with an average result being used.

### **A1.1.2 Archimedes principle**

The density of fabricated pellets was calculated using the Archimedes principle using a Mettler Toledo balance with density kit. The weight of each sample is measured first in air on the balance and then in the medium of water also on the balance, Figure A1.1. The difference between the weights due to the buoyancy of the sample material can be used to calculate the density by dividing the weight in air by the difference of in air and in water values. Each sample was measured in triplicate.

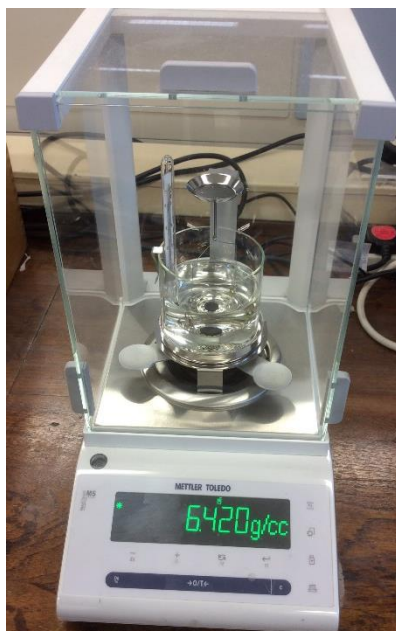


**Figure A1.1 – Mettler Toledo balance with density apparatus.**

### **A1.1.3 Geometric**

Densities of fabricated pellets were also calculated by geometric methods. The diameter and thickness of each sample disk were measured using a digital vernier caliper and the weight of each sample was measured on a glass wall enclosed balance. Using the volume and weight of the sample densities were then calculated. All measurements were undertaken in triplicate.

## **A1.2 Particle size analysis**

Particle size analysis of each raw powder was undertaken to determine the initial average sizes of powder before they were mixed. A Malvern Mastersizer 3000, a laser diffraction particle size analyser, was used for this procedure. This particle analyser fires a laser onto the particles, which diffracts the beam, and the intensity of scattered light as a material passes through determines the size of the particle [4].

The dispersion fluid used was distilled water with 0.5 g of material used for each run depending on how visible the powder was to the laser. Sonication was used on the dispersant liquid in order to prevent it from clumping together with measurements being carried out in triplicate. Background measurements were carried out on the dispersant water to adjust the measurements taken for the sample.

## **A1.3 Laser flash**

Laser flash technique is one of the most common methods used for measuring the thermal conductivity of different types of materials [5]. This technique was first developed by Parker et al. as a fast method of determining the thermal properties of samples [6]. The method uses a laser to provide a heat source that is applied onto one side of a sample whilst an infrared detector determines the change in temperature against time on the other side of the sample. From this, the thermal diffusivity can be calculated, meaning the measure of heat propagation through a sample, and the specific heat capacity can be determined by comparing the temperature rise of the sample to that of a reference sample of known specific heat.

The thermal conductivity ( $\lambda$ ) sample can be calculated using the thermal diffusivity ( $\alpha$ ), specific heat capacity ( $C_p$ ) and density ( $\rho$ ) of a sample with the following relationship:

$$\lambda = \alpha C_p \rho$$

The laser flash equipment used for this testing was a Netzsch LFA 457 MicroFlash, Figure A1.2. This was setup to test from a temperature range of between 0°C and 1100°C. The unit houses an auto sample changer capable of holding 3 samples inside a furnace. On top of the unit is a liquid nitrogen dewar to provide cooling for the temperature sensor. The laser is positioned at the bottom below the sample changer. The unit is connected to vacuum pump and gas input. For testing, nitrogen was used as an inert flow gas through the unit at a throughput of 100 ml/min. This was done to remove any oxygen in the furnace, and thereby prevent any reaction with the samples.

Samples were prepared for laser flash analysis by applying a thin graphite coating with a spray can. Each sample was coated three times on each side. The graphite coating was to enable a uniform conductive surface for both sides of the pellet. The thickness of the coating was very small so as not to incur any significant error on the results.

A standard sample with known thermal properties was run at periodic times throughout the testing period. This sample was a ceramic material and was supplied by the manufacturer.

Prepared samples were loaded three at a time into the sample auto changer for a run. The system was flushed with nitrogen gas and the liquid nitrogen dewar filled, both allowed to settle for 15 minutes before commencing the run. Samples were heated from room temperature to 1000°C at a ramp rate of 5°C/min to 400°C and then at 10°C/min to 1000°C with testing at 100°C and then at 100°C intervals, with 5 measurements taken for each interval for each sample. Once the run had been completed the system was cooled to room temperature at 20°C/min.

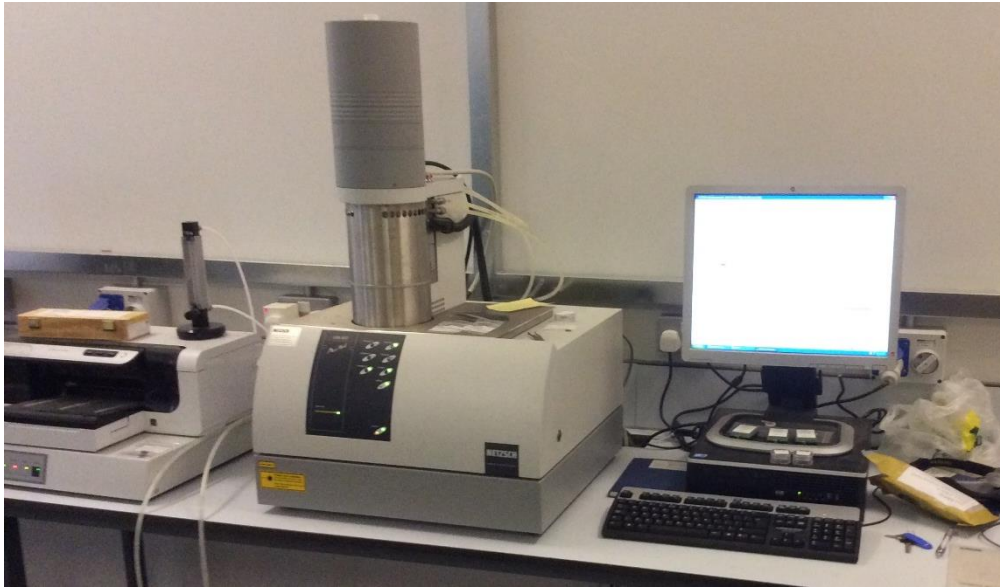


**Figure A1.2 – Laser flash equipment centre with controller left and control computer right.**

The pure stabilised YSZ samples were found to shed their graphite coating during the laser flash process and provided erroneous results at the higher measured temperatures. So a gold coating was applied to the top and bottom surface using a Peltier cooled sputter coater, Figure A1.3. Tape was applied around the sides to ensure no gold was deposited. This was to prevent errors of the heat from the laser passing around the sides quicker than through the middle of the sample.

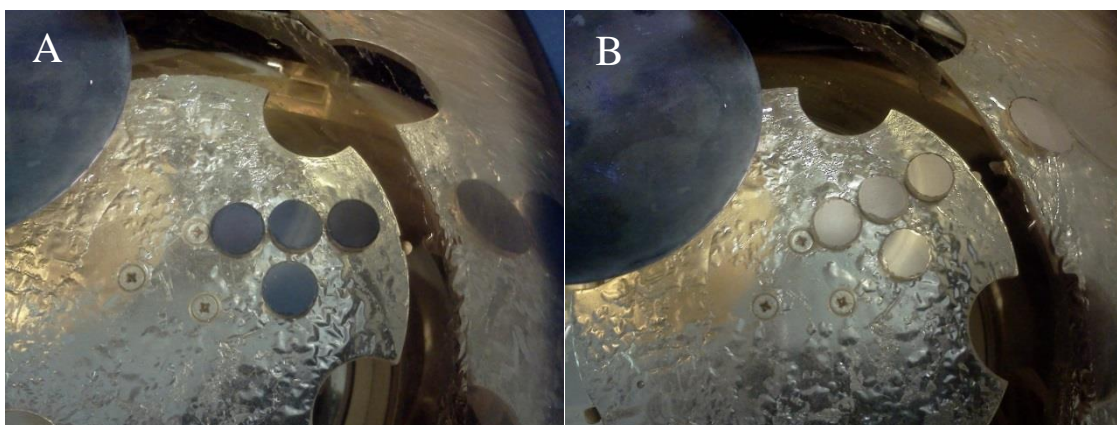


**Figure A1.3 – A – YSZ pellets setup inside peltier coater before gold application, B - YSZ pellets after peltier gold application.**

## A1.4 X-ray Diffraction

X-ray diffraction (XRD) was carried out to determine the composition of all the fabricated pellets, as well as the green powders. All runs were conducted at  $2\theta$  angles between  $20^\circ$  and  $80^\circ$  at  $1.04^\circ/\text{min}$ .

A D2 PHASER by Bruker was used, Figure A1.4, which is a desktop XRD that can use a small amount of sample powder in order to carry out analysis. This XRD was chosen for analysis as the compositions were expected to be crystalline with no complicated phases.

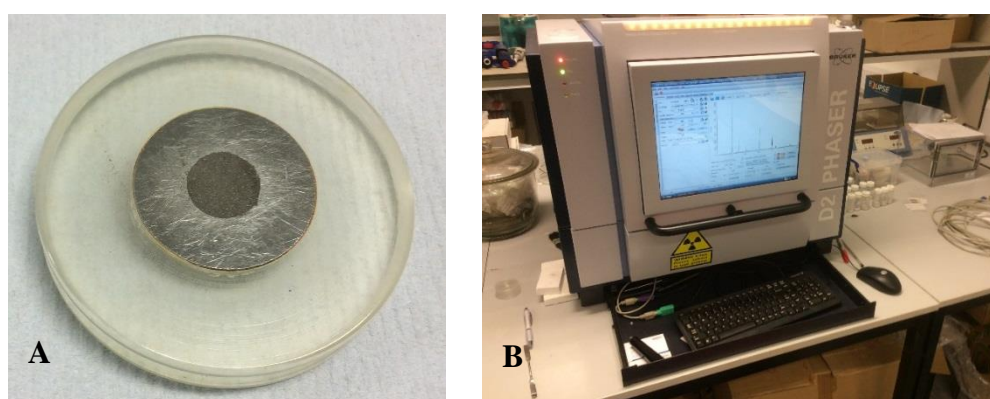


**Figure A1.4– A – Sample holder with powder specimen for use in XRD, B – XRD D2 PHASER that was used for the analysis.**

X-ray diffraction is a technique that utilises the scattering of X-rays directed at a crystalline sample in a beam at given angles, determined by the crystal structure, in accordance with Bragg's law and which can be registered by a detector. X-rays are used as they are a form of electromagnetic radiation, their energy is high and their wavelength is short and in the order of atomic spacing for solids [7].

Bragg's law refers to the equation:  $n\lambda = 2d\sin\theta$ . This equation was derived by W.L. Bragg, with ( $\theta$ ) representing the X-Ray incident angle or scattering angle, ( $\lambda$ ) refers to the X-Ray beam wavelength, ( $d$ ) is the distance between the crystal lattice planes, with ( $n$ ) being the order of reflection and any integer. The intensity of X-rays detected from the scattering of a given sample can be monitored for when the Bragg equation is satisfied (when there is constructive

interference) [7]. As known elements and compounds each have a unique scattering angle, an X-ray intensity at given angles can be used to match known phases from reference to diffraction patterns from a database.

### **A1.5 Scanning Electron Microscopy (SEM)**

SEM was used to image green powder particles as well as all fabricated samples. A Phillips XL 30 FEGSEM and a Hitachi TM3030 desktop SEM, Figure A1.5, were used to carry out this analysis. This was done for imaging of the microstructure of samples and for using energy-dispersive X-ray spectroscopy (EDX) to obtain information of the material compositions.

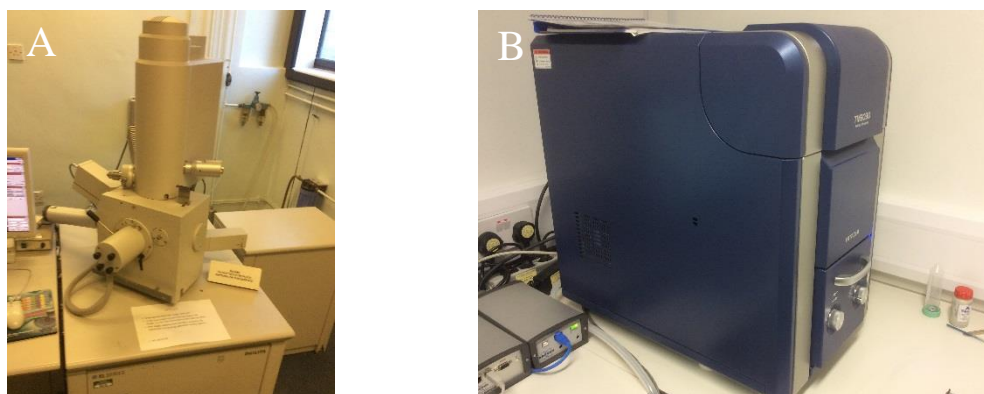


**Figure A1.5 – A – Phillips XL 30 SEM, B – Hitachi TM3030 desktop SEM that were both used to carry out analysis.**

SEM is used over conventional optical microscopy because of the magnification that is possible and it can also be used for elemental identification. A beam of electrons is generated via an electron source/gun such as a field emission gun that is used to scan the surface of a sample [7]. The beam of electrons, once generated, passes through a series of steps in order to make it useful before the beam hits the sample surfaces. These being aperture, condenser and objective lens in order to control the diameter of the beam and focus it, Figure A1.6 [8].

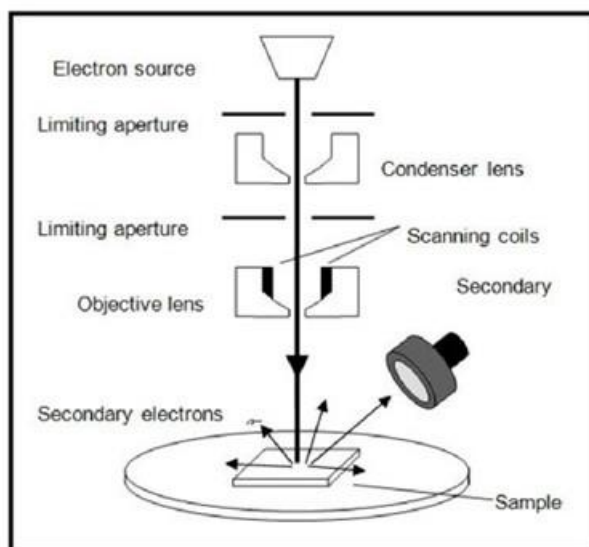


**Figure A1.6 – Schematic of an SEM [8].**

The energy that electrons are accelerated to is variable and depends on the power available of the equipment. For this work imaging was carried out at 15 keV and 20 keV on the Hitachi and Phillips, respectively.

When the beam of electrons interacts with the sample surface, secondary electrons are produced, as well as backscattered electrons (BSE). Imaging was primarily carried out with BSE, which result from a deflection of electrons from an atom on the sample that lose very little energy. The signal intensity of these electrons is proportional to the atomic number of the material interacted with and so different elements can be determined.

All samples were carbon coated in order to increase the conductance on the sample surface for electrons to travel through. Samples were first mounted onto an aluminium stub with all fabricated samples ground and polished down using a manual polishing wheel. Samples were cleaned in a sonic water bath before being carbon coated using a Gatan Inc. PECS, Figure A1.7, for 3 minutes each, and using a rotate and rock setting to obtain good coverage across the whole sample. Silver paint was then applied from the edge of the sample down to the stub to allow a conductive path for electrons to pass. If this had not been carried out, then electrons in a low

conductive sample would build up and the detector would saturate due to the intensity of the electrons. Alternatively lowering the operating voltage can help reduce this effect too, however the image quality would suffer.



**Figure A1.7 – Gatan Inc. PECS used for carbon coating samples for SEM.**

The SEM technique of energy-dispersive X-ray spectroscopy (EDS) was used to determine if stable cermets were fabricated by determining the elemental composition. EDS analyses emitted X-rays from atoms when electrons return to the ground state after being excited by the SEM electron beam. Each X-ray emitted has a characteristic energy relevant to the element it has been emitted from and this can be used to determine the composition of a sample [9]. For this investigation EDS maps were conducted of areas of interest that showed clear lines between different elemental regions observed by SEM. Runs were conducted for 5 minutes as this was determined to achieve an appropriate amount of data as clear maps were produced. A1.6 Vickers hardness.

The Vickers hardness of each sample material was carried out to determine the variation between composition and heating temperatures of the samples. This is not a material property but more a characterisation of a material's resistance to indentation. From knowing the hardness of a material, the yield stress can be inferred [10].

Vickers hardness testing was chosen as it is a form of non-destructive testing. Also, it was chosen over other types of types of hardness testing such as Knoop and Rockwell due to the availability of testing equipment available [10].

The Vickers hardness testing was carried out on a micro Vickers CV instrument tester, Figure A1.8, which conforms to EN-ISO 6507 standard for Vickers hardness testing. Samples were first aligned using the microscope of the indenter to bring the material into focus, and to identify a suitable region on the sample surface to test. Smooth areas were preferable and testing with areas of cracks, sample edge or other indentations were avoided. Once an area was identified, the indenter was aligned above the sample and a diamond shape indentation was made into the material. Indentations were held for a period of 10 seconds with a force of 10 kgf set equating to 98 N.

The two diagonal lengths were measured from the indent using the microscope, and the average of these was calculated. The sloping surface area of the indentation is calculated from the indenter being a diamond shape with an angle of  $136^\circ$  between surfaces. The load used is then divided by square indentation in mm to determine the Vickers hardness HV.

Periodic testing with a standard steel material was carried out to confirm that the equipment was accurately measuring throughout the testing process. Each sample had five good measurements taken with the average being used.



**Figure A1.8 – Vickers hardness tester used for characterisation work.**

### **A1.7 XAS spectroscopy**

X-ray absorption spectroscopy (XAS) was used to determine the oxidation state of fabricated samples using the technique X-ray absorption near edge spectroscopy (XANES). This was done to confirm that the metallic component of the samples was not oxidised.

This characterisation was carried out at the Brookhaven National laboratory (BNL) using the National Synchrotron Light Source (NSLS). XANES is a technique that measures the linear absorption coefficient of a material, which is the amount of x-rays or gamma rays that is scattered or absorbed by a material.

A synchrotron uses a linear particle accelerator to produce electrons from a cathode ray tube, to then accelerate them up to high energy. These are then fed into a storage ring that uses magnets and a symmetric shape to control the electrons into a prescribed shape forming an electron beam, with there being straight and curved sections to the ring. The magnetic bending

of the electrons cause them to follow circular arcs generating synchrotron radiation. Power is supplied along straight sections to replace the energy lost from the synchrotron radiation.

The synchrotron radiation is then channelled out of the storage ring and passes through a series of mirrors and a monochromatic correcting divergence, and focuses to form a beam and to turn white light into monochromatic light, respectively. The radiation beam is then sent to the experiment station. For XANES, the x-ray from the radiation, at the correct binding energy of electrons on the sample, will eject them out and is known as the absorption edge. This is then used to compare samples of the element of interest at different oxidation states to determine the state it is at by looking at the absorption edge pattern [11]. For this work, known samples at different oxidation states were tested and compared to samples of selected fabricated samples to determine the oxidation state of the fabricated samples.

These experiments were carried out by members of my research group that had time on the light source. Sample preparation was carried out by myself by determining the amount of material required which was then mixed with a non-reactive element powder. This powder was then pressed into pellets that were taped onto a film and holder for ease of handling.

## A1.8 References

- [1] O. Ast, M. Perez, and S. Carlet, "PuAl alloys density measurements using gas pycnometer: First results," *J. Alloys Compd.*, vol. 444–445, no. October 2006, pp. 226–229, 2007.
- [2] H. J. B. Couto, P. F. A. Braga, and S. C. A. França, "Use of gas pycnometry for estimating the iron content in mineral samples," *Miner. Eng.*, vol. 39, pp. 45–47, 2012.
- [3] J. Thudium, "A Gas Pycnometer (microliter) for determining the mean density of atmospheric aerosol particles," *J. Aerosol Sci.*, vol. 7, no. 2, pp. 167–173, 1976.
- [4] Z. Stojanovic and S. Markovic, "Determination of Particle Size by Lase Diffraction," *Tech. - New Mater.*, vol. 21, pp. 11–20, 2012.
- [5] S. Min, J. Blumm, and a. Lindemann, "A new laser flash system for measurement of the thermophysical properties," *Thermochim. Acta*, vol. 455, no. 1–2, pp. 46–49, 2007.

- [6] W. J. Parker, R. J. Jenkins, C. P. Butler, and G. L. Abbott, "Flash method of determining thermal diffusivity, heat capacity, and thermal conductivity," *J. Appl. Phys.*, vol. 32, no. 9, pp. 1679–1684, 1961.
- [7] W. D. Callister, *Materials Science and Engineering an Intorduction*, 7th ed. New York: John Wiley & Sons, 2007.
- [8] J. Goldstein, D. E. Newbury, D. C. Joy, C. E. Lyman, and P. Echlin, *Scanning electron microscopy and X-ray microanalysis*, 3rd ed. New York: Springer, 2007.
- [9] University of California Riverside, "Introduction to Energy Dispersive X-ray Spectrometry (EDS)," *Cent. Facil. Adv. Microsc. Microanal. Manuals*, vol. 2013, no. June 6, pp. 1–12, 2011.
- [10] A. E. Giannakopoulos, P. L. Larsson, and R. Vestergaard, "Analysis of Vickers indentation," *Int. J. Solids Struct.*, vol. 31, no. 19, pp. 2679–2708, 1994.
- [11] J. E. Penner-Hahn, "X-ray absorption spectroscopy in coordination chemistry," *Coord. Chem. Rev.*, vol. 190–192, pp. 1101–1123, 1999.